Silica Nanoparticles as a platform for intelligent cofactor immobilisation for biosynthetic applications

by

Rowan McDonough

Thesis
Submitted to Flinders University
for the degree of

BSc (Nanotechnology) (Honours)

College of Science and Engineering

July 2020

Declaration

‘I certify that this thesis does not incorporate without acknowledgement any material previously submitted for a degree or diploma in any university; and that to the best of my knowledge and belief it does not contain any material previously published or written by another person except where due reference is made in the text.’

Rowan McDonough

Acknowledgements

It has been a great privilege and opportunity to undertake this work. I must acknowledge Flinders University for awarding me the Flinders University Research Scholarship Award which has allowed me to undertake this research.

I would also like to acknowledge and thank David Lewis for being my supervisor and mentor throughout the years. I like to think that a bit of your genius has rubbed off on me and do my best to apply aspects of your wisdom in all parts of my life. You have also been instrumental in developing my science communication skills which has been very rewarding for me.

I would like to thank Colin Scott, Carol Hartley and Nigel French from the CSIRO in Canberra. Their support, guidance and access to the opportunity to undertake aspects of my research in their facilities was truly crucial to my work. I would also like to thank Charlotte Williams and Andrea North and Quentin Churches from the CSIRO in Clayton for synthesising and purifying the functionalised NAD.

To the many research group members throughout the years, Anirudh Sharma, Daniel Gruszecki, Jeremiah Toster, Sean Clark, Chris Hassam, Rebecca Norman, Andrew Blok, Stefan Martino, Kaili Stacey, I would like to thank you for your encouragement, friendship and thought-provoking discussions. I would especially like to thank Daniel Mangos and Oskar Majewski. You boys were always an excellent source of knowledge, constructive criticism and good mates. A big thank you to Oskar for commenting on the first draft of my thesis while on holidays in Poland.

I would like to thank my family, especially my mother Jan for putting up with me. To my partner Stefania, thank you for also putting up with me. You and your family, Aneta, Gabriela and Robert, have been a wonderful support throughout the years and for that, I am very thankful. You were also a big bloody distraction, but I'll forgive you. I would also like to thank my dog, Doggie, for always greeting me at the door when I got home, even on the late nights.

Lastly, I would like to thank Catherine Abbott for allowing me to use your plate reader which completely revolutionised my PhD and allowed me to generate a lot of data very quickly.

Summary

Immobilisation of NAD onto the surface of solid support materials such as nanoparticles facilitates in situ regeneration, recovery, re-use, stabilization and simplified product separation in biosynthetic applications. However, previous examples of surface tethered NAD have utilised non-specific attachment routes, leading to relatively low efficiencies when applied to enzymatic reactions. These investigations also neglect to analyse the kinetics of the interfacial enzymatic catalysis of the immobilised NAD in comparison to the kinetics of the equivalent freely diffusing NAD reaction.

This thesis reports the highly specific covalent surface tethering of NAD, which has been modified with long linker arms at the N^6 position, containing terminal functionality that is complementary to the functionality of our platform material, silica nanoparticles. The length and flexibility, as well as the chemical location of the tether arm on the N^6-linked-2AE NAD has been carefully engineered in order to allow NAD to retain maximum activity and dynamic interactions in enzymatic catalysis reactions once tethered.

A modified one-pot Stöber method was used to synthesise thiol terminated SiNPs and an ethanolic version used to prepare vinyl terminated SiNPs. This ethanolic method was also found to be capable of producing SiNPs from organosilanes containing various hydrophobic R groups. The growth of these hydrophobic SiNPs was explored and the effects of silane precursor, solvent concentration, pH and growth kinetics investigated.

N^6-linked-2AE NAD containing thiol and vinyl terminal functionality was then covalently tethered to the surface of vinyl and thiol terminated SiNPs via a simplistic yet robust thiol-ene ‘click’ reaction. The attachment density of NAD on the SiNP surfaces was determined to reach 0.5 attachments/nm^2 using a quantitative ATR-FTIR technique, where the Si-O-SI vibrational mode of the SiNPs is used as an internal standard and the C=O band of NAD is sampled.

Tethered NAD is then enzymatically reduced, the rate of which is tracked using a resazurin/PMS^+ coupled reaction, allowing highly sensitive and accurate fluorescence detection. This allowed measurement of enzyme activity at very low enzyme

concentrations, where the rate of enzymatic reduction of tethered NAD was found to be greater than that of freely diffusing NAD. By combining Langmuir adsorption kinetics with classical Michaelis-Menten kinetics concepts, a kinetic rate equation was derived describing the rate of tethered NAD reduction as a function of both enzyme and NAD concentration. Application of the Langmuir adsorption isotherm and reaction rates as a function of enzyme concentration to this rate equation revealed a kinetic enhancement in the reduction of tethered NAD compared to freely diffusing NAD for two different enzymes. Similar results were obtained when the kinetics were analysed as a function of NAD concentration, which also considered the inhibition of the reaction by the increasing concentration of SiNPs. Investigation of the surface characteristics of the tethered NAD surfaces and enzymes by molecular dynamics simulations allowed a mechanism of the observed kinetic enhancement to be proposed.

Tethered NAD is then enzymatically regenerated in a multi-enzyme reaction system and mathematical modelling used to analyse the reaction kinetics, revealing a similar kinetic enhancement in the catalysis of tethered NAD compared to freely diffusing NAD.

Lastly, the thermal stability of NAD is investigated and compared to freely diffusing NAD, revealing a large enhancement in half-life at two different temperatures.

In summary, the specific covalent attachment of N^6-linked-2AE-NAD to the surface of SiNPs has been demonstrated, with accurate determination of surface attachment density. In depth kinetic analysis by two different strategies has revealed a kinetic enhancement in the rate of enzymatic catalysis of tethered NAD compared to freely diffusing NAD. This, along with the ability of the tethered NAD to be enzymatically regenerated, as well as its demonstrated enhanced thermal stability makes it an ideal candidate for the integration into NAD dependent biosynthetic pathways.

Dedicated to

Jan and Stefania

Table of Contents

List of Figures

List of Tables

CHAPTER 1 : INTRODUCTION

Motivation

Enzyme catalysed reactions offer highly specific and efficient routes to the synthesis of a wide range of valuable chemicals. Enzymatic biocatalysis is, however, limited by feedback inhibition, limited process conditions including temperatures and solvents and long-term instability of the biocatalysts. While the kinetics can be accelerated through the use of co-factors, in many cases, these are consumed in the reaction, fugitive, and expensive.

One approach to overcoming the limitations of enzymatic reactions is to tether the biocatalytic components to a solid support, allowing for the in-situ regeneration, recovery, re-use and stabilization while simplifying product separation. Immobilisation also facilitates integration into rapid, highly controllable and efficient flow chemistry systems, overcoming product inhibition limitations of enzyme reactions. The main challenge, however, is retaining the native interactions, function and activity of the tethered biocatalysts.

The broad aim of this research is to explore the efficacy of tethering a cofactor to the surface of a nanoparticle in a highly controlled manner and to then gain a detailed understanding of the kinetic processes that govern the surface catalysed reaction with various enzymes. This will be achieved through the:

1. Attachment and quantification of a cofactor (NAD(H)), that has been modified at the N^6 position with a flexible linker arm, to the surface of silica nanoparticles via a highly specific thiol-ene “click” reaction.
2. Analyse the interfacial kinetics of the enzymatic catalysis of surface tethered N^6-linked-2AE-NAD.
3. Investigate the regeneration of surface tethered N^6-linked-2AE-NAD enzymatically in a multi-enzyme reaction system and investigate the kinetics of this process.
4. Investigate the thermal stability of surface tethered N^6-linked-2AE-NAD.

1.1 Enzyme Catalysis

Biocatalytic reactions have been utilised for thousands of years in the production of food and beverages such as bread, cheese, beer, wine and vinegar [1]. In the process of beer brewing, for example, yeasts are utilised to convert the starch and sugars of malted barley into ethanol, carbon dioxide and other flavour compounds [2]. The key to these biotransformation reactions is biological catalysts known as enzymes [3]. Enzymes are protein molecules that catalyse a wide range of highly complex chemical reactions under mild conditions [3]. These molecules are comprised of a sequence of covalently bound amino acids that, through hydrogen bonding interactions, transform into a three-dimensional tertiary structure which acts as a scaffold with a comparatively very small number of amino acids forming one or more active sites which can catalyse reactions of other molecules. The active site has a geometry and chemical characteristics that are complementary to that of its reactant, facilitating highly specific binding [3] which consequently results in highly specific reactions taking place. Binding of the reactant to the active site induces a conformational change in the enzyme structure, orientating the catalytic groups in a way for the enzyme to perform its catalytic function. The outcome is the reduction in activation energy as illustrated in Figure 1.1.

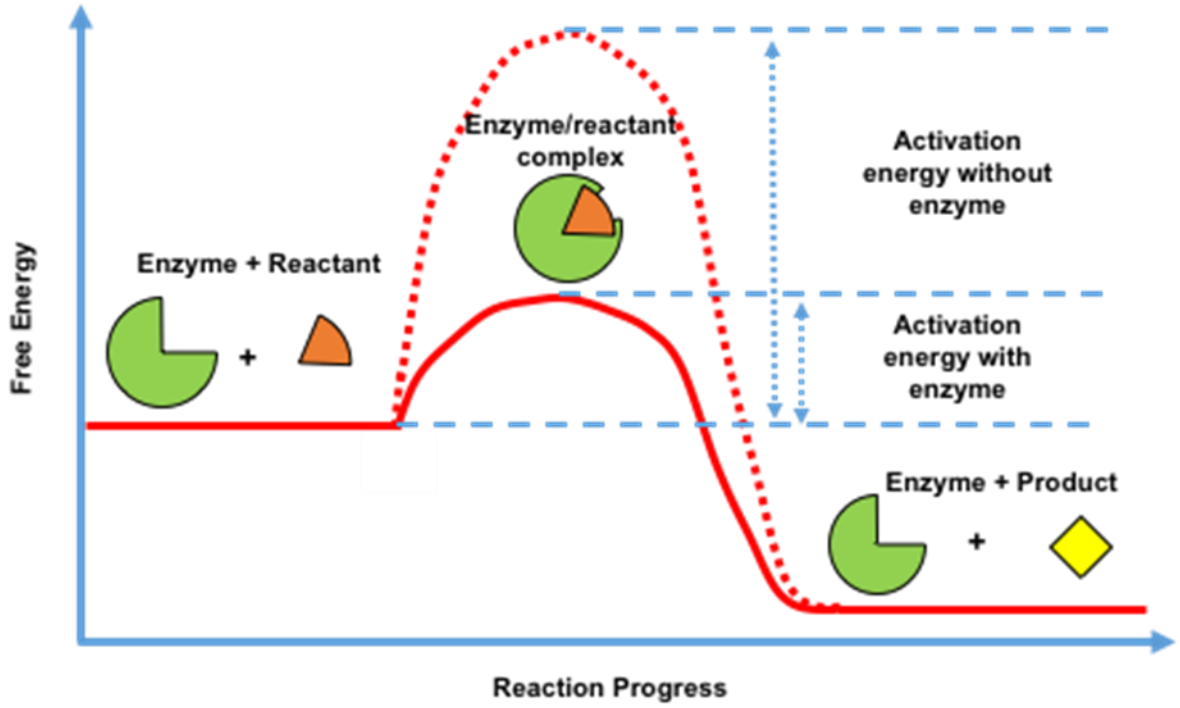

Figure 1.1: Activation free energy of an enzyme catalysed reaction compared to an uncatalyzed reaction.

1.2 Synthetic Biocatalysis

More recently, the field of industrial biocatalysis has utilised the vast catalytic capabilities of enzymes for the production of useful chemicals, giving rise to the field of synthetic biocatalysis [4]. The rapid growth of synthetic biocatalysis has been made possible by recent advances in genetic engineering and proteomic research and is quickly becoming one of the most important areas of biotechnology, offering extensive impact on health [5], food production [6], and industrial synthetic chemistry [7-9]. Synthetic biocatalysis employs biological agents, either whole cells or isolated enzymes for biotransformations with mild reaction conditions, aqueous solvents, and high chemo-, regio- and stereo-selectivity [10, 11].

Biocatalytic synthesis also generally bypasses traditional synthetic steps such as functional group protection and activation, yielding shorter and more efficient routes to important chemicals with reduced waste and by-products [10]. These features have led to several applications of enzymes where high selectivity on complex substrates is critical, such as in pharmaceutical, food and cosmetic industries [5, 12-14]. In these

processes, enzymes may be used to perform a single complex step within a synthetic pathway, such as a stereospecific addition, or a cascade of multiple enzymes may be utilised to produce a single target compound [4]. However, due to the high cost of purified enzymes and cofactors, as well as their short lifetimes, whole cell or *in vivo* processes have so far dominated biosynthetic applications. For example, nitrile hydratase has been over-expressed in *Rhodococcus rhodochorus* for the enzymatic hydration of acrylonitrile to acrylamide under mild conditions (Figure 1.2) [15]. This process avoids the use of toxic copper catalysts, sulphuric acid and high temperatures [6]. In Japan, over 650,000 tonnes of acrylamide is produced annually by this biotransformation process [6].

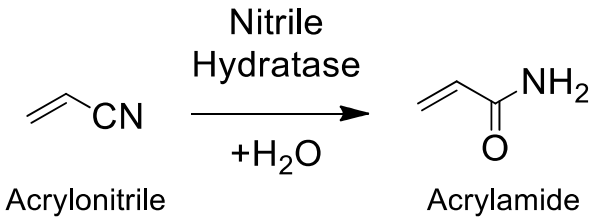

Figure 1.2: Nitrile hydratase catalysed hydration of acrylonitrile to acrylamide. Adapted from [6].

In the pharmaceutical industry, the anti-diabetic drug sitagliptin has been synthesised with >99.95% enantio-purity by genetically engineered R-selective transaminase from *Arthrobactor sp.* via the asymmetric amination of prositagliptin ketone (Figure 1.3) [16, 17]. Compared to the traditional chemical synthesis, this whole cell biosynthetic process avoids the use of toxic ruthenium catalysts while increasing yield by 10% [6].

Figure 1.3: R-selective transaminase ((R)-ATA) catalysed asymmetric amination of prositagliptin ketone to the anti-diabetic drug sitagliptin. Taken from [6].

1.2.1 Cell Free Synthetic Biology

Although promising, whole cell biosynthetic processes suffer from several fundamental limitations and challenges [18, 19]. These include complicated genetic engineering and cell growth operations of the living host organisms, transport of reactants and products across the cell membrane, competition of other enzyme pathways, complicated product separations and limited conversion due to product inhibition [18-21]. One viable approach to overcome these challenges is the rapidly expanding field of cell-free synthetic biology. In cell free systems, structural cellular components such as the cell walls are eliminated, and biosynthetic pathways are re-constructed *in vitro* using either purified enzymes or a concentrated crude cellular extract. These cell free processes also benefit from simple manipulation, monitoring and manipulation and can provide high product yields by removal of undesired by-product forming side reactions [12]. However, the instability of purified enzymes to high temperatures, non-aqueous solvents and long-term use, along with the cost of their continual replacement is one of biggest challenges limiting cell free synthetic approaches [19, 20].

1.2.2 Biocatalyst Immobilisation

To overcome the challenge of biocatalyst instability, cell free approaches are often implemented with the essential enzymes immobilised and co-localised on the surface of a solid support material [4, 19, 20, 22-24]. Not only does enzyme immobilisation enhance enzyme stability, it also allows for more convenient handling, recovery and re-use of the enzyme, as well as simplistic product separations, [4, 19, 20]. There are two general methods of enzyme immobilisation onto solid substrates [25]:

(i) Adsorption immobilisation – based on physical binding interactions such as van der Waals interactions, dipole-dipole or hydrogen bonding, resulting in weak bonding between the enzyme and support material.
(ii) Covalent immobilisation – enzyme is attached to the solid substrate by strong covalent bonds preventing leaching from the surface.

However, these enzyme immobilisation techniques often lead to a reduction in enzyme activity or impeded access of reactant to the enzyme's active site as a result of non-optimal immobilisation geometry [4, 20]. Recent efforts towards site-specific chemical modifications of enzymes for oriented surface immobilisation have been shown to overcome this limitation, while utilization of nanomaterials as carriers for enzyme

display has been shown to result in high, and in some cases, enhanced enzyme activity [4, 19, 20].

1.2.3 Nanobiocatalysis

Several different nanomaterials and structures have been employed in bioprocessing applications, giving rise to the field of nanobiocatalysis [26, 27]. The unique properties of a broad spectrum of nanostructures, including nano-porous media [28], nanofibers [29], nanotubes [30], DNA scaffolds [31] and nanoparticles [24] offer several advantages in biocatalytic systems. In particular, the high surface area to volume ratio of nanoscale materials has allowed improved enzyme loading, and thus activity, per unit mass compared to other immobilized enzyme systems [26]. Highly controllable size and surface chemistry of nanomaterials, as well as novel properties such as conductivity and magnetism have so far led to many improvements in enzyme stability, activity and lifetime [26]. An extensively explored class of nanomaterial in nanobiocatalysis is the nanoparticle [4, 19, 20, 24, 32-35]. Nanoparticles offer high surface area to volume ratios, tailorable size and surface functionality as well as simple synthesis and preparation. Dispersed nanoparticles exhibit Brownian motion, improving access and interactions of freely diffusing reactants to the surface immobilised enzymes [36]. This results in higher activities as compared to enzymes immobilised to bulk flat surfaces, limiting diffusion of reactants to and from the surface [19, 20, 36]. For example, lipase has been immobilised on the surface of magnetic silica nanoparticles for the production of biodiesel from waste cooking oil. Conversion of cooking oil to biodiesel reached 91 % over a 35 hour period [37].

1.3 Cofactor Dependent reactions in Synthetic Biology

The catalytic activity of many enzymatic reactions is dependent on small organic molecules known as cofactors. Cofactors reversibly bind at distinct sites in the enzyme structure in highly specific orientations, resulting in the enzyme-cofactor complex. The synergy of this enzyme-cofactor complex results in a drastic kinetic acceleration of the chemical transformation, facilitated by group or electron transfer of the cofactor [38].

Currently, efficient industrial biosynthetic processes are limited to cofactor independent enzymes such as lipases [37] and hydrases [6], eliminating the many critical and synthetically useful reactions offered by cofactor dependent enzymes such

as NAD(H)-dependent reductases and oxidases [7, 23]. Generally whole cell processes are used when a cofactor dependent transformation is required as they enable cofactor regeneration [39]. An example of a cofactor dependent enzyme reaction is the NAD(H) dependent reversible oxidoreduction between pyruvate and lactate by Lactate dehydrogenase shown in Figure 1.4.

Figure 1.4: Cofactor dependent conversion of pyruvate to lactate by lactate dehydrogenase with simultaneous oxidation of NADH to NAD. Taken from [40].

1.3.1 β-Nicotinamide adenine dinucleotide (NAD)

β-Nicotinamide adenine dinucleotide (NAD/NADH) is an essential hydride accepting and donating cofactor, central to the cellular metabolism and energy production. Both the oxidised (NAD) and reduced (NADH) form absorbs strongly at 260 nm due to the adenine base, with an extinction coefficient of 16,900 M^{-1} as shown in Figure 1.5. NADH also exhibits a second absorbance peak at 340 nm (ε = 6220 M^{-1}) due to the resonance quenching of the protonated nicotinamide nucleotide [40]. Tracking the change in absorbance at 340 nm due to the formation or consumption of NADH has been extensively used as a method to quantify enzyme activity [14, 41, 42].

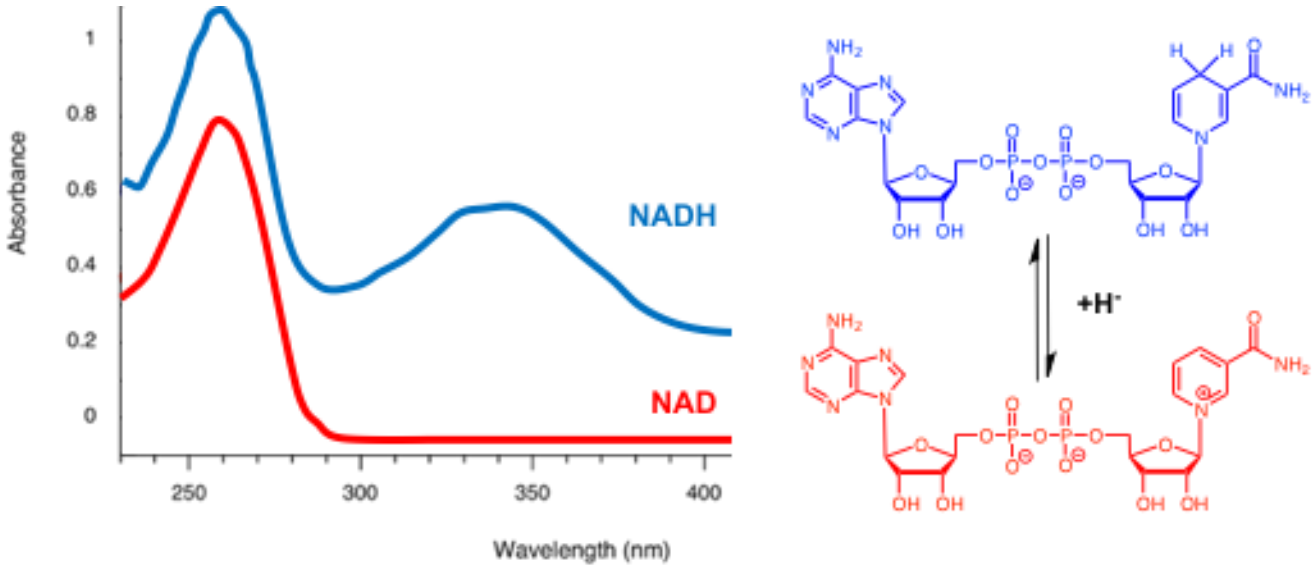

Figure 1.5: UV/Vis absorbance spectra of NADH (blue) and NAD (red).

1.3.2 Cofactor Regeneration

The high cost and stoichiometric consumption of cofactors is one of the contributing factors hindering the development of large-scale cofactor dependent processes [43]. Thus, it is essential for cofactors to be regenerated *in situ* for industrial viability, allowing catalytic amounts of expensive cofactors to be used [18, 23, 44]. Cofactors can be regenerated chemically [45], electrochemically [46], photo-chemically [47] or through the use of a second substrate driven enzyme reaction [43]. Electrochemical regeneration is typically favoured in electrode-based biosensors and biofuel cells, but is less attractive in bioprocessing applications [18]. Enzymatic regeneration is often the favoured approach and is achieved by coupling a second cofactor dependent enzyme to perform the cofactor regenerating reaction. This approach has the added potential of affording the production of multiple valuable chemicals within the same system (Figure 1.6) [43]. Several examples of multi-enzyme systems with cofactor regeneration can be found in Section 1.3.4.

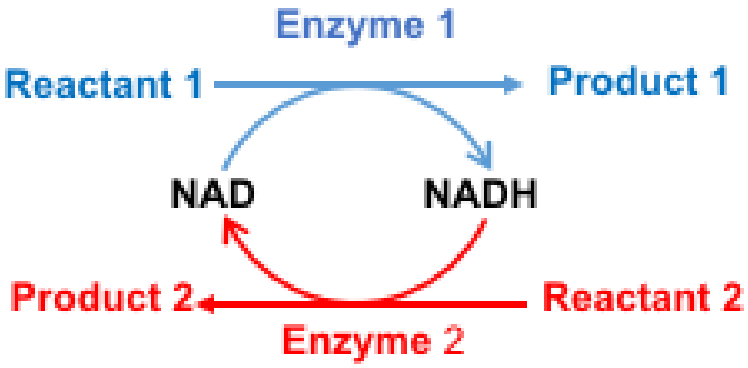

Figure 1.6: Multi-enzyme approach to cofactor regeneration.

1.3,3 Cofactor Immobilisation

Enzymatic regeneration of cofactors can drastically increase efficiency of biosynthetic processes by reducing the amount of cofactor required. However, the efficiency of these processes can be further increased by immobilisation of the cofactor. Like enzyme immobilisation, cofactor immobilisation allows re-use and retention, simplifies product purification as well as aids the stabilisation of the cofactor [48]. Cofactor immobilisation is particularly useful under flow conditions, facilitating simplistic product separations as shown in Figure 1.7(b) where cofactor is co-immobilised with product forming and cofactor recycling enzymes.

Immobilization of cofactors to solid supports has been achieved with various degrees of success [18, 36, 41, 48-59]. From these studies, one of the most challenging aspects has been achieving efficient enzyme-cofactor interactions within the immobilized systems [36]. Early efforts involved retention of cofactors and enzymes by microcapsules and semi permeable membranes within flow reactors, which only allow permeation of small molecules such as the product and reactant [18, 60-63]. The biotransformation reactions within these systems are heavily limited by mass transfer resistance of the aqueous reactant to, and the product from, the microcapsules and membranes [60-62, 64]. Recent efforts have shown promising catalysis rates with covalent immobilisation of cofactors to more open supports, such as nanostructures, providing efficient cofactor retention while maximising cofactor-enzyme interactions and diffusion of reactants and products [18, 41, 48-50, 52, 54, 57].

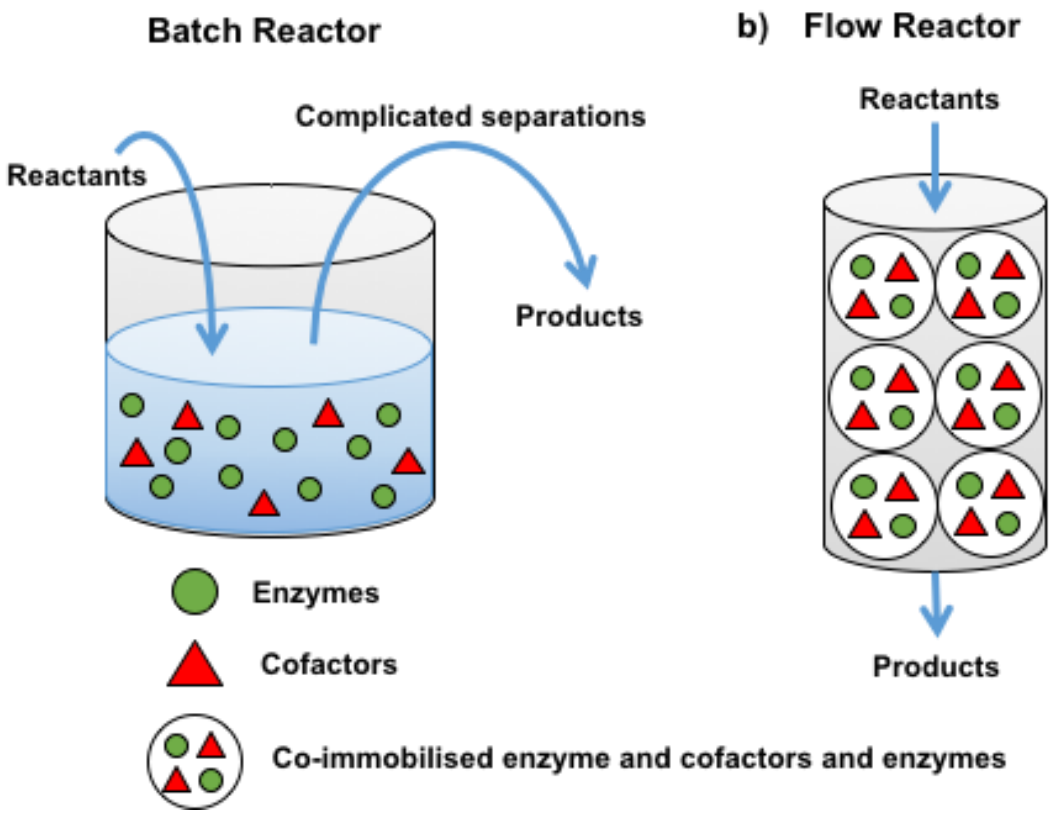

Figure 1.7**:** Comparison of cofactor dependent biocatalytic processes in a (a) batch bioreactor and (b) flow bioreactor.

1.3.4 Recent examples of NAD immobilisation

In 2008, El-Zahab *et al*. co-immobilized NADH along with formate dehydrogenase (FDH), formaldehyde dehydrogenase (FaldDH), alcohol dehydrogenase (ADH) and glutamate dehydrogenase (GDH in Figure) on polystyrene particles with an average diameter of ~500nm via succinimide coupling as depicted in Figure 1.8(a) [18]. NADH attachment was determined by UV/Vis analysis of the reaction washings and reported to be 2.3-3.7mg/g particles which we have calculated to be equivalent to 0.35-0.56 attachments/nm^2. The co-immobilised enzymes and NADH were applied to the reaction scheme depicted in Figure 1.8(b) where, through a multi-enzyme cascade, dissolved carbon dioxide (CO_2) was transformed to methanol with continuous cofactor regeneration. The immobilised system was found to produce methanol at a rate 50% of that of the free enzyme/cofactor system under equivalent conditions and showed little loss in activity after 11 re-use cycles [18].

Figure 1.8: El-Zahab *et al.* [18] strategy for immobilisation of enzymes (and NADH) onto polystyrene particles (a) and multi-enzyme cascade reaction for the production of methanol from CO_2 (b).

In 2009, Liu *et al*. covalently tethered NAD to the surface of epoxide terminated silica nanoparticles (SiNPs) with an average diameter of 30 nm. Like El-Zahab *et al*., the exact chemical orientation NADH immobilisation was not specified. NAD attachment was reported to reach loadings of 0.4 g/g of particles, however, it was not stated how this was determined – this is calculated to be 3.6 attachments/nm^2 assuming a density of 2.0 g/cm^3 for the silica particles. Glutamate Dehydrogenase (GLDH) and Lactate Dehydrogenase (LDH) were similarly immobilized to separate SiNPs of the same size. Applying the immobilised enzymes and cofactor to the reaction depicted in Figure 1.9 resulted in reaction rates reaching 50% of the free enzyme/cofactor system under equivalent conditions. However, it was reported that the rate was increased when either only the cofactor or enzyme were immobilized [48].

Figure 1.9: Reaction scheme of the regeneration of SiNP immobilised NAD by immobilised GLDH and LDH. Taken from [48].

In 2011, Zheng *et al.* covalently immobilised NADH, Glutamate Dehydrogenase and Glucose Dehydrogenase to the surface of 124 nm silica coated magnetic nanoparticles via coupling with PEG spacer arms of different length containing terminal epoxide groups [36]. NAD attachment density was measured by UV/Vis analysis and reported to be 20 mg/g of particles, (calculated to be 1.3 attachments/nm^2 assuming spherical geometry and a density of 2 g/cm^3). The authors believed the NADH attachment orientation to be through the amino of the adenosine moiety (N^6), however this was not characterised. The enzymes and cofactor were immobilised in different configurations as shown schematically in Figure 1.10(a), and applied to the multi-enzyme reaction Figure 1.10(b). The highest rate of catalysis was observed when the enzymes and cofactor were co-immobilised on the same particle, reaching 72% of the rate of the free enzyme/cofactor system under the same reaction conditions. Enzymes and cofactors immobilised on separate particles exhibited the slowest catalytic rate. Interestingly, this reaction rate for separately immobilised enzymes and co-factors could be more than doubled by using an alternating magnetic field to mix the magnetic support particles or significantly increased by using a longer PEG spacer arm, demonstrating the importance of the mobility and translocation of the immobilised biocatalyst [36]

Figure 1.10: Different patterns of cofactor and enzyme immobilisation on super-paramagnetic nanoparticles (a) and coupled enzyme reaction with regeneration of tethered cofactor (b). Taken from [36].

In 2013, Li *et al.* covalently immobilised NAD to the surface of amine functionalised SiNPs with an average diameter of 15nm via carbodiimide promoted coupling to a short carboxyl-terminated-spacer-arm [54]. NAD attachment was determined to be 73mg/g-particles (calculated to be 0.3 attachments/nm^2) by HPLC analysis of the reaction washings and attachment confirmed by thermogravimetric analysis (TGA) and Fourier-Transform-Infrared-Spectroscopy (FTIR). Tethered NAD was then applied to the Formate Dehydrogenase (FDH) and L-Lactate Dehydrogenase (LDH) coupled reaction shown in Figure 1.11. Turnover number (TN), defined as the total number of moles of product formed per mole of cofactor per unit time, was reported to reach 82.9 h^{-1}, but was not compared to free NAD. Other recent examples of NAD tethering to solid nanocarriers are summarised below in Table 1.1.

Figure 1.11: Reaction scheme for coupled enzyme reaction with regeneration of tethered NAD. Taken from [54].

Table 1.1: Summary of other recent examples of NAD tethering.

Support material	Cofactor/Enzyme	Loading	Application	Results	Re
105nm super-paramagnetic nanoparticles	NAD(H)	20 mg/g	Synthesis of Glutamate and D-glucono-1,5-lactone	NAD(H) and enzymes covalently linked via epoxy functionality of particle surface. Reaction rate co-immobilised enzymes and NAD doubled when mixed with an alternating magnetic field.	[53
	Glutamate Dehydrogenase	65 mg/g			
	Glucose Dehydrogenase	48 mg/g			
Chitosan coated magnetic nanoparticles	NAD+	3 mg/g	Simultaneous synthesis of Benzaldehyde and ethanol by Alcohol Dehydrogenase	NAD(H) covalently linked to a azelaic acid on particle surface using NHS/EDC coupling. Free NADH, free NAD+, immobilized NADH and immobilized NAD+ regenerated 1111, 1157, 1235 and 3904 times, respectively.	[50
	NADH	10 mg/g			
Hollow Polyurethane nanofibers	NADH	NA	Enzymatic synthesis of methanol from CO2	NADH immobilised inside hollow nanofibres by ionic interactions and enzymes co-encapsulated within lumen of hollow nanofibers. Proximity of co-encapsulated enzymes and cofactor resulted in tripled methanol yield from CO_2 compared to free enzyme/cofactor system.	[49
	Glutamate Dehydrogenase , Formate Dehydrogenase, Formaldehyde Dehydrogenase, Alcohol Dehydrogenase and Carbonic Anhydrase	~4 mg/g			

1.3.5 NAD modification

Covalent tethering of NAD to the surface of solid supports is generally achieved via non-specific approaches that rely on carbodiimide [18, 54] or epoxide [36, 48, 53] reactions that target the nucleophilic N^6 nitrogen of the amine group of the adenosine moiety of NAD. However, it has been demonstrated that NAD can be tethered through the nucleophilic phosphate groups [65]. Therefore, it is possible that in the previously mentioned studies, NAD is tethered from multiple chemical anchor points, leading to different surface structures. This complicates the characterisation of the tethered NAD, as the different tether sites will result in different complexation and catalysis efficiencies. This problem can be overcome by pre-modification of NAD in order to

incorporate a chemical handle that can be specifically targeted without disruption of other functional groups, leading to a single surface structure.

NAD has been chemically modified to either facilitate covalent immobilization on solid supports or to increase its molecular weight to allow its retention within flow cell bioreactors [66-68]. Riva *et al.* investigated the influence of modification site on the properties of several cofactors, finding that NAD linked at the N^6 position of the adenine moiety showed the highest activity with many different dehydrogenases [58]. Similar results were observed by Forde *et al.* in 2005 [69]. In short, alkylation of NAD at the N^6 position is generally achieved in three steps as shown in Figure 1.12:

(i) Alkylation at the N^1 position of the adenine ring with ethyleneimine to form N^6-2-aminoethyl-NAD (N^6-2AE-NAD). This may also include the introduction of other terminal functionality by carbodiimide/succinimide crosslinking.
(ii) Reduction of the nicotinamide nucleotide with sodium dithionite
(iii) Alkylation of the N^6 amino position by a Dimroth rearrangement from the N^1 position [70]. The oxidised form is then obtained by enzymatic reduction of the N^6-linked NADH derivative.

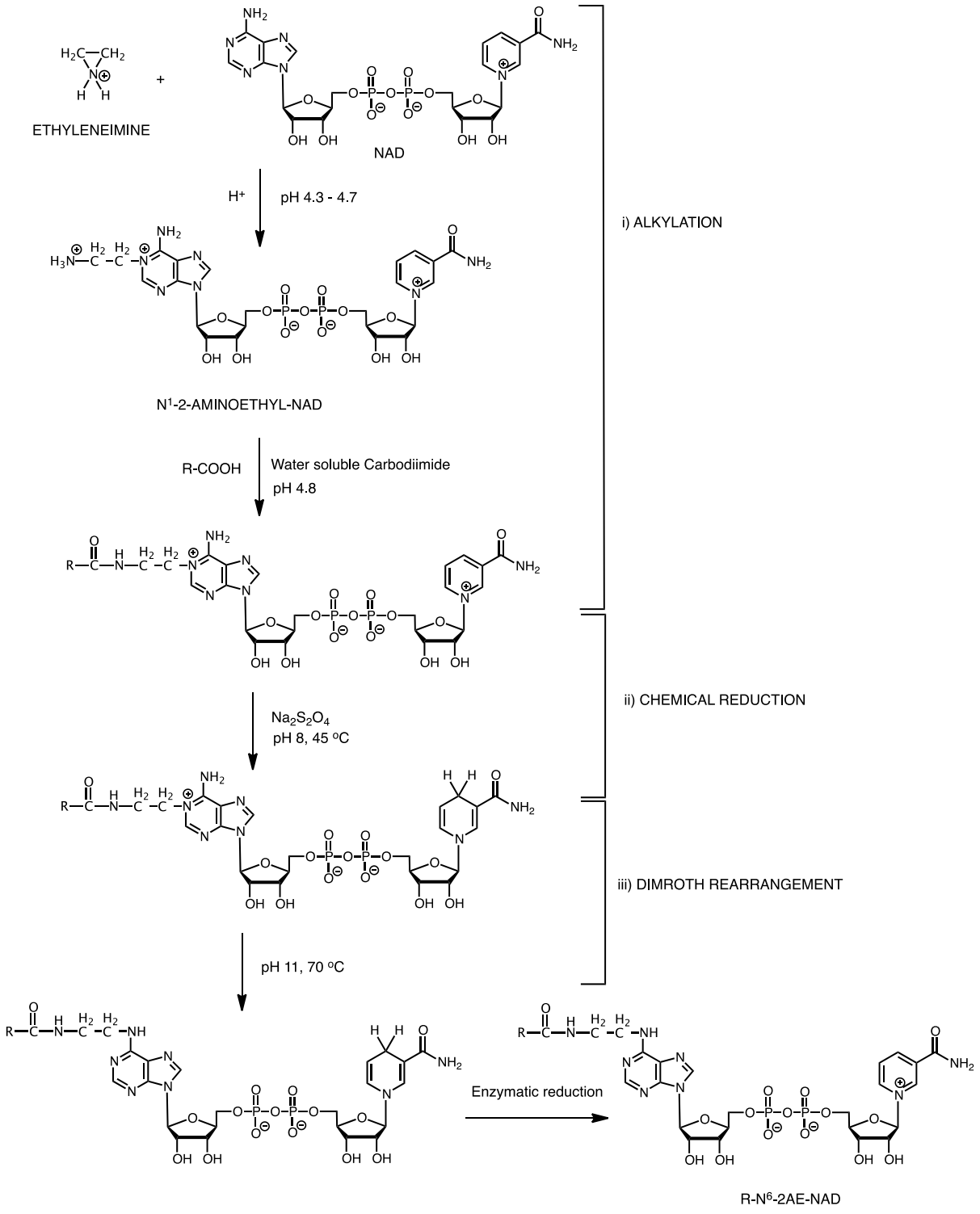

Figure 1.12: Generalised reaction pathway for the alkylation of NAD at the N^6 position. Adapted from [70].

1.3.6 Specific tethering of NAD

Recently, N^6-2AE-NAD modified with a long poly$(T)_{20}$ oligonucleotide swinging arm has been tethered to a DNA scaffold between two tethered NAD dependent enzymes, glucose-6-phosphate dehydrogenase (G6pDH) and malic dehydrogenase (MDH) as shown in Figure 1.14 [52]. This was achieved via the targeted conjugation of the aminoethyl group of N^6-2AE-NAD with the 5' amine group of modified DNA using resin-based disuccinimidyl suberate (DSS) crosslinking chemistry as shown in Figure 1.13. The accessibility and translocation of the tethered NAD between each enzyme was found to be a crucial factor in the performance of the system. Optimal performance was achieved when the NAD tether was positioned in close proximity (7 nm) between each tethered enzyme, leading to a 90-fold enhancement in activity compared to the equivalent free NAD and enzyme system. This enhancement was shown to decrease as the distance between the NAD and the enzymes was increased, when the NAD was tethered on different planes of the scaffold, or when the enzymes or NAD were un-tethered. This demonstrates the significance of the special organisation of the tethered biocatalytic components in order to facilitate efficient transport, interactions and catalysis [31, 52]

Figure 1.13: Conjugation of N^6-2AE-NAD to modified DNA through resin-based DSS crosslinking. Taken from [52]

Figure 1.14: N^6-2AE-NAD tethered by a long oligonucleotide between G6pDH and MDH on a DNA scaffold. Taken from [52]

1.3.7 N^6-linked-2AE-NAD

In order to facilitate highly specific surface immobilisation of NAD, while retaining maximum catalytic activity with enzymes, N^6-2AE-NAD has been modified with long, flexible tether arms containing terminal thiol or vinyl functionality as shown in Figure 1.15. These chemical handles allow directed and highly specific covalent tethering of NAD to the surface of vinyl and thiol terminated SiNPs via a simple and mild thiol-ene 'click' reaction, resulting in a single surface NAD structure [71]. The high density of surface functional groups on the SiNPs facilitates a high surface coverage of NAD to be obtained, which can be quantified using a simple ATR-FTIR technique. This allows the creation of a robust, highly active bio-conjugated surface structure that can be accurately compared to freely diffusing NAD through kinetic analysis in order to characterise its catalytic behaviour in enzyme catalysed reactions. In depth kinetic knowledge of the tethered NAD system then allows improvements to be made in order to maximise the efficiency of the biocatalytic processes.

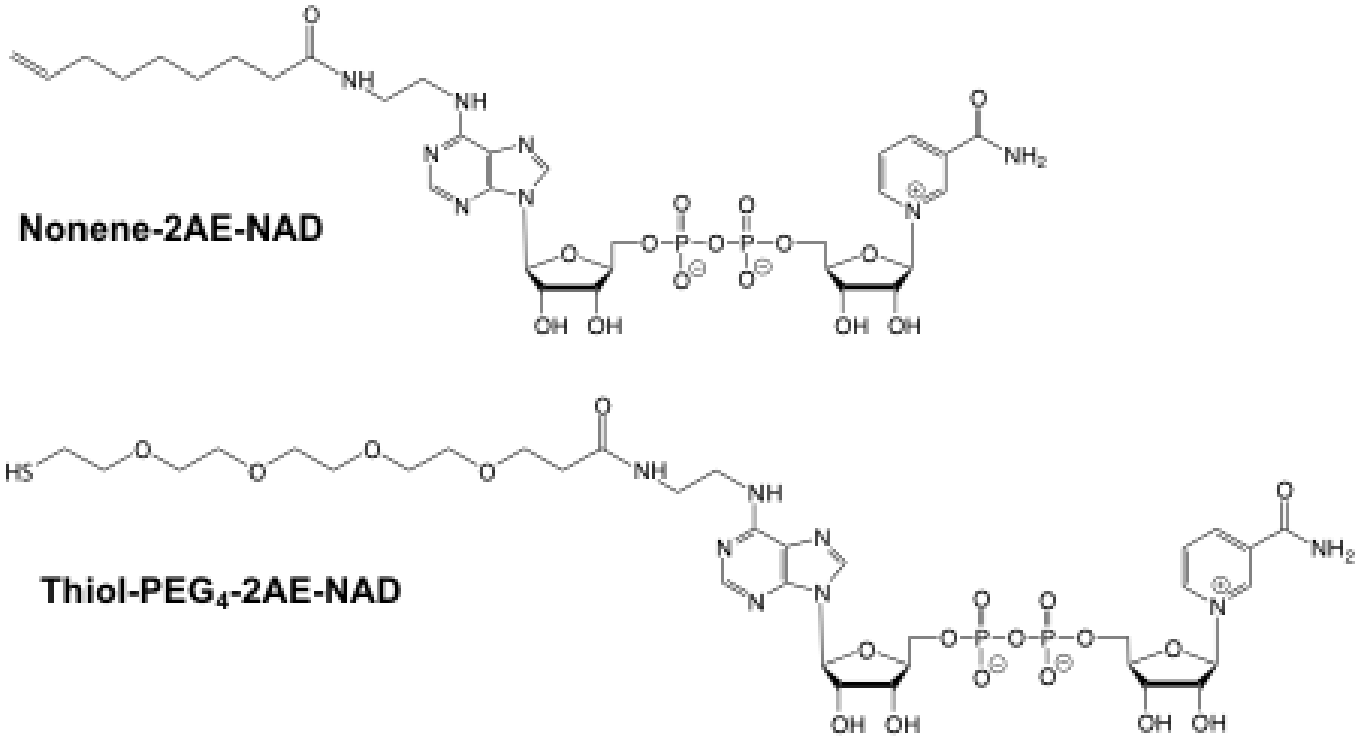

Figure 1.15: Structures of N^6-linked-2AE-NAD.

1.4 Substrates

A wide variety of solid substrates have been used for the covalent immobilisation of NAD including [18], silica nanoparticles [36, 48, 53, 54], chitosan coated magnetic nanoparticles [50] and DNA [31, 52, 72].

Silica nanoparticles as a substrate material have been shown to retain a significant amount of function and activity of the immobilised enzymes and cofactors [36, 48, 53, 54]. This, along with the wide range of surface functionalities, broad size range, cost effectiveness, and biostability make silica nanoparticles a highly attractive substrate for covalent tethering. However, in order to achieve highly specific attachment, the surface of the silica nanoparticles must possess the appropriate, complimentary chemical anchor groups for the tether.

1.4.1 Silica Nanoparticles (SiNPs)

Silica (SiO_2) is one of the most abundant materials found in nature and is produced by sponges, diatoms, and plants in many different forms, generally from the condensation of silicic acid [73]. Synthetically, SiO_2 is produced by hydrolysis and subsequent

condensation of alkoxy silanes. The non-toxic nature of silica and its potential for modification with many different functional groups makes it very attractive for biomedical and biological applications [74]. Recently, a number of methods of synthesising silica nanoparticles have been documented, including several post functionalisation strategies which allow tailorable surface chemistry [75-78].

1.4.2 Stöber SiNP Synthesis

SiNPs were first produced by the 'Stöber' sol-gel method in 1968 [79]. Monodisperse particles with controllable sizes are produced by hydrolysis and condensation of tetraethyloerthosilicate (TEOS) in ethanol in the presence of ammonia and catalytic water(Figure 1.16) [77]. In this approach, the size of the SiNP is controlled by varying the concentrations of TEOS, ammonia and ethanol. It has also been found that the alkyl chain length of alcohol solvent, silane precursor and using different base catalysts such as primary amines can also influence the size of SiNPs [80]. A limitation is that not all silane precursors are suitable for this approach. The Stöber method is widely used commercially, with SiNPs produced by this approach applied to applications such as catalysis [81], thin film substrates [82], insulators [83], ceramics [84], polymer additives [85] and chromatography support material [76, 86]. Attachment of biological molecules such as proteins, enzymes, peptides, cofactors and DNA to SiNPs offers many significant advances in bioassay, imaging, drug delivery and biocatalytic applications [77, 87].

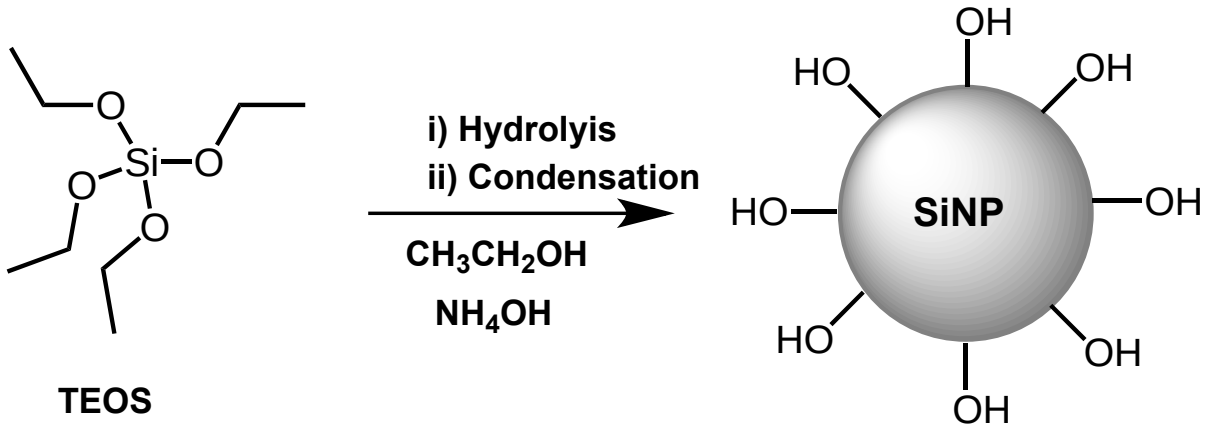

Figure 1.16: Stöber synthesis of SiNPs from TEOS [79].

1.4.3 Stöber Synthesis Mechanism

Although the Stöber synthesis method has been widely studied for many years, the formation mechanism of the particles is still under debate [73]. After decades of devoted effort, two opposing models have been identified as the mechanism;

1. In the monomer addition model, silica nuclei are formed through hydrolysis and condensation of TEOS, which then grow by deposition of silanol subunits (Figure 1.17(a)) [88],
2. The aggregation model postulates the aggregation of small primary particles into seeds which grow by surface attachment and coalescence of silanol monomers and oligomers (Figure 1.17(b)) [88].

Figure 1.17: Schematic of monomer addition (a) and aggregation (b) growth mechanisms for SiNP synthesis via Stöber method. Adapted from [88].

However, neither model comprehensively explains all experimental observations [89]. As a general explanation, the growth of SiNPs by the Stöber method is initiated by the hydrolysis of the ethoxy groups of TEOS to silanol groups in the ammonia/ethanol solution. Silanol monomers condense together, generating branched siloxane clusters (a). These clusters act as nucleation sites, with further condensation of siloxane oligomers leading to particle growth (b). Growth can also simultaneously occur via condensation of silanol monomers with the unreacted ethoxy groups of TEOS (c) [88].

$$Si(OEt)_4 + xH_2O \rightleftharpoons Si(OEt)_{4-x}(OH)_x + xEtOH \quad (a)$$

$$2Si(OEt)_{4-x}(OH)_x \rightleftharpoons (EtO)_{8-2x}(Si{-}O{-}Si)(OH)_{2x-2} + H_2O \quad (b)$$

$$Si(OEt)_4 + Si(OEt)_{4-x}(OH)_x \rightleftharpoons (EtO)_{7-x}(Si{-}O{-}Si)_1(OH)_{x-1} + EtOH \quad (c)$$

TEOS is hydrolysed via nucleophilic substitution, where the hydrolysis rate increases with ammonia concentration due to the nucleophilicity of hydroxide compared to water molecules. The hydrolysis rate is also increased as more ethoxy groups are converted to silanol groups. This is due to nucleophilic attack of hydroxide becoming more favourable as the silicon atoms increase in positive charge while the steric hindrance due to ethoxy groups around the silicon atom is reduced. Like TEOS hydrolysis, condensation occurs through nucleophilic attack between adjacent silanol groups and/or ethoxy groups to form branched siloxane networks. Ethoxy groups within a highly condensed matrix are hindered against nucleophilic attack by hydroxyl ions. This results in an increased rate of condensation as the nucleophilic silanol groups are more easily deprotonated than water, leading to electrophilic silicon atoms. Thus, silanol monomers are favourably condensed to siloxane networks rather than to other monomers or much smaller networks [88]. Incomplete hydrolysis and condensation of TEOS within the siloxane networks due to steric hindrance leads to a small amount of residual ethoxy groups, affecting the external morphology and internal homogeneity of the silica particle network structure [88].

Growth of silica nanoparticles can also be described by applying the LaMer model as shown in Figure 1.18 [90]. The model divides nanoparticle nucleation and growth into three phases. In the first phase, monomer (silane) concentration is raised above supersaturation (S). Further increase in monomer concentration overcomes the energy barrier of homogenous nucleation, where a critical point (S_c) is reached (phase II), resulting in the simultaneous formation of a large number of nuclei known as ‘burst’ nucleation. Consequently, the rapid drop in monomer concentration restricts the further formation of nuclei, resulting in the highly uniform growth of nanoparticle (Phase III) [90].

Figure 1.18: Plot of the LaMer model showing the change in monomer concentration over time and subsequent growth of nanoparticles, where S represents supersaturation and S_c represents the critical point. Taken from [90].

1.5 Routes to Functional SiNP surface

In complex systems, where highly specific surface chemistry is required, surface hydroxyl groups must be modified to introduce the desired chemical functionality. A number of approaches have been used to attach chemical moieties to the silica surface including reactions such as aminations, esterification and coupling based transfer catalysis [91, 92]. Surface functionality can also be introduced via co-hydrolysis of TEOS with other silanes containing a desirable functional silane monomer, or by condensing a functionalised silane onto the surface of a preformed silica nanoparticle.

1.5.1 Particle surface modification

The functionalisation possibilities for SiNPs is dependent on the surface chemistry of the prepared particles. Conventional Stöber particles possess silanol groups on their surface, which have limited chemistry and generally require modification prior to further functionalization [77]. This is typically achieved either by co-hydrolysis of TEOS with other organosilanes (Figure 1.19(a)), or through subsequent silanization of the particle surface by other organosilicates (Figure 1.19(b)) [75-78]. However, these two methods generally lead to the formation of particles which are non-uniform in size and composition. This is a result of secondary reactions, including reaction with the solvent, self-condensation and nucleating before being grafted to the particles [75].

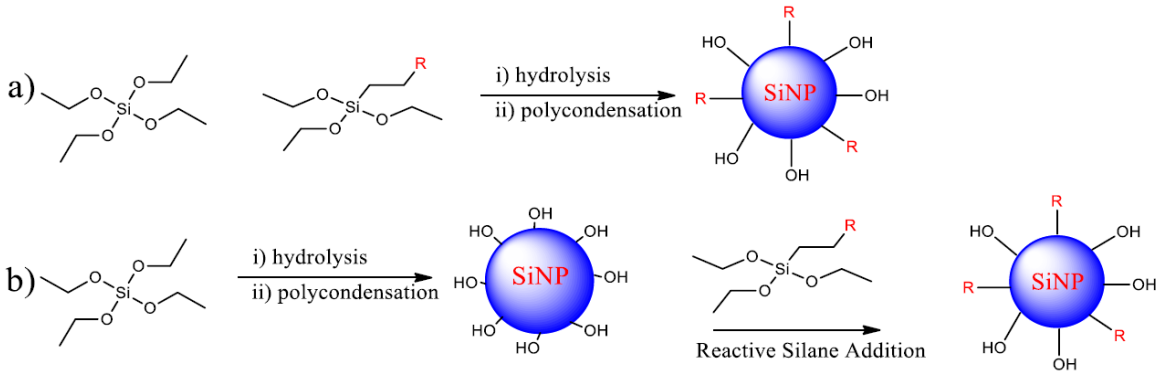

Figure 1.19: Schematic of (a) co-hydrolysis of TEOS with other organosilanes and (b) silanization of the particle surface matrix by organosilanes. Taken with permission from [93].

1.5.2 Single Silane Synthesis of Thiol SiNPs

Recently, SiNPs have been prepared using a single organosilane precursor to directly incorporate unhydrolysable organic groups into the silica matrix while evenly covering the silica surface in high density of surface functionality [71, 77, 94, 95]. Using 3-mercaptopropyltrimethoxysilane (3-MPTMS) as the sole organosilane in aqueous solution with ammonia as the catalyst, Nakamura *et al.* produced highly monodisperse, spherical nanoparticles over a broad range of sizes as shown in Figure 1.20 [96]. The particles were found to possess a surface thiol group density of 4.9/nm^2, much higher than can be achieved via previously mentioned post-modification strategies [71]. These particles have proven useful for achieving high density functional surfaces for incorporation into coatings for self-cleaning surfaces [71, 94]

Figure 1.20: Synthesis of thiol terminated SiNPs directly from 3-MPTMS. Taken with permission from [71, 94].

Lu *et al*. studied the mechanism of this single silane, one pot method. They proposed that the mercapto-silica particles are produced through an emulsion based process, similar to the aggregation-only route previously described [95]. Hydrolysis of 3-MPTMS, catalysed by ammonia, leads to amphiphilic structures of mercaptopropylsilicate monomers and oligomers with hydrophilic silanol groups and hydrophobic mercaptopropyl chains, forming an oil-in-water emulsion as shown in Figure 1.21. Hydrolysis and condensation, along with coalescence allow the emulsion droplets to grow to a point where the residual precursor is depleted. Further condensation restricts coalescence of emulsion droplets, eventually leading to a uniform population of mercapto-propyl terminated solid spheres. These spheres can continue to grow through Ostwald ripening leading to less uniform particles [95].

Figure 1.21: Schematic Illustration of synthesis mechanism of thiol terminated SiNPs directly from 3-MPTMS [95].

1.5.2.1 Factors affecting particle growth of alkoxysilanes

The hydrolysis and polycondensation of alkoxysilanes and the morphology and type of the resulting silica network structure is highly dependent on the alkoxysilane used, its concentration and ratio to water, solvent effects and concentration, pH, nature of the catalyst and temperature [93].

1.5.2.2 Effect of solvent concentration

In ethanolic media, the alcohol contributes to the back reaction of the hydrolysis step, thus slowing the rate and leading to incomplete hydrolysis of the alkoxysilane precursor. Less siloxane groups results in a decreased rate of condensation, leading to a reduced rate of particle formation. It is also possible for the alcoholate (SiOR) and silanol (SiOH) groups to reversibly exchange throughout the condensation of the silica matrix. This “relaxation” mechanism of reversible exchange allows a slower, more controlled growth mechanism of particle formation, leading more monodisperse SiNPs [73].

1.5.2.3 Effect of pH

The relative hydrolysis and condensation rates of silanes is highly dependent on pH as shown in Figure 1.22 [97]. The size and morphology of the particles synthesised by sol-gel processes is also highly dependent on pH, with basic conditions favoured when synthesising discrete spherical particles [93].

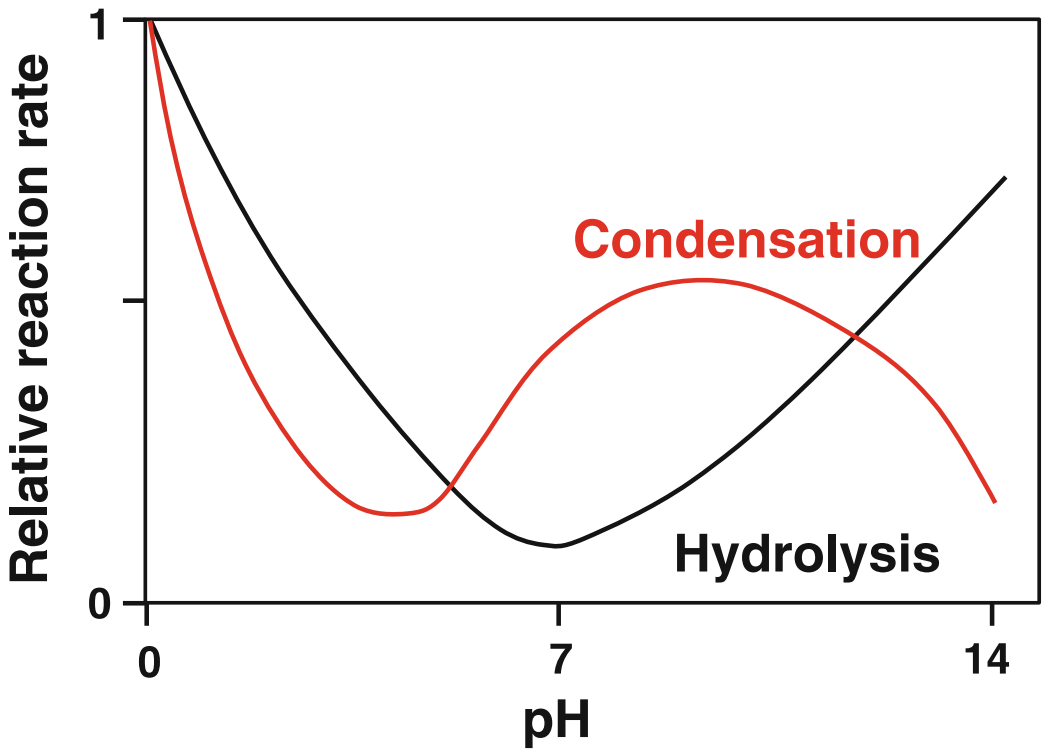

Figure 1.22: Relative hydrolysis and condensation rates of silanes as a function of pH. Adapted from [97].

The preparation of SiNPs with highly controllable surface functionality provides useful chemical handles for the introduction of subsequent chemical functionalities by a wide range of chemical reactions. The past decade has seen growing interest and devotion in finding rapid reactions that are efficient, versatile and selective. The most popular reactions that have fulfilled this criterion are 'click' reactions [98]. One such member is the free radical addition of a thiol across a carbon-carbon double bond, known as the thiol-ene 'click' reaction [99, 100]. This reaction has proven to be highly efficient in delivering new functionality to the surface of thiol terminated SiNPs [71, 93].

1.5.3 Thiol-ene ‘click’ chemistry

Thiol-ene ‘click’ chemistry has been known for over 100 years and successfully used for modification of polymers and surfaces, synthesis of star polymers, dendrimers, disaccharides and bio-conjugated polymers [98, 101, 102]. It has also proven useful for the surface functionalization of both vinyl and thiol terminated SiNPs [71, 87, 103-105]. These reactions yield a single regioselective product, can be run in benign solvents such as water, proceed under mild reaction conditions, can tolerate many different alkene and thiol functionalities, and give quantitative yields that generally require no chromatographic separation [99]. Thus, thiol-ene ‘click’ chemistry provides an ideal route for the chemical modification of materials in biological systems [106].

Thiol-ene reactions are conducted under radical conditions and proceed via a typical chain process with initiation, propagation and termination (Figure 1.23). Thiol-ene reactions can be initiated photolytically by photo-initiators such as benzophenone, or thermally by initiators such as azobisisobutyronitrile (AIBN) [98]. As shown in Figure 1.23, initiation generates a thiyl radical (RS•) which then adds to a carbon-carbon double bond, yielding a carbon centered radical which is then transferred to a second thiol molecule to give the anti-Markovnikov thiol-ene product and subsequent generation of a new thiyl radical. Termination occurs by radical-radical coupling [101].

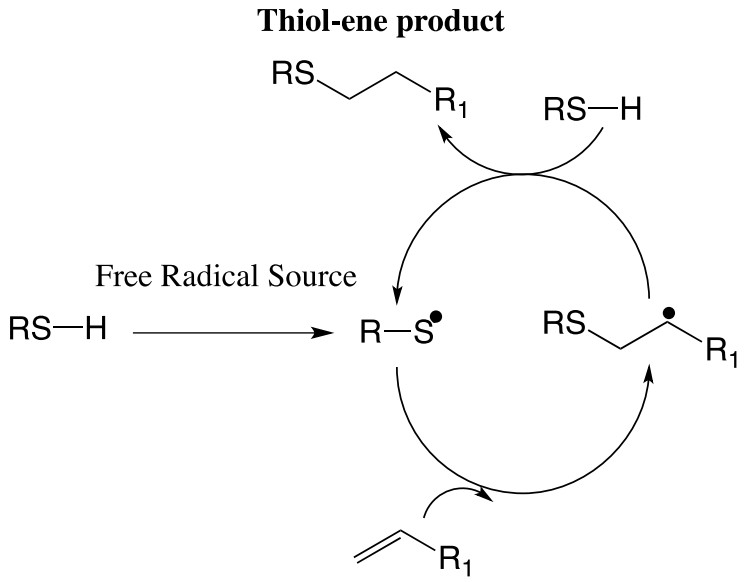

Figure 1.23: General mechanism of a thiol-ene ‘click’ reaction. Adapted from [101].

1.6 Characterisation of tethered NAD activity

The techniques listed above allow highly controlled synthesis of SiNP substrates and subsequent surface attachment of N^6-2AE-NAD. Techniques used to characterise and quantify SiNP size and surface area, as well as N^6-2AE-NAD attachment are covered in Chapter 2. In order to accurately and precisely quantify the catalytic activity of the tethered N^6-2AE-NAD with enzymes requires extensive analysis and understanding of the reaction kinetics of the surface-active heterogeneous system. Therefore, fundamental kinetic concepts of enzyme catalysed reactions, both in solution and at surfaces, must be investigated.

1.6.1 Enzyme Kinetics

Enzyme kinetics is the study of the chemical reaction rates catalysed by enzymes under different reaction conditions, allowing the mechanism, catalytic function and activity of the enzyme to be quantitatively investigated. In the most simplistic form of an enzyme reaction, the reactant (S) reversible binds to the active site of the enzyme (E) to form the enzyme/reactant-complex (ES), where the reactant is biochemically transformed to the product (P), which is subsequently released, regenerating the free enzyme for the next catalytic cycle [3]. This is represented in the following equation.

$$E + S \underset{k_{-1}}{\overset{k_1}{\rightleftharpoons}} ES \overset{k_{cat}}{\rightarrow} P + E \tag{1.1}$$

Michaelis and Menten proposed a rapid-equilibrium simplification, where the complexation reaction is significantly faster than the catalysis step and ES can be considered at steady state, i.e. $k_{-1} >> k_{cat}$ [107]. However, this is an oversimplification since ES is continuously being converted to product and cannot form an equilibrium. A few years later, Briggs and Haldane proposed a quasi-steady-state-approximation (QSSA) where, soon after mixing the enzyme and reactant, the concentration of ES remains constant throughout the course of the reaction as shown in Figure 1.24 [108]. This led to a superior version of the Michaelis Menten equation, where the initial velocity (v_o) of the enzyme reaction is described as a function of the reactant concentration.

$$v_0 = \frac{k_{cat}[E][S]}{K_M + [S]} \tag{1.2}$$

Where K_M is a pseudo-dissociation constant known as the Michaelis constant given by:

$$K_{M=}\frac{k_{-1}+k_{cat}}{k_1} \tag{1.3}$$

The reactant concentration S in Equation 1.2 represents the free reactant concentration and is assumed to equal the total reactant concentration in the system. This is known as the reactant stationary assumption and requires that the reactant concentration be significantly higher than the total enzyme concentration in the reaction system [40]. By measuring the initial velocity of an enzyme reaction over a range of reactant concentrations, while keeping all other conditions constant, Equation 2 can be satisfied, and fitted to experimental data in order to determine its parameters. This is known as an enzyme assay [40].

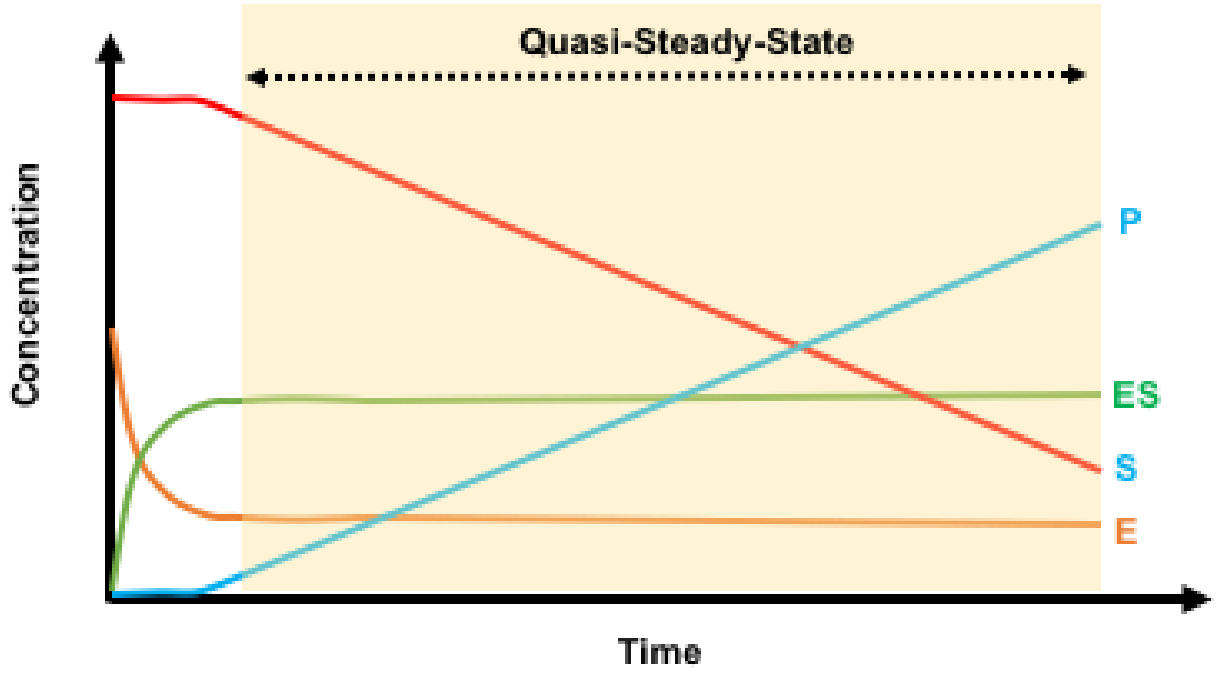

Figure 1.24: Concentration of the different reaction species in Equation 1.1 over time showing the quasi-steady-state (QSS) where the concentration of ES is constant over time.

1.6.1.1 Competitive inhibition

An enzyme inhibitor (I) is a compound that reversibly binds to the enzyme, decreasing the rate of catalysis [109]. A competitive inhibitor competes for the same active site of the enzyme, where binding excludes the reactant from binding and catalysis [3].

Competitive inhibitors may also block the active site of the enzyme, restricting access and binding of the reactant and thus inhibiting the reaction [110, 111]. Figure 1.25 shows a schematic of competitive inhibition.

Figure 1.25: Schematic of competitive inhibition where both reactant (S) and inhibitor (I) compete for the same active site. Taken from [109].

Applying the quasi-steady-state approximation gives:

$$v_0 = \frac{k_{cat}[E][S]}{K_M\left(1 + \frac{[I]}{K_I}\right) + [S]} \tag{1.4}$$

Where:

$$K_{I=}\frac{[E][I]}{[EI]} \tag{1.5}$$

1.6.2 Surface enzyme kinetics

Compared to homogenous systems, where the kinetics of enzyme catalysis in solution has reached a high degree of understanding, interfacial enzyme catalysis with reactants attached to solid surfaces is not well defined [112, 113]. However, the recent development of technologies and applications utilising the action of enzymes at interfaces such as biosensors [114], DNA microarrays [115], protein chip technologies [116] and biosynthesis [48] has driven the need to investigate the fine kinetic details of heterogeneous enzyme catalysis [4, 24, 33, 34, 110, 112-134]. Heterogeneous enzyme catalysis is dependent on surface structure and functionality, surface density

of reactant and changes to the enzyme conformation at the surface leading to changes in adsorbed enzyme activity [135]. All of these factors result in homogeneous enzyme kinetics being a poor approximation of heterogeneous enzyme systems.

1.6.2.1 Enzyme kinetics on surface bound reactants

To date, interfacial enzyme kinetic studies have mainly focused on enzymes conjugated to a surface acting on substrates in bulk solution, with scarce investigation of the converse surface bound reactant configuration [110]. In the latter configuration, it is difficult to achieve a large molar excess of surface bound reactant relative to enzyme concentration. Thus, an enzyme excess approach is instead applied, where activity is measured as a function of enzyme concentration at a fixed surface bound reactant concentration [117, 126]. In this approach, the reactant stationarity assumption is applied to the enzyme and mass conservation applied to the surface bound reactant, allowing the quasi-steady-state assumption (QSSA) to be applied. In these instances, the inverse version of the Michaelis-Menten equation is applied [117, 136].

$$v_0 = \frac{k_{cat}[S][E]}{K_M + [E]} \tag{1.6}$$

1.6.2.2 Examples of interfacial enzyme kinetic analysis with surface bound reactants

Gaspers *et al*. determined the kinetics of collagenase reacting with peptides immobilised on a glass slide, finding that the rate was dependent on the intrinsic enzyme reaction rate and the diffusion of the enzyme to the surface [137]. They later proposed a modified Michaelis-Menten model for the surface reaction of protease on monolayers of bovine serum albumin (BSA) which accounted for the adsorption of enzyme onto the active surface [138]. Later in a series of papers, Corn *et al.* used SPR techniques to characterise and model the enzyme kinetics of nuclease enzymes in solution reacting with surface immobilised biopolymer arrays of DNA and RNA as shown in Figure 1.26 [114-116]. The surface coverage of the enzyme-substrate intermediate and reaction rate was found to be dependent on a combination Langmuir adsorption kinetics and classic Michaelis Menten kinetic concepts, respectively. In general, the enzyme reaction rate constant (k_{cat}) was found to be ~10 fold lower at the surface than observed with free reactant in solution [116].

Figure 1.26: Schematic of surface enzyme reaction of enzyme and biopolymer array. Taken from [115].

Foose *et al.* characterised the interfacial kinetics of proteolytic cleavage of multilayer films of ovalbumin by the enzyme Subtilisin Carlsberg using ellipsometry [135]. By combining the Langmuir adsorption isotherm to classical Michaelis-Menten-Briggs-Haldane kinetic concepts, they developed a model describing the change in film thickness due to proteolytic breakdown of the ovalbumin film as a function of aqueous enzyme concentration [135]. Figure 1.27 depicts their proposed model, where a dynamic equilibrium was assumed to exist between the surface adsorbed and aqueous enzyme. Surface adsorbed enzyme then reversibly binds to the surface reactant, forming a surface bound enzyme-reactant complex, resulting in cleavage of peptides within the ovalbumin film [135]. A direct link between surface adsorption and surface activity of the enzyme was observed with a plateau in activity and adsorption occurring at a similar aqueous enzyme concentration, suggesting saturation of the surface with enzyme. Experimental data was fitted to their proposed model, providing apparent rate constants that were found to be comparable to those for aqueous proteolysis.

Figure 1.27: Schematic of enzyme adsorption, complexation and cleavage of the enzyme Subtilisin Carlsberg onto and with the multilayer ovalbumin film. Taken from [135].

1.6.2.3 Interfacial cellulase kinetics

One of the most widely studied heterogeneous enzyme reactions is the hydrolysis of insoluble cellulose of lignocellulosic biomass by cellulase enzymes for the production of biofuels [117, 118, 139]. Although a full mechanistic understanding has remained elusive, many different studies have highlighted the following critical and unique steps in their analysis as depicted in Figure 1.28:

A. Adsorption of cellulase onto the surface of insoluble cellulose.
B. Complexation of the chain end of cellulose with the active site of surface adsorbed cellulase to form the enzyme-substrate complex.
C. Catalytic hydrolysis of the cellulose chain bond to yield a soluble cellobiose subunit.
D. Desorption of cellulase to either the fluid phase or to an adsorbed catalytically inactive phase.

For an excellent summary of work in this area, the reader is referred to the following reviews [118, 139].

Figure 1.28: Schematic of the catalytic action of cellulase on cellulose surfaces. Taken from [118].

Recently, Kari *et al.* compared the conventional approach to Michaelis Menten kinetic analysis to the inverse Michaelis-Menten approach, for kinetic analysis of the interfacial reaction of cellulase on cellulose surfaces (Figure 1.29) [117]. Although they did not directly consider adsorption of cellulase onto the cellulose surface in their kinetic analysis, they introduced a new term for the surface density of the kinetically active/available enzyme attack sites. When compared to the quantity of total enzyme adsorption, the quantity of kinetically active sites was found to be lower, showing that not all adsorption of enzyme to the surface results in kinetically successful complexation [117].

Figure 1.29: Illustration of enzyme saturation (A) and substrate saturation (B) of the interfacial reaction of cellulase on cellulose surfaces. Taken from [117].

1.6.2.4 Kinetic enhancement of enzymes acting on surface bound reactants

Recently, several studies have observed enhanced enzyme activity with reactants when they are conjugated to the surface of nanoparticles. Mirkin *et al.* observed a 2 fold enhancement in ribonuclease H activity with Polyvalent DNA tethered to the surface of gold nanoparticles compared to that of free DNA in solution [140]. The enhanced activity was attributed to enzyme/reactant co-localization resulting from ribonuclease H association with the high concentration of DNA localised to the nanoparticle surface.

Medintz *et al.* have extensively studied the kinetic action of freely diffusing proteases on the lysis of peptides conjugated to the surface of quantum dots [4]. In an early study, they found a 3-5 fold increase in enzyme efficiency (k_{cat}/K_M) compared the freely diffusing peptide system [126]. Kinetic data was found to be consistent with an enzyme hopping model, first described by Berg *et al.*, where the surface localised enzyme cleaves all peptides from a single quantum dot surface before moving onto another quantum dot as shown in Figure 1.30 [126, 133].

Figure 1.30: Hopping mechanism of protease catalysed lysis of peptides conjugated to the surface of quantum dots. Taken from [126].

The proposed surface localised hopping model was further supported when Wu *et al.* observed increases in enzyme efficiency up to 80 fold when the surface ligand chemistry of the zinc sulphide (ZnS) QD was varied with several different small anionic thiol compounds [110]. Multiple copies of the peptide reactant were self-assembled onto the QD surface along with Cysteine (CYS), dihydrolipoic acid (DHLA), glutathione (GSH) or 3-mercaptopropionic acid (MPA) and the protease activity of thrombin or trypsin measured for different combinations of the surface ligands (Figure 1.31). Analysis of surface enzyme adsorption showed that the affinity of the proteases for each QD interface could significantly increase surface proteolytic activity up to a point where too much affinity started to inhibit activity. Although thrombin carried a net negative charge within the assay conditions, it was found to adsorb more strongly and was more sensitive to changes in the anionic surface coating than trypsin. This was postulated to be due to thrombin possessing two positively charged anion binding exo-sites. In general, the highest levels of proteolytic activity were observed for GSH and CYS coatings which are zwitterionic in character. Zwitterionic surfaces are resistant to non-specific protein adsorption and were thought to temper the protease adsorption in such a way as to promote acceleration in proteolytic activity.

Figure 1.31: Protease catalysed lysis of peptides conjugated to the surface of quantum dots capped with different small anionic thiol compounds. Taken from [110].

The importance of how the nanoparticle surface characteristics can influence localised enzyme activity was further explored by changing the chemical nature of the QD surface ligands [33]. Peptides were self-assembled on the QD surface along with seven different ligands that were either neutral, zwitterionic, positively or negatively charged or of different length (Figure 1.32). Surface proteolytic activity of trypsin was found to accelerated with all ligand functionalities compared to aqueous peptide, with the largest increase in activity (~35 fold) observed with the shortest zwitterionic ligand. Molecular dynamics simulations revealed several complex factors contributing to this enhancement change in activity with different surface ligands. These include the configuration of how the peptide was displayed on the surface with each ligand chemistry as well as attractive forces between the enzyme and functional quantum dot surface [4, 33].

Figure 1.32: Protease catalysed lysis of peptides conjugated to the surface of quantum dots capped with 7 different surface ligands. Taken from [33].

1.6.2.5 Analysis of interfacial enzyme kinetics with surface tethered N^6-2AE-NAD

Analysis of the interfacial kinetics of enzymes catalysis with tethered N^6-2AE-NAD at the SiNP surface with two different enzymes allows different kinetic factors to be investigated. This allows a greater understanding of the catalytic action of enzymes with N^6-2AE-NAD at the SiNP surface to be gained. In this work, the enzymes applied to N^6-2AE-NAD tethered to the SiNP surface are Glycerol-3-Phosphate Dehydrogenase isolated from *E. coli* (EcG3PD), commercially available alcohol dehydrogenase (ADH) from baker's yeast (*S. cerevisiae*) and commercially available glutamate dehydrogenase (GluDH) from bovine liver. Although these enzymes belong to the oxidoreductase family, they differ significantly in structure and surface properties as discussed below in Section 1.7.

1.7 Enzymes

1.7.1 Glycerol-3-Phosphate Dehydrogenase from *E. coli* (EcG3PD)

Glycerol-3-Phosphate Dehydrogenase (EcG3PD) catalyses the NAD dependent interconversion of glycerol-3-phosphate (G3P) and dihydroxyacetone phosphate (DHAP) as shown in Figure 1.33 [141].

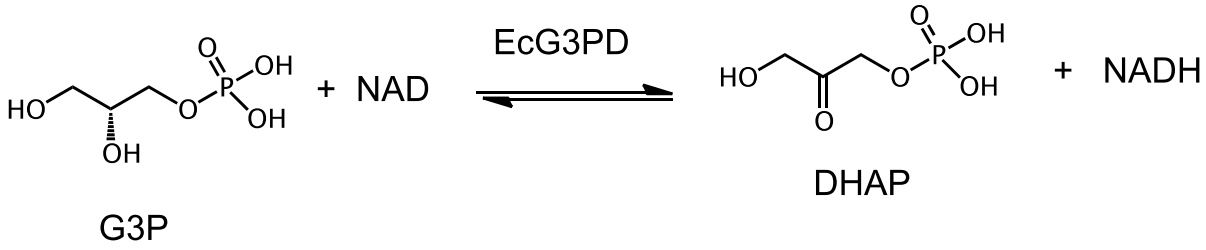

Figure 1.33: NAD dependent catalysed interconversion of glycerol-3-phosphate (G3P) and dihydroxyacetone phosphate (DHAP) by EcG3PD.

EcG3PD was encoded from the *E. coli* G3PD gene (WP_001076194) and expressed in *E. coli* as previously reported [14, 142]. EcG3PD is a polypeptide of 339 amino acids forming a 73 kDA homodimer. However, the three-dimensional crystal structure for this gene product has not yet been determined. For protein modelling, the homologous isozyme G3PD from *Leishmania Mexicana* (LmG3PD) was used [141]. LmG3PD is a 78 kDa homodimer made up of 366 amino acid polypeptides and shares 32.2 % sequence identity with EcG3PD as determined by the Uniprot sequence alignment tool [143]. Structural analysis of LmG3PD revealed several similarities in the N-terminal NAD binding domain to all previously studied NAD-dependent G3PDs, which, along with size similarity and relative sequence homology, makes it a good candidate as a model for EcG3PD [141]. Figure 1.34 shows the structure of LmG3PD with bound NADH/DHAP intermediate.

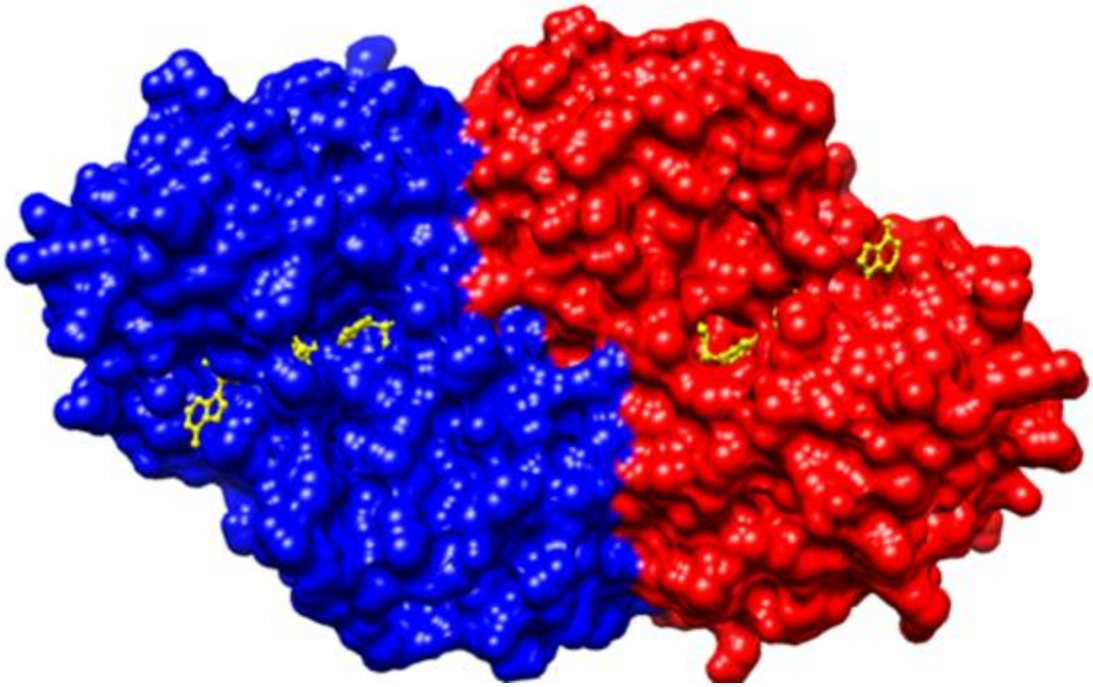

Figure 1.34: Tertiary structure of LmG3PD with each homodimer coloured in blue and red and NAD/DHAP intermediate coloured in yellow [141]. Image generated with Chimera [144].

1.7.2 Alcohol Dehydrogenase (ADH) from baker's yeast (*S. cerevisiae*)

Alcohol Dehydrogenase (ADH) catalyses the NAD dependent interconversion of ethanol and acetaldehyde as shown in Figure 1.35 [145].

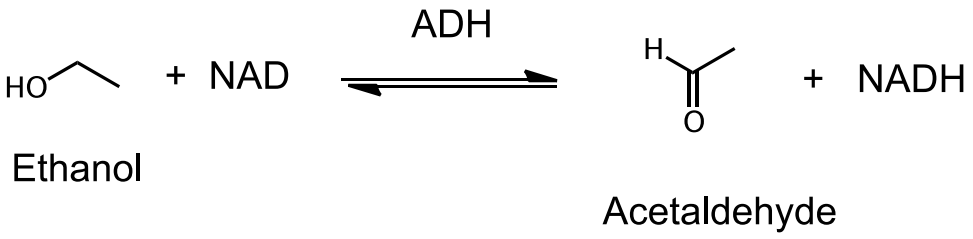

Figure 1.35: NAD dependent catalysed interconversion of ethanol and acetaldehyde by ADH.

ADH is a tetrameric dimer of dimers made up of four identical 347 amino acid subunits totalling 147 kDA [145]. One of these dimers is shown in Figure 1.36 below.

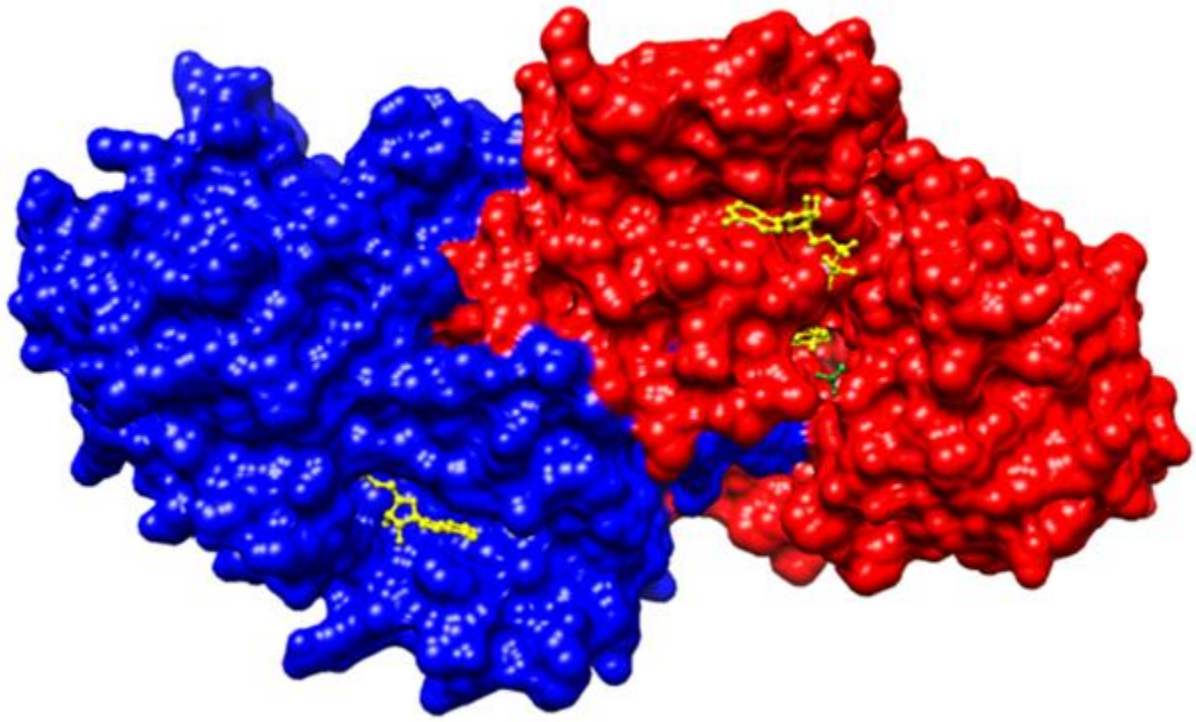

Figure 1.36: Tertiary structure of one ADH dimer with each subunit coloured in blue and red and NAD (yellow) and trifluoroethanol (green) [145]. Image generated with Chimera [144].

1.7.3 Glutamate Dehydrogenase (GluDH) from bovine liver

Glutamate Dehydrogenase (GluDH) catalyses the reversible oxidative deamination of L-glutamate to α-ketoglutarate as shown in Figure 1.37 [146, 147].

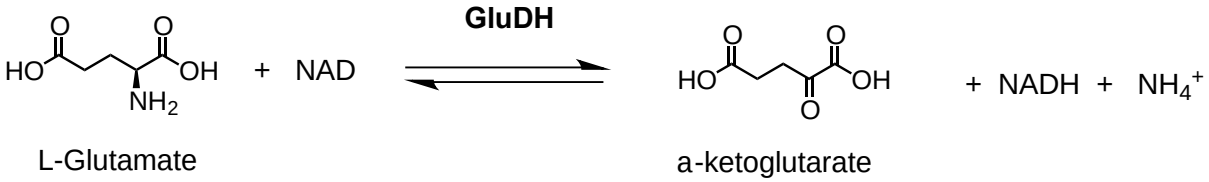

Figure 1.37: Reversible oxidative deamination of L-glutamate to α-ketoglutarate catalysed by GluDH with reduction of NAD to NADH.

GluDH is a homohexamer made up of six identical subunits of 501 amino acids totalling 345 kDA [146, 147]. One of these homohexamers is shown in Figure 1.38 below.

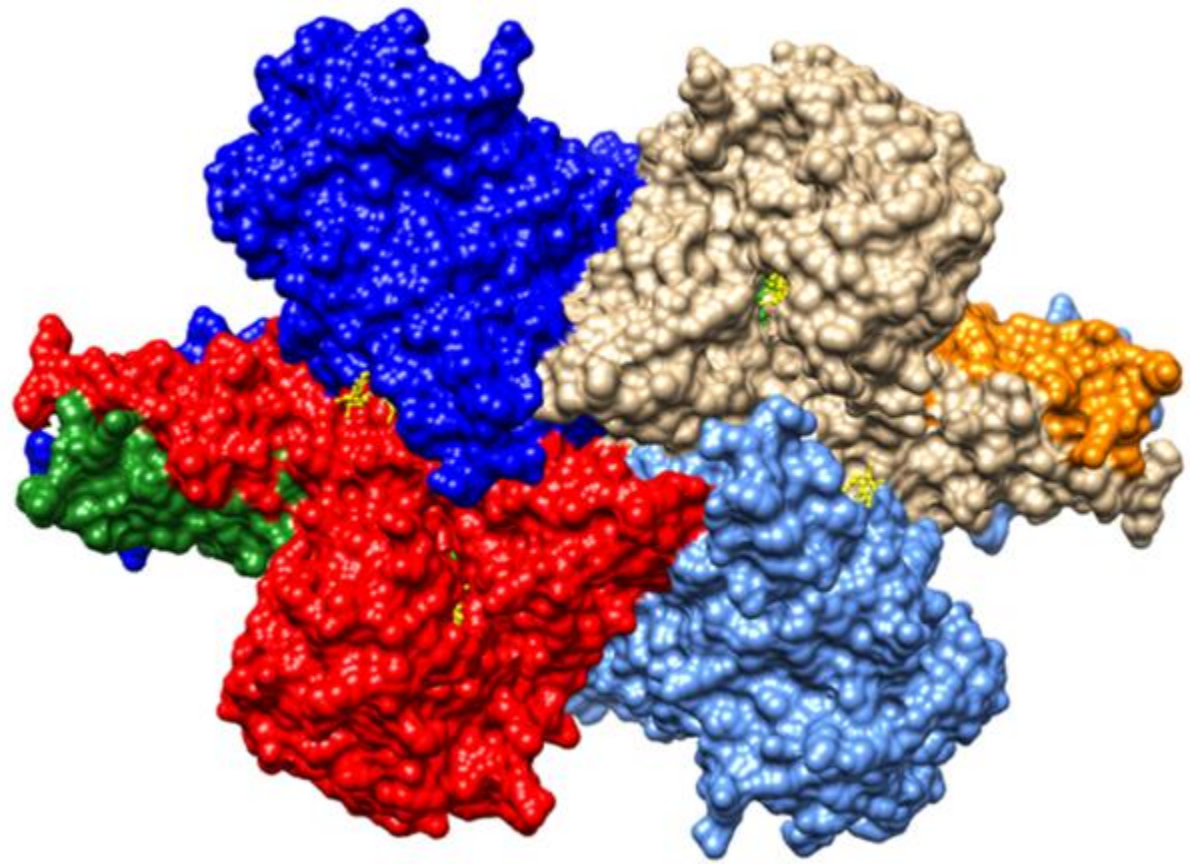

Figure 1.38: Tertiary structure of GluDH homohexamer with each subunit coloured in in a different colour and NAD (yellow) and α-ketoglutarate (green) [146, 147]. Image generated with Chimera [144].

1.8 Enzyme assays

Enzyme assays are usually performed by measuring the increase or decrease in reactant concentration over the course of the reaction. This is commonly achieved using analytical techniques such as UV/Vis spectroscopy [14, 41, 42], fluorescence spectroscopy [31, 45, 52, 72, 148-150] and chromatography [151, 152].

1.8.1 Resazurin/PMS fluorometric detection of NADH

The resazurin fluorescence assay, also known as the Alamar blue bioassay, has been used to indicate cellular viability, activity and cytotoxicity in a range of biological systems [150]. Resazurin is a weakly fluorescent blue dye that, in the reducing environment of living cells, is converted to the highly fluorescent pink resorufin (Excitation 545nm, Emission 590nm) as shown in Figure 1.40. The chemistry behind this reaction is the reduction of resazurin by cellular components such as NADH, NADPH, FADH, FMNH and cytochromes [150]. Thus, the resazurin bioassay can be

used as an extremely useful tool for selectively monitoring the formation of NADH from NAD in enzyme catalyzed reactions in the presence of the reducing agent phenazine methosulfate (PMS^+) as shown in Figure 1.39 [31, 45, 52, 72, 148-150].

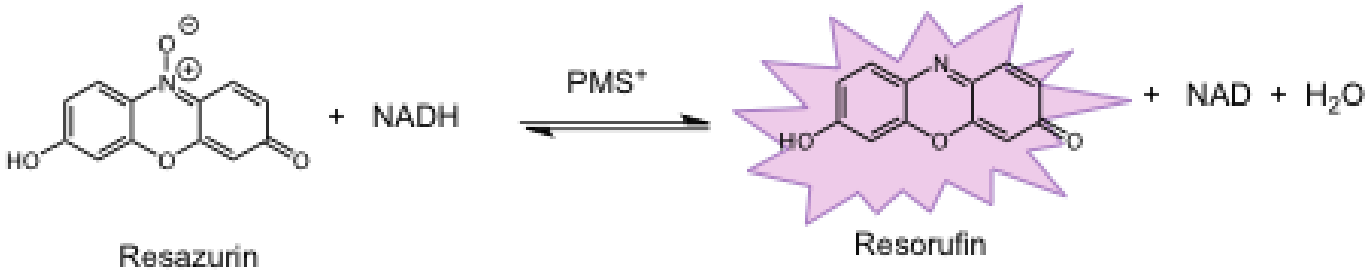

Figure 1.39: Schematic of PMS^+ mediated oxidation of resazurin to highly fluorescent resorufin by NADH.

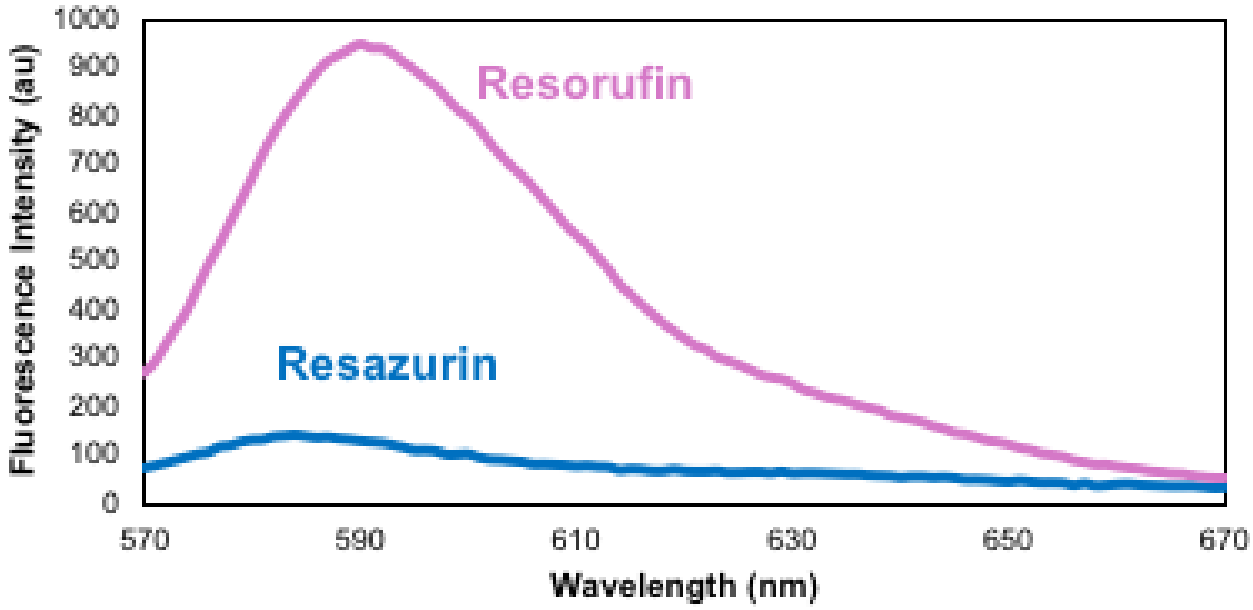

Figure 1.40: Fluorescence Intensity of weak fluorescent resazurin (blue line) and resorufin (pink line).

This chapter has introduced the concept of utilising the catalytic capability of enzymes and cofactors in industrial biosynthetic applications and some of the associated limitations. It has also introduced the idea of specifically tethering the cofactor NAD to

the surface of silica nanoparticles and its viability as a strategy to overcome some of these limitations. A literature review of previous reports of the covalent tethering of NAD to nanostructures is performed, highlighting the gap in understanding of the surface interactions and kinetics of these processes. An informative literature review on interfacial enzyme kinetics analysis is provided as context for later discussions. Lastly, the enzymes relevant to this work are introduced as well as a strategy to assay their activity.

CHAPTER 2 EXPERIMENTAL: MATERIALS AND METHODS

2.1 Overview

This chapter covers the materials and experimental methods used in this work. This includes a list of all chemicals used, followed by a brief description of experimental procedures covering silica nanoparticle synthesis and characterisation, surface attachment and quantification of N^6-linked-2AE-NAD, enzyme purification, enzyme assays and other relevant general preparations. Lastly, information regarding analytical techniques and instruments is provided.

2.2 Chemicals

Table 2.1: Chemicals used in this work

Chemical	Abbreviation	Purity	Supplier
3-Mercaptopropyltrimethoxysilane	3-MPTMS	95%	Sigma Aldrich
Triethoxyvinylsilane	VTES	97%	Sigma Aldrich
Triethoxyphenylsilane	PTES	98%	Sigma Aldrich
Trimethoxy(propyl)silane	PTMS	97%	Sigma Aldrich
(3-Chloropropyl)triethoxysilane	ClPTES	95%	Sigma Aldrich
3-Cyanopropyltriethoxysilane	CNTES	98%	Santa Cruz Biochemicals
Ammonium Hydroxide (25% in H2O)	NH4OH	99%	Sigma Aldrich
Absolute Ethanol	EtOH	99%	Chem-Supply
Potassium persulfate	KPS	99%	Sigma Aldrich
nonene-2AE-NAD	N/A	99%	CSIRO
thiol-PEG4-2AE-NAD	N/A	99%	CSIRO
acetonitrile	ACN	99%	Sigma Aldrich
β-Nicotinamide adenine dinucleotide hydrate	NAD	≥96.5%	Sigma Aldrich
β-Nicotinamide adenine dinucleotide, reduced disodium salt hydrate	NADH	≥97%	Sigma Aldrich
Resazurin sodium salt	Resazurin	~80%	Sigma Aldrich
Phenazine methosulfate	PMS+	≥90%	Sigma Aldrich
sn-Glycerol 3-phosphate bis(cyclohexylammonium) salt	G3P	≥93%	Sigma Aldrich
Tris(hydroxymethyl)aminomethane hydrochloride	TRIS	≥99%	Sigma Aldrich
Glycerol-3-Phosphate Dehydrogenase from *E. coli*	EcG3PD	N/A	CSIRO
Alcohol Dehydrogenase from *Saccharomyces cerevisiae*	ADH	N/A	Sigma Aldrich
Sodium phosphate dibasic anhydrous	Na_2HPO4	≥99%	Sigma Aldrich
L-Glutamic Dehydrogenase from bovine liver	GluDH	N/A	Sigma Aldrich
L-Glutamic acid	N/A	≥99%	Sigma Aldrich
α-Ketoglutaric acid	N/A	≥99.5%	Sigma Aldrich
Acetaldehyde	N/A	≥99.5%	Sigma Aldrich
Ammonium chloride	NH_4Cl	≥99.5%	Sigma Aldrich
2, 4- Dinitrophenol	2,4-DNP	≥99.5%	BDH
Iodoacetamide	N/A	≥99%	Sigma Aldrich
Benzyl Bromide	N/A	98%	Sigma Aldrich

2.3 SiNP synthesis

2.3.1 Aqueous synthesis of thiol terminated SiNPs

Stable colloidal suspensions of thiol functionalized silica nanoparticles were synthesized using a revised and up-scaled version of Nakamura's method [71, 75, 77, 94, 96]. In general, thiol terminated SiNPs were prepared by adding MPTMS (2-15 mM) to a blend of 25% ammonia (72 mL, 0.9 M) and water (428 mL) and stirred at room temperature for 3 days.

2.3.2 Ethanolic synthesis of thiol terminated SiNPs

Thiol terminated SiNPs were also synthesised within ethanolic media. SiNPs were prepared by dispersing 2 mL (10.9 mM) MPTMS in 100 mL (1.7 M) ethanol, which was then slowly added to a blend of 25% ammonia (150 mL, 1 M) and water (750 mL) and stirred at room temperature for 4 days.

2.3.3 Synthesis of vinyl terminated SiNPs

The ethanolic method of SiNP synthesis was also applied to vinyl silane to prepare vinyl terminated SiNPs. In general, a mixture of VTES (1 mL, 23 mM) in Ethanol (39 mL, 3.3 M) was added drop-wise to a stirred solution of 25% ammonia (32 mL, 1 M) and water (128 mL) and stirred at room temperature for 7 days.

2.3.4 Synthesis of hydrophobic SiNPs

For preparation of vinyl, propyl, phenyl, chloropropyl and cynaopropyl functionalized silica nanoparticles of different particle sizes, the concentration of VTES, PTMS, PTES, ClTES and CNTES was altered to 4 mM,10 mM, 20 mM, 40 mM, 80 mM 120 mM and 200 mM in 3.4 M ethanol and 0.64 M NH_4OH. Mixtures were stirred for 7 days with 1 mL samples taken at different time points. Samples were washed 3 times with 1 mL ethanol by centrifugation before SEM analysis.

2.3.5 Effect of ammonia concentration on the synthesis of hydrophobic SiNPs

For preparation of vinyl functionalised SiNPs at different ammonia concentrations, mixtures of 0.5 mL (40 mM) VTES and 10 mL (3.4 M) ethanol were added to stirred solutions of ammonium hydroxide varying from 0 to 2.6 M. Mixtures were stirred for 7 days with 1 mL samples taken at different time points. Samples were washed 3 times with 1 mL ethanol by centrifugation before SEM analysis.

2.3.6 Effect of ethanol concentration on the synthesis of hydrophobic SiNPs

For preparation of vinyl functionalised SiNPs at different ethanol concentrations, mixtures of 0.5 mL (40 mM) VTES and different amounts of ethanol from 0 to 25 mL

(0 to 8.6 M) were added to stirred solutions of ammonium hydroxide (5 mL, 0.64 M) and varying amounts of deionised water to make up 50 mL. Mixtures were stirred for 7 days with 1 mL samples taken at different time points. Samples were washed 3 times with 1 mL ethanol by centrifugation before SEM analysis.

2.3.7 Effect of reaction scale on the synthesis of hydrophobic SiNPs

For preparation of vinyl and propyl functionalised SiNPs at different reaction scales, mixtures of (200 mM) VTES in ethanol (3.4 mM) were added to stirred solutions of ammonium hydroxide (0.64 M) and varying amounts of deionised water to make up 1, 50, 100 and 1000 mL. Mixtures were stirred overnight with a 1 mL samples taken washed 3 times with 1 mL ethanol by centrifugation before SEM analysis.

2.4 Characterisation of SiNPs

Accurate quantification of surface based biocatalytic reactions is essential to understand the impact of tethered species on the reaction rate. To achieve this, the SiNP supports must be thoroughly and accurately characterised. Information regarding the size, size dispersity, specific surface area and zeta potential is obtained using a combination of scanning electron microscopy, dynamic light scattering, gas adsorption analysis and electrophoretic mobility analysis.

2.4.1 Scanning Electron Microscopy (SEM)

Scanning Electron Microscopy (SEM) is a powerful electron microscopy technique capable of providing high resolution information of topography on the nanoscale and is a common technique for the accurate determination of the size and size distribution of nanoparticles [71, 75, 153]. In short, an electron beam is generated by the electron gun with an energy between 2-40keV. A series of electromagnetic condenser lenses then focus the electron beam into a fine probe which is scanned across the sample surface in a raster-pattern by coils [154]. The electrons interact with and penetrate the specimen, producing secondary, backscattered, and Auger electrons as well as x-rays, all of which are collected by various detectors and transformed into a raster image. From this image, the dimensions and properties of the sample can be determined.

2.4.2 Dynamic Light Scattering (DLS)

Dynamic Light Scattering is another common method for determining the size of nanoparticles, offering rapid and potentially very accurate analysis. DLS has proven

useful for the accurate determination of nanoparticle size and size distribution [155-157]. Briefly, the nanoparticle solution is irradiated by a beam of light over a range of angles which is then scattered by the particles, altering its direction and intensity as shown in Figure 2.1 This variation in intensity over time is dependent on the kinetic energy of the constant random (Brownian) motion of the particles and can be used to measure their diffusion coefficient D_f. Using the Stokes-Einstein equation, the diffusion coefficient can be used to calculate the hydrodynamic radius R_H of the particles:

$$D_f = \frac{k_B T}{6\pi\eta R_H} \tag{2.1}$$

where k_B is the Boltzmann constant, T is the suspension temperature, η is the viscosity of the media [157]. The results of DLS is dependent on the data processing algorithm that is used and while the median particle size is often representative, the breadth of particle size distribution can be problematic.

Figure 2.1: Schematic of dynamic light scattering analysis of magnetic nanoparticles (MNPs). Taken from [157].

2.4.3 Zeta potential

The zeta potential (ζ) of a charged particle is the electric potential in the interfacial double layer at the shear plane, where the velocity of the dispersion liquid relative to the dispersed particle is zero [158]. The electric potential at the particle surface and shear place are approximately equal to each other and thus the zeta potential is often used for the quantification of the particle surface charge and as an indicator of the stability of colloidal suspensions [158]. The zeta potential of a colloidal solution is obtained from the electrophoretic mobility of the dispersed particles. When an electric field is applied to a solution of colloidal particles, the particles will move with a constant

velocity dependent on the magnitude of the zeta potential. The velocity is measured by DLS and converted to the zeta potential by applying Smoluchowski's Equation [158].

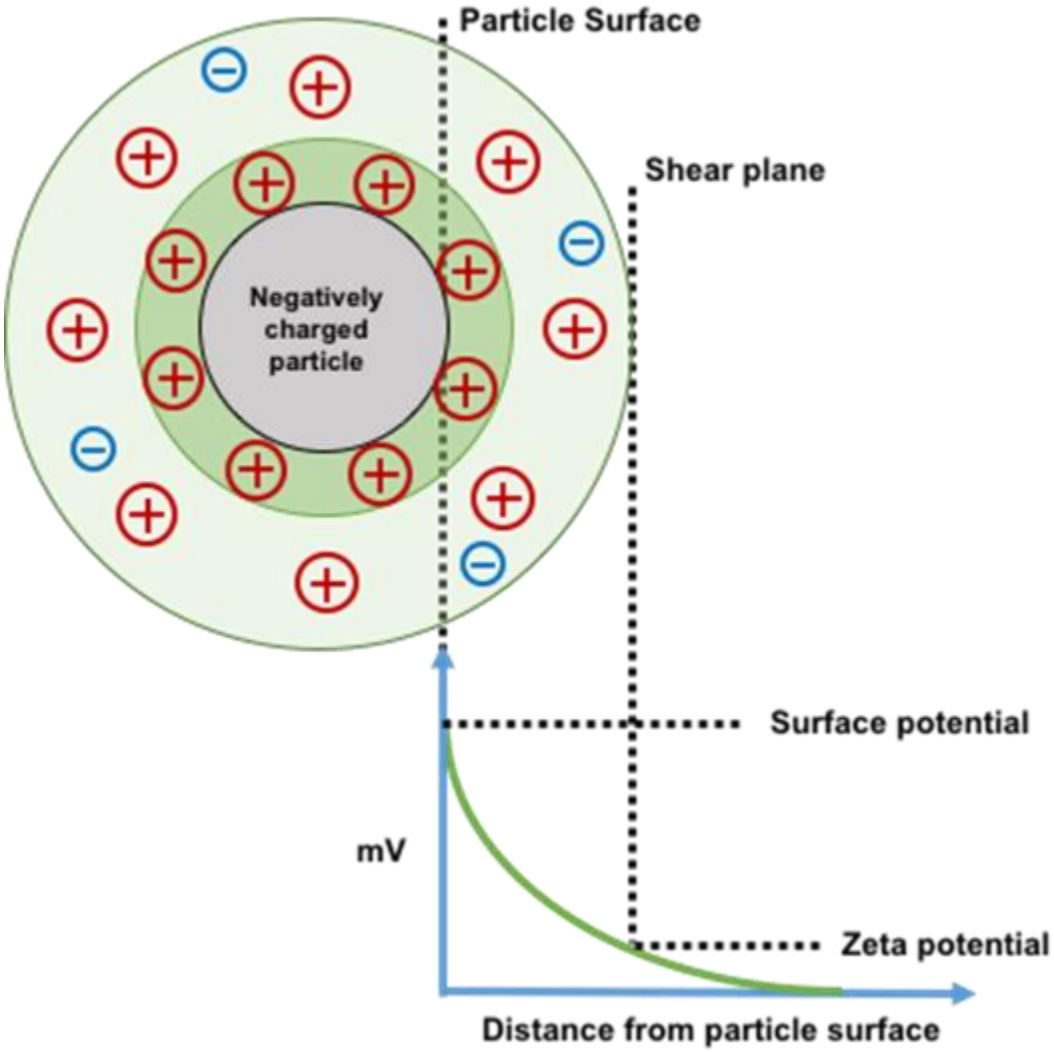

Figure 2.2: Surface potential and zeta potential as a function of distance from the surface of a dispersed charged particle.

2.4.4 BET Surface area analysis

In BET surface area analysis, the amount of nitrogen adsorbed onto a known mass of dried sample is measured at low temperatures over a range pressures below atmospheric pressure [159]. Information from the adsorption isotherm is used to determine the surface area of the sample using the BET equation:

$$\frac{1}{X\left[\left(\frac{P_0}{P}\right)-1\right]} = \frac{1}{X_m C} + \frac{C-1}{X_m C}\left(\frac{P_0}{P}\right) \tag{2.2}$$

Where X is the mass of Nitrogen gas adsorbed at any relative pressure (P/P_0), X_m is the monolayer adsorption capacity at standard temperature and pressure (273 K and 1 atm) and C is the BET constant [159]. Adsorption data is plotted as $1/X[(P/P_0)-1]$ vs (P/P_0), known as a BET plot as shown in Figure 2.3. The linear portion in the middle of the plot represents monolayer formation and can be fit with (2.2) to determine X_m, where S is the slope and I is the y-intercept:

$$X_m = \frac{1}{S+I} \tag{2.3}$$

Once X_m is determined, the total surface area, S_t, can be calculated from:

$$S_t = \frac{X_m L_{av} A_m}{M_v} \tag{2.4}$$

$$S_{BET} = \frac{S_t}{m} \tag{2.5}$$

Where L_{av} is Avogadro's number, A_m is the cross section area of Nitrogen and M_v is the molar volume. The BET surface area S_{BET} is obtained from the total surface area and the total mass of the absorbent sample m.

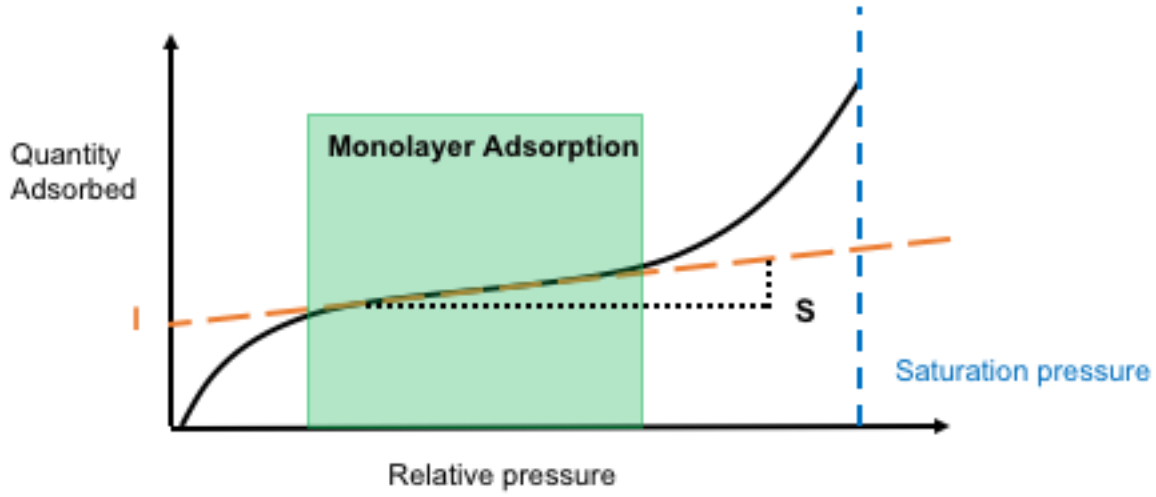

Figure 2.3: Schematic of BET plot of adsorbed quantity of gas onto the surface with increasing relative pressure of a Type II isotherm.

2.4.5 Attenuated Total Reflectance Fourier Transform Infrared Spectroscopy (ATR-FTIR)

Attenuated Total Reflectance Fourier Transform Infrared Spectroscopy (ATR-FTIR) has become the most widely used FTIR analysis method as it offers rapid qualitative and quantitative analysis with simple sample preparation. ATR-FTIR functions by measuring changes in a totally internally reflected IR beam when in contact with a sample. Briefly, an IR beam is passed at a specific angle into an optically dense crystal with a high refractive index total internal reflectance occurs (Figure 2.4). The internal reflectance causes an evanescent wave that interacts with the sample in contact with the crystal surface. The energy of the evanescent wave will then be attenuated at IR regions absorbed by the sample, which is then passed back to the IR beam and detected by the IR spectrometer, generating an IR spectrum [160].

Figure 2.4: Schematic of an ATR-FTIR accessory [160].

However, due to the highly un-reproducible level of contact between the sample and crystal, quantitative ATR-FTIR can be difficult. It has been demonstrated that this can be overcome by using a reliable IR active mode as an internal reference. [71, 161]

2.5 Construction of ATR-FTIR standard curves

2.5.1 nonene-2AE-NAD with thiol terminated SiNPs

For creation of the calibration curve for nonene-2AE-NAD attachment to thiol terminated SiNPs, 0.9, 1.8, 2.6, 3.5, 4.4, 5.3, 7.1 and 8.8 µL of a 75 mM NAD solution was homogenized by mixing with 20 mg batches of thiol terminated SiNPs with an average diameter of 149 nm and a specific surface area of 25.3 m^2/g. The particles were then dried overnight at 30 mbar and 25 °C for ATR-FTIR analysis.

2.5.2 thiol-PEG_4-2AE-NAD with vinyl terminated SiNPs

For creation of the standard curve for SH-PEG_4-2AE-NAD attachment to vinyl terminated SiNPs, 0.66, 1.3, 2.0, 2.6, 3.3, 4.0, 5.3 and 6.6 µL of a 75 mM NAD solution was homogenized with 20 mg batches of vinyl terminated SiNPs with an average diameter of 204 nm and a specific surface area of 15.7 m^2/g. Particles were then dried and analysed as previous.

2.6 SiNP surface attachment reaction

2.6.1 Attachment of nonene-2AE-NAD to thiol SiNPs

Nonene-2AE-NAD was covalently tethered to the surface of thiol terminated SiNPs via a radical initiated thiol-ene 'click' reaction. In general, an equivalent of 5 nonene-2AE-NAD molecules/nm^2 of SiNP surface (2-9.7 mg, 2.4-11.5 µmol) was added to thiol terminated SiNPs (20-100 mg) dispersed in 2-10 mL water. The reaction was initiated by the addition of potassium persulfate (10mg, 37 µmol). The mixture was stirred at high speed at room temperature for 48 hours or at 60°C for 18 hours before being washed 5 times with 50 mL deionised water by centrifugation.

2.6.2 Attachment of thiol-PEG_4-2AE-NAD and thiol-PEG_{12}-2AE-NAD to vinyl SiNPs

Thiol-PEG_4-2AE-NAD and thiol-PEG_{12}-2AE-NAD were alsp covalently tethered to the surface of vinyl terminated SiNPs via a radical initiated thiol-ene 'click' reaction. In general, an equivalent of 5 thiol-PEG_4-2AE-NAD or thiol-PEG_{12}-2AE-NAD molecules/nm^2 of SiNP surface (5 mg, 5 µmol) was added to thiol terminated SiNPs (20 mg) dispersed in 5 mL of a 50:50 water:acetonitrile solution. The reaction was

initiated by the addition of potassium persulfate (10mg, 37 μmol). The mixture was stirred at high speed at 60°C for 18 hours before being washed 5 times with 50 mL deionised water by centrifugation.

2.6.3 Recovery of unreacted N^6-linked-2AE-NAD.
Washings of the reacted particles were reduced to ~2-5ml by rotary evaporation and excess acetone was added, causing the NAD to precipitate which was then collected by centrifugation and re-dissolved in water.

2.6.4 Alkylation of Thiols
Residual thiols of NAD tethered SiNPs were chemically capped by adding iodoacetamide or benzyl bromide (20 mg 0.1 mmol) to 12 mg of thiol SiNPs with tethered nonane-2AE-NAD dispersed in 5 ml 10 mM Na_2HPO_4 buffer pH 8.8. The mixture was stirred at room temperature for 48 hours in a covered flask. After 48 hours, the particles were washed 3 times with 50 ml deionised water by centrifugation.

2.7 EcG3PD Purification

2.7.1 EcG3PD expression and purification
EcG3PD was obtained by cloning, expression and purification from E. coli cells. In summary, the appropriate synthetic genes were transformed into *E. coli* cells and cultured at 37 °C overnight then induced with arabinose. Harvested cells were suspended in 30 mL of resuspension buffer (50 mM Tris buffer, 300 mM NaCl, pH 7.5). The suspension was vortexed before being passed through a microfluidic homogeniser four times at 1600 psi. Cell debris was removed by centrifugation at 20000 rpm for 30 minutes and the supernatant filtered through a 0.45 uM syringe filter. Expression of EcG3PD was checked by SDS-PAGE separation. The protein solutions were purified by HIS-tagged Fast Protein Liquid Chromatography (FPLC) by elution with resuspension buffer (50 mM Tris buffer, 300 mM NaCl, pH 7.5). The desired EcG3PD containing fractions were collected and ran on SDS page gel at 150 V for 1 hour to confirm EcG3PD presence. The fractions were further purified using a Superdex 200 size exclusion column and concentration with a 10 kDA molecular weight cut off (MWCO) centrifugal filter and stored at 4 °C, or -80 °C, as required.

2.8 Enzyme adsorption

2.8.1 Adsorption of EcG3PD to nanoparticles

For EcG3PD adsorption analysis, EcG3PD was mixed with thiol terminated SiNPs with tethered nonene-2AE-NAD between 0.006, and 3 equivalents of EcG3PD/nm^2 at room temperature for 1 hour. This was repeated for vinyl SiNPs with tethered SH-PEG$_4$-2AE-NAD attachments per square nanometer. The particles were separated from free EcG3PD by centrifugation at 10,000 rpm for 5 minutes and washed 3 times in tris buffer by centrifugation. The UV/Vis absorbance of the combined washings was recorded at 280 nm to determine EcG3PD concentration.

2.8.2 ADH adsorption

For ADH adsorption analysis, ADH was mixed with thiol terminated SiNPs with tethered nonene-2AE-NAD between 0.014, and 1.4 equivalents of ADH/nm^2 at room temperature for 1 hour. The particles were separated from free ADH by centrifugation at 10,000 rpm for 5 minutes and washed 3 times in 1 ml Tris buffer by centrifugation. In order to determine the change in aqueous ADH concentration, and thus the quantity adsorbed onto the particles, the enzyme activity of aqueous ADH was measured before and after adsorption using UV/Vis analysis of NADH formation.

2.8.3 GluDH adsorption

For GluDH adsorption analysis, GluDH was mixed with thiol terminated SiNPs with tethered nonene-2AE-NAD between 0.0023, and 0.23 equivalents of GluDH/nm^2 at room temperature for 1 hour. The particles were separated from free GluDH by centrifugation at 10,000 rpm for 5 minutes and washed 3 times in 1 ml Tris buffer by centrifugation. In order to determine the change in aqueous GluDH concentration, and thus the quantity adsorbed onto the particles, the enzyme activity of aqueous GluDH was measured before and after adsorption using UV/Vis analysis of NADH formation.

2.9 Enzyme reaction assays

2.9.1 Resazurin/PMS+ coupled EcG3PD activity assay

EcG3PD activity assays were performed within 200 µL wells of 96 well plates containing 150 µM PMS$^+$, 100 µM resazurin, 20 mM G3P, and varying amounts of EcG3PD, free NAD and SiNP tethered NAD in 0.01 M Tris buffer pH 7.5. Assays were performed using a CLARIOstar multi-mode microplate reader at 37°C with an excitation wavelength 545nm and emission 585nm with shaking.

2.9.2 Resazurin/PMS+ coupled ADH activity assay

ADH activity assays were performed within 200 µL wells of 96 well plates containing 150 µM PMS^+, 100 µM resazurin, 3.5 M ethanol, and varying amounts of ADH, free NAD and SiNP tethered NAD in 0.01 M Tris buffer pH 7.5. Assays were performed using a CLARIOstar multi-mode microplate reader at 37°C with an excitation wavelength 545nm and emission 585nm with shaking.

2.9.3 SiNP Inhibition of EcG3PD activity

For *in situ* activity measurements of EcG3PD with thiol terminated SiNPs, assay solutions containing 0.83 µM EcG3PD, 0, 0.05, 0.1, 0.5, 1 and 5 % (w/w) thiol terminated SiNPs with an average diameter of 204 nm, 10mM G3P, 0.005, 0.01, 0.05, 0.1 and 1mM NAD, 100 µM resazurin and 150 µM PMS in 0.01 M Tris buffer pH 7.5 were heated at at 37°C. The formation of highly fluorescent resorufin was tracked with an excitation wavelength 545nm and emission 585nm with shaking. Inhibition of EcG3PD was also performed with 0.5 % (w/w) viny SiNPs with an average diameter of 204 nm.

2.9.4 Resazurin/Resorufin NADH fluorescence calibration curve

For creation of a calibration curve relating the fluorescence intensity of resorufin to concentration of NADH formed in the resazurin/PMS^+ coupled assay, NADH concentration was varied between 0 to 100 µM with 150 µM PMS^+ and 100 µM resazurin in 0.01 M Tris buffer pH 7.5. Fluorescence Intensity was measured at 37°C with an excitation wavelength 545nm and emission 585nm.

2.9.5 ADH/GluDH coupled Reaction

ADH/GluDH coupled enzyme reactions were performed with 2 mg/ml ADH and 2 mg/ml GluDH with 3.5 M ethanol, 100 mM NH_4Cl, 10 mM a-ketoglutarate, and 0.5 to 5 µM free or thiol SiNPs with an average diameter of 204 nm with 0.2 nonene-2AE-NAD attachments per square nanometer in 10 mM Tris HCl buffer pH 7.5 in 2 ml volume. Reaction mixtures were mixed with an orbital shaker at 120 rpm at 37 °C and 0.1 mL samples taken at different time intervals up to 24 hours. Reaction was stopped by centrifugation of the samples at 14,500 rpm for 10 minutes to remove the enzyme and SiNP tethered NAD. Acetaldehyde produced was converted to ADNP by addition of the supernatant to a mixture of 0.1 ml 20 mM DNP, 10 µL of 1M phosphoric acid and 190 µL of acetonitrile and allowing to incubate at room temperature for 1 hour. 200 µL was then transferred to HPLC sample vial for HPLC analysis.

2.10 NAD Stability

2.10.1 Heat degradation of NAD

NAD stability was tested by heating samples of free and SiNP tethered NAD at different temperatures (37-100 °C) and taking samples at different time points which were refrigerated at 4 °C to prevent further degradation. Heat treated NAD samples were then assayed using the fluorometric resazurin/PMS^+ detection method or the ADH/GluDH coupled assay as described above.

2.11 General Preparations

2.11.1 Synthesis of Acetaldehyde-2,4-dinitrophenylhydrazine (ADNP)

Acetaldehyde-2,4-dinitrophenylhydrazine (ADNP) was synthesises by the well known reaction between 2,4-dinitrophenylhydrazine with carbonyl compounds [162]. 0.8 g of 2,4-dinitrophenylhydrazine (4.04 mmol) was dissolved in 5 mL concentrated phosphoric acid, to which 2 g of acetaldehyde (44 mmol) dissolved in 15 mL ethanol was added. The reaction mixture was stirred for one hour at room temperature before the yellow/orange solid product was separated by filtration. The product was recrystallised twice from ethanol to yield 0.6 g (2.7 mmol, 66% yield) of bright yellow ADNP flaky crystals.

2.11.2 Preparation of N^6-linked-2AE-NAD

N^6-linked-2AE-NAD was synthesised and supplied by CSIRO Manufacturing Flagship, Clayton, Victoria.

2.12 Analytic Techniques

2.12.1 Dynamic Light Scattering (DLS)

The average size and size distribution of nanoparticle solutions was analysed by Dynamic Light Scattering (DLS) with a Malvern Instruments Zetasizer Nano ZS90. DLS measurements were made at 25 °C, 1cm path length, attenuation index 8, mean position 1.6 mm, 13 scan run duration. All measurements were made in triplicate. Particles were prepared for DLS measurements by dissolving 1-2 drops of unwashed particle solution in 1ml of water in a plastic cuvette.

2.12.2 Sputter Coating

A Quorumtech K757X Sputter coater was used to coat the surface of dried, drop-cast SiNPs on silicon wafer with a 5 nm thick platinum coating.

2.12.3 Scanning Electron Microscopy (SEM)

SiNPs were analysed using a Inspect FEI F50 SEM with a 20 keV electron beam with a spot size of 2 nm. Samples were prepared by drop casting 20 μL of dispersed nanoparticles on silicon wafer and drying at 50 °C overnight. SEM images were analysed using ImageJ to analyse SiNP size and size distribution [163].

2.12.4 Surface Area Analysis

SiNP surface area was determined by Brunauer-Emmet-Teller (BET) isotherm analysis on a micromeritics TriStar II 3030 surface area and porosity analyser. SiNPs were dried at 0.1 mbar and 80 °C overnight prior to isothermal analysis.

2.12.5 Attenuated Total Reflectance Fourier Transform Infrared Spectroscopy (ATR-FTIR)

ATR-FTIR spectra were obtained using a Perkin Elmer Spectrum 400 with 64 scans, 4 cm^{-1} resolution, 1 cm^{-1} data points, 0.5 cm^{-1}/second scan speed. IR Spectra were recorded between 4000-550 cm^{-1}.

2.12.6 Zeta potential

The zeta potential of nanoparticle solutions was analysed by the electrophoretic mobility of the particle solutions, measured by DLS analysis with a Malvern Instruments Zetasizer Nano ZS90. Zeta potential measurements were performed with similar parameters to DLS measurements in Section 2.3.1 with particles dispersed in 0.01 M tris buffer pH 7.5.

2.12.7 UV/Vis Spectrophotometry

UV/Vis absorbance measurements were performed using a CLARIOstar multi-mode microplate reader with 200 μL 96 well clear polycarbonate plates. Kinetic based measurements for enzyme activity were performed at 37 °C at a wavelength of 340 nm with 5 seconds of orbital shaking at 500 rpm between each measurement cycle. Resazurin concentration-based measurements were performed using scanning mode from 450 to 700 nm.

2.12.8 UV/Vis measurement of EcG3PD concentration

UV/Vis measurements of EcG3PD concentration were performed using a Thermo Fisher NanoDrop ND-1000 spectrophotometer from 220 to 350 nm. Measurements were blanked with water and zeroed with 0.1 M tris buffer pH 7.5.

2.12.9 Fluorescence Spectrophotometry

Fluorescence intensity measurements were performed using a CLARIOstar multi-mode microplate reader with 200 μL 96 well white opaque polystyrene plates. Enzyme assays were performed at 37 °C with an excitation wavelength of 545 nm and an emission wavelength of 600 nm with 200 flashes per well, a focal height of 9.2 mm, gain set between 500 and 1000 with 5 seconds of orbital shaking at 500 rpm between each measurement cycle.

2.12.10 High Performance Liquid Chromatography (HPLC)

2.12.10.1 Analysis of NAD attachment reaction washings

HPLC analysis of NAD was performed as described by Yoshino *et*. *al.* Samples were separated using an Agilent 1200 series HPLC system equipped with a 150 mm x 4.6 mm Phenomenex PhenoSphere-Next 5 μM C-18 column and UV/Vis diode array detector. 2.5 μL samples were separated using a 50 mM KH_2PO_4 buffer pH 7.0 mobile phase run at 1 mL/min at 20 °C. NAD was detected by UV/Vis at 260 nm, eluting at 9.75 minutes [164].

2.12.10.2 Analysis of ADNP in GluDH/ADH coupled reaction

HPLC analysis of ADNP was performed described by Saczk *et*. *al.* Samples were separated using an Agilent 1200 series HPLC system equipped with a 150 mm x 4.6 mm Phenomenex PhenoSphere-Next 5 μM C-18 column and UV/Vis diode array detector. 2.5 μL samples were run through with a 50:50 acetonitrile:H_2O mobile phase run at 2 mL/min at 40 °C. ADNP was detected by UV/Vis at 360 nm [162].

2.13 Computation Chemistry

2.13.1 Protein Modelling

The electrostatic potential maps of enzymes were generated using UCFS Chimera version 1.13.1 [144]. Using a similar method to Wu *et al*. [110], protein structures were located and imported from the Protein Data Bank (1N1E for EcG3PD, 5ENV for ADH and 1HWY for GluDH). The PDB2PQR function was used to assign charges and radii using the PARSE force field. Using the PROPKA function, the protonation state of enzyme was determined at pH 7.5 and the surface electrostatic potential mapped by the Adaptive Poisson-Boltzmann Solver (APBS) function.

2.13.2 Solubility Parameter Calculation

In order to calculate the solubility of each alkoxy silane in water, each alkoxy silane was drawn using Materials Studio 2017. The geometry of each was then optimised using Forcite geometry optimisation with 200 iterations. This was repeated with the structure of water. Each alkoxy silane and water was then combined in an amorphous cell at a ratio of 50:1 silane to water and at a density of 1 g/cm^3. The system was then equilibrated using Forcite dynamics with NVT ensemble. The cohesive energy density and solubility parameters were then calculated using the Cohesive Energy Density task of the Forcite Calculation tab.

2.13.3 Construction of amorphous silica surfaces with tethered NAD

Materials Studio 2017 was used to construct amorphous silica surfaces with tethered NAD. This was achieved by first importing the low crystalline quartz structure "SiO2_cristobalite_low". Using the 'Cleave surface dialog', the (0 0 -1) plane was cleaved to a thickness of 12.159 Angstroms to expose a single surface silicon atom. A mercaptopropyl or methyl vinyl was then attached to the surface exposed silicon atom and the geometry optimised using Forcite geometry optimisation. A 3 x 3 supercell was then constructed making a 1.5 x 1.5 nm amorphous silica surface containing 9 mercaptopropyl or vinyl surface groups. Forcite geometry optimised nonene-2AE-NAD or thiol-PEG$_4$-2AE-NAD were then attached to the central mercaptopropyl or vinyl surface groups of the super cell, respectively, and the geometry optimised using Forcite geometry optimisation. The supercell range was further extended by 3 x 3, creating 4.5 x 4.5 nm surfaces containing 81 surface groups (4.1/nm^2) and 9 NAD surface attachments (0.45/nm^2). The system was then equilibrated using Forcite dynamics with NVT ensemble

CHAPTER 3 SYNTHESIS OF SINP PLATFORMS FOR BIOCATALYST IMMOBILISATION: OPTIMISATION AND MECHANISTIC STUDY

3.1 Overview

This chapter describes research to optimise the reaction conditions for the synthesis of thiol functionalised SiNPs as well as a new modified Stöber process method of synthesising vinyl functionalised SiNPs. The method for vinyl SiNP synthesis was also successfully applied to other hydrophobic organosilanes, to prepare SiNPs with phenyl, propyl, chloropropyl and cyanopropyl functionality with controllable size and narrow size dispersity. The growth of SiNPs derived from these hydrophobic silanes was explored in order to gain an understanding of the reaction mechanism and the factors that govern the growth of the particles. This included investigation of the influence of silane concentration, pH, ethanol concentration and reaction scale.

3.2 Introduction

Simple preparation, non-toxicity and a vast range of potential chemical surface functionalities make silica nanoparticles (SiNPs) a highly useful class of nanostructure [80]. The most important factor controlling the functional properties such as dispersion, interactions with surroundings and potential for delivery/carrier systems of SiNPs in these applications is the fine tuning of the external surface chemistry [71, 95]. SiNPs are commonly prepared via the Stöber method, producing size controllable and monodisperse particles with hydroxyl terminal functionality. Strategies to chemically incorporate more useful surface functionalities, such as co-hydrolysis or post-silinization with another organosilane, lead to detrimental changes in particle morphology and low surface coverages. Therefore, a simple synthesis method for the direct preparation of monodisperse and size controllable SiNPs with useful surface functionalities would prove highly useful to the development of nanoparticle technologies.

This chapter outlines the synthesis of thiol terminated SiNPs that serve as a platform for the surface tethering of N^6-linked-2AE-NAD structures. SiNPs produced are analysed by SEM and DLS to determine their size and size dispersity, while nitrogen sorption is used to determine the specific surface area by BET surface area analysis. A new synthetic method is introduced for the size controllable synthesis of monodisperse SiNPs with vinyl functionality directly from vinyl silane. The vinyl terminated SiNPs also serve as a platform for N^6-linked-2AE-NAD tethering. The method for the single silane growth of vinyl terminated SiNPs is also successfully applied to other organosilane precursors with useful hydrophobic R group functionalities. The size of these hydrophobic functional SiNPs can be controlled by changing the organosilane concentration, with narrow size dispersions achieved over a range of sizes for all functionalities. The vinyl terminated SiNP synthesis method is used a model system to investigate the influence of ammonia catalyst concentration, ethanol dispersant concentration and reaction scale on the growth of hydrophobic SiNPs.

3.3 Formation of Thiol SiNPs

As previously reported, monodisperse SiNPs with high density surface coverage of thiol functionality were prepared directly from 3-MPTMS [71, 77, 94-96, 165, 166]. This process is similar to the traditional Stöber method, however, water is used as the main solvent instead of ethanol. Thiol terminated SiNPs were also successfully prepared when the solution contained 10% ethanol. The synthesis parameters and size analysis for the prepared SiNPs are shown below in Table 3.1 and SEM images of SiNPs in Figure 3.1.

Table 3.1: Summary of reaction conditions and size analysis by DLS and SEM of the prepared thiol terminated SiNPs. Average diameter of SiNPs from SEM analysis is obtained from measuring the average diameter of 100 particles using ImageJ. Error is standard deviation.

Average SiNP Diameter (nm)		3-MPTMS		NH_4OH (25%)		EtOH		H_2O	Scale
DLS	SEM	mL	mM	mL	M	mL	M	mL	mL
53 ± 4	50 ± 4	0.4	2.2	216	1.4	0	0	784	1000
101 ± 9	98 ± 8	0.72	7.9	72	0.9	0	0	428	500
155 ± 5	149 ± 12	1.04	11.4	72	0.9	0	0	428	500
170 ± 7	166 ± 10	2	10.9	150	1.0	100	1.7	750	1000
201 ± 15	204 ± 17	1.36	14.9	72	0.9	0	0	428	500
248 ± 1	247 ± 9	2	10.9	100	0.6	100	1.7	800	1000
304 ± 26	296 ± 7	2.5	13.7	100	0.6	100	1.7	800	1000

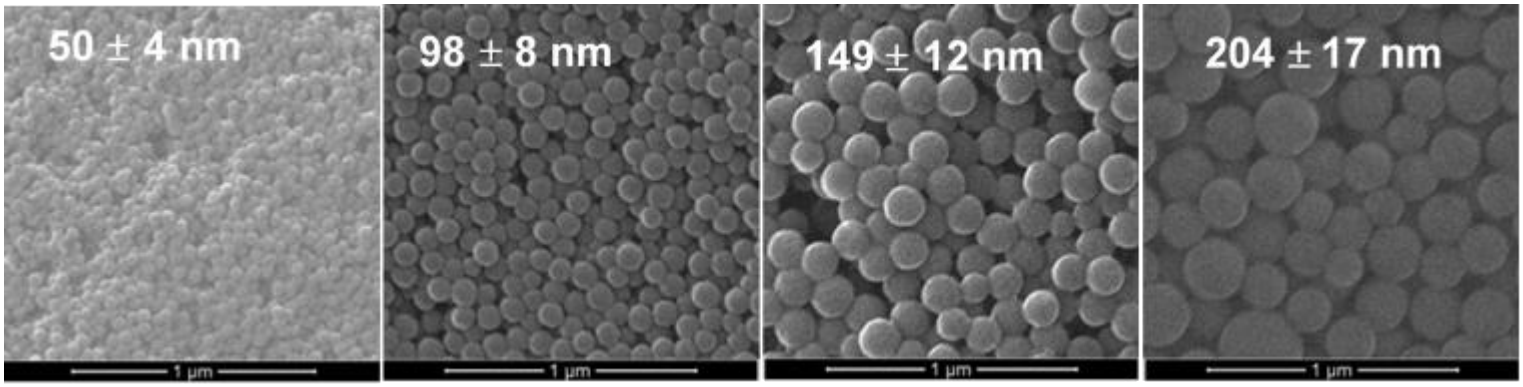

Figure 3.1: SEM images of thiol terminated SiNPs with average diameter of 50 ± 4 nm, 98 ± 8 nm, 149 ± 12 nm, and 204 ± 17 nm.

3.3.1 Comparison of aqueous and ethanolic synthesis of thiol terminated SiNPs

When no ethanol is present in the reaction, 3-MPTMS is added dropwise to a stirred solution of ammonia in water so as to allow each drop to disperse in the solution before the next is added. This results in a clear solution which starts to become cloudy after 24 hours of stirring before appearing milky within 48 hours indicating the formation of solid silica spheres (Figure 3.2(a)).

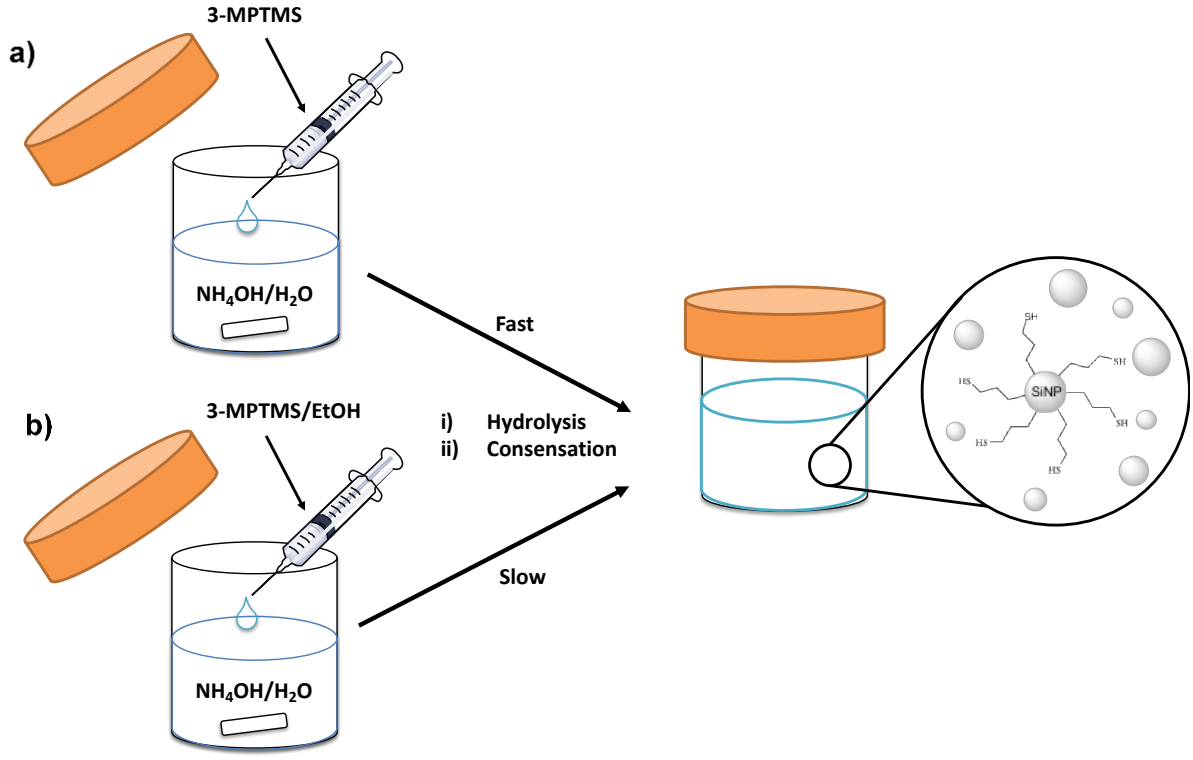

Figure 3.2: Diagram of 3-MPTMS addition method for (a) aqueous and (b) ethanolic synthesis methods

In the ethanolic approach, 3-MPTMS was first dispersed in ethanol which was then slowly poured into the stirred ammonia and water solution. This resulted in a cloudy solution that became clear within minutes and remained clear for at least 48 hours of reaction. The reaction was complete after 72 hours giving a milky solution of solid spheres (Figure 3.2(b)). The ethanolic method also prevented the formation of large visible aggregates of silica that were otherwise observed to form on the walls of the reaction vessel and solution surface. The observed decrease in rate of particle formation and reduced size distribution in the ethanolic reaction conditions is due to the difference in the condensation reactions in the two media. During the formation of the SiNPs, the condensation of two silanol groups results in the irreversible formation of a Si-O-Si bond. However, in ethanolic media, the hydrolysis and condensation rates are reduced by the reverse reaction of the hydrolysis step, driven by the high ethanol concentration, as discussed in Section 1.5.4. This "relaxation" mechanism of reversible exchange allows a slower, more controlled growth mechanism of particle formation, leading more monodisperse SiNPs [73].

3.3.2 BET surface area analysis of Thiol SiNPs

For accurate quantification of attachments on the surface of SiNPs, knowing the specific surface area of a given batch of SiNPs is crucial. If the SiNPs are perfectly uniform in size, simple geometry calculations along with the diameter determined by SEM analysis can be used to obtain the specific surface area. However, Figure 3.1 shows variation in the size, size distribution and morphology of the obtained SiNPs and thus geometrical calculations will only serve as an estimate for the surface area of the particles. Table 3.2 compares the experimentally determined BET surface areas of the thiol terminated SiNPs to the theoretically calculated surface areas, assuming the density of the SiNPs to be 2.0 g/cm^3 [71]. As the average particle diameter decreases, the experimentally determined BET surface area lies further away from the theoretical value as shown in Figure 3.3. This is due to the relationship between surface area to volume ratio and particle radius as shown in the following equations.

$$Surface\ Area = 4\pi r^2 \qquad (3.1)$$

$$Volume = \frac{4}{3}\pi r^3 \tag{3.2}$$

$$Surface\ area{:}Volume = \frac{3}{r} \tag{3.3}$$

Smaller particles within the dispersity index will skew the surface area more than larger ones as they have a higher ratio of surface area to their volume. This is especially apparent SiNPs batches with smaller diameters such as 50 and 98 nm.

Table 3.2: Theoretic Surface area and BET Surface area of different sized Thiol SiNPs. See Appendix for BET isotherms.

Diameter (nm)	Theoretical SA (m^2/g)	BET SA (m^2/g)
50	60.0	92.1 ± 1.7
98	30.6	36.7 ± 4.9
149	20.1	25.3 ± 1.7
166	17.8	22.3 ± 1.5
204	14.7	17.0 ± 0.7
247	12.1	13.5 ± 1.2
296	10.1	11.2 ± 0.5

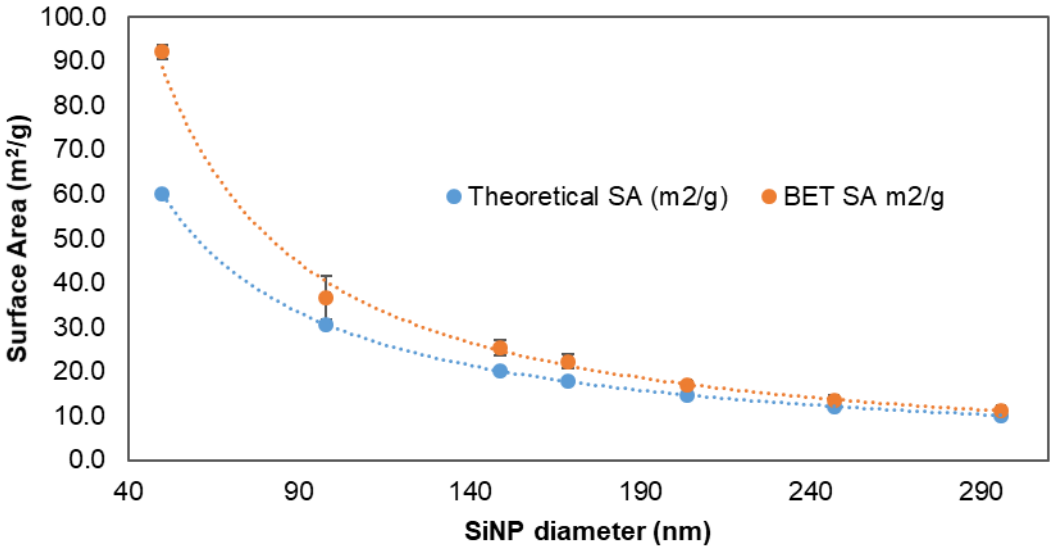

Figure 3.3: Theoretic Surface area and experimentally determined BET Surface area of thiol terminated SiNPs of different sizes.

3.4 Formation of Vinyl SiNPs

Previously, SiNPs with terminal vinyl functionality have been prepared via post functionalisation or co-hydrolysis of TEOS particles with vinyl organosilanes [75, 76, 167]. However, as discussed in Chapter 1, there are several issues associated with post functionalisation methods.

Vinyl terminated SiNPs have been produced directly from the vinyl organosilane, VTES using a similarly approach as for the synthesis of thiol terminated SiNPs. As with the ethanolic synthesis of thiol terminated SiNPs, VTES was first dispersed in ethanol before being slowly added to the stirred aqueous ammonia solution. VTES is significantly more hydrophobic than 3-MPTMS and thus caused the solution to become cloudy (semi-opaque grey) upon addition, indicating the formation of an oil in water emulsion. A milky solution (opaque white) was then observed within minutes to 7 days of mixing, depending on the silane concentration, indicating the formation of solid particles. Figure 3.4 shows a diagram of the addition of VTES, dissolved in ethanol, into the aqueous ammonium hydroxide solution and subsequent synthesis of vinyl terminated SiNPs. The synthesis parameters and size analysis for the prepared SiNPs are shown below in Table 3.3 and SEM images of SiNPs in Figure 3.5.

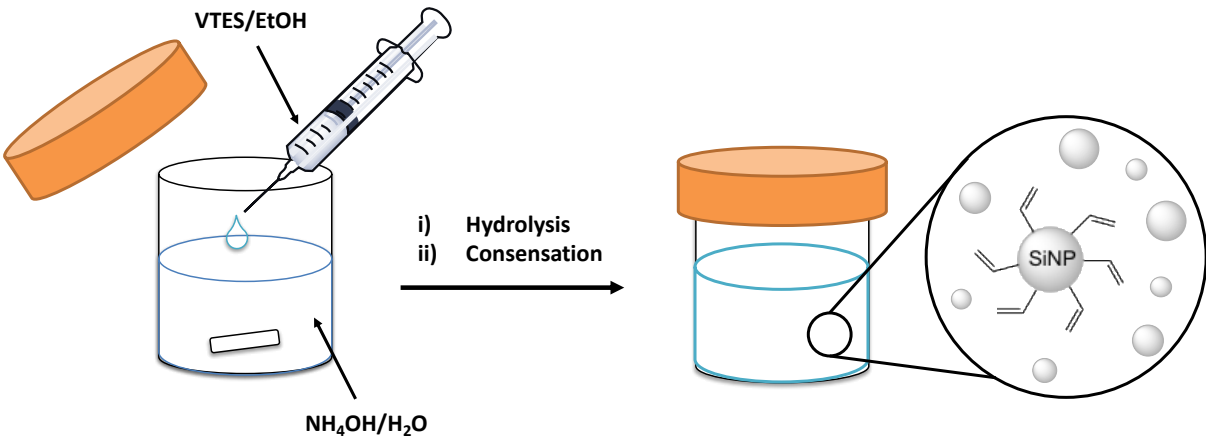

Figure 3.4: Reaction schematic of vinyl terminated SiNPs from VTES (left), illustration of VTES and ethanol mixture to stirred ammonia solution (right).

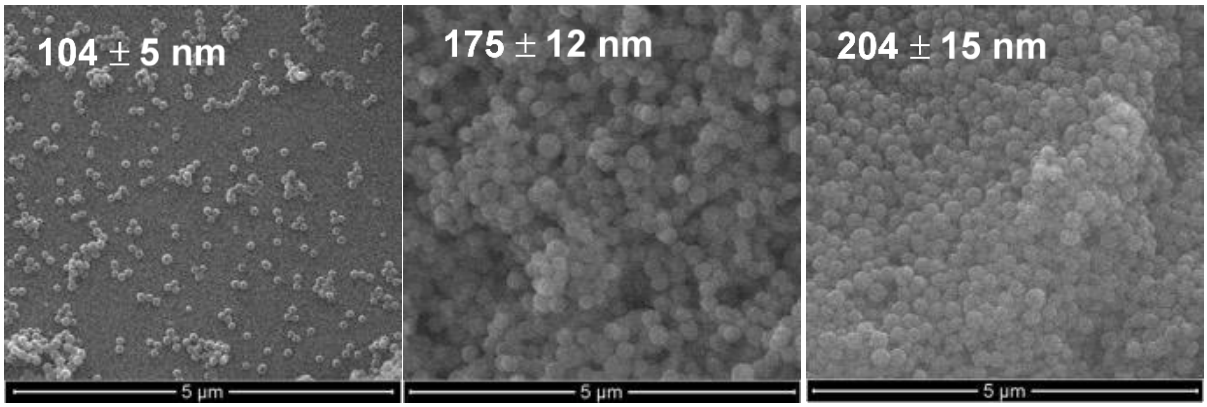

Figure 3.5: SEM images of vinyl terminated SiNPs with an average diameter of 104 nm ± 4 nm, 175 nm ± 12 nm and 204 nm ± 15 nm.

Table 3.3: Summary of reaction conditions and size analysis by DLS and SEM of the prepared vinyl terminated SiNPs.

Average SiNP Diameter (nm)		VTES		NH4OH (25%)		EtOH		H2O	Scale
DLS	SEM	mL	mM	mL	M	mL	M	mL	mL
109 ± 4	104 ± 5	1	24	32	1	39	3.3	128	200
174 ± 12	175 ± 12	5	24	150	1	200	3.4	650	1000
205 ± 22	204 ± 15	1	95	3.6	0.5	4	1.4	41.4	50

3.4.1 BET surface area analysis of vinyl terminated SiNPs

The vinyl terminated SiNPs listed in Table 3.3 will serve as a platform for the surface tethering of N^6-linked-2AE-NAD. Assuming the density of vinyl terminated SiNPs to be the same as that of thiol terminated SiNPs, 2.0 g/cm^3 [71], the specific surface area for vinyl terminated SiNPs shown below in Table 3.4.

Table 3.4: BET Surface area of the vinyl terminated SiNPs.

Diameter (nm)	BET SA (m^2/g)
104	33.3 ± 0.5
175	20.8 ± 3.5
204	15.7 ± 1.7

3.5 Investigation of Hydrophobic SiNP synthesis

The method used to prepare vinyl terminated silica nanoparticles above has also been applied to prepare monodisperse and size controllable SiNPs directly from hydrophobic organosilanes bearing propyl, phenyl, chloropropyl and cyanopropyl functionalities (Figure 3.6). As in the synthesis of vinyl terminated SiNPs, addition of silane dispersed in ethanol caused the formation of a cloudy oil in water emulsion. High silane concentrations resulted in the formation of a milky solution of colloidal particles within minutes while lower concentrations required several days of mixing. To further investigate the growth of these hydrophobic functional SiNPs, the synthesis of vinyl terminated SiNP from VTES is used as a model system.

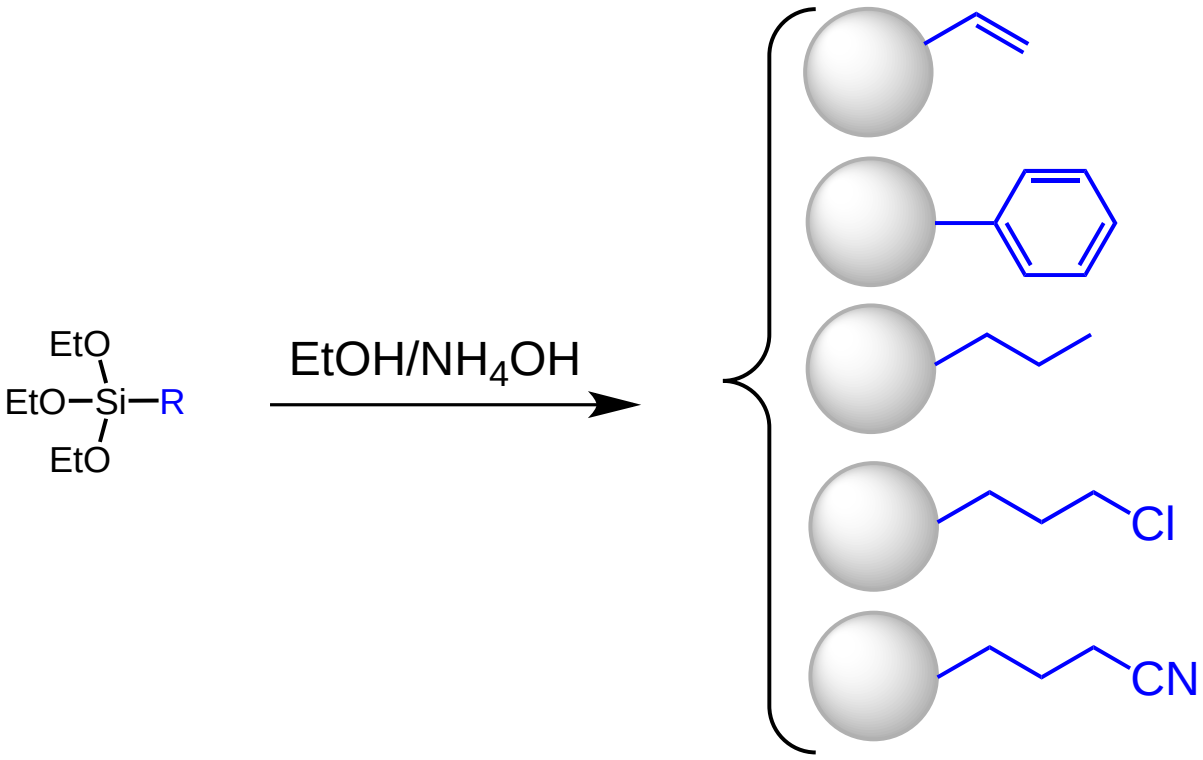

Figure 3.6: Schematic of the universal one-pot method for the synthesis of hydrophobic functional SiNPs directly from a single silane.

3.5.1 Effect of organosilane precursor concentration

Similarly to the synthesis of thiol terminated SiNPs, the size of hydrophobic terminated SiNPs is strongly dependent on the concentration of the corresponding hydrophobic organosilane precursors [71, 77, 95]. In order to demonstrate silane concentration dependent size control, the concentration of each hydrophobic organosilane precursor was varied between 4 mM and 200 mM while the concentration of ammonia catalyst and ethanol were held at 0.64 M and 3.4 M, respectively. The synthesis of vinyl terminated SiNPs was performed at a total volume of 50 mL, while the other silanes were grown in 1 mL volumes due to restricted availability of the silanes. Figure 3.7 shows the increase in the size of the obtained particles with increasing concentration of the different hydrophobic organosilane precursors with example SEM images of SiNPs produced at a silane concentration of 20 mM and 200 mM. Particle size was observed to increase with silane precursor concentration, presumably due to the availability of more precursor allowing more extensive particle growth [95]. A linear increase in particle size was observed at lower silane concentrations (<120 mM) with

a plateau in size observed at 200 mM. A similar plateau in SiNP size at high silane concentrations was observed in the synthesis of thiol terminated SiNPs by Nakamura *et al*. and Lu *et al*. who attributed the plateau to agglomeration of the large, unstable particles during growth [77, 95]. At silane concentrations below 20 mM, no particle formation was detected with VTES and CNpropTES. This suggests that the hydrolysed monomers and oligomers remain soluble in solution without further condensation due to the size of the primary particles in the steady state being too small to act as nucleation sites. Table 3.5 shows the theoretical solubility parameters of each silane precursor, calculated from the cohesive energy density using the Amorphous Cell and Forcite functions of Materials Studio. It can be seen that VTES has the lowest solubility parameter of 16.66 $(J/cm^3)^{0.5}$ indicating that it is the most hydrophobic silane, and least soluble in the reaction solution while. CNpropTES has the highest solubility parameter of 19.05 $(J/cm^3)^{0.5}$ and is thus the most soluble. This indicates that the minimum silane concentration at which particle formation is observed is not related to the solubility of the silane precursor in the reaction solution. Further investigation is required to determine the cause of the observed differences in the dependence of silane concentration on particle formation for the different silanes.

Examination of the plots of particle size as a function of silane concentration in Figure 3.7 show that low silane concentrations produced small, highly monodisperse particles below 100 nm in diameter. As the silane concentration was increased, particle diameters increased up to 1000 nm but became increasingly less uniform. This increase in size dispersity was not observed for the synthesis of vinyl terminated SiNPs which was performed on a 50 ml scale, as compared to 1 mL for the other hydrophobic silanes. This relationship between size and size dispersity and reaction scale explored is explored below in Section 3.5.2. Therefore, for more accurate analysis of the dependence of size and size dispersity on the concentration of the various hydrophobic alkoxysilane monomers, experiments should be repeated at least 10 mL in scale to facilitate more homogeneous mixing, especially at higher concentrations.

Table 3.5: Solubility parameters of the silane precursors generated using Materials Studio modelling software.

Silane	Solubility parameter $(J/cm^3)^{0.5}$
VTES	16.66
PTES	17.93
PropTES	18.75
ClpropTES	17.64
CNpropTES	19.05

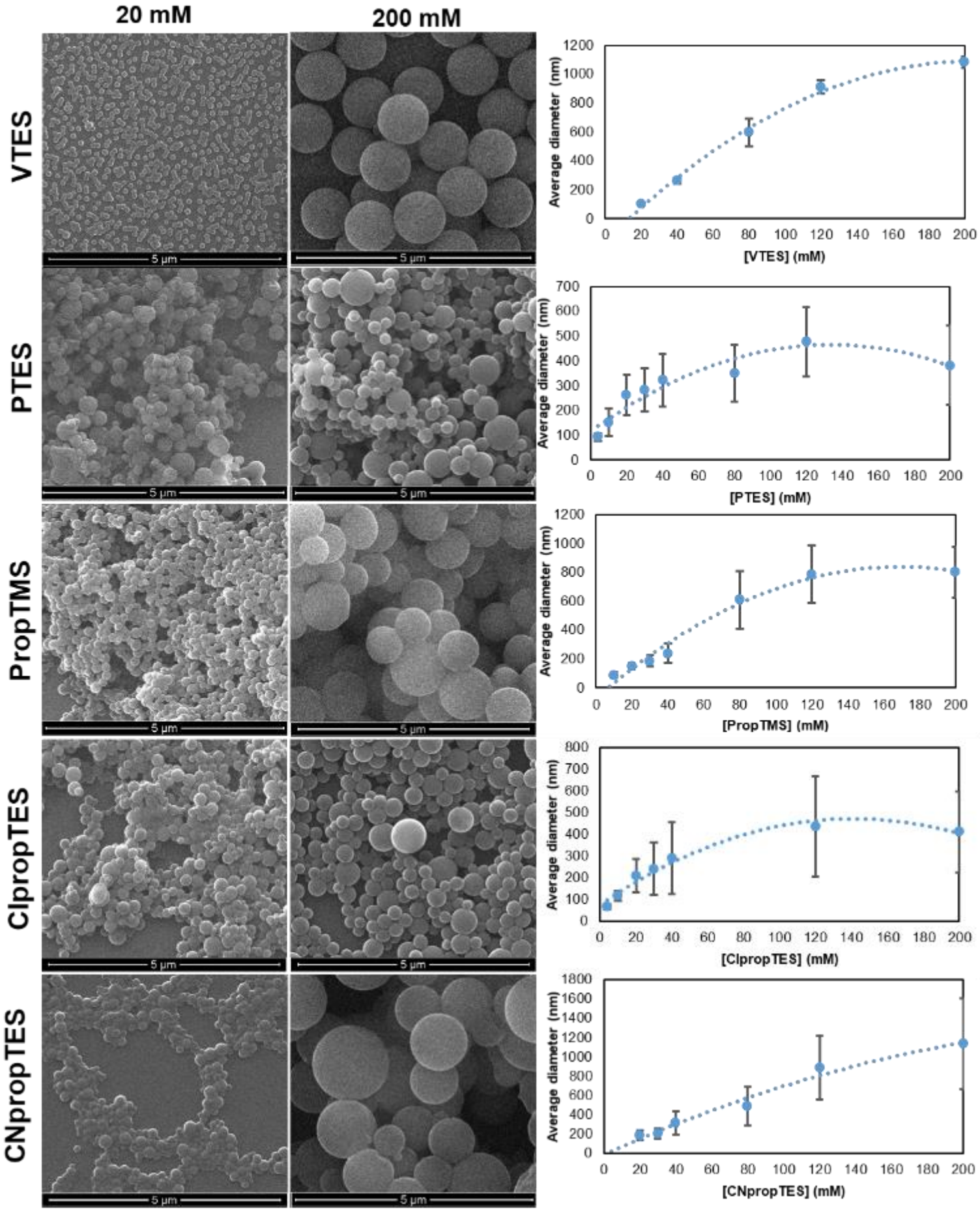
20 mM
200 mM
VTES
PTES
PropTMS
ClpropTES
CNpropTES
5 µm
Average diameter (nm)
[VTES] (mM)
[PTES] (mM)
[PropTMS] (mM)
[ClpropTES] (mM)
[CNpropTES] (mM)

Figure 3.7: : Example SEM images of showing increase in size of SiNPs as silane concentration is increased.

3.5.2 Effect of Reaction Scale

As shown in Section 3.5.1, the scale of a particle synthesis reaction can significantly impact the dispersity and shape of the resultant particles, especially in systems that are heterogeneous as the oil phase can partition at the air surface or the walls of the reaction vessel. We have observed aggregation of particles at both the air interface as well as on the walls, often as a crust. As a result, the particle size achieved is not predictable due to the effective concentrations being different.

Most of the published work in this area produces about 100 mg of particles or less and a significant aspect of this project has been to increase the reaction volume. As a result, highly monodisperse, vinyl terminated SiNPs have been produced at large reaction scales for use as platforms for tethered NAD.

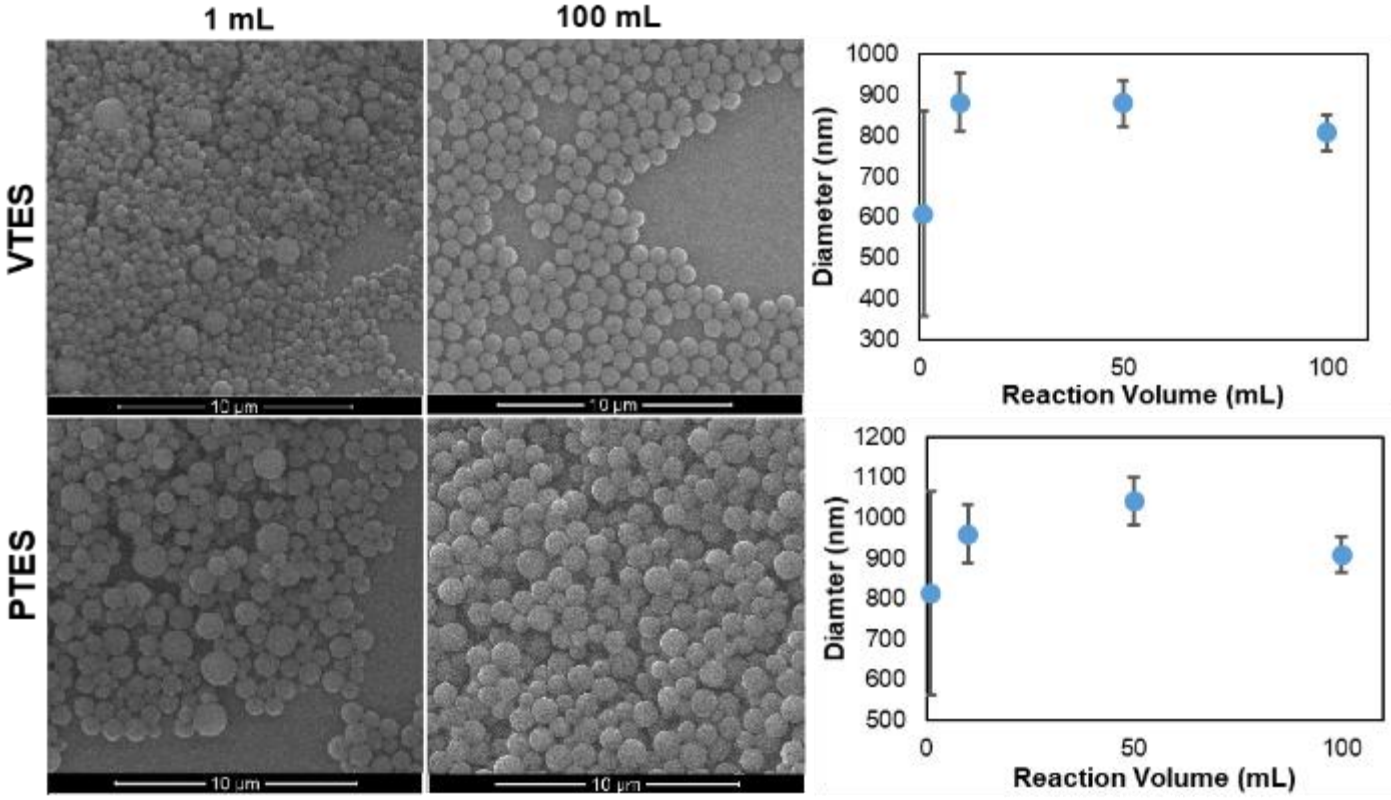

Figure 3.8: Reaction scale effect on size and size distribution of vinyl and phenyl terminated SiNPs.

To test the effect of reaction scale, vinyl and phenyl terminated SiNPs were synthesised at a silane concentration of 200 mM in reaction volumes from 1 mL to 1000 mL. Ammonia and ethanol concentrations were held at 0.64 M and 3.4 M, respectively. Figure 3.8 shows that vinyl and phenyl terminated particles with a very broad size distribution were synthesised on the 1 mL reaction scale. Increasing the reaction volume to 10 mL resulted in a significant reduction in size distribution of both vinyl and phenyl terminated particles and also increased the average size. As the scale was further increased to 100 mL, the particles became increasingly monodisperse. The large size distribution of particles produced on a 1 mL reaction scale is attributed to inhomogeneous mixing of the reaction mixtures as shown schematically in Figure 3.9. 1 mL scale reactions were performed in a 2 mL Eppendorf tube and were stirred by a small 6 mm magnetic stirrer bar, while larger scale reactions were performed in 70 mL or 250 mL specimen vial with a much larger stirrer bar. Due to the small radius of the stirrer bar, turbulence generated by stirring is only able to homogenise the lower section of the solution of in the Eppendorf tube as shown in Figure 3.9. When the silane concentration is low, small particles condense over a period of days and inhomogeneous mixing is less detrimental to the size distribution as the components are mixed by diffusion. However, at high silane concentrations, where are particles form within minutes, homogeneous mixing is critical for the consistent addition and condensation of silane monomers and oligomers to the growing particle. Inhomogeneous mixing results in a concentration gradient of the silane monomers, oligomers and growing particles, leading different growth rates in particles and subsequently, a broad range of particle sizes.

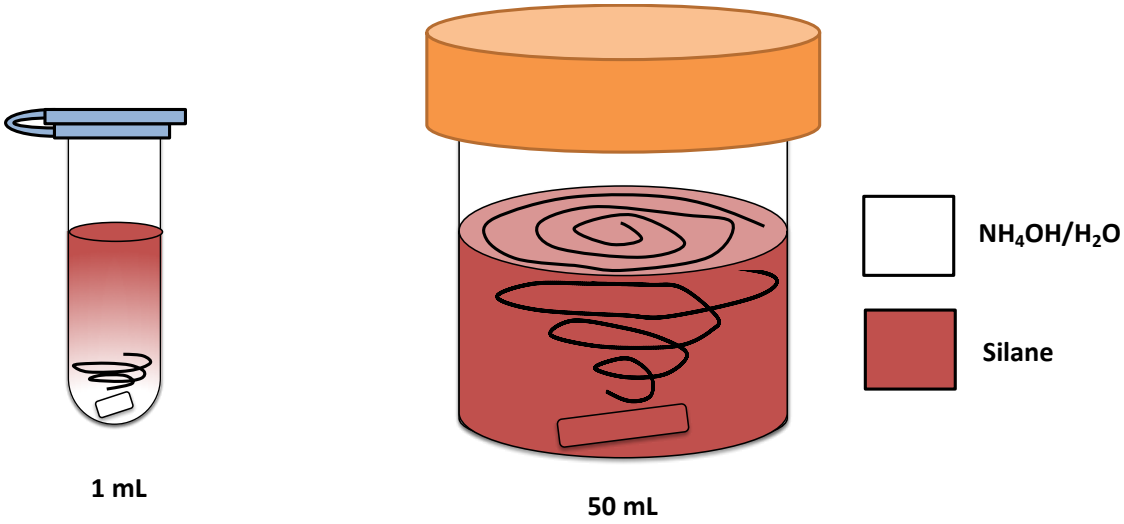

Figure 3.9: Comparison SiNP synthesis reaction performed on a 1 mL scale in a 2 ml Eppendorf tube with a small stirrer bar leading to inhomogeneous mixing of the red silane and homogeneous mixing of reaction performed on a 50 mL scale.

3.5.3 Effect of NH_4OH concentration (pH)

Similarly to the synthesis thiol terminated SiNPs, the size distribution of vinyl terminated SiNPs is dependent on the concentration of the ammonia catalyst [95]. The concentration of ammonia was varied between 0 M and 2.6 M while the concentration of VTES and ethanol were held at 40 mM at 3.4 M, respectively. SEM images of the particle produced after 4 days of reaction are shown in Figure 3.10 and the average particle diameters plotted as a function of pH in Figure 3.11. When no ammonia catalyst was present (pH 5.5), no particle formation was observed. This is due to the low rate of hydrolysis and condensation, as shown in the plot of the proposed relative hydrolysis and condensation rates as a function of pH for VTES in Figure 3.12. At low ammonia catalyst concentration (0.16 M, pH 11), particle formation was observed within an hour of reaction, whereas at high concentrations (2.6 M, pH 13.5) particle formation was not observed until 1-2 days of mixing. This can be explained by the competing hydrolysis and condensation reaction rates as illustrated in Figure 3.12. At pH 11, the rate of condensation dominates the rate of hydrolysis, resulting in the rapid condensation of any partially hydrolysed VTES monomers and oligomers forming large particles with a wide size distribution. Conversely at pH 13.5, the rate of hydrolysis dominates the rate of condensation, resulting in very slow condensation, and thus slow particle formation, of fully hydrolysed VTES monomers. Similarly to Lu *et al.*, a wide size distribution was also observed at high pH [95]. Although the average

size of the particles grown (within error) did not change, the particle size distribution was significantly influenced by the reaction pH. An optimal pH for narrow particle distribution was identified to occur at 1.3 M NH_4OH (pH 13). This is likely to be close to the pH where the rate of hydrolysis and condensation are equal and there is balance between the two as shown in Figure 3.12.

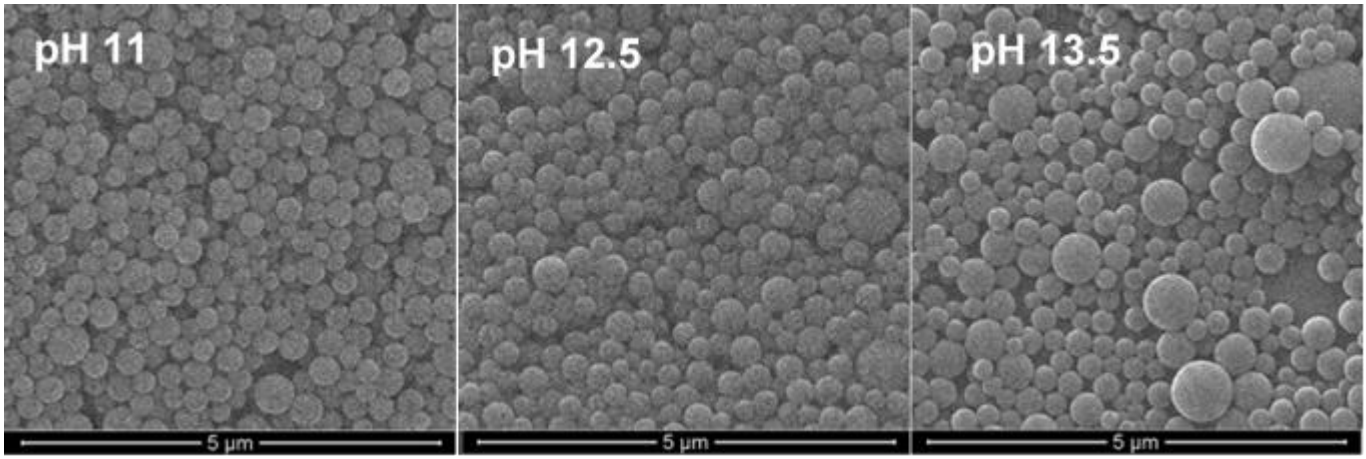

Figure 3.10: SEM images of vinyl terminated SiNPs synthesised at different pH.

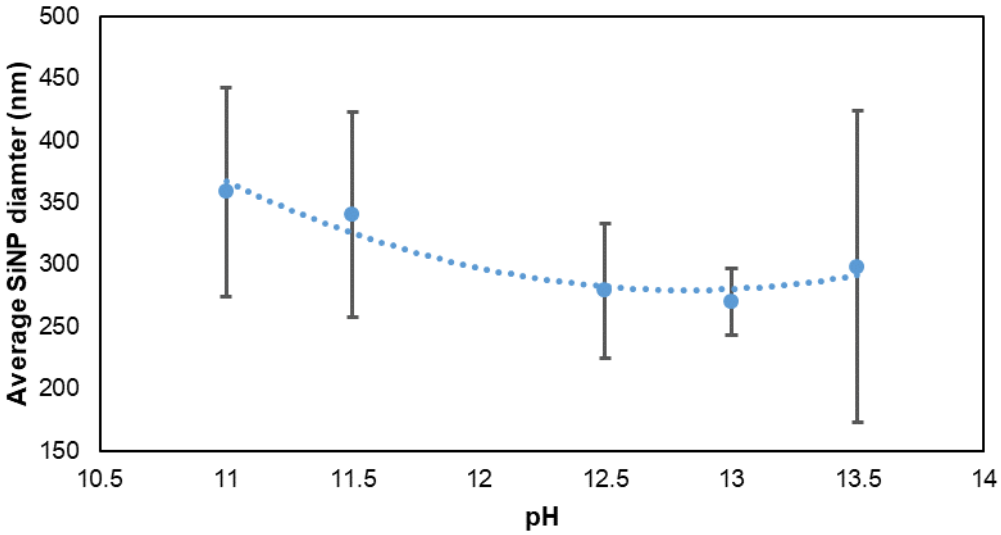

Figure 3.11: Average diameter of SiNPs with different concentrations of NH_4OH with 40 mM VTES and 3.4 M EtOH. Error bars represent standard deviation.

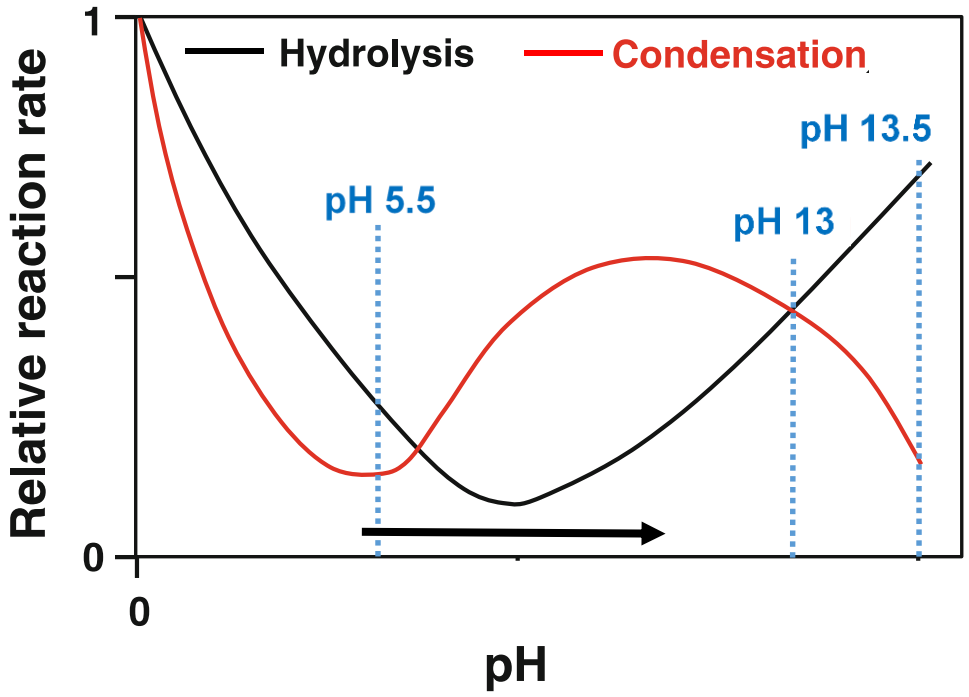

Figure 3.12: Proposed hypothetical relative hydrolysis and condensation rates at different pH for VTES based on results, showing pH values at 5.5 (no ammonia), 13 and 13.5, the pH range examined [97].

3.5.4 Effect of ethanol concentration

The size and size distribution of vinyl terminated SiNPs was also found to be dependent on the concentration of ethanol. Figure 3.13 shows the particles formed when VTES (40 mM) was dispersed in different concentrations of ethanol from 0 to 8.6 M before addition to 0.64 M ammonia hydroxide solution. The particle size is plotted as a function of ethanol concentration in Figure 3.14. Ethanol acts as a mutual solvent to homogenise the hydrophobic VTES in the aqueous ammonia solution and also contributes to the reverse hydrolysis and condensation reactions. When no ethanol was present or at very low concentration (0.43 M), VTES was not soluble in the reaction mixture, resulting in large agglomerates of solid silica, revealed to be composed of highly non-uniform particles by SEM analysis (Figure 3.13). Ethanol concentration was also found to affect the rate of particle formation with particle formation observed within hours at 0.86 M and after 7 days at 8.6 M. This is due to the

increased contribution to the reverse hydrolysis and condensation step with increasing ethanol concentration, resulting a reduced rate of particle formation and smaller particle diameter. It was also found that narrow size distributions were obtained at higher ethanol concentrations, likely due to reversible exchange relaxation mechanism between silanol and alcoholate groups within the silica matrix.

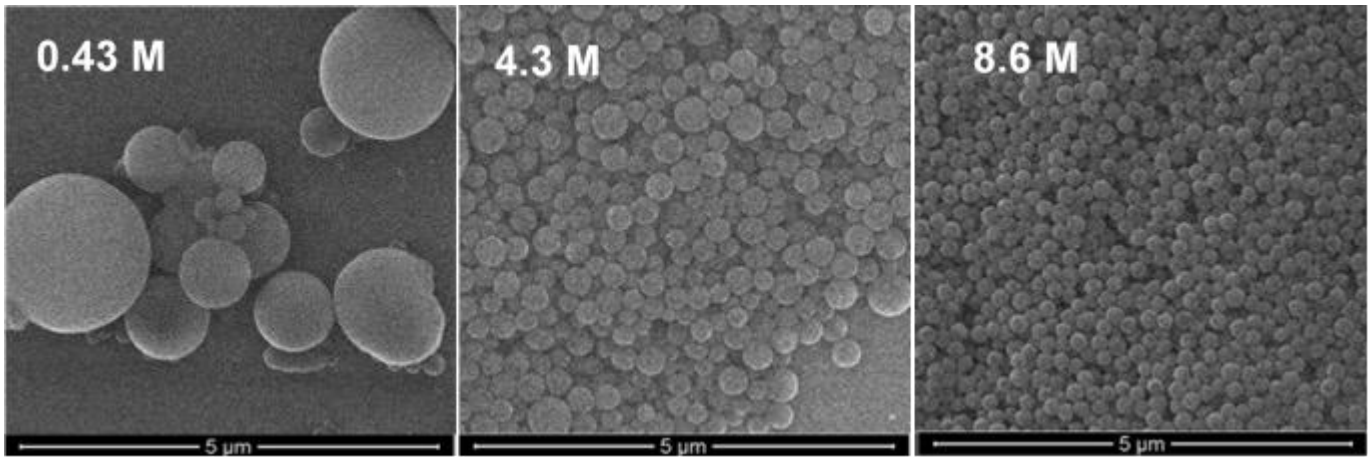

Figure 3.13: SEM images of vinyl terminated SiNPs synthesised at different ethanol concentrations.

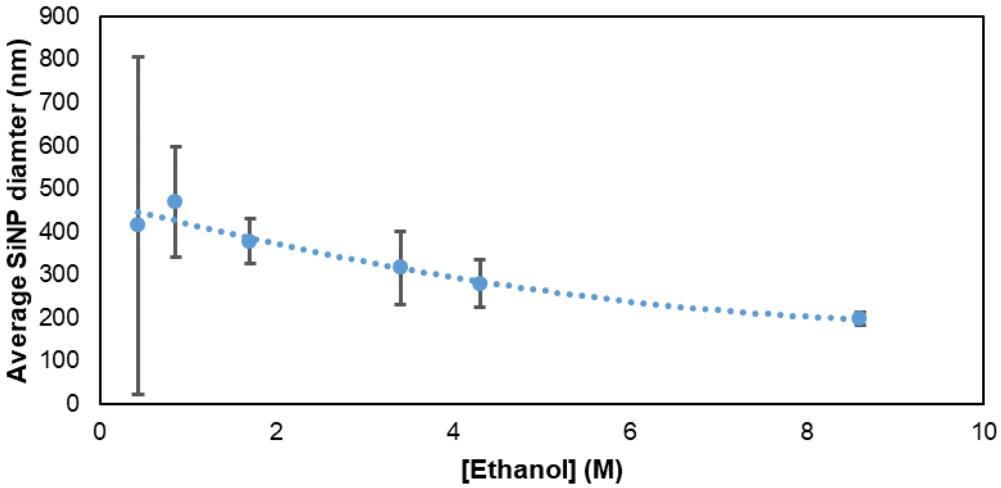

Figure 3.14: Average diameter of SiNPs with different concentrations of ethanol with 40 mM VTES and 0.64 M NH_4OH. Error bars represent standard deviation.

3.5.5 Growth kinetics

The growth kinetics of vinyl terminated SiNPs were measured at three different VTES precursor concentrations and the growth kinetics can be explained by application of the LaMer model discussed in Chapter 1. The increase in particle diameter with time was measured via SEM analysis, as shown in Figure 3.15. At high VTES concentration (200 mM), the critical supersaturation point (S_c) of VTES is reached within minutes, resulting in the hydrolysis and condensation of large nuclei which rapidly grow by addition of further VTES monomers and oligomers to form solid spheres with a diameter of 725 nm within 15 minutes of reaction. These spheres continue to rapidly grow, depleting VTES concentration, resulting in a monodisperse colloid of 1080 nm particles after just 4 hours of reaction, as shown in Figure 3.16. No change in particle size or size dispersion was observed with extended reaction time, suggesting that all VTES has been consumed. At moderate VTES concentration (80 mM), S_c is reached after a longer time period, resulting in slower particle growth, with 512 nm solid spheres observed after 30 minutes of reaction. These particles continue to slowly grow by the addition of hydrolysed VTES monomers and oligomers, reaching a maximum size of 600 nm after 18 hours. At low VTES concentration (40 mM), S_c is reached after an even longer time period with solid particle formation (186 nm) not observed until 18 hours of reaction. Particles continued to grow slowly due to the low concentration of available VTES precursor, with fully formed particles with a diameter of 280 nm produced after 7 days of reaction. The growth kinetics are consistent with the conventional mechanism of growth of SiNPs described in Chapter 1, where particle growth follows a monomer addition or aggregation growth model resulting in the uniform growth of nuclei until all monomer in solution is depleted.

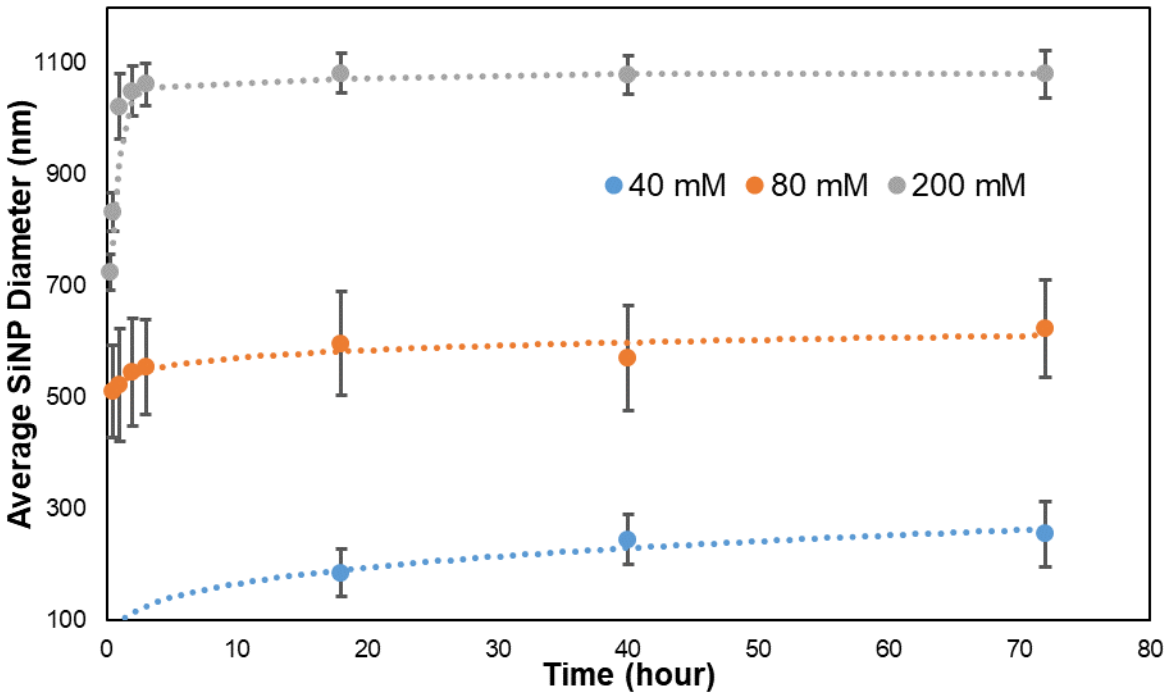

Figure 3.15: SEM analysis of the growth of vinyl SiNPs synthesised at different VTES concentrations over time.

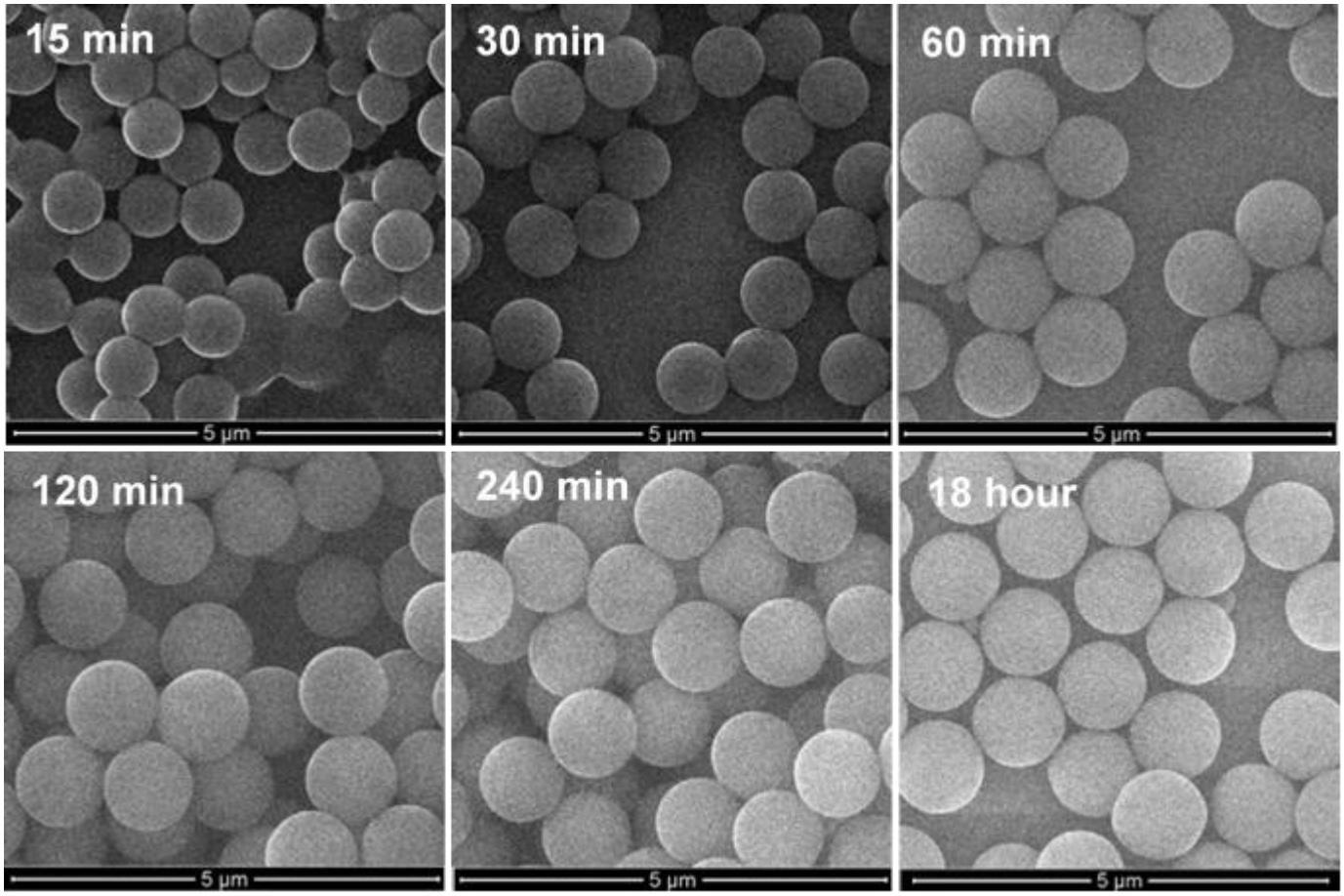

Figure 3.16: SEM images of the growth of vinyl terminated SiNPs over time prepared with 200 mM VTES.

3.6 Conclusion

Thiol terminated SiNPs were synthesised by a modified one-pot Stöber synthetic method in both aqueous and ethanolic media. Growth of thiol terminated SiNPs in ethanolic media was found to proceed at a slower, more controlled rate of hydrolysis and condensation leading to more monodisperse SiNPs compared to the aqueous route. The ethanolic media synthetic method was applied to the vinyl terminal organosilane VTES, resulting in the growth of uniform vinyl terminated SiNPs. The ethanolic method was further explored by applying a range of other hydrophobic organosilane precursors bearing propyl, phenyl, chloropropyl and cyanopropyl R groups. It was demonstrated that the homogenous mixing of the reaction solution was a critical factor in obtaining monodisperse particles, especially at high silane

concentrations. The size of the hydrophobic SiNPs was demonstrated to be controllable by altering the concentration of the organosilane precursors, with a linear increase in SiNP size with silane concentration up to 120 mM before destabilisation of large particles resulted in a plateau in size. Using VTES as a model hydrophobic silane, the role of pH (ammonia catalyst concentration), ethanol concentration and growth kinetics were explored. Varying the pH of the reaction mixture was found to influence the competing rates of hydrolysis and condensation, and thus the rate of particle growth and their size uniformity. At pH 13, highly monodisperse vinyl terminated SiNPs were produced, indicating a balance between the competing hydrolysis and condensation rates of the vinyl silane. Ethanol concentration was found to influence the size, uniformity and growth rate of the SiNPs with rapid growth of disperse particles at low ethanol concentrations and very slow growth of highly uniform particles at high ethanol concentration. Lastly, the growth kinetics were analysed by measuring the increase in size of vinyl terminated SiNPs over time by SEM at different VTES concentration. The LaMer model was then applied in to explain the difference in particle growth rates at different VTES concentrations. Kinetic analysis revealed that the growth of the hydrophobic functional SiNPs follow the conventional mechanism of growth where nuclei grow at a uniform rate by the addition of silane monomers to the growing particle surface until all silane is depleted.

CHAPTER 4 : TETHERING AND QUANTIFICATION OF SURFACE ATTACHMENT DENSITY OF N^6-LINKED-2AE-NAD

4.1: Overview

This chapter discusses the tethering and attachment quantification of N^6-linked-2AE-NAD to the surface of SiNPs. N^6-linked-2AE-NAD is covalently tethered via a thiol-ene 'click' reaction, coupling the terminal thiol or vinyl groups on the N^6-linked spacer arm of NAD to the vinyl or thiol functional groups on the SiNP surface. The surface attachment density of NAD resulting from the tethering reaction is determined using a quantitative ATR-FTIR method. The attachment densities of N^6-linked-2AE-NAD on the surface of thiol and vinyl terminated SiNPs are then compared to other values for NAD surface attachment density found in literature. The change in zeta potential, measured by the electrophoretic mobility of the functionalised nanoparticles, is then determined in order to confirm NAD attachment and the configuration of the surface tethered NAD investigated using Molecular Dynamics (MD) simulations. Residual thiol groups on the particle surface are covalently 'capped' with small alkylating agents and their attachment confirmed by ATR-FTIR analysis.

4.2 Introduction

Mangos *et al*. developed a thiol-ene 'click' reaction system used to attach 11-bromoundecene to the surface of thiol terminated SiNPs **[71]**. Using photoinduced benzophenone initiation, a maximum of 4.9 11-bromoundecene attachments per square nanometer were achieved on the thiol terminated SiNP surface. Attachment density of 11-bromoundecene on the thiol SiNP particle surface was determined via a quantitative ATR-FTIR technique, which was supported by thermogravimetric analysis (TGA) **[71, 93]**. The experimental attachment density of 4.9 attachments/nm^2 was found agree well with 4.7 thiols per nm^2 calculated computationally, suggesting reaction of all surface thiols. Such high attachment density was only achieved after 2 hours when 4500 equivalents of 11-bromoundecene molecules were applied per square meter of nanoparticle surface. However, due to the limited quantity of N^6-linked-2AE-NAD available, the excess of N^6-linked-2AE-NAD molecules that could be applied to the SiNPs is severely limited. Therefore, an appropriate procedure for the thiol-ene 'click' attachment of N^6-linked-2AE-NAD to the surface of thiol and vinyl terminated SiNPs must be developed.

4.3 Tethering of N^6-linked-2AE-NAD to the SiNP surface

A facile thiol-ene 'click' reaction was selected to covalently tether N^6-linked-2AE-NAD to the surface of thiol and vinyl terminated SiNPs, through the terminal vinyl and thiol groups of the N^6 spacer arm, respectively. The photo-initiator, benzophenone, has shown to effectively initiate the successful attachment of a hydrophobic long chain alkene molecule to the surface of thiol terminated SiNPs by thiol-ene 'click' chemistry [71, 93]. However, the sensitivity of N^6-linked-2AE-NAD requires the careful selection of an appropriate initiator for the thiol-ene 'click' reaction.

4.3.1 Initiator Choice

Due to the thermal and photosensitivity of NAD, as well as its insolubility in organic solvents, a suitable free radical initiator for the thiol-ene 'click' reaction had to be chosen [168]. Although photo-initiators such as benzophenone and thioxanthone have been shown to induce thiol-ene 'click' reactions with high efficiencies, they are unsuitable due to their UV light requirement and their hydrophobic nature [98]. Thermal initiators such as AIBN have also shown provide high reaction efficiencies but require

high temperatures (>80°C) and are also insoluble in water. The most effective approach to generating radicals under mild, aqueous conditions is via the one-electron transfer reaction by redox initiators such as persulfates [169].

4.3.2 Tethering of N6-linked-2AE-NAD to thiol and vinyl terminated SiNPs

N^6-linked-2AE-NAD was tethered to the surface of thiol and vinyl terminated SiNPs via a thiol-ene 'click' reaction initiated by potassium persulfate. Thiol terminated SiNPs were first dispersed in water by extensive sonication to assure particles were un-agglomerated and all particle surface was exposed to the solution. Nonene-2AE-NAD and potassium persulfate were added, and the mixture stirred vigorously at room temperature for 48 hours. Thiol-PEG_4-2AE-NAD was tethered in the same manner, except the vinyl terminated SiNPs were dispersed in a 75:25 solution of deionized water and acetonitrile due to the hydrophobic nature of the vinyl terminated SiNPs.

In general, 5 equivalents of N^6-linked-2AE-NAD molecules were applied per square nanometer of SiNP surface, allowing a large enough excess to obtain a quantifiable attachment density while maintaining a large enough quantity of particles for analysis and use in enzyme reactions. An extended reaction time of 48 hours accounted for the limited excess of N^6-linked-2AE-NAD and low reaction temperature. Figure 4.1 shows a schematic for the surface tethering of nonene-2AE-NAD to thiol terminated SiNPs via a potassium persulfate-initiated thiol-ene 'click' reaction.

Particles were thoroughly washed by centrifugation after the attachment reaction in order to remove all un-attached NAD. HPLC analysis of the washings in the Appendix show that all un-attached NAD is removed from the SiNPs after three wash cycles.

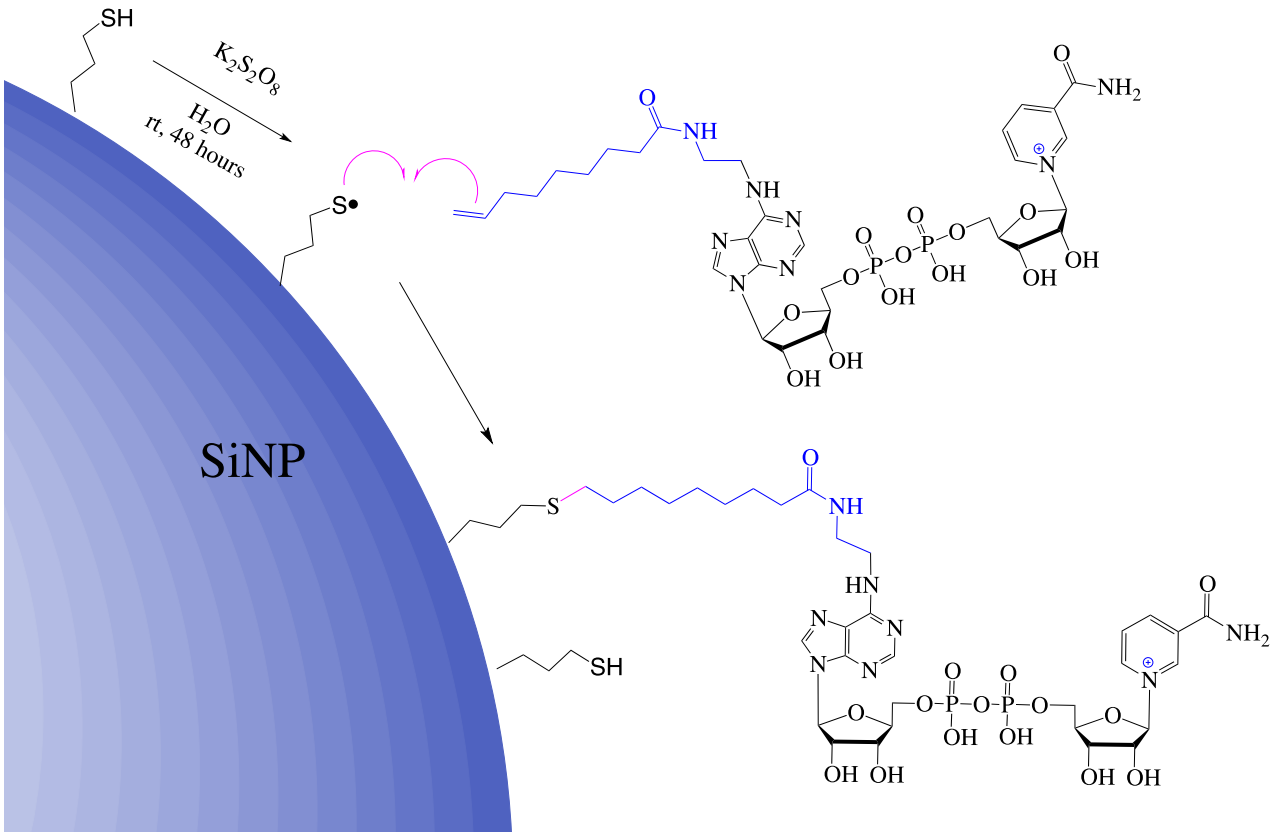

Figure 4.1: Schematic of the thiol-ene 'click' tethering reaction of nonene-2AE-NAD to the surface of thiol terminated SiNPs.

4.4 Quantification of N^6-linked-2AE-NAD attachment to the SiNP surface

4.4.1 Construction of calibration curves for quantification of attachment of N^6-linked-2AE-NAD to thiol and vinyl terminated SiNPs.

In Chapter 3, SEM and DLS analysis revealed the average diameter of each particle batch and the specific surface area determined by BET surface area analysis. Therefore, for a given mass of particles with a given molecular surface coverage, a molar quantity of the attaching molecule can be calculated. This is achieved by conversion of an attachment density to the total number of molecules per mass of SiNPs to a molar quantity using Avogadro's number. This molar quantity can easily be prepared through dilution of a starting stock solution and be applied to a controlled mass of SiNPs of known specific surface area in order to simulate a desired average attachment density. This can then be sampled over a range of appropriate attachment

density simulations in order to construct a calibration curve relating the increase of an FTIR active mode of the sampled molecules against a reference band of the SiNPs. Using this logic, calibration curves for the attachment of NAD to thiol and vinyl terminated SiNPs were prepared by the addition of appropriate amounts of NAD solution to dried thiol and vinyl particles [71]. NAD is a far bulkier molecule than the alkyl chains previously attached to thiol terminated SiNPs [71]. Therefore, a far lower attachment density of NAD is expected to be obtained than the upper limit of ~5 attachments/nm^2. Consequently, the NAD attachment calibration range was set between 0-0.8 attachments/nm^2 for thiol SiNPs and 0-1 attachment/nm^2 for vinyl SiNPs. A higher NAD attachment density was expected on the surface of vinyl terminated SiNPs due to the nature of thiol-ene reaction mechanism. This is because the nucleophilic attack of small free thiol radicals on surface vinyl groups is expected to be more efficient than the nucleophilic attack of a surface thiol radical on freely diffusing vinyl groups. The carbonyl (C=O) stretch of the amide of the nicotinamide nucleotide of NAD at ~1700 cm^{-1} was chosen as the IR reference band for quantitative ATR-FTIR analysis of surface attachment as shown in the Appendix.

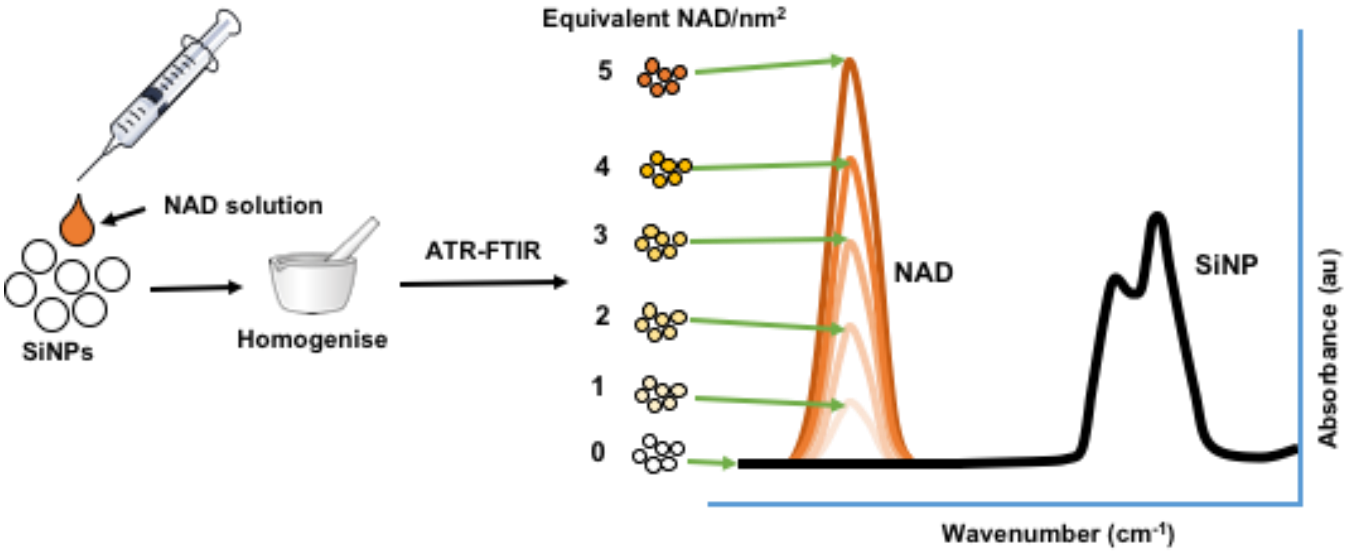

Figure 4.2: Diagram of method used to construct ATR-FTIR calibration curves

4.4.2 Standard curve construction

For the construction of the NAD attachment calibration curves, the NAD overlap region between 600 and 1200 cm^{-1} of the Si-O-Si peak was first corrected as described in the Appendix. The resulting NAD calibration curves are shown in Figure 4.2(b) and Figure 4.2(d) where the addition of NAD to the dried SiNP powders resulted in a linear increase in the C=O stretch at 1700 cm^{-1} with respect to the normalized Si-O-Si reference band of both thiol and vinyl terminated SiNPs, respectively. A non-zero y-intercept was observed in the calibration curve for the attachment of nonene-2AE-NAD to thiol SiNPs (Figure 4.2(b)). This is due to the slight overlap between the C=O band of the NAD amide with small thiol SiNP band at 1650 cm^{-1} due to surface adsorbed water within the condensed SiNP matrix as shown in the Appendix. Assuming the ratio of this band to be constant to the Si-O-Si band in thiol SiNPs, this intercept will be constant and independent of particle size and amount of SiNPs on the ATR crystal.

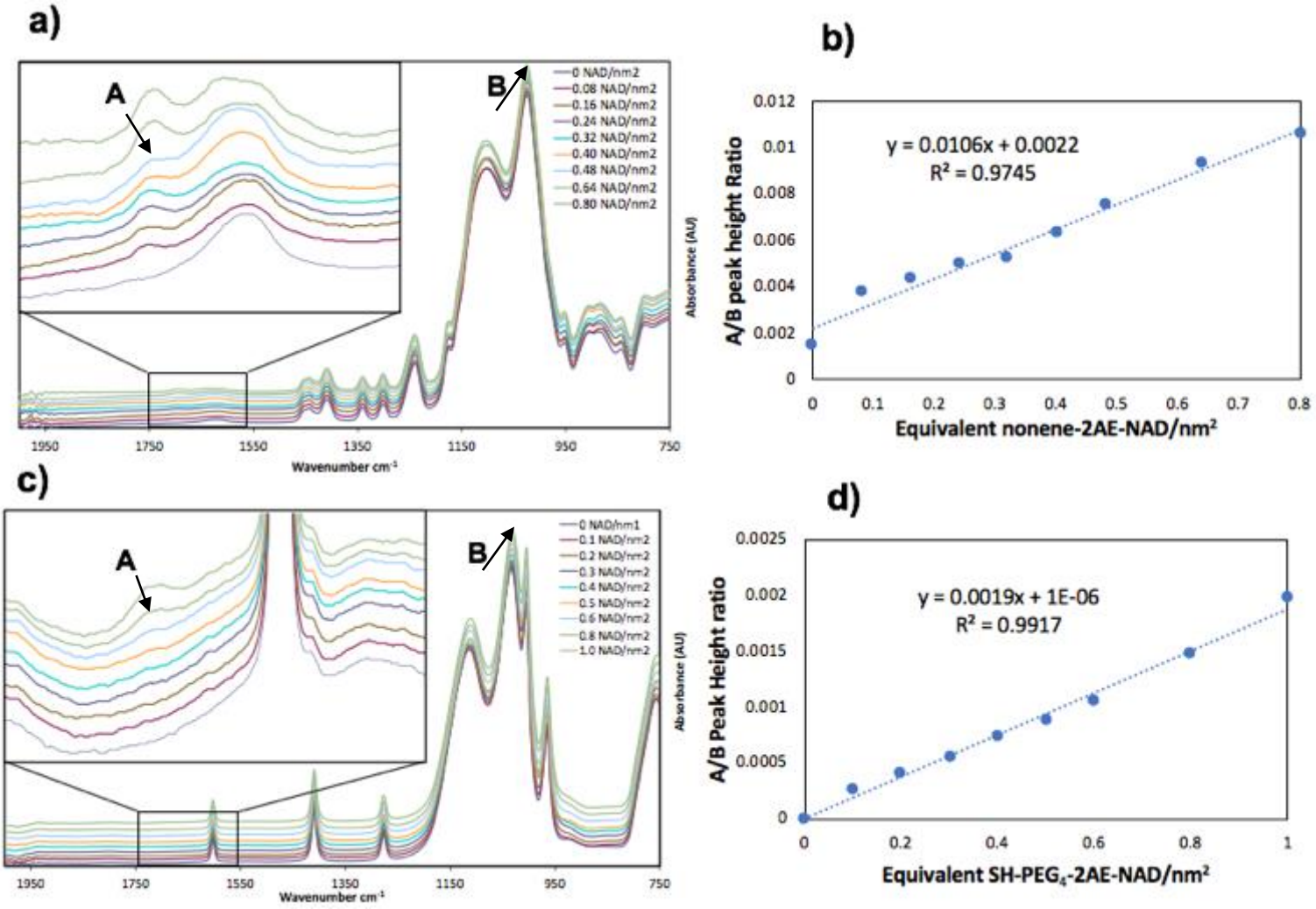

Figure 4.3: Overlayed ATR-FTIR spectra of thiol terminated SiNP/NAD standard mixtures with inset region from 1550 to 1750 cm^{-1} showing the C=O peak of NAD at 1700 cm^{-1} (a) used to construct used calibration curve of nonene-2AE-NAD attachment to thiol terminated SiNPs (b). Similarly, the inset region from 1500 to 1800 cm^{-1} shows the C=O peak of NAD at 1700 cm^{-1} in ATR-FTIR spectra of the vinyl terminated SiNP/standard mixtures (c) used to construct the calibration curve for thiol-PEG4-2AE-NAD attachment to vinyl terminated SiNPs (d). Note that spacing between absorbance spectra in inset plot do not match the spacing of the spectra in the outset plot in (a) and (c).

4.4.3 ATR-FTIR analysis of tethered N^6-linked-2AE-NAD SiNPs

Reaction mixtures were washed thoroughly with water to remove unreacted N^6-linked-2AE-NAD and potassium persulfate initiator. A small sample of particles were dried for ATR-FTIR analysis. Figure 4.4 and Figure 4.5 show the ATR-FTIR spectra of

nonene-2AE-NAD tethered to the surface of thiol terminated SiNPs and thiol-PEG$_4$-2AE-NAD tethered to the surface of vinyl terminated SiNPs, respectively.

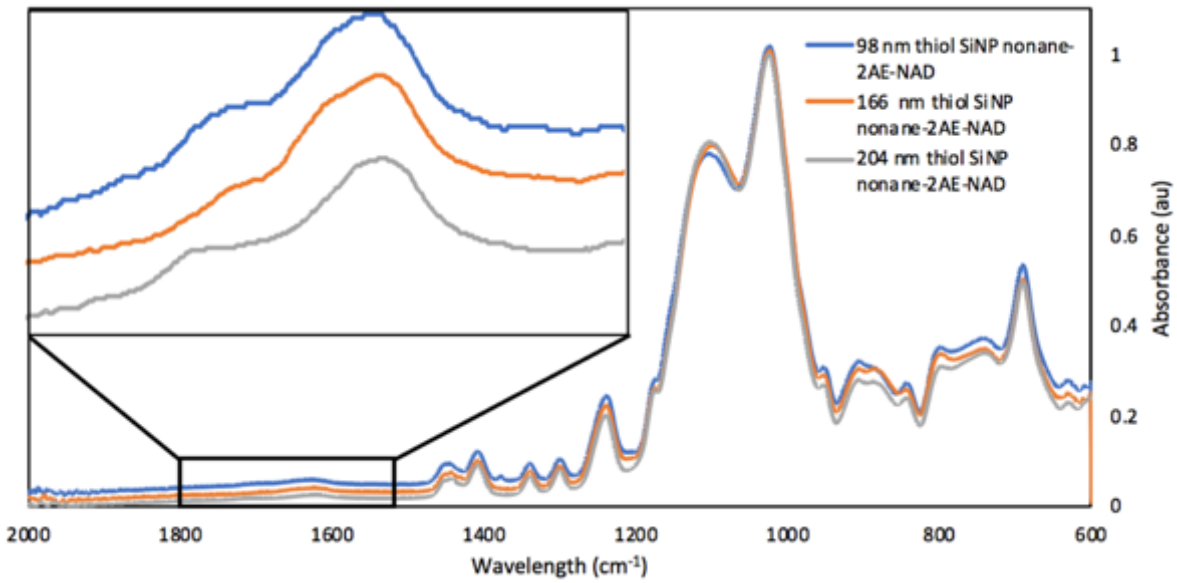

Figure 4.4: ATR-FTIR spectra of nonene-2AE-NAD tethered to the surface of thiol terminated SiNPs of different sizes with inset of region between 1500 and 1800 cm^{-1} showing C=O peak of nonene-2AE-NAD at 1700 cm^{-1}.

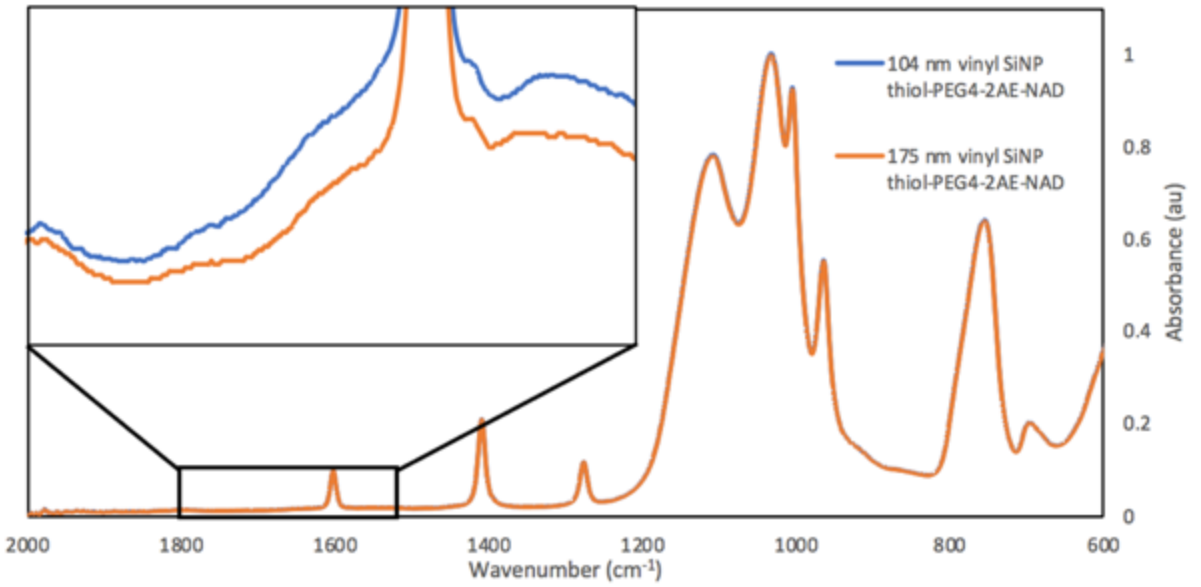

Figure 4.5: ATR-FTIR spectra of thiol-PEG$_4$-2AE-NAD tethered to the surface of vinyl terminated SiNPs of different sizes with inset of region between 1500 and 1800 cm^{-1} showing C=O peak of thiol-PEG$_4$-2AE-NAD at 1700 cm^{-1}.

Table 4.1 shows the surface coverage of N^6-linked-2AE-NAD achieved for each batch of thiol and vinyl terminated SiNPs determined by quantitative ATR-FTIR analysis. NAD attachment densities as high as 0.50 attachments/nm^2 were achieved, comparable to that observed previously, as shown in Table 4.2 [18, 54]. Knowing the specific surface area of each batch of particles, as quantified by BET surface area analysis in Chapter 3, along with the total mass of particles, allows the NAD attachment density to be transformed into a total molar amount of NAD. Thus, the volume of the NAD tethered SiNP solution can be controlled to accurately achieve the desired total molar concentration. This is essential for subsequent enzyme assays where tethered and free NAD are compared at equivalent concentrations.

Table 4.1: Attachment density of N^6-linked-2AE-NAD on the surface of thiol and vinyl terminated SiNPs determined by quantitative ATR-FTIR.

Sample	A/B ratio	NAD/nm^2
98 nm thiol SiNP nonane-2AE-NAD	0.0079	0.50
166 nm thiol SiNP nonane-2AE-NAD	0.0047	0.20
204 nm thiol SiNP nonane-2AE-NAD	0.0050	0.20
104 nm vinyl SiNP thiol-PEG_4-2AE-NAD	0.0009	0.50
175 nm vinyl SiNP thiol-PEG_4-2AE-NAD	0.0005	0.25

Table 4.2: Attachment densities of NAD found in literature. NAD attachment densities were calculated using the reported NAD loading in mg/g of support material and the reported size and/or surface area of the support materials.

Reference	Support Material	NAD attachments/nm^2
[18]	500 nm Polystyrene particles	0.35-0.56
[48]	30 nm silica nanoparticles	3.6
[36]	124 nm silica coated magnetic nanoparticles	1.3
[54]	15 nm silica nanoparticles	0.3
[53]	105 nm super-paramagnetic nanoparticles	0.6
[50]	Chitosan coated 9 nm magnetic nanoparticles	0.03

Other less quantitative techniques can be used to confirm the attachment of new functional groups of to the surface of nanoparticles. One such method is measurement of the zeta potential of the nanoparticle surface.

4.4.4 Zeta potential of functional SiNP surfaces

Zeta potential can be used to confirm the attachment of chemical moieties to the surface of SiNPs by monitoring change in electrophoretic mobility. The magnitude and charge of the zeta potential can also give information regarding the charge of the nanoparticle surface. Table 4.3 shows the zeta potential charge of thiol and vinyl terminated SiNPs before and after attachment of N^6-linked-2AE-NAD in 10 mM tris buffer pH 7.5, based on electrophoretic light scattering. Thiol terminated SiNPs showed a zeta potential of -35 mV, indicating a stable colloid of negatively charged particles at this pH. Tethering of N^6-linked-2AE-NAD to the surface of thiol terminated SiNPs increased the zeta potential to -51.9 mV, indicating a large increase in colloidal stability due to an increase in surface net negative charge. This is due to the two negatively charged hydroxyl groups of the pyrophosphate bonds of N^6-linked-2AE-NAD. The highly hydrophobic terminal vinyl groups of vinyl terminated SiNPs rendered the particles unmeasurable in the aqueous buffer solution. However, tethering of hydrophilic N^6-2AE-NAD significantly increased the zeta potential to -15 mV, indicating weak colloidal stability.

Table 4.3: Zeta potential of SiNPs before and after N^6-2AE-NAD tethering.

Nanoparticle	Zeta potential (mV)
Thiol SiNP	-35
Thiol SiNP tethered alkenyl-2AE-NAD	-51.9
Vinyl SiNP	NA
Vinyl SiNP tethered PEG_4-2AE-NAD	-15.0

The surface configuration of chemicals attached to the surface of nanoparticles is a critical factor controlling the surface properties of the nanoparticle. This is especially important in the present study where the surface tethered NAD must be displayed on the silica surface in a configuration that can be readily accessed and bound by the active site of enzymes in order to perform their catalytic function. Since this cannot be directly visualised by any existing methods, surface structures can be simulated and investigated with great accuracy using Molecular Dynamics computer simulations.

4.4.5 Molecular dynamics simulations of N^6-linked-2AE-NAD tethered surfaces

Figure 4.6 shows a Forcite geometry optimised and equilibrated 4.48 nm x 4.48 nm (19.9 nm^2) amorphous silica surface with all surface silica atoms functionalized with mercaptopropyl groups. The density of surface mercaptopropyl groups equates to 4.1/nm^2, closely simulating the upper limit of 5/nm^2 [71, 93]. Nonene-2AE-NAD has been attached to the surface thiols at an attachment density of 0.45 attachments/nm^2, closely simulating the highest attachment density achieved for this configuration of 0.5 attachments/nm^2. Analysis of the simulated structure shows that NAD is well separated from the silica surface by the nonane linker and points up and away from the surface into the bulk solution. Each NAD molecule is separated by 1.5 nm and do not overlap, demonstrating that an attachment of 0.5 attachments/nm^2 is physically possible for nonene-2AE-NAD. A similar surface structure was obtained for thiol-PEG_4-2AE-NAD attached to the surface of a vinyl functionalised amorphous silica surface of similar dimensions, as shown in Figure 4.7. NAD is well separated from the vinyl functionalized surface by the PEG_4 spacer arm, while the NAD is well exposed to the bulk solution. Like previous, the average spacing between each surface tethered NAD was determined to be 1.5 nm with no overlap of the structures. Thus, MD simulations have revealed that the attachment densities obtained for tethered NAD on

both thiol and vinyl terminated SiNPs are reasonable. The tethered NAD has also shown to have favorable surface configurations for use in catalytic enzyme reactions.

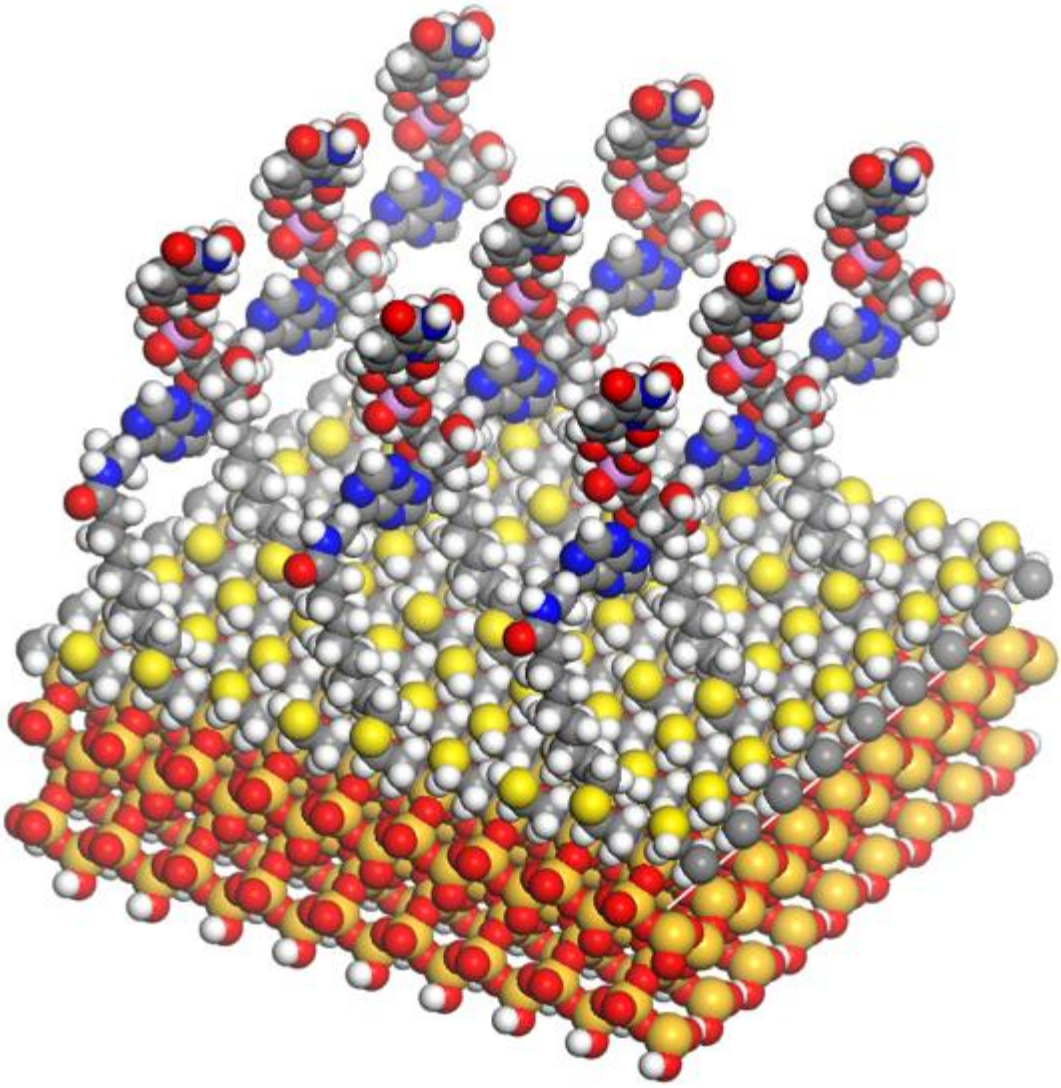

Figure 4.6: Forcite geometry optimised silica surface simulating a thiol terminated SiNP with 0,5 nonene-2AE-NAD attachments/nm^2. Produced using Materials Studio.

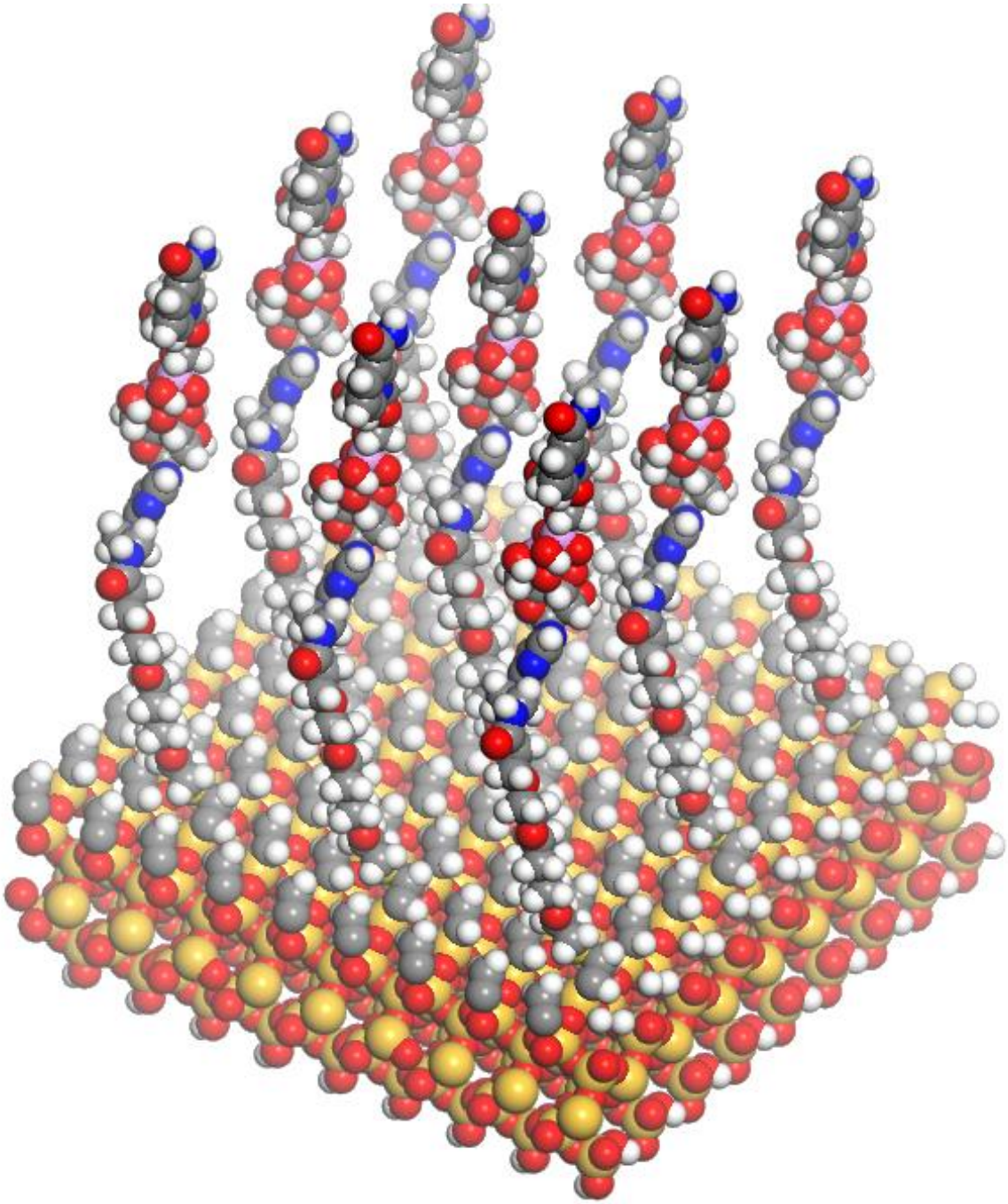

Figure 4.7: Forcite geometry optimised silica surface simulating a vinyl terminated SiNP with 0,5 thiol-PEG_4-2AE-NAD attachments/nm^2. Produced using Materials Studio.

4.5 Alkylation of residual surface thiol groups

Strong electrostatic interactions between residual surface thiols on the nanoparticle surface and adsorbed enzymes can lead to inhibition of enzyme activity. Therefore, in order to achieve maximum surface enzyme catalytic activity with tethered NAD, it is important to reduce the magnitude of these interactions. This can be achieved by chemically attaching a small molecule to the surface thiols in order to introduce a surface chemical functionality that will interact with the enzyme less. Iodoacetamide is commonly used to alkylate thiol groups of proteins in order to stop the formation of disulfide bonds [170, 171]. Here, iodoacetamide, along with two other similar alkylating agents, benzyl bromide and bromoethanol, are used to alkylate the residual thiol groups on the SiNP surface after the tethering of NAD. Alkylation of the thiol groups was performed in pH 8.8 buffer in order to deprotonate the surface thiol groups, facilitating the nucleophilic substitution reaction depicted in Figure 4.6. The reaction mixture was stirred at room temperature for 48 hours in the dark before the un-attached alkylating agents were removed by centrifugation. A small aliquot of each particle batch was dried for ATR-FTIR analysis as shown in Figure 4.7, 4.9 and 4.11. The attachment of the alkylating agents was not quantified, and therefore the degree of thiol capping is not known. The reader should also note that the implications of the alkylation of surface thiols not explored until Chapter 7, where particle-enzyme interactions are investigated in further depth.

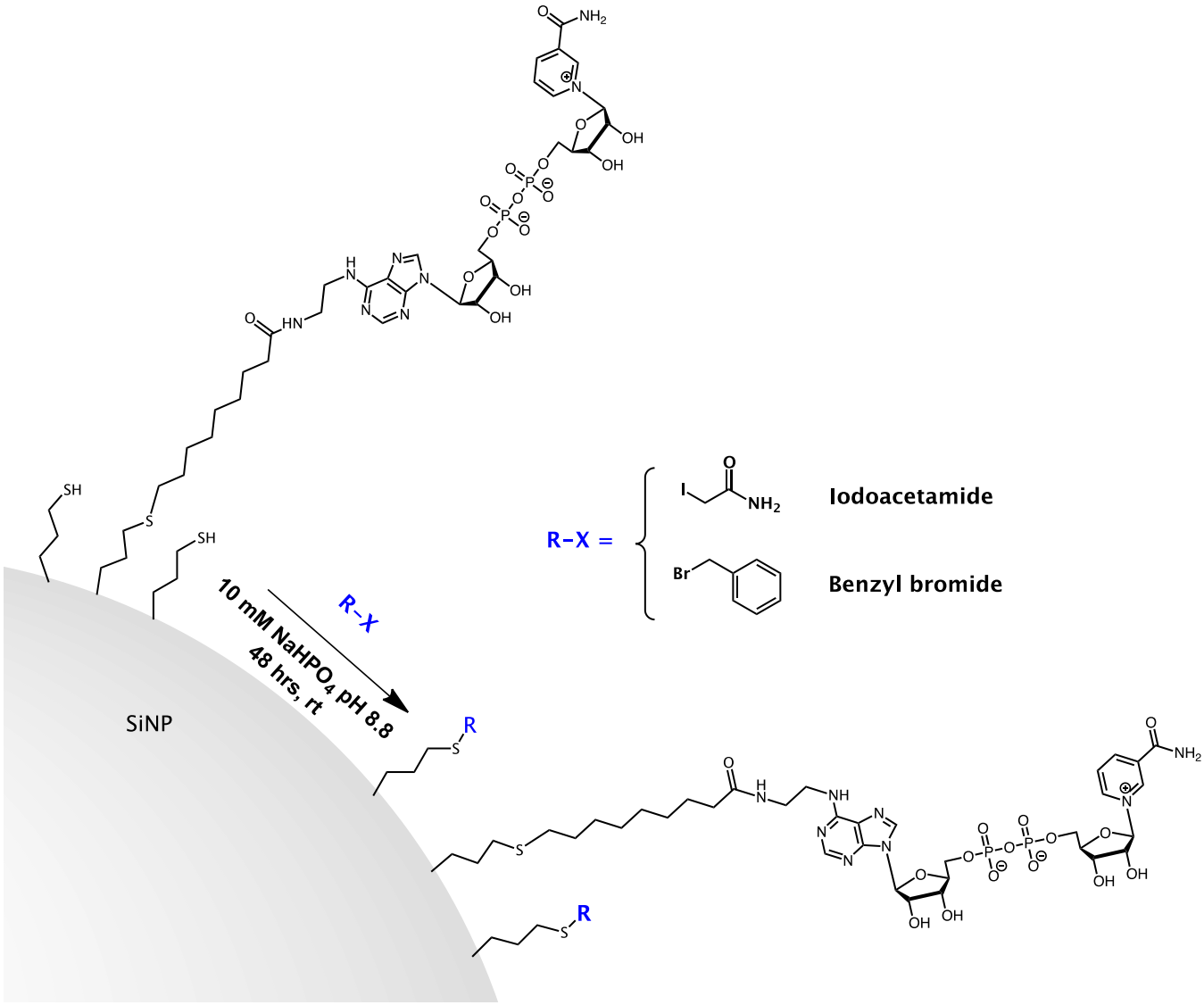

Figure 4.8: Schematic of the covalent capping of unreacted surface thiols with alkylating agents.

4.5.1 Alkylation of residual surface thiol groups by iodoacetamide

Figure 4.9 shows an overlay of the ATR-FTIR spectra of 166 nm thiol terminated SiNPs with 0.2 NAD attachments/nm^2 before (blue) and after alkylation of the residual surface thiols by iodoacetamide (orange). It can be seen that alkylation did not affect the NAD C=O peak at 1700 cm^{-1}, but it did result in an increase in peak height of the SiNP band at 1620 cm^{-1} and the appearance of a small shouldering peak at 1670 cm^{-1}. These signals are characteristic of the amide C=O of iodoacetamide as shown in the iodoacetamide FTIR spectra in the Appendix.

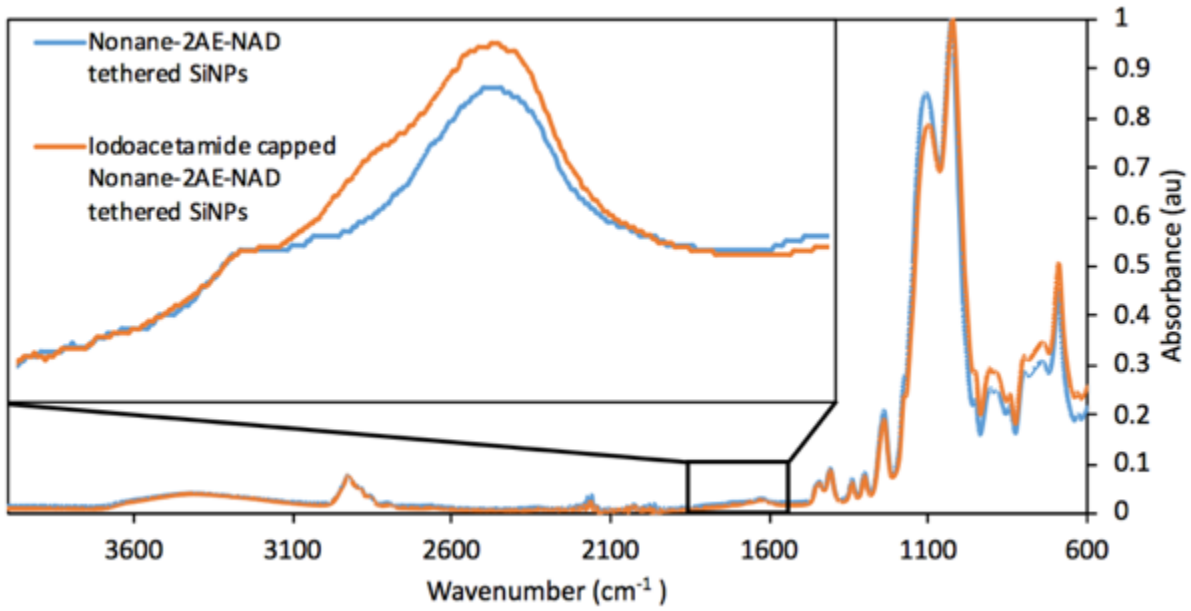

Figure 4.9: ATR-FTIR spectra of thiol terminated SiNPs with tethered NAD (blue) and with surface thiols capped by iodoacetamide (orange).

.

4.5.2 Alkylation of residual surface thiol groups by benzyl bromide

Alkylation of residual surface thiols by benzyl bromide also did not affect the NAD C=O peak at 1700 cm^{-1} as shown in Figure 4.10. It did, however, result in the appearance of a sharp peak at ~1490 cm^{-1}, characteristic of the aromatic C=C bending of the benzene group of benzyl bromide as shown in the benzyl bromide FTIR spectra in the Appendix. This indicates the successful alkylation of surface thiols by benzyl bromide.

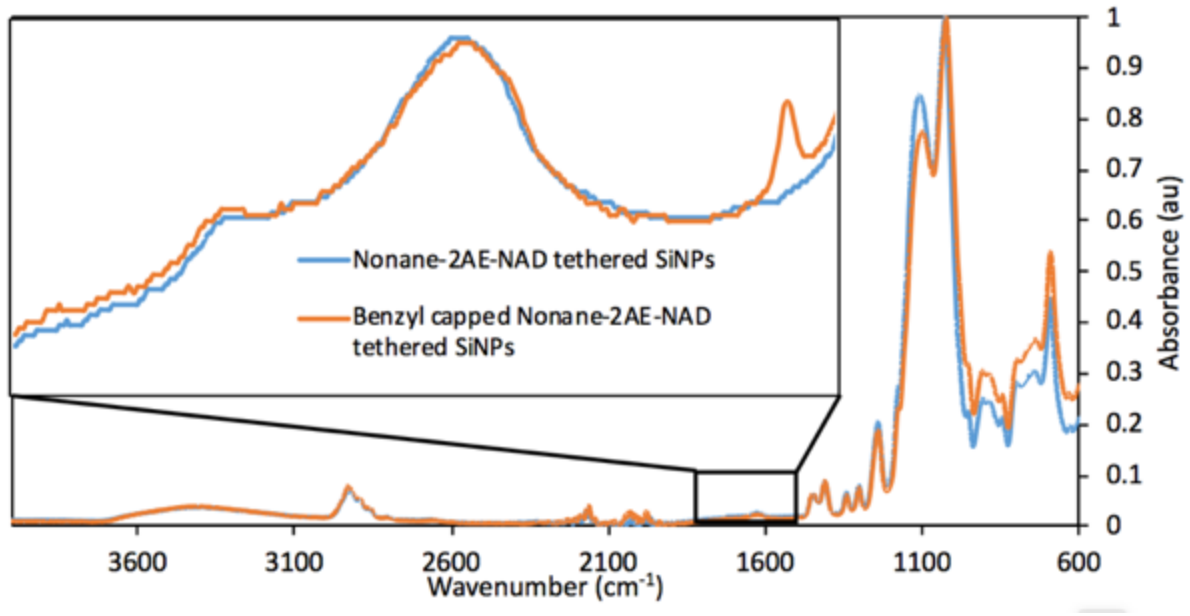

Figure 4.10: ATR-FTIR spectra of thiol terminated SiNPs with tethered NAD (blue) and with surface thiols capped by benzyl bromide (orange).

4.6 Conclusion

N^6-linked-2AE-NAD has been specifically attached to the surface of SiNPs using a thiol-ene 'click' reaction to couple the terminal thiol or vinyl groups of the N^6-linked spacer arm of NAD to the vinyl or thiol functional groups on the SiNP surface. This was achieved through careful selection of an appropriate radical initiator, potassium persulfate, which suited the aqueous solubility and thermal instability of the NAD derivatives. ATR-FTIR analysis of the washed and dried SiNPs revealed the appearance of a band at ~1700 cm^{-1}, characteristic of the intense C=O stretch of the nicotinamide moiety of NAD, This band was used to determine the surface attachment density of the NAD on the particle surface using a quantitative ATR-FTIR technique that required the careful construction of standard mixtures of NAD and SiNPs to simulate attachment densities. NAD attachment densities were determined to within the range of 0.2-0,5 attachments/nm^2, which compared well with attachment densities of NAD on particles calculated from literature. Attachment of NAD was confirmed by zeta potential measurements, where attachment resulted in an increase in the zeta potential of thiol terminated SiNPs from -31 mV to -51.9 mV, while vinyl terminated particles when from being unmeasurable to -15 mV. MD computer simulations were then used to construct simulations of the tethered NAD surfaces, showing the obtained

attachment densities are indeed possible and NAD adopts a favourable conformation pointing out to bulk solution on both SiNP surfaces. Lastly, residual thiol groups on the particle surface are covalently ‘capped’ with several different small alkylating agents in order to decrease the interactions between the surface thiols and enzymes. Attachment of the small alkylating agents were then confirmed by ATR-FTIR analysis.

CHAPTER 5 : ENZYME ADSORPTION

5.1: Overview

Enzyme interaction with the surface holding the co-factor is a key step in the reaction mechanism. This chapter describes the adsorption of the enzymes used in this project (EcG3PD, ADH and GluDH) onto the surface of thiol and vinyl terminated SiNPs with tethered NAD. Enzyme adsorption onto the particle surface was found to follow a Langmuir model of adsorption, allowing the determination of a Langmuir constant (K_L) and a maximum adsorption capacity ($[*]_{max}$). Molecular Dynamic simulations of the enzymes were used to explain the differences in the observed adsorption properties of the enzymes on the thiol and vinyl terminated SiNP surfaces.

5.2 Introduction

The enzymes are very large compared to the size of the co-factor and since the co-factor is tethered to the surface of the SiNP, the interaction between tethered NAD and freely diffusing enzymes is likely to also involve the enzyme interacting with the surface of the SiNP. Most likely, for the interfacial enzyme reaction to proceed, the enzyme must first adsorb to the active surface. In order to accurately quantify the surface catalysis kinetics of tethered NAD with enzymes a highly detailed understanding of this adsorption process is critical. Several previous studies focusing on the catalytic action of freely diffusing enzymes on surface bound reactants have utilised Langmuir adsorption kinetics to describe the adsorption of the enzyme to a surface [115, 116, 172]. A schematic for the reversible adsorption of freely diffusing enzyme to the surface of a dispersed SiNP with surface tethered NAD is shown in Figure 5.1. In order to develop a mathematical kinetic model of the catalytic enzyme reaction with surface tethered NAD, the adsorption of freely diffusing enzymes onto the nanoparticle surface must be considered.

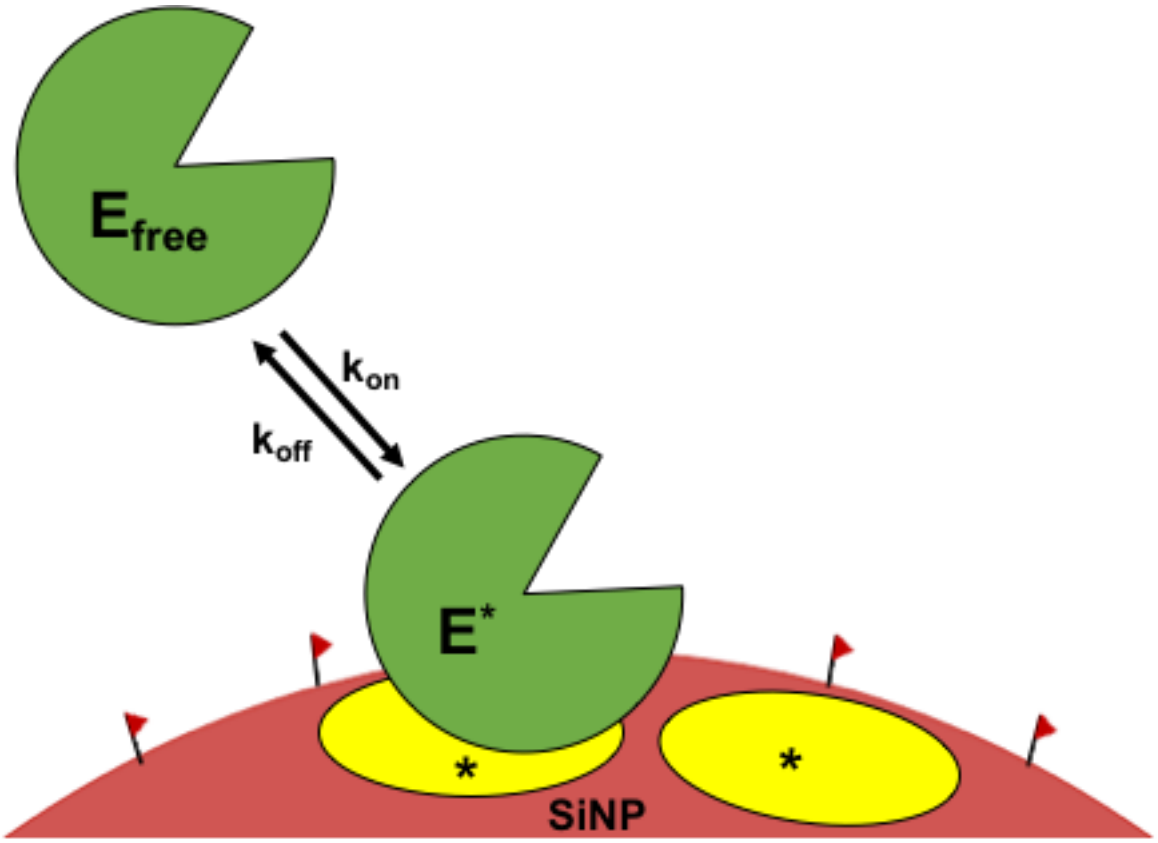

Figure 5.1: Adsorption of enzyme onto SiNP surface

5.3 Langmuir adsorption kinetics

The first step in the reaction model is the reversible adsorption of freely diffusing enzyme in solution (E_{free}) onto an available surface site ($*$) on the nanoparticle surface, resulting in a surface adsorbed enzyme (E^*) Figure 5.1.

$$E_{free} + * \underset{k_{off}}{\overset{k_{on}}{\rightleftharpoons}} E^* \tag{5.1}$$

The maximum number of enzyme adsorption sites on the nanoparticle surface can be expressed by the following:

$$[*]_{max} = [*] + [E^*] \tag{5.2}$$

Where $[*]_{max}$ is the total concentration of available adsorption sites for enzyme in the system. Reversible adsorption of enzyme onto the surface of SiNPs without catalytic action of the enzyme can be reduced to Langmuir surface adsorption and desorption kinetics.

$$\frac{d[E^*]}{dt} = k_{on}[E_{free}]([*]_{max} - [E^*]) - k_{off}[E^*] \tag{5.3}$$

The surface concentration of enzyme at equilibrium $[E^*]_{eq}$ as a function of aqueous enzyme concentration can then be expressed as:

$$\frac{[E^*]_{eq}}{[*]_{max}} = \frac{K_L[E_{free}]}{1 + K_L[E_{free}]} \tag{5.4}$$

Where K_L is the Langmuir constant expressed as:

$$K_L = \frac{k_{on}}{k_{off}} \tag{5.5}$$

Equation 5.4 is known as the Langmuir adsorption equation. It describes the adsorption of an adsorbate onto an adsorbent with limited surface adsorption sites. Adsorption sites are linearly filled with increasing adsorbate concentration. As adsorption sites are depleted, adsorption begins to plateau to a point where no more adsorption can occur.

5.4 Adsorption of EcG3PD, ADH and GluDH onto the surface of SiNPs

Accurate determination of interfacial kinetic constants requires knowledge of the Langmuir adsorption kinetics of the enzymes onto the NAD tethered SiNP surfaces. To determine the adsorption kinetics, EcG3PD, ADH and GluDH were adsorbed onto thiol and vinyl terminated SiNPs with tethered NAD simply by mixing different equivalents of the aqueous enzymes with the dispersed SiNPs. After mixing, the nanoparticles were isolated and washed of free, unbound enzyme by centrifugation, which has been shown to be an effective method for the separation of free proteins from protein/nanoparticle complexes [111]. Proteins that have associated strongly with the nanoparticles will travel with them, whereas weakly interacting proteins will be removed by both exchange with proteins in the bulk liquid and by the shear force of the particles in motion through the liquid [111]. The change in enzyme concentration in the supernatant liquid can then be used to determine the quantity of enzyme adsorbed onto the particle surface by difference. UV/Vis spectroscopy can be used to determine the supernatant concentration of enzymes if the enzyme has a convenient absorbance and/or the change in enzyme activity of the solution before and after mixing with the particles can be used to quantify the remaining enzyme, as shown schematically in Figure 5.2(a) and Figure 5.2(b) respectively.

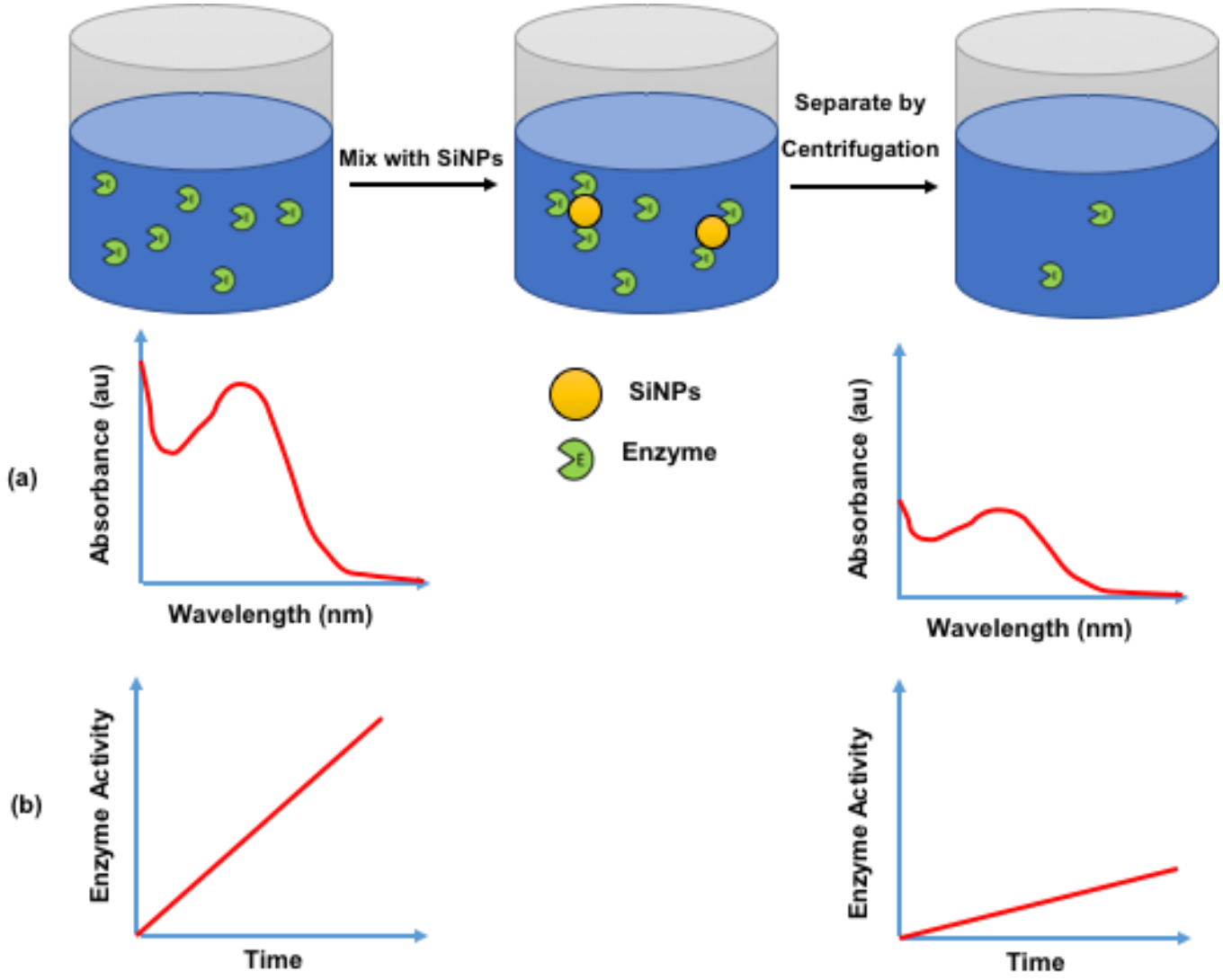

Figure 5.2: Change in enzyme concentration after mixing with SiNPs measured by (a) UV/Vis absorbance and (b) analysis of the change in enzyme activity.

EcG3PD absorbs in the UV range and Figure 5.3(a-b) shows the change in the spectrum for various concentration of EcG3PD on thiol and vinyl particles respectively. The quantity of EcG3PD adsorbed/nm^2 of SiNP surface was plotted as a function of the quantity of EcG3PD applied/nm^2 of SiNP surface in order to generate the characteristic adsorption isotherm in Figure 5.3(c).

For ADH and GluDH, quantification of residual activity is a convenient method to determine the adsorption onto the SiNP surface (Figure 5.2(b)). Knowing the activity of these enzymes per mass of enzyme under specific conditions, i.e. μmol/min/mg, the change in the total activity of the aqueous enzyme before and after mixing with SiNPs can be used to determine the change in concentration of the enzyme. However, this assumes that the enzyme suffers no loss in catalytic activity while in dynamic equilibrium with the SiNP surface and bulk solution. The activity of ADH and GluDH, before and after mixing with SiNPs, was quantified by tracking the increase in UV/Vis absorbance at 340 nm due to the enzyme catalysed reduction of NAD to NADH Determining the change in enzyme activity with increasing amounts of enzyme applied/nm^2 of SiNP surface in allows the amount of enzyme adsorbed/nm^2 of SiNP surface to be determined. These values are plotted together in order to generate the Langmuir adsorption isotherm for ADH (Figure 5.4(b)) and GluDH (Figure 5.5(b)). Adsorption analysis of ADH and GluDH onto vinyl terminated SiNPs with tethered NAD was not performed.

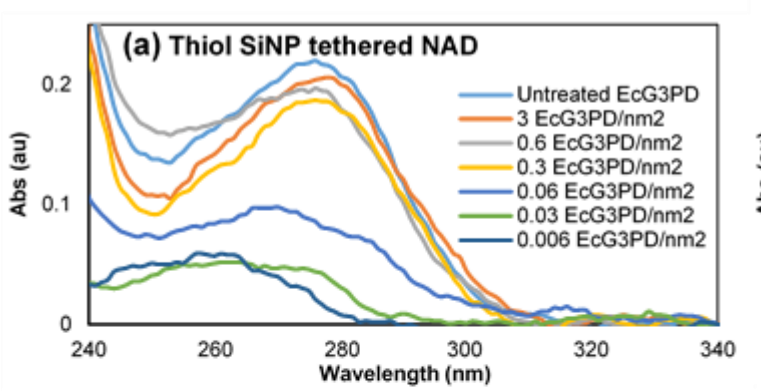

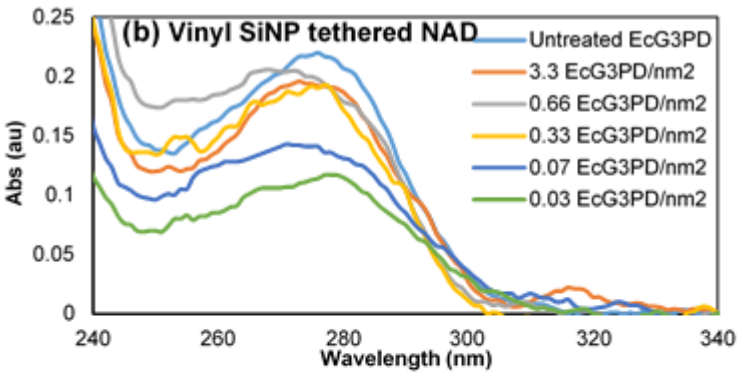

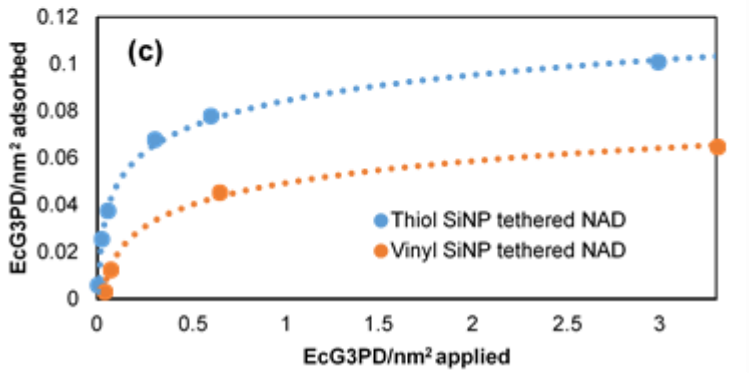

Figure 5.3: UV/Vis spectra of EcG3PD left in particle washings after adsorption onto thiol terminated SiNPs (a), and vinyl terminated SiNPs (b) with surface tethered NAD. The amount of EcG3PD applied/nm^2 is then plotted against the quantity of EcG3PD adsorbed/nm^2 to generate a Langmuir adsorption isotherm for each SiNP species (c).

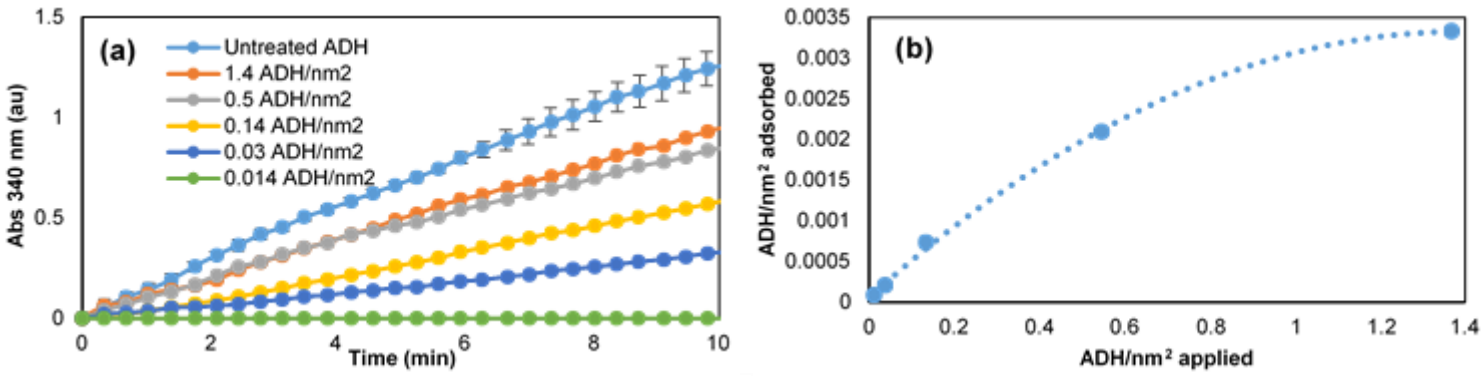

Figure 5.4: Increase in UV/Vis absorbance at 340nm due to the formation of NADH by the catalysis of ADH remaining in particle washings after adsorption onto thiol terminated SiNPs with tethered NAD (a). The change in ADH activity is used to determine the amount of ADH adsorbed/nm^2 of SiNP surface, which is then plotted as a function of the quantity of ADH applied/nm^2 to generate the Langmuir adsorption isotherm (b).

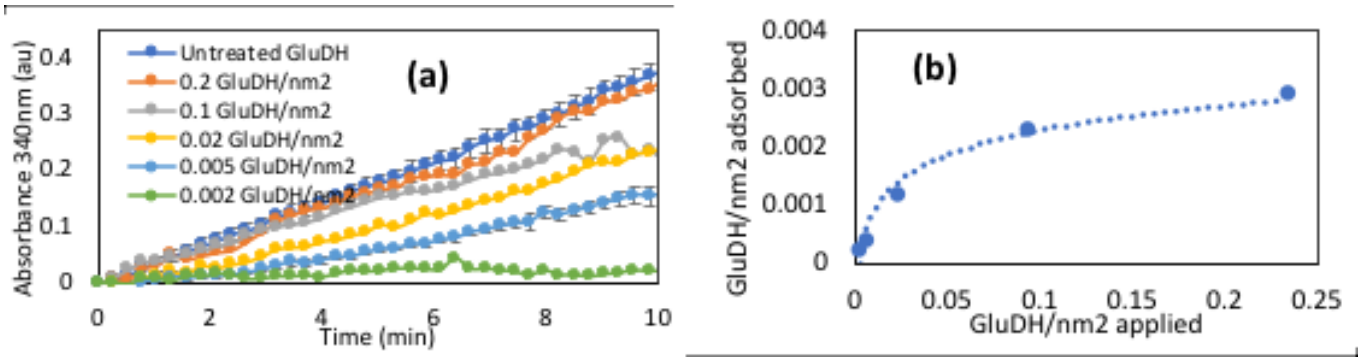

Figure 5.5: (a) Activity of GluDH before and after mixing with thiol terminated SiNPs with tethered NAD and (b) corresponding amount of GluDH adsorbed onto the thiol SiNP surface.

5.4.1 Langmuir adsorption kinetics

The Langmuir constant, K_L, and maximum equilibrium adsorption capacity, $[*]_{max}$ (Table 5.1) for each surface and enzyme combination were determined by fitting the Langmuir adsorption expression (Equation 5.4) to the adsorption isotherms (Figure

5.3(c), Figure 5.4(b) and Figure 5.5(b)). Knowing the specific surface area of the SiNPs allows the Langmuir constants to be converted to a molar concentration.

Table 5.1: : The Langmuir constants, K_L, and maximum equilibrium adsorption capacities, $[*]_{max}$, derived by fitting Equation 5.4 to the adsorption isotherms of EcG3PD, ADH and GluDH on thiol and vinyl terminated SiNPS with tethered NAD in (Figure 5.3(c), Figure 5.4(b) and Figure 5.5(b)).

Enzyme	SiNP Surface	K_L $(E/nm^2)^{-1}$	$[*]_{max}$ (E/nm^2)	Theoretical $[*]_{max}$ (E/nm^2)
EcG3PD	Thiol/NAD	9.6	0.1	0.02
	Vinyl/NAD	1.4	0.09	0.02
ADH	Thiol/NAD	1.9	0.005	0.007
GluDH	Thiol/NAD	14	0.004	0.005

The Langmuir constant, K_L, is the equilibrium constant for the forward enzyme adsorption reaction, given by Equation 5.5. The high K_L value for EcG3PD adsorption onto thiol terminated SiNPs (9.6 $(E/nm^2)^{-1}$) compared to the vinyl particle (1.4 $(E/nm^2)^{-1}$) indicates a much stronger affinity of EcG3PD towards the thiol surface compared with a vinyl surface on the particle. This is schematically illustrated in Figure 5.6(a).

The maximum number of enzymes /nm^2 adsorbed onto the surface is approximately 0.1 Enzymes / nm^2 for both nanoparticles as shown in Table 5.1. The largest length dimension of the enzyme determined from the crystal structure of LmG3PD, a model for EcG3PD, was 8nm [141]. Assuming EcG3PD is spherical with a diameter of 8 nm, highly ordered packing only physically allows a calculated 0.02 enzymes/nm^2. This indicates that either the enzyme conformation is significantly altered upon adsorption or more likely the formation of a multi-layered second order structure on the SiNP surface such as the commonly reported protein corona [173, 174]. This suggests strong protein-protein interactions between EcG3PD molecules.

Interestingly, the maximum adsorption of both ADH and GluDH is about 200 times less than that for EcG3PD at about 0.005 enzymes /nm^2. This compares well to the theoretical value of 0.007 ADH molecules/nm^2, assuming high density packing of spherical ADH with diameter of ~14 nm as determined by crystal structure [145]. A lower experimentally determined value for the maximum surface coverage than the theoretical value suggests the formation of a single layer of ADH on the particle surface with much weaker protein-protein interactions than suggested in the EcG3PD adsorption analysis. GluDH has a diameter of 16.5 nm as determined from analysis of its crystal structure [146, 147]. Assuming high packing efficiency on the SiNP surface, a maximum adsorption capacity of 0.005 GluDH/nm^2 is possible. This correlates well with the experimental value of 0.004 GluDH/nm^2.

Similar to EcG3PD adsorption onto vinyl terminated SiNPs with tethered NAD, adsorption of ADH onto thiol terminated SiNPs with tethered NAD resulted in a low Langmuir constant suggesting weak enzyme-surface interactions. This is schematically illustrated in Figure 5.6(b). The maximum equilibrium surface coverage of ADH was found to be 0.005 ADH molecules/nm^2 on the thiol particle surface.

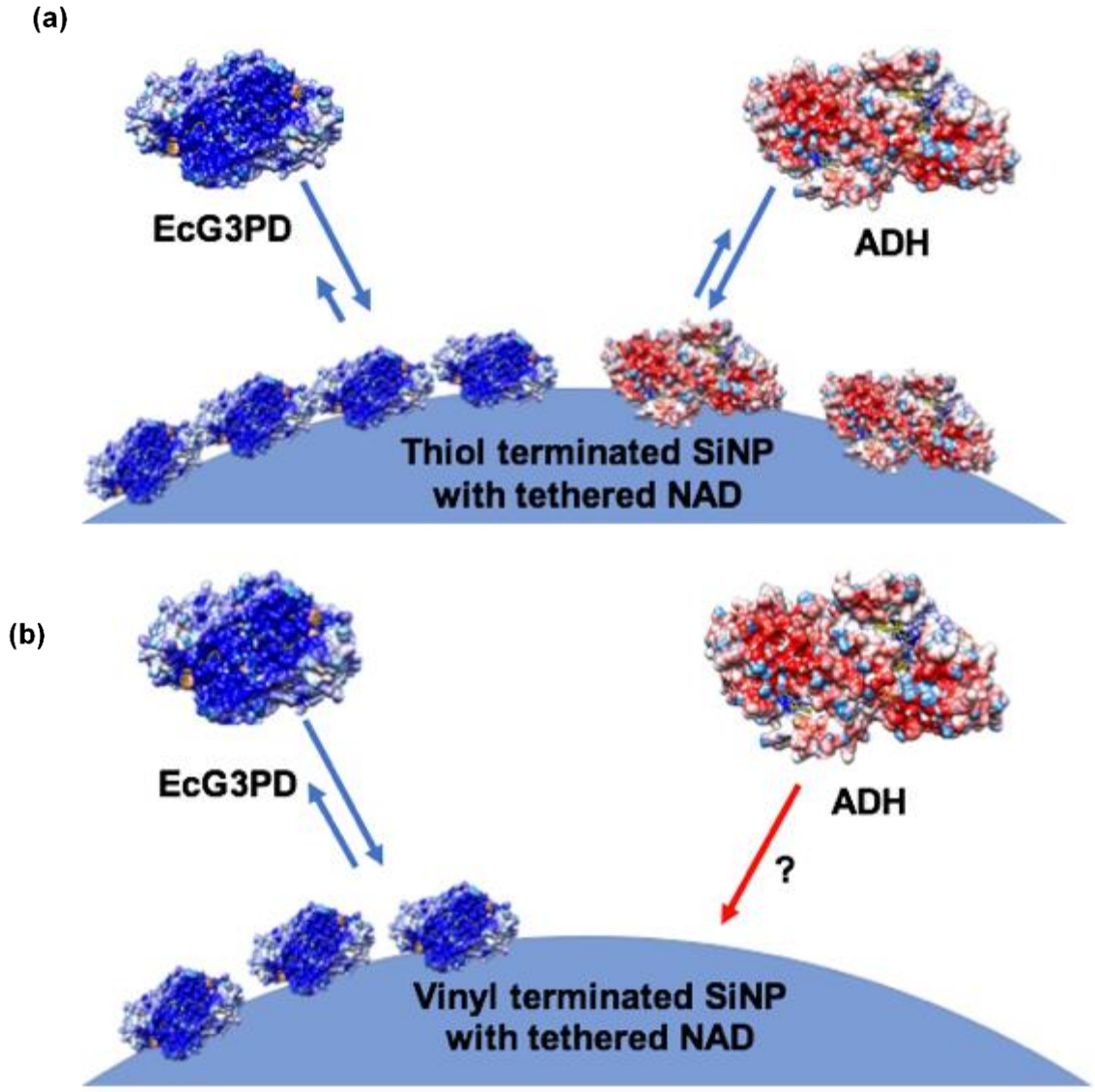

Figure 5.6: Graphical representation of EcG3PD and ADH adsorption onto thiol terminated SiNPs with tethered NAD (a) and EcG3PD and ADH adsorption onto vinyl terminated SiNPs with tethered NAD (b).

Like EcG3PD, GluDH has a higher Langmuir constant, indicating the adsorption equilibrium towards enzyme adsorption, suggesting strong interactions between the enzyme and surface. Therefore, GluDH exhibits a similar adsorption to the surface of thiol terminated SiNPs as EcG3PD depicted in Figure 5.6(a). However, the lower experimental maximum adsorption capacity compared to the theoretical value suggests the formation of a single layer of GluDH on the particle surface. This suggests weaker protein-protein interactions as in the case of ADH. Therefore, the

SiNP surface is occupied by GluDH molecules at low concentrations before all vacant adsorption sites are filled and adsorption plateaus, as observed in Figure 5.5(b).

In order to explain differences in adsorption properties of the different enzymes on the different surfaces, the physical and chemical properties of the enzymes and surfaces must be examined. This can be achieved by considering the surface electrostatic properties of both the nanoparticle and enzyme, which can be achieved by zeta potential analysis and MD simulations, respectively.

5.4.2 Comparison of thiol and vinyl terminated SiNP surfaces

As discussed in Chapter 4, Zeta potential (ζ) measurements of thiol and vinyl terminated SiNPs with tethered NAD were measured in pH 7.5 buffer solution, simulating the enzyme adsorption and reaction conditions. At pH 7.5, the zeta potential of thiol terminated SiNPs with tethered NAD was found to be -51.9 mV while that of vinyl terminated SiNPs with tethered NAD was -15.0 mV. This shows that thiol terminated SiNPs are highly stable in the reaction solution and carry a large negative charge. This negative charge is caused by the small amount of deprotonated surface silanol and thiol groups, as well as the high density of negatively charged surface tethered NAD. The zeta potential of vinyl terminated SiNPs with tethered NAD indicates mild stability in solution and a weak negative surface charge, resulting from deprotonated surface silanol groups and negatively charged surface tethered NAD.

5.4.3 Comparison of EcG3PD, ADH and GluDH

EcG3PD is a small homodimer ~8 nm in diameter with a molecular mass of 72 kDa [141]. Langmuir adsorption analysis of EcG3PD onto the SiNP surfaces with tethered NAD in revealed that EcG3PD adsorbs strongly onto the surface of thiol terminated SiNPs with tethered NAD compared to weaker adsorption onto the vinyl terminated SiNP surface with tethered NAD. The maximum adsorption capacity of EcG3PD onto the SiNP surfaces was determined to be 0.1 EcG3PD/nm^2. Since the calculated maximum adsorption with highly ordered packing was calculated to be 0.02 EcG3PD/nm^2, it is likely that multiple layers of EcG3PD were adsorbed. EcG3PD was also determined to have much stronger adsorption than ADH onto the surface of thiol

terminated SiNPs with tethered NAD. Langmuir adsorption analysis revealed the maximum adsorption capacity of ADH to be 0.0055 ADH/nm^2 which correlated well with the calculated value of 0.007 ADH/nm^2 for the much larger 146 kDa homo-tetramer with a diameter of ~14 nm [145]. GluDH is a large homo-hexameric protein with a molecular mass of 345 kDA and a diameter of ~16.5 nm. Like EcG3PD, GluDH was found to have strong interactions with the thiol terminated SiNP surface as determined by Langmuir adsorption analysis. GluDH was found to have maximum adsorption density of 0.004 GluDH/nm^2, just under the maximum theoretical value of 0.005 GluDH/nm^2. Therefore, like ADH, it is likely that GluDH has weaker protein-protein interactions. These observed differences in adsorption properties of each enzyme can be explained by analysis of their electrostatic potential maps in Figures 5.7-5.9.

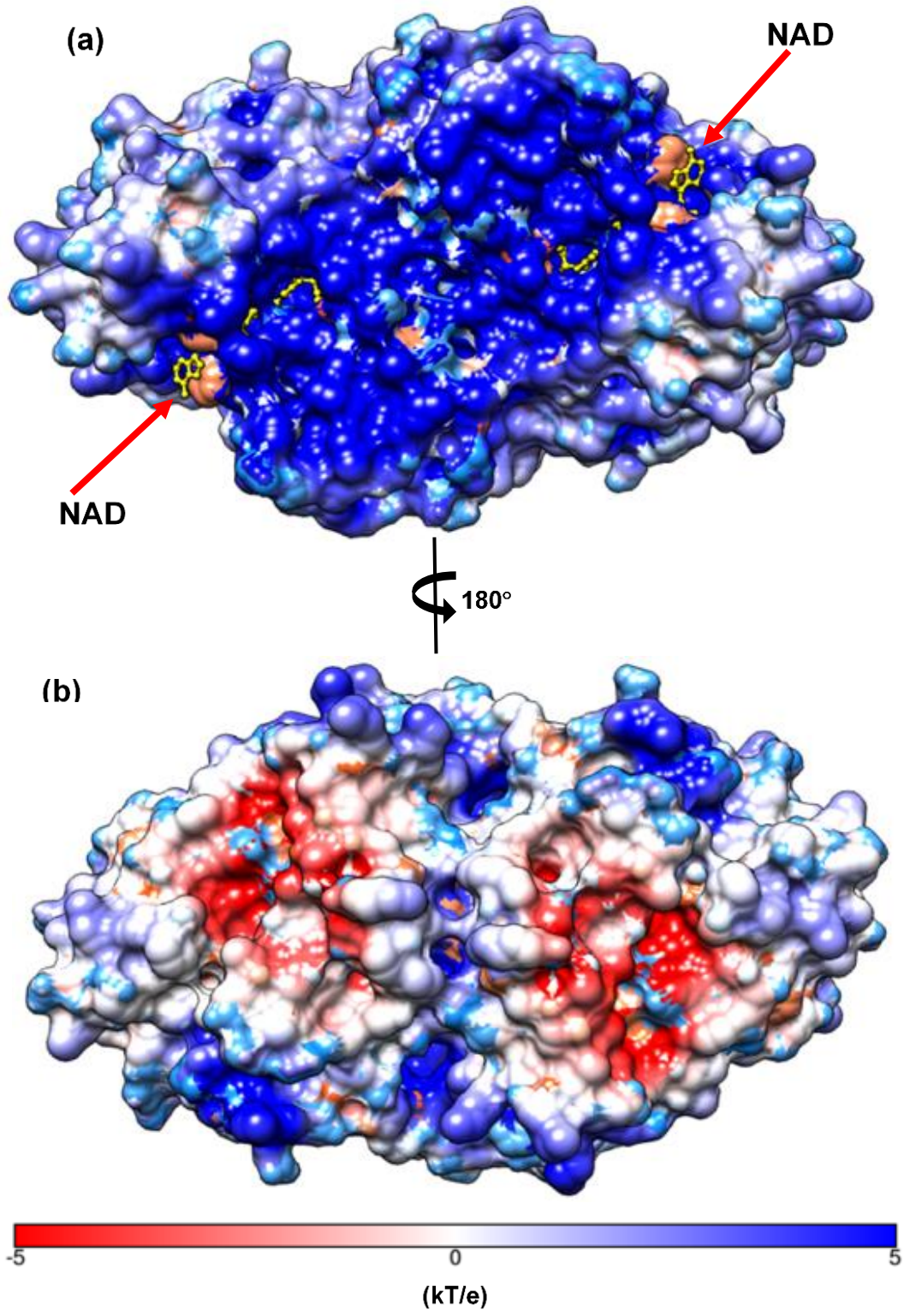

Figure 5.7: Surface electrostatic potential maps of EcG3PD (PDB ID: 1N1E) at pH 7.5, showing the NAD binding face with bound NAD (yellow) (a) and the reverse face (b). Generated using the Chimera [144]. Red corresponds to negatively charged surface regions while blue is positively charged surface regions.

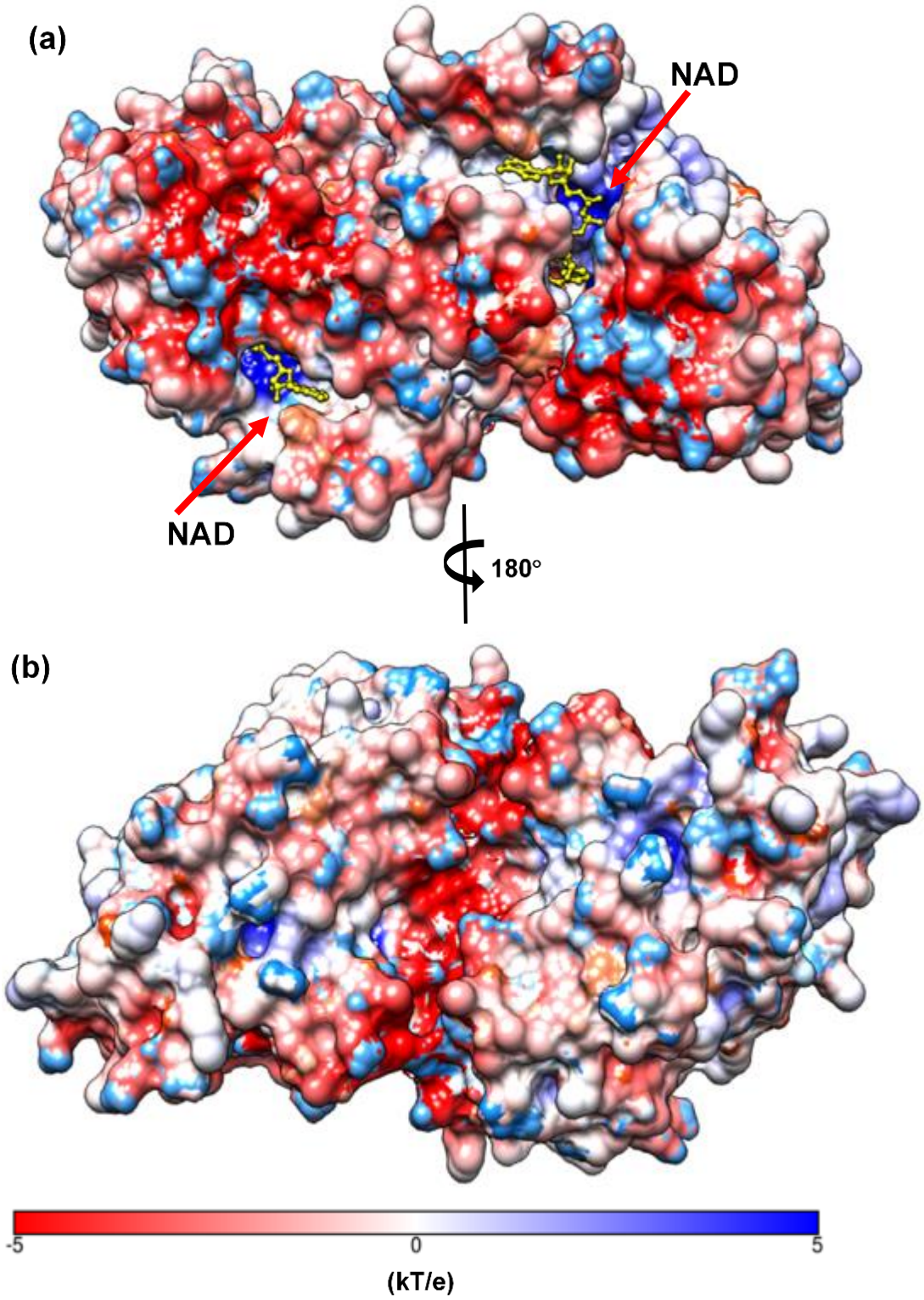

Figure 5.8: Surface electrostatic potential maps of ADH (PDB ID: 5ENV) at pH 7.5, showing the NAD binding face with bound NAD (yellow) (a) and the reverse face (b). Generated using the Chimera [144]. Red corresponds to negatively charged surface regions while blue is positively charged surface regions.

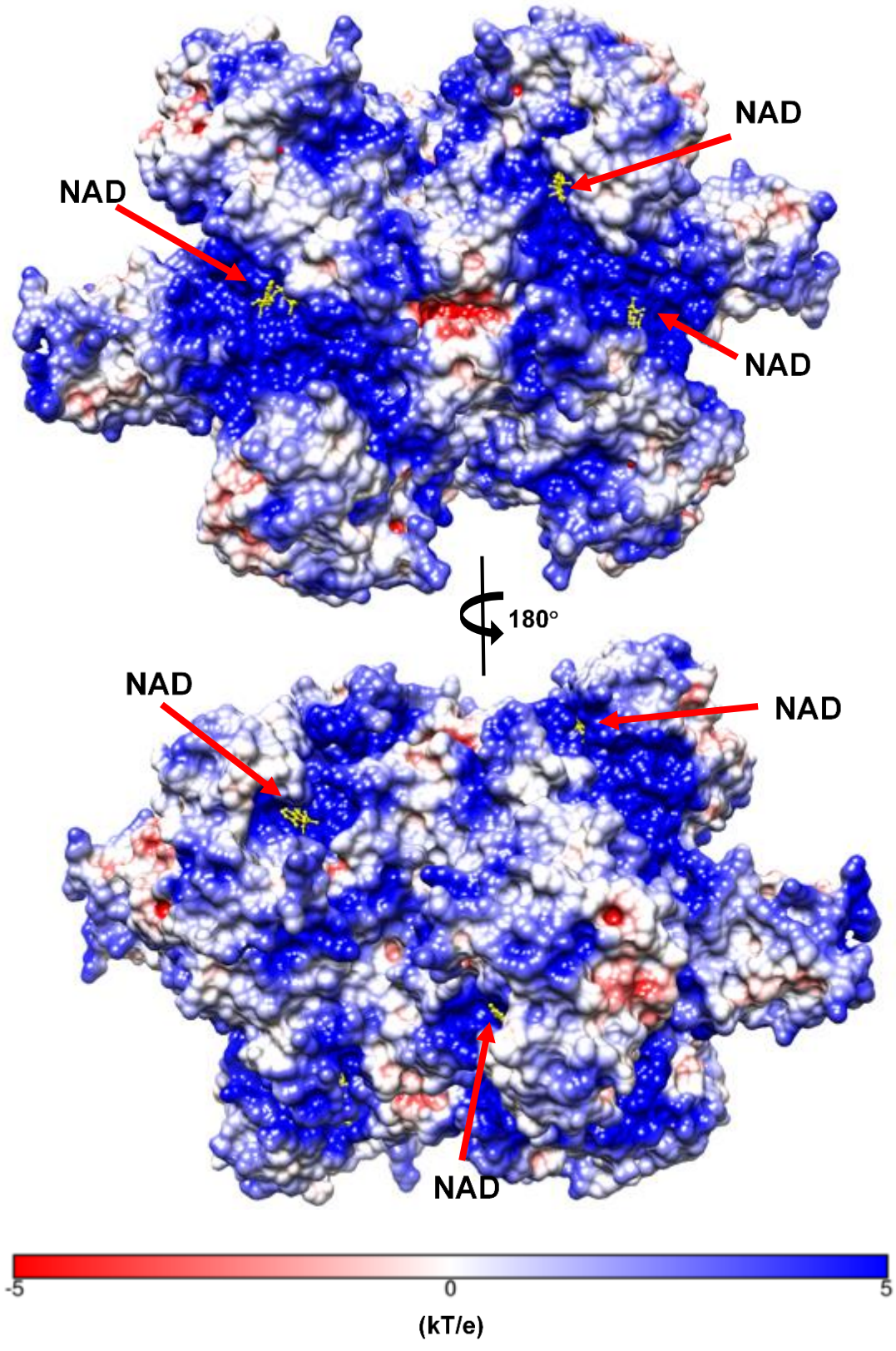

Figure 5.9: Surface electrostatic potential maps of GluDH (PDB ID: 1HWY) at pH 7.5, showing the NAD binding pockets with bound NAD of homo-hexamer subunits. Generated using the Chimera [144]. Red corresponds to negatively charged surface regions while blue is positively charged surface regions.

EcG3PD has an isoelectric point of 9.5 [141]. Therefore, at pH of 7.5, the pH at which all adsorption and enzyme activity experiments were carried out, EcG3PD will possess a net positive surface charge. ADH has an isoelectric point of 5.4-5.8 and thus will carry a net negative surface charge at pH 7.5. The electrostatic potential map of the EcG3PD homo-dimer shows a large, strongly positive region on the face containing the NAD binding sites (Figure 5.7(a)) and two small, negatively charged regions on the opposite face (Figure 5.7(b)). ADH (Figure 5.8), however, possesses a mixed coverage of surface charged regions, with a slightly higher density of negatively charged regions on the side containing the NAD binding sites (Figure 5.8(a)). These NAD binding sites carry a positive charge within their cavity, facilitating the binding of negatively charged NAD [145]. ADH dimers dimerise in a “back-to-back” configuration, forming a large homo-tetramer where the active sites are fully exposed to bind reactants [145]. Therefore, in its native state, either side of ADH would most closely resemble the NAD binding face Figure 5.14(a) with both sides of the tetramer possessing a net negative surface charge. The electrostatic potential map of the GluDH homo-hexamer (Figure 5.9) shows regions of dense positive charge within and surrounding the NAD binding pockets which are separated by neutral and slightly positive regions. Although a literature value for the isoelectric point of GluDH from bovine liver could not be found, the electrostatic surface mapping correlates well with the adsorption data. The large proportion of surface positive charge of GluDH would facilitate strong interactions between the negatively charged thiol terminated SiNP surface with tethered NAD. Therefore, a large Langmuir constant is expected with monolayer adsorption due to weak protein-protein interactions. The structural properties of the surfaces of both SiNPs and enzymes as determined by molecular dynamics simulations are therefore highly consistent with the adsorption properties experimentally observed in Section 5.4 and are consistent when compared to the reaction pH and their literature isoelectric point values.

5.6 Conclusion

In order to facilitate the accurate determination of surface enzyme catalysis of kinetics of tethered NAD, the adsorption of the enzymes EcG3PD, ADH and GluDH onto the surface of thiol and vinyl terminated SiNPs with tethered NAD was investigated. This was performed by mixing controlled amounts of each enzyme with SiNPs, separation by centrifugation and then determination of the amount of enzyme adsorbed by UV/Vis

analysis or by measuring the change in activity of the enzyme solutions. Enzyme adsorption was characteristic of reversible Langmuir adsorption allowing the calculation of a Langmuir constant (K_L) and a maximum adsorption capacity ($[*]_{max}$) for each enzyme on the SiNP surfaces. The difference in adsorption properties of each enzyme was then explained by investigation of the SiNP surface zeta-potential and MD simulations of the surface electrostatic potential of the enzymes.

CHAPTER 6 : SURFACE CATALYSIS KINETICS OF TETHERED NAD: AN EXCESS ENZYME APPROACH

6.1 Overview

This chapter describes the development of a kinetic model describing the interfacial kinetics of the catalytic action of NAD dependent enzymes with surface tethered NAD. This allows the determination of the kinetic rate constants for several critical reaction steps such as reversible enzyme adsorption, complexation, de-complexation and catalysis of the surface-bound-enzyme/NAD-complex. These kinetic constants are then compared to those of an equivalent enzyme reaction system containing free NAD, modelled by conventional Michaelis-Menten kinetics.

Utilising the Langmuir adsorption kinetics determined in Chapter 5, a quasi-steady-state-assumption (QSSA) is applied to the surface adsorbed enzyme and the reactant stationary assumption to the freely diffusing enzyme, allowing the derivation of an expression that accurately described the enzyme reaction rate with surface tethered NAD as a function of enzyme concentrations. Kinetic constants derived from the rate expression are then supported via theoretically modelling the reaction against experimental data. The rate constant of surface catalysis of EcG3PD and ADH were found to be enhanced with SiNP tethered NAD up to ~25 fold for catalysis and ~2.4 fold for complexation as compared to equivalent concentrations of freely diffusing NAD. Kinetic analysis, along with molecular dynamic simulation of the interfacial interactions between the NAD/SiNP surface and enzymes revealed a combination of tuneable factors giving rise to the observed kinetic enhancement. These factors included the strength of the electrostatic attraction or repulsion between the enzymes and SiNP surface, the enzyme size, adsorption orientation and surface protein-protein interactions.

6.2 Introduction

Biorecognition, binding and catalytic action of biological agents such as enzymes, antibodies and peptides at cellular interfaces are highly prevalent processes in nature [113, 117, 123, 125, 129, 134]. Membrane bound proteins are thought to comprise 30% of all proteins within the cell, playing a critical role in cellular activity [175]. Some enzymes such as cellulases, lysozymes, lipases, collagenases, amylases and receptor tyrosine kinases have also evolved to target, bind and react with chemicals localised to cellular interfaces [113, 125]. The prevalence of surfaces decorated with many different chemical functionalities in living cells, along with the abundance of surface active enzymes indicate that these natural systems take advantage of principles of heterogeneous catalysis in ways yet to be understood [34].

Due to several factors, homogeneous enzyme kinetics are a poor approximation of the kinetics of enzyme reactions at surfaces, as discussed in depth in Chapter 1. This is especially apparent in the case where aqueous enzymes act on surface bound reactants. Efforts to characterise the interfacial enzyme kinetics in this configuration usually employ an enzyme excess approach, where enzyme reaction rates are measured as a function of enzyme concentration at a fixed concentration of the surface bound reactant. This approach has been used to analyse the kinetics of nuclease cleavage of surface tethered DNA [115, 116], proteolytic cleavage of ovalbumin films [135], hydrolysis of insoluble cellulose by cellulase [117, 118, 139] and the lysis of peptides conjugated to the surface of quantum dots (QDs) by aqueous proteases [33, 110, 126], as described in Chapter 1. This “inverse” approach to enzyme kinetic analysis, compared to the conventional Michealis-Menten (MM) configuration is shown below in Figure 5.1.

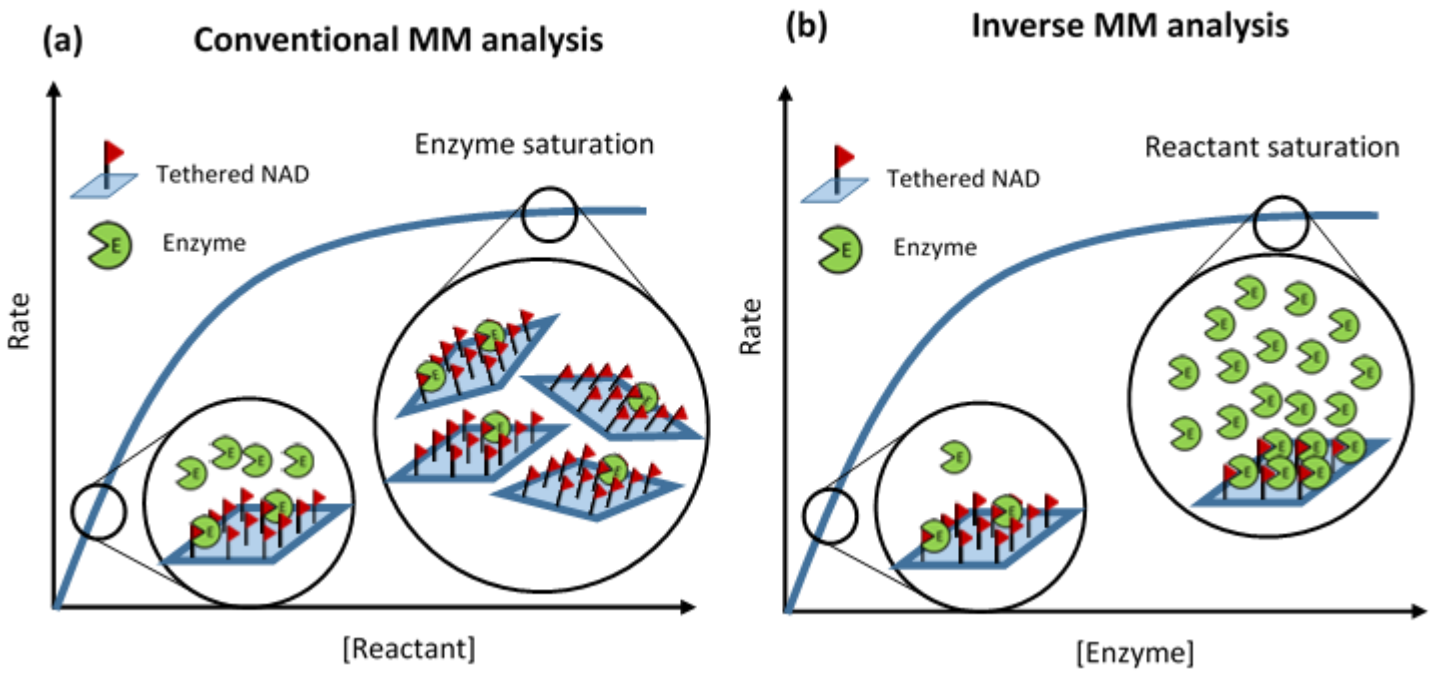

Figure 6.1: Comparison of (a) enzyme saturation by the reactant in the conventional Michaelis-Menten (MM) approach and (b) reactant saturation by the enzyme in the inverse approach where surface tethered NAD is the example reactant. In the conventional approach, the enzyme reaction rate (blue line) is measured as a function of reactant concentration resulting in saturation of the enzyme at high reactant concentrations. In the inverse configuration, enzyme reaction rates are measured as a function of enzyme concentration resulting in saturation of the reactant at high enzyme concentrations. Adapted from [117].

6.3 Kinetic Model

Several reports have explored the catalytic action of enzymes on surface tethered NAD as discussed in Chapter 1 [18, 41, 48, 50, 52-54, 72]. However, in order to develop efficient biotechnological applications of surface tethered NAD, the rate of enzyme reactions with the immobilised cofactor must be maximised. This can only be achieved by gaining a detailed kinetic understanding of the complexation and catalysis between enzymes and surface tethered NAD. Towards this, this chapter describes the kinetics of two different cofactor dependent enzymes acting on NAD tethered to the surface of SiNPs, characterised by a combination of Langmuir adsorption isotherm described in Chapter 5 and Michaelis-Menten kinetic concepts. Scheme 6.1 depicts the proposed mechanism of enzyme catalysis with surface tethered NAD. The first

step shows the adsorption equilibrium between freely diffusing enzyme in solution (E_{free}) and surface adsorbed enzyme (E*), Scheme 6.1(i). Surface adsorbed enzyme, for which there is a limited amount of surface adsorption sites (∗), depicted by the yellow area, then reversibly binds to surface tethered NAD (NAD) forming the surface-bound-enzyme/NAD-complex (ENAD*), Scheme 6.1(ii). Catalysis of the surface-bound-enzyme/NAD-complex reduces surface bound NAD to NADH Scheme 6.1(iii) which can then participate in the detection assay Scheme 6.1(iv). Applying a quasi-steady-state-assumption (QSSA) to the surface-bound-enzyme/NAD-complex and subsequently, the surface bound enzyme, allows the development of an expression for rate of surface enzymatic catalysis as a function of aqueous enzyme concentration. Fitting this interfacial rate expression with experimental data allows the kinetic rate constants for the processes depicted in Scheme 6.1 to be determined. Rate constants are then verified via integration of the mass balance equations by Euler's method against raw kinetic data.

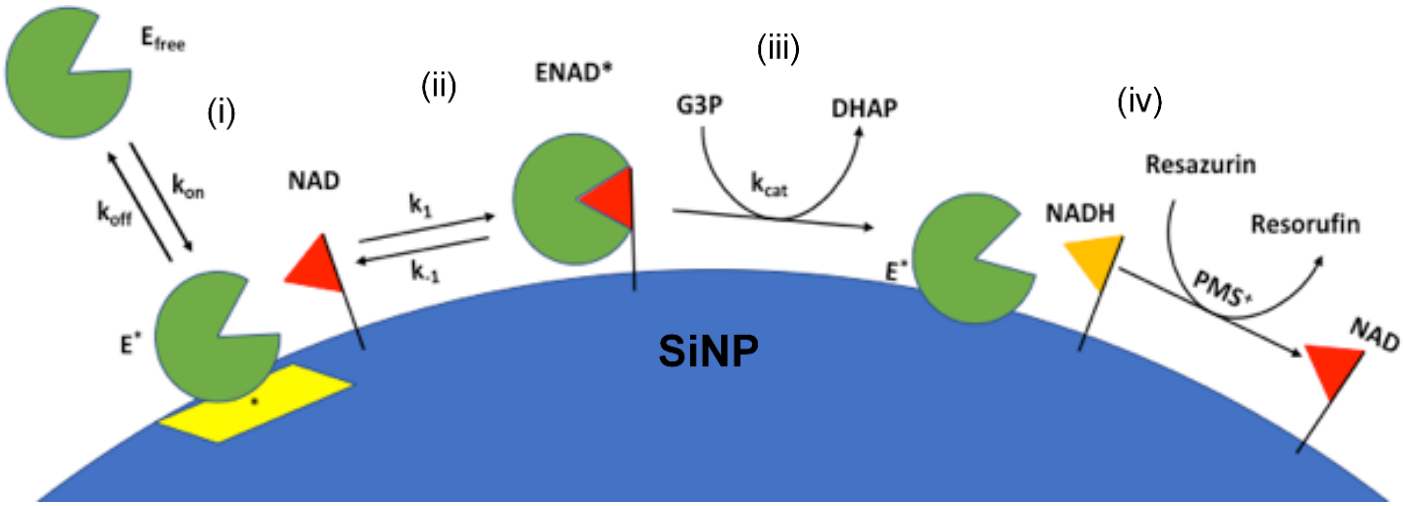

Scheme 6.1: Schematic of heterogeneous enzyme reaction with NAD tethered to the surface of SiNPs showing i) adsorption, ii) complexation, iii) surface catalysis and iv) regeneration of surface bound NAD by the resazurin/PMS^+ coupled assay.

This proposed kinetic model shown in Scheme 6.1 accounts for the adsorption of free enzyme onto the SiNP surface, complexation of the surface adsorbed enzyme with

NAD, surface catalytic reaction with decomplexation of enzyme surface NAD. Kinetic analysis of this model does not consider the rate of the PMS^+ mediated reaction of NADH with resazurin to form resorufin, which has been shown to have a second order rate constant of 180 M^{-1} s^{-1} under similar reaction conditions, which, as will be demonstrated, is several orders of magnitude greater than any rate constant determined in this study [176]. Thus, the fluorometric detection of resorufin produced in the resazurin/PMS^+ coupled assay is an accurate indicator of NADH formation and therefore an accurate measure of the enzyme reaction rate. The proposed kinetic model also does not consider the rate of the reversible binding of G3P and ethanol to EcG3PD and ADH respectively. This is because the concentration of these reactants in the assay systems (0.2 M G3P and ~3.5 M ethanol) are several orders of magnitude greater than any other reacting species. Thus, the diffusion and rate of complexation of these reactants to the surface adsorbed enzymes is assumed to not be a limiting factor in surface catalysed enzyme reactions.

6.3.1 Development of the mathematical kinetic model

In order to analyse the kinetics of the catalytic enzyme reaction with surface tethered NAD, a model has been developed combining Langmuir adsorption of the enzymes with QSS assumptions of the surface catalysed reaction. As discussed in Chapter 5, the first step in the reaction model is to determine the concentration of surface adsorbed enzyme (E*) onto an available surface site ($*$) on the nanoparticle surface based on the reversible adsorption of freely diffusing enzyme in solution (E_{free}), from Scheme 6.1(i).

$$E_{free} + * \underset{k_{off}}{\overset{k_{on}}{\rightleftharpoons}} E^* \tag{6.1}$$

In the next step, surface adsorbed enzyme reversibly complexes with tethered NAD (NAD) on the nanoparticle surface to form the surface-bound-enzyme/NAD-complex (ENAD*) Scheme 6.1 (ii).

$$E^* + NAD \underset{k_{-1}}{\overset{k_1}{\rightleftharpoons}} ENAD^* \quad (6.2)$$

Reaction can then occur at the surface, liberating product (P) with decomplexation of ENAD to E* and NADH which is regenerated to NAD in the resazurin/PMS^+ coupled assay Scheme 6.1 (iii-iv).

$$ENAD^* \overset{k_{cat}}{\rightarrow} P + E^* + NADH \quad (6.3)$$

The maximum amount of enzyme adsorption sites on the nanoparticle surface can be expressed by the following:

$$[*]_{max} = [*] + [E^*] + [ENAD^*] \quad (6.4)$$

Where $[*]_{max}$ is the total concentration of available adsorption sites for enzyme in the system.

The adsorption of enzyme onto the nanoparticle surface, complexation with surface bound NAD and catalytic formation of product and decomplexation of the surface-bound-enzyme/NAD-complex can be described with the following differential equations:

$$\frac{d[E^*]}{dt} = k_{on}[E_{free}]([*]_{max} - ([E^*] + [ENAD^*])) - k_{off}[E^*] - k_1[E^*][NAD] + k_{-1}[ENAD^*] \quad (6.5)$$

$$\frac{d[ENAD^*]}{dt} = k_1[E^*][NAD] - k_{-1}[ENAD^*] \quad (6.6)$$

$$\frac{d[P]}{dt} = k_{cat}[ENAD^*] \quad (6.7)$$

d[P]/dt provides the term for the change in product with time. When the change in product is constant, it is indicative of the establishment of a quasi-steady-state (QSS) where the concentration of surface-bound-enzyme/NAD-complex (ENAD*) remains constant with time, i.e.

$$\frac{d[ENAD^*]}{dt} = 0 \quad (6.8)$$

Consequently, the concentration of surface-bound-enzyme/NAD-complex is only constant when the surface enzyme concentration is also constant as described by Equation 6.9.

$$\frac{d[E^*]}{dt} = 0 \quad (6.9)$$

Thus, under a QSSA, Equations 6.5 to 6.7 yield the following rate expression representing the rate of product formation (v_0) at equilibrium adsorbed enzyme surface concentration as a function of the aqueous enzyme concentration:

$$\frac{d[P]}{dt} = v_0 = \frac{k_{cat}k_1[NAD][*]_{max}K_L[E_{free}]}{k_{-1} + K_L[E_{free}](k_{-1} + k_1[NAD])} \quad (6.10)$$

Note that K_l was defined in the Langmuir adsorption analysis in Chapter 5.

6.3.2 Measurement of enzyme reaction rates

The reaction rates of EcG3PD and ADH were characterised using the resazurin/PMS^+ coupled reaction described in Chapter 1. In the reaction, highly fluorescent resorufin is produced from the PMS^+ mediated reduction of resazurin by the NADH produced in the enzyme catalysed reaction, which is subsequently regenerated to NAD, as shown in Scheme 6.1(iv). Since NADH is regenerated to NAD within each catalytic/detection cycle, the reaction is not limited by the small concentration of NAD (≤ 1 μM) within the system and the reaction can continue until all resazurin, the limiting reagent, is depleted. This intrinsic NAD regeneration within the highly sensitive fluorometric detection assay becomes highly useful for two reasons.

(i) regeneration of NAD allows a QSS between NAD and NADH to be established, subsequently allowing the surface-tethered-enzyme/NAD-complex to form a QSS . This allows enzyme activity to be measured over extended time periods without depletion of the small concentration of NAD within each system. This allows more accurate determination of reaction rates at high enzyme concentrations, which would be difficult to accurately determine using techniques such as UV/Vis analysis of NADH formation, where most of the reaction is complete before analysis can be initiated.

(ii) Secondly, it allows detection of enzyme activity at extremely low enzyme concentrations since measurements can be obtained over extended periods of time, allowing resorufin concentration to accumulate to a detectable and quantifiable level. This allows accurate determination of reaction rates as a function of a large range of enzyme concentrations with small concentrations of NAD.

The relationship between fluorescence intensity and the concentration of resorufin, and thus NADH, produced in the coupled assay reaction is quantified using linear regression in the Appendix.

6.3.3 Approach to surface kinetic analysis

SiNPs with surface tethered N^6-linked-2AE-NAD as well as an equivalent amount of freely diffusing NAD under identical reaction conditions were applied to the EcG3PD and ADH catalysed reactions. Thiol terminated SiNPs had an average diameter of 98 nm with a surface attachment density of nonene-2AE-NAD of 0.5 attachments/nm^2.

Vinyl terminated SiNPs had an average diameter of 105 nm with a coverage of 0.5 attachments/nm^2 of SH-PEG_4-2AE-NAD. Although NAD surface coverage is relatively high, applying the large excess of NAD concentration that is required to satisfy the reactant stationary assumption of conventional Michaelis-Menten kinetic analysis in order to acquire the maximum enzyme velocity becomes exceedingly difficult to achieve. This is because, as the total concentration of NAD is increased within the system, so too is the total SiNP concentration, to a point where the SiNPs start to inhibit the enzyme catalysis as discussed later in Chapter 7. This limitation can be overcome by using an enzyme excess approach, where reaction rate is measured as a function of enzyme concentration at a fixed concentration of reactant [33, 110, 117, 126, 135]. In our kinetic analysis, EcG3PD reaction rates were measured as a function of excess EcG3PD concentrations while the total concentration of surface tethered NAD or free NAD within the system was held at 1 μM. Analogously, ADH reaction rates were measured as a function of excess ADH concentration with 0.5 μM surface tethered NAD or free NAD.

6.3.4 Measurement of surface kinetics under enzyme excess conditions

Application of different concentrations of EcG3PD and ADH to fixed concentrations of freely diffusing NAD (Figure 6.2(a) and Figure 6.3(a)) and surface tethered NAD (Figure 6.2(b-c) and Figure 6.3(b)) resulted in linear rates of NADH production over time, as measured by the resazurin/PMS^+ coupled reaction. This linear enzyme reaction rate indicates the establishment of a quasi-steady-state concentration of the surface-bound-enzyme-NAD complex on the particle surface, and analogously, the enzyme/NAD complex (ENAD) in solution. The reaction rate as a function of enzyme concentration for EcG3PD (Figure 6.2(d)) and for ADH (Figure 6.3(d), shows a linear increase in activity at low enzyme concentrations with each source of NAD. However, as the enzyme concentration is increased, a plateau in activity is reached, probably due to saturation of NAD with enzyme as depicted in Figure 5.1(b).

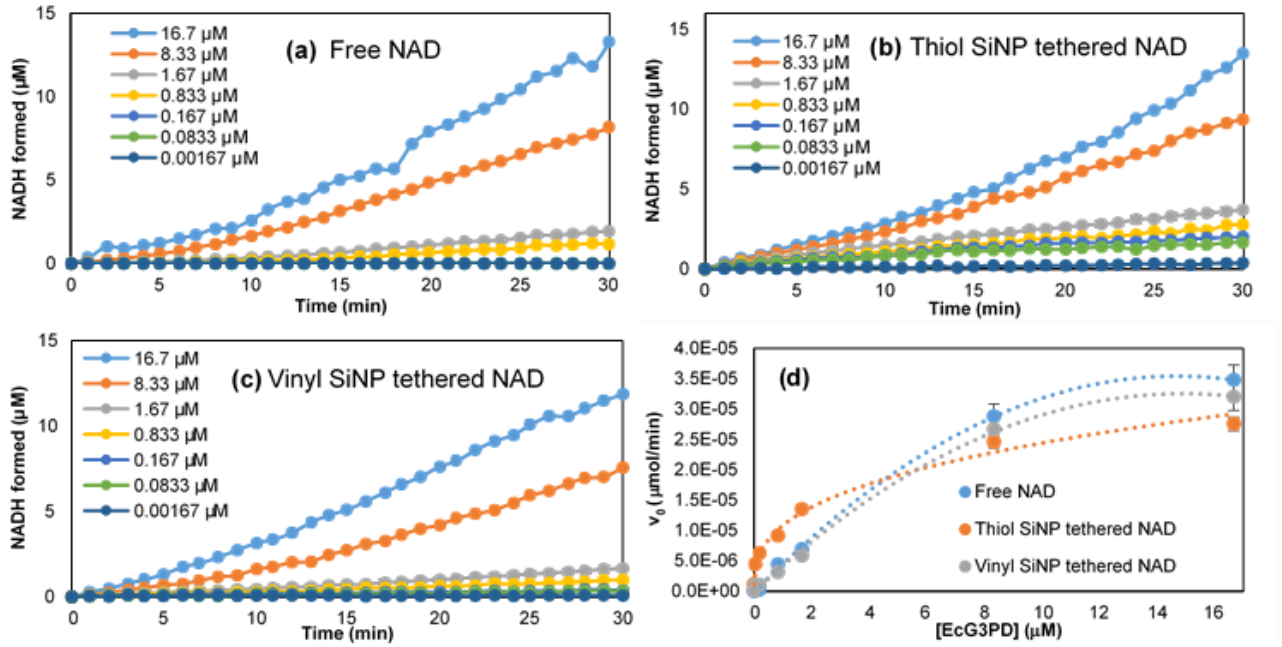

Figure 6.2: Total concentration of NADH formed with time in the resazurin/PMS$^+$ assay of the EcG3PD catalysed reaction at different EcG3PD concentrations with (a) free NAD, (b) thiol SiNP tethered NAD and (c) vinyl SiNP tethered NAD. The rates of NADH production with time are then plotted as a as a function of EcG3PD concentration (d).

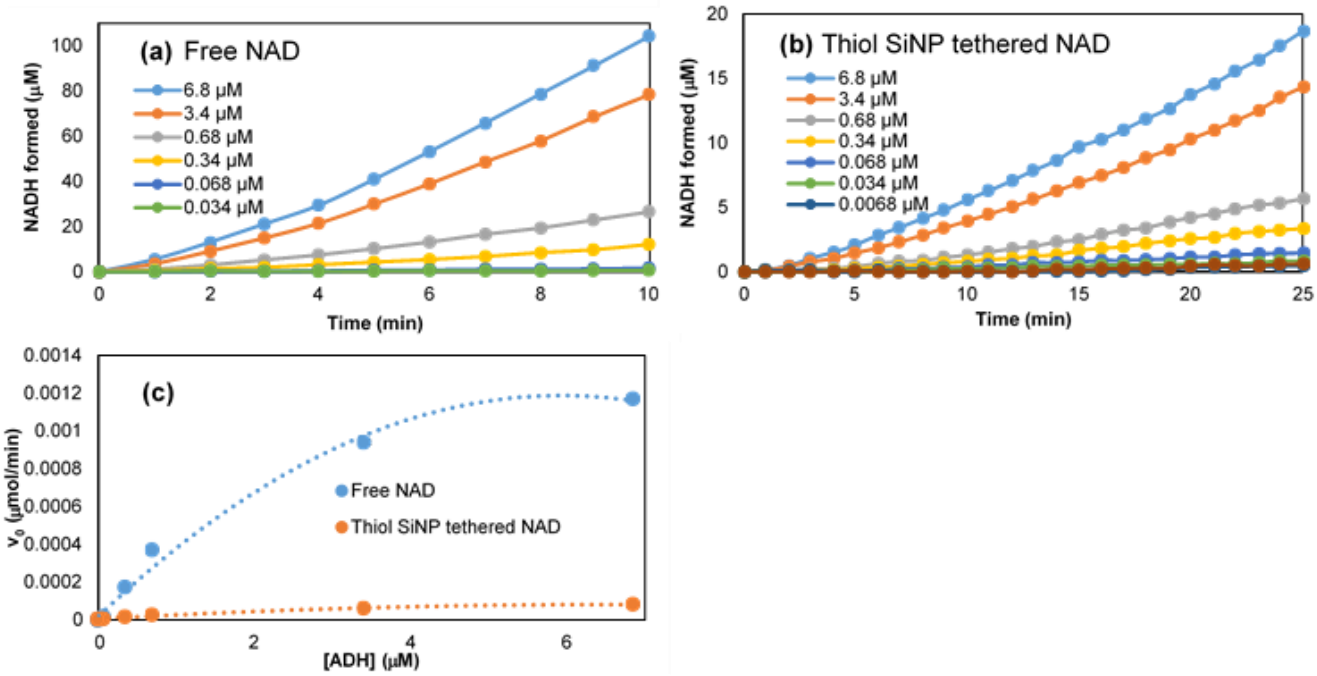

Figure 6.3: Total concentration of NADH formed with time in the resazurin/PMS$^+$ assay of the ADH catalysed reaction at different ADH concentrations with (a) free NAD, (b) thiol SiNP tethered NAD and the rates of NADH production with time are plotted as a as a function of ADH concentration (c).

EcG3PD activity with NAD tethered to the surface of thiol and vinyl terminated SiNPs was comparable to that with free NAD at higher concentrations examined in these Figures. At low concentrations, the reaction rate of EcG3PD with aqueous NAD goes to zero (undetectable) at EcG3PD concentrations below 0.167 μM, probably due to productive collisions between EcG3PD and aqueous NAD becoming increasingly diffusion limited in this range.

Significantly, at low concentrations of EcG3PD, higher reaction rates were observed for the thiol SiNPs compared to that of free NAD and NAD tethered to vinyl terminated SiNPs (Figure 6.2(d)). Adsorption analysis indicated that there are strong interactions between EcG3PD and thiol terminated SiNPs with tethered NAD which could facilitate the adsorption of EcG3PD onto the surface of thiol terminated SiNPs with tethered NAD at very low enzyme concentrations. Conversely, the much weaker interactions with vinyl terminated SiNPs with tethered NAD could explain the lower reaction rate.

ADH reaction rates with free NAD were significantly higher than that with NAD tethered to thiol terminated SiNPs. This is likely due to the weak interactions between ADH and the surface of thiol terminated SiNP with tethered NAD and the significantly lower surface adsorption capacity compared to EcG3PD, due to it's larger size. ADH showed little to no activity with NAD tethered to the surface of vinyl terminated SiNPs, with activity undetectable below 0.68 μM ADH. This is possibly due to even weaker interactions between ADH and the vinyl/NAD surface.

6.3.5 Kinetic analysis of the excess enzyme approach

Equation 6.10 predicts that the rate of product formation will increase linearly with enzyme concentration with an upper limit reached at high aqueous enzyme concentrations, as described by Langmuir adsorption. At this limit, the nanoparticle surface is saturated with enzyme and additional increase in enzyme concentration will not increase the surface enzyme concentration or corresponding surface-enzyme/NAD-complex concentration. At this point, the rate of surface enzyme

catalysis reaches an upper limit. Therefore, Equation 6.10 described the trends seen in the experimental kinetic data for surface tethered NAD.

6.3.6 Determination of kinetic constants

Therefore, Equation 6.10 can be fitted to the experimental kinetic data for EcG3PD in Figure 6.2(d) and ADH in Figure 6.3(c) to determine the values for k_{cat}, k_1 and k_{-1}. The values for these constants can then be compared with Euler integration of the mass balance equations for the processes described in equations 6.5 to 6.7, which also allows specific values for the adsorption constants, k_{on} and k_{off}, to be determined. For the free NAD system, kinetic data is fit to the inverse Michaelis-Menten Equation (6.11) which describes enzyme rate as a function of enzyme concentration at a fixed reactant concentration [117, 136].

$$\frac{d[P]}{dt} = \frac{k_{cat}[NAD]\left[E_{free}\right]}{\frac{k_{-1} + k_{cat}}{k_1} + \left[E_{free}\right]} \tag{6.11}$$

The values obtained from fitting the experimental data to Equation 6.10 for SiNP tethered NAD and Equation 6.11 for free NAD are specified in Table 6.1

Table 6.1: Kinetic rate constants of the EcG3PD and ADH catalysed reaction derived from Equation 6.10.

Enzyme	NAD source	k_{on} (μmol^{-1} min^{-1})	k_{off} (min^{-1})	K_L (μmol^{-1})	k_1 (μmol^{-1} min^{-1})	k_{-1} (min^{-1})	k_{cat} (min^{-1})
	Free NAD	N/A	N/A	N/A	631	0.0047	0.54
EcG3PD	Thiol SiNP tethered NAD	1450	0.033	44000	19361	0.076	8.0
	Vinyl SiNP tethered NAD	210	0.031	6800	26187	0.0431	13.6
ADH	Free NAD	N/A	N/A	N/A	132740	0.005	31.7
	Thiol SiNP tethered NAD	250	0.026	9700	29296	0.029	210

6.3.7 Kinetic modelling

In order to confirm the validity of the values of the rate constants determined by fitting Equation 6.10 to experimental data shown in Table 6.1, the reactions were simulated via kinetic modelling. Kinetic simulation allows the theoretical concentration of each species within the reaction to be examined over time to verify that the values of these kinetic constants are reasonable and accurately describe the reaction processes. It also allows the assumptions made in the construction of the kinetic expressions to be validated. Kinetic simulations were performed manually using Euler's method to integrate the mass balance equations for the reactions described in equations 6.5 to 6.7 of the kinetic model for each EcG3PD and ADH concentration with each NAD source. The simulated increase in product formation, i.e. the total quantity of NADH formation, were compared to the experimental values in order to verify the values of the rate constants as shown in the example simulations for each system in Figures 6.4-6.8.

6.3.7.1 Modelling of the EcG3PD reaction with free NAD

As shown in Figure 6.4(a-b), free NAD in solution rapidly complexes with aqueous EcG3PD to form the enzyme/NAD-complex within first 3 minutes of mixing, establishing a QSS where the enzyme/NAD-complex remains constant in concentration at ~0.5 μM. Thus, half of the total free NAD is participating in the reaction at the QSS. Complexation is governed by the forward second order rate constant k_1 which was determined to be 631 $\mu mol^{-1}\ min^{-1}$ and the reverse first order rate constant k_{-1} which was found to be 0.0047 min^{-1}. The enzyme/NAD-complex then catalyses the product formation step with reduction of NAD to NADH with subsequent decomplexation back into free enzyme and NADH. The rate of this step is dependent on the irreversible first order rate constant, k_{cat} which was determined to be 0.54 min^{-1}. This is also the rate limiting step of the reaction, typical of enzyme catalysed reactions. Figure 6.4(c) shows the simulated rate of product (NADH) formation which agrees well with the experimentally determined reaction trajectory.

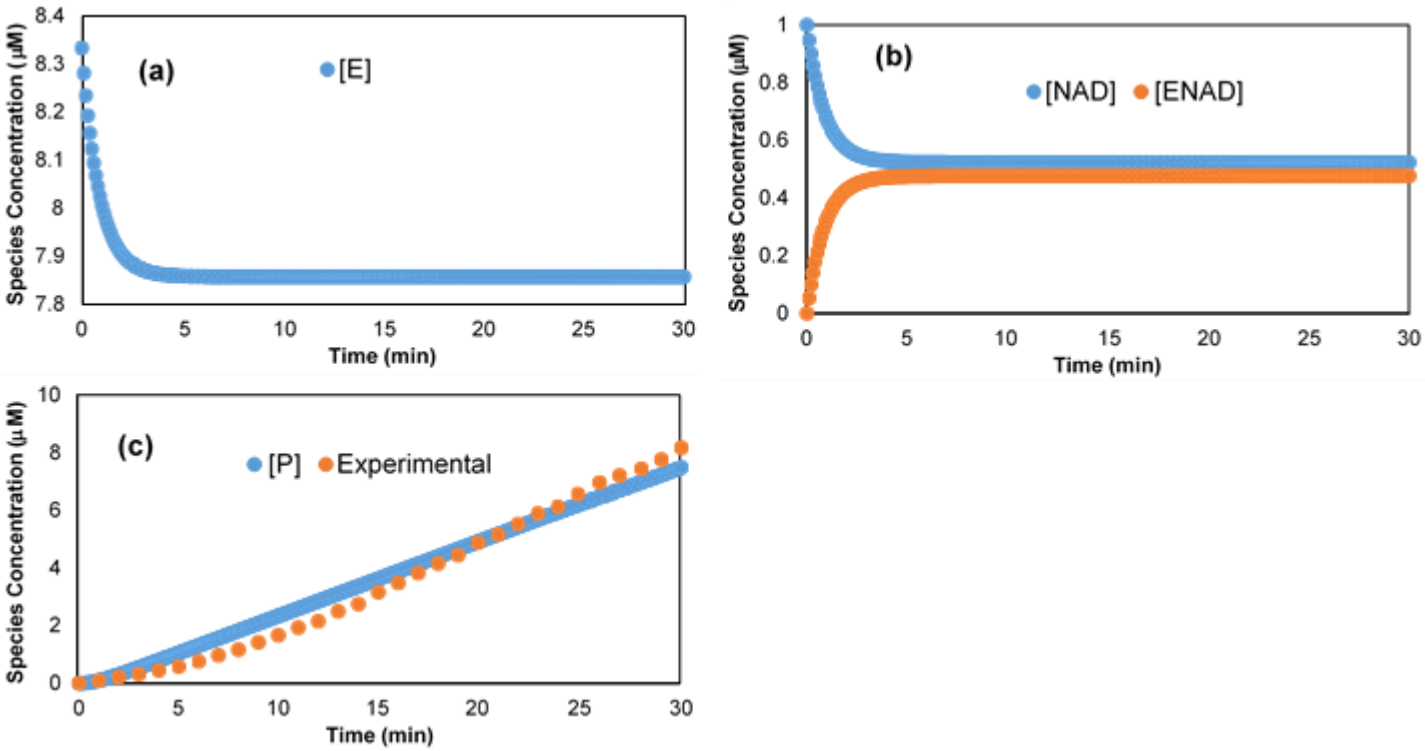

Figure 6.4: Kinetic simulation of the EcG3PD catalysed reaction with 1 μM free NAD and 8.33 μM EcG3PD showing the concentration of (a) free enzyme, (b) NAD and the enzyme/NAD-complex throughout the course of the reaction and (c) comparison of simulated and experimental reaction trajectories.

6.3.7.2 Modelling of the EcG3PD reaction with thiol SiNP tethered NAD

Langmuir adsorption analysis in Chapter 5 showed that the adsorption equilibrium of EcG3PD onto thiol terminated SiNPs with surface tethered NAD lies towards the adsorption of enzyme onto the available surface sites on the particle surface. Figure 6.5(a-b) shows that free enzyme is rapidly adsorbed onto the SiNP surface with all available surface sites being filled, establishing a steady state after 3 minutes. Kinetic simulation revealed the specific values for k_{on} and k_{off} to be 1450 μmol $^{-1}$ min^{-1} and 0.033 min^{-1}, respectively. Adsorbed enzyme E* then complexes with tethered NAD on the SiNP surface to form the surface-bound-enzyme/NAD-complex (Figure 6.5(c-d)). This results in a rapid decrease of un-complexed tethered NAD concentration and a sharp increase in surface-bound-enzyme/NAD-complex to 0.038 μM at QSS, below the calculated maximum value of 0.04 μM assuming a maximum of 0.02 EcG3PD/nm^2 can physically access the surface at any point in time. This step leans heavily towards the formation of the surface-bound-enzyme/NAD-complex with the second order rate constant k_1 found to be 19361 μmol^{-1} min^{-1} and the first order rate constant k_{-1} found

to be 0.076 min^{-1} in the reverse direction. This equates to a ~30 fold enhancement in the forward rate of complexation of surface adsorbed EcG3PD with surface tethered NAD compared to that of the free NAD system. Surface catalysis of the surface-bound-enzyme/NAD-complex catalytically releases product with decomplexation to surface bound enzyme and surface tethered NADH which then participates in the rapid resazurin/PMS coupled assay reaction. The rate of this enzymatic catalytic step was determined to be k_{cat} = 8.0, ~15 fold greater than that of the free NAD system. The simulated reaction rate was found to agree well with the experimental rates at 8.33 μM EcG3PD as shown in Figure 6.5(e).

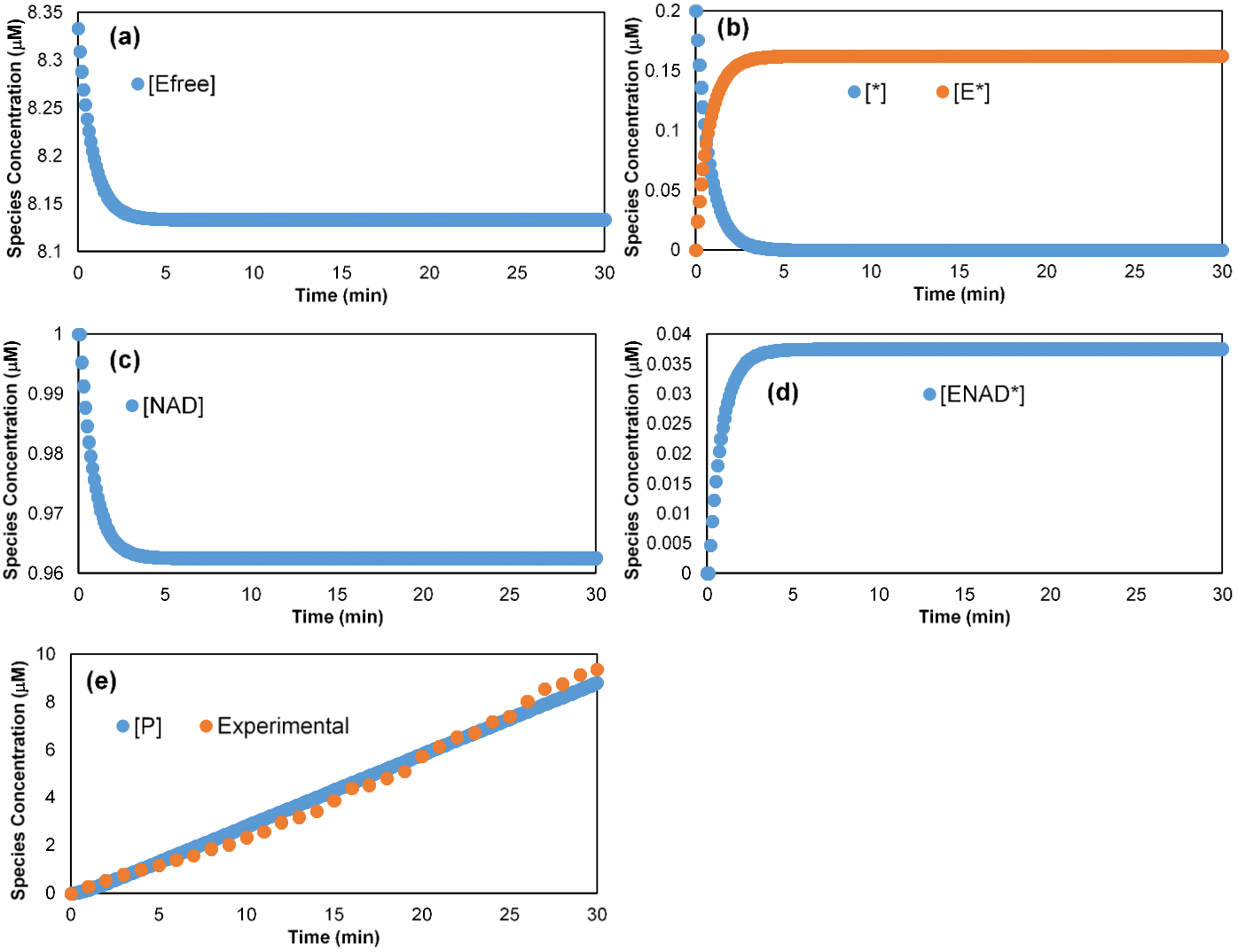

Figure 6.5: Kinetic simulation of the EcG3PD catalysed reaction with 1μM thiol SiNP tethered NAD and 8.33 μM EcG3PD showing the concentration of (a) free enzyme. (b) available surface sites and surface adsorbed enzyme, (c) surface tethered NAD and (d) surface-bound-enzyme/NAD-complex throughout the course of the reaction. comparing theoretical and experimentally determined reaction rates and (e) comparison of simulated and experimental reaction trajectories.

6.3.7.3 Modelling of the EcG3PD reaction with vinyl SiNP tethered NAD

In the case of the vinyl SiNP tethered NAD, Langmuir adsorption analysis of EcG3PD revealed much weaker adsorption than that of thiol SiNP tethered NAD. This is shown by the much slower adsorption of the enzyme onto the particle surface (Figure 6.6(a-b) with the second order rate constant k_{on} determined to be 210 μmol $^{-1}$ min^{-1} and the

first order reverse rate constant k_{off} found to be 0.031 min^{-1}. Surface adsorbed enzyme is rapidly complexed with surface tethered NAD (Figure 6.6(c-d)) with the second order rate constant k_1 found to be 26187 μmol^{-1} min^{-1} and the de-complexation first order rate constant k_{-1} found to be 0.0431 min^{-1}. Like the thiol SiNP tethered NAD system, a large enhancement (~40 fold) in the forward complexation reaction rate was observed compared to the free NAD system. At QSS the concentration of the surface-bound-enzyme/NAD-complex was 0.025 μM, about one third of that of the thiol SiNP tethered NAD reaction. The slow adsorption of enzyme, but rapid complexation with surface tethered NAD results in a very slow establishment of a QSS (~30 mins). This is evident in the lag period of activity over the first 15 to 20 minutes of enzyme reaction with the vinyl SiNP tethered NAD. This lag period was accurately modelled in our kinetic analysis (Figure 6.6(e)) with the first order rate constant of the enzymatic catalytic step determined to be k_{cat} = 13.6 min^{-1}, equating to a ~25 fold enhancement over the free NAD system.

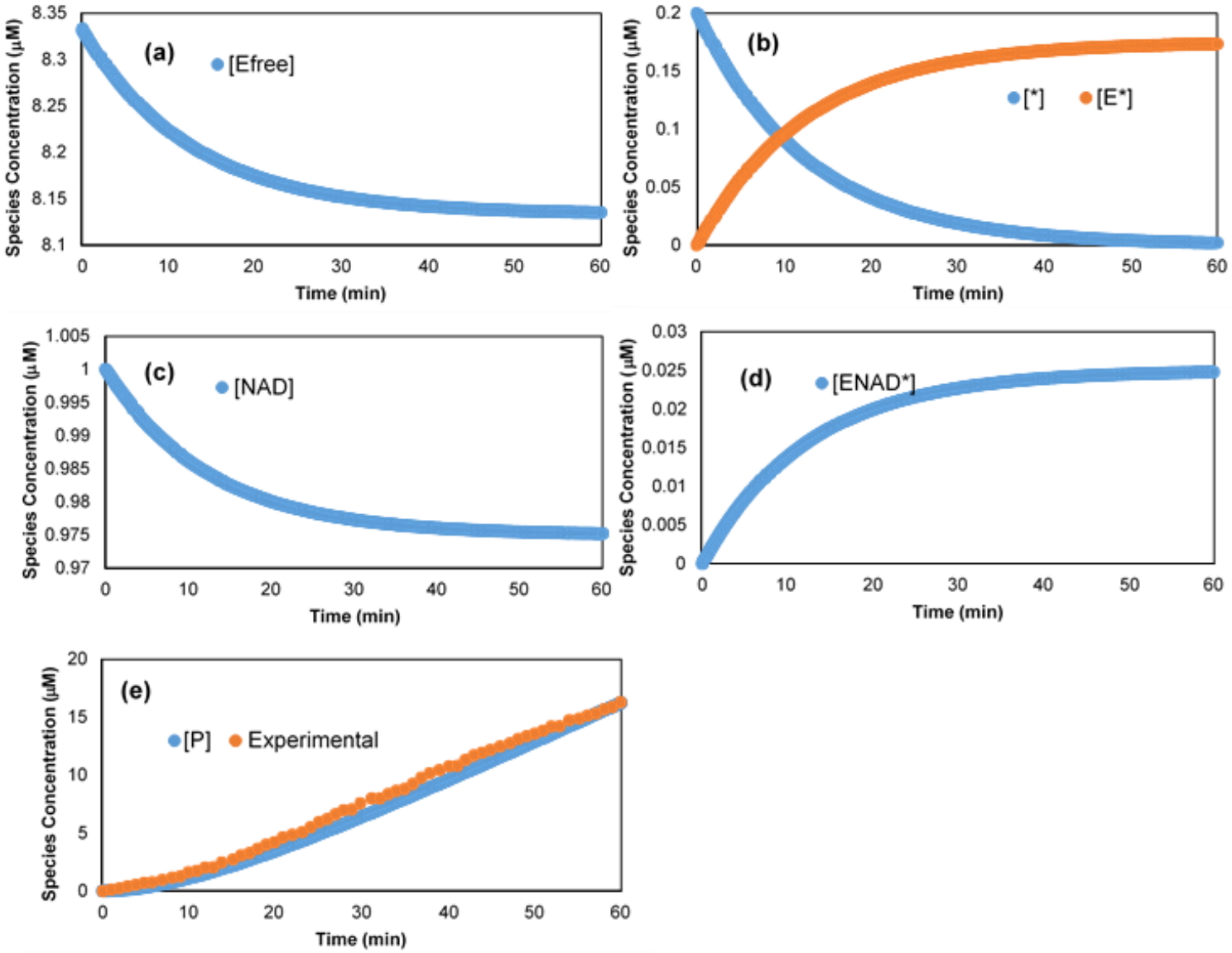

Figure 6.6: Kinetic simulation of the EcG3PD catalysed reaction with 1µM vinyl SiNP tethered NAD and 8.33 µM EcG3PD showing the concentration of (a) free enzyme. (b) available surface sites and surface adsorbed enzyme, (c) surface tethered NAD and (d) surface-bound-enzyme/NAD-complex throughout the course of the reaction. comparing theoretical and experimentally determined reaction rates and (e) comparison of simulated and experimental reaction trajectories.

6.3.7.4 Modelling of the ADH reaction with free NAD

Like EcG3PD, rapid complexation of aqueous ADH and aqueous NAD occurs within seconds of mixing as shown in the reaction simulation in Figure 6.7(a-b). NAD, ADH and the ADH/NAD complex (ENAD) exist in a dynamic QSS governed by the second order rate constant for complexation k_1 of 132740 $umol^{-1}$ min^{-1} and the de-

complexation first order rate constant of 0.005 min^{-1}. Reaction simulation reveals that almost all of the NAD present in the reaction exists as the ADH/NAD complex at any point in time after establishment of the QSS. Product is then formed by the high concentration of ADH/NAD complex, governed by the first order rate constant k_{cat} which was found to be 31.7 min^{-1}. The formation of product with time in the reaction simulation was found to agree well with the experimentally measured reaction rate as shown in Figure 6.7(c).

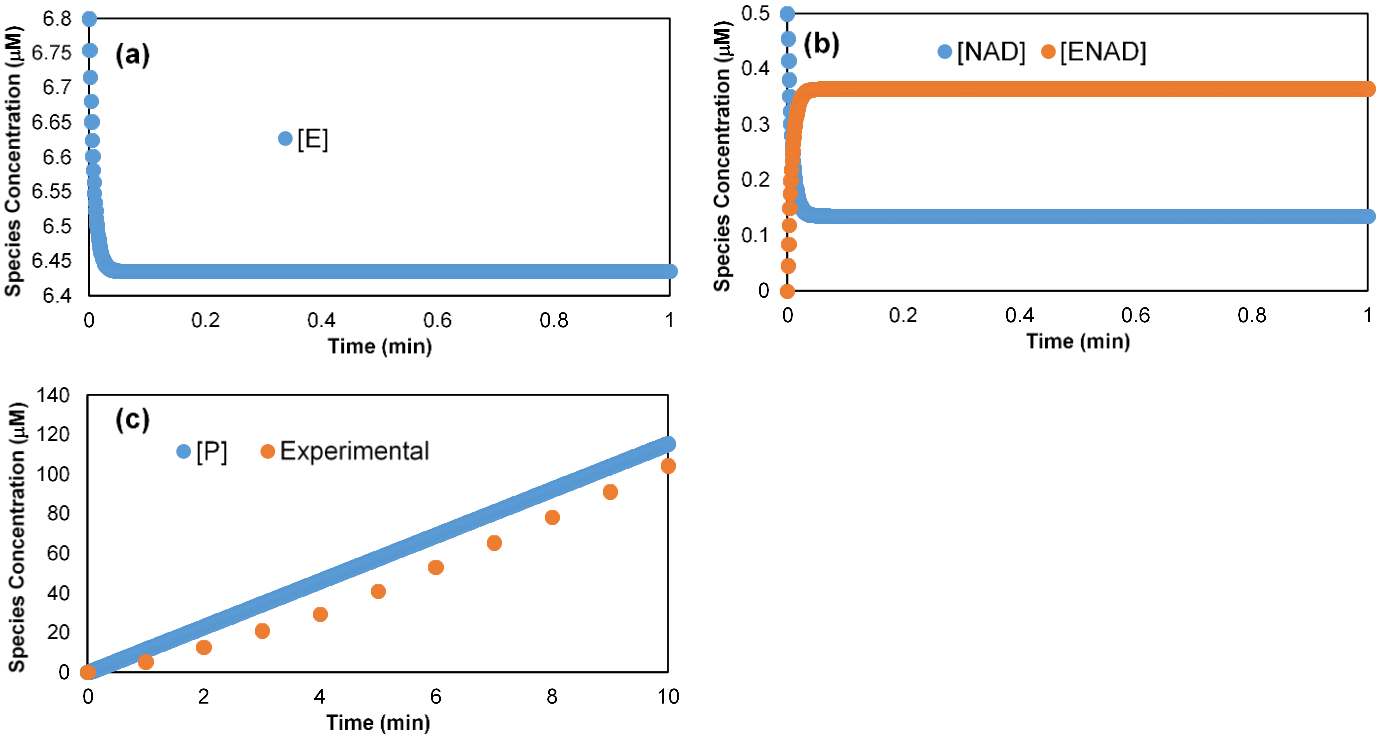

Figure 6.7: Kinetic simulation of the ADH catalysed reaction with 0.5 μM free NAD and 6.8 μM ADH showing the concentration a) free enzyme, (b) NAD and the enzyme/NAD-complex throughout the course of the reaction and (c) comparison of simulated and experimental reaction trajectories. Note that (a) and (b) are on a 1 minute time scale while (c) is on a 10 minute scale.

6.3.7.5 Modelling of the ADH reaction with thiol SiNP tethered NAD

Langmuir adsorption analysis of ADH onto the surface of thiol terminated SiNPs with tethered NAD revealed adsorption to be significantly less favourable than that of EcG3PD, suggesting much lower attractive forces between ADH and the SiNP surface. This is shown in the reaction simulation in Figure 6.8(a-c) where ADH adsorption on the particle surface takes ~20 minutes to reach equilibrium compared

to 3 minutes for a similar concentration of EcG3PD. The model predicts that all available ADH adsorption sites are filled once equilibrium is reached at this ADH concentration. Kinetic simulation revealed the specific values for k_{on} and k_{off} to be 250 μmol^{-1} min^{-1} and 0.026 min^{-1}, respectively. Adsorbed ADH then complexes with tethered NAD on the SiNP surface to form the surface-bound-enzyme/NAD-complex Figure 6.8(d-e). The rate of this complexation step was determined to be similar to that of EcG3PD, with the second order rate constant for complexation k_1 found to be 29296 μmol^{-1} min^{-1} and the first order de-complexation rate constant k_{-1} found to be 0.026 min^{-1}. Since the rate of ADH complexation is far more rapid than ADH adsorption, the QSS lies heavily in favour of surface bound enzyme-NAD-complex formation with a predicted concentration of ~0.0048 μM approaching the theoretically calculated maximum of 0.005 μM, assuming a maximum of 0.005 ADH/nm^2 can physically access the surface at any point in time as discussed in Chapter 5. This accounts for the rapid decrease in surface adsorbed ADH after ~2.5 minutes of reaction as it is rapidly complexed with surface tethered NAD. An extremely high rate of surface catalysis was determined for ADH with the first order rate constant k_{cat} found to be 210 min^{-1}, seven times greater than that of the free system. Using rate constants derived from Equation 13, the simulated reaction rate agreed well with the experimentally measured rate as shown in Figure 6.8(f). As with the EcG3PD reaction with vinyl SiNP tethered NAD, the model accounts for the initial lag in the reaction as a QSS is established.

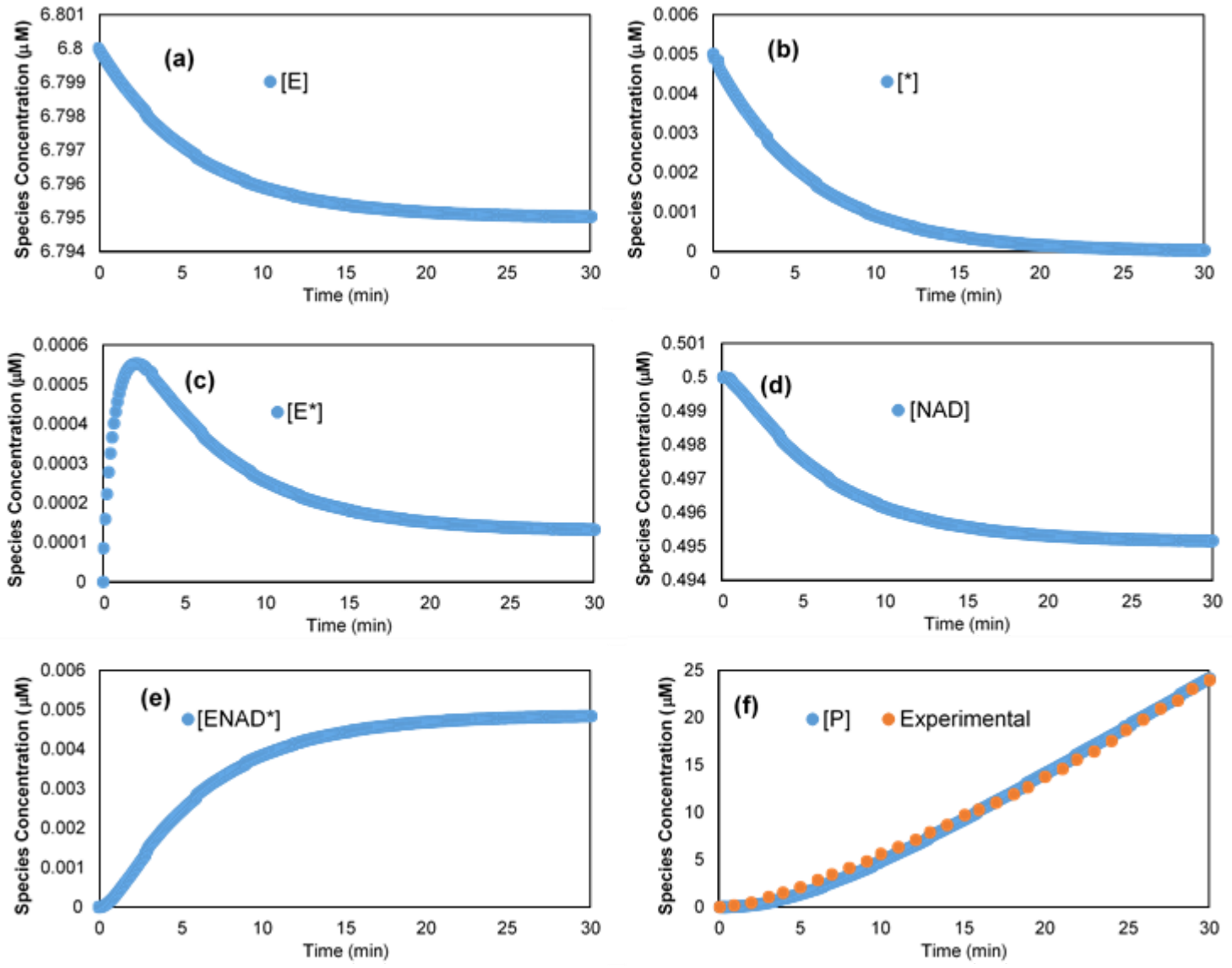

Figure 6.8: Kinetic simulation of the ADH catalysed reaction with 0.5 µM thiol SiNP tethered NAD and 6.8 µM ADH showing the concentration of (a) free enzyme. (b) available surface sites (c) surface adsorbed enzyme, (d) surface tethered NAD and (e) surface-bound-enzyme/NAD-complex throughout the course of the reaction. comparing theoretical and experimentally determined reaction rates and (f) comparison of simulated and experimental reaction trajectories.

6.4 Discussion

Analysis of kinetic data of the enzyme reactions with free and surface tethered NAD has revealed a linear increase in the formation of fluorometrically detected resorufin with time, as a result of the continuous cycling of NAD to NADH within the coupled reaction system. This confirms the establishment of a QSS of the surface-bound-enzyme/NAD-complex. Since a dynamic equilibrium exists between aqueous and

adsorbed enzyme on the SiNP surface, a QSS can also be simultaneously applied to the adsorbed enzyme. Applying the reactant stationary assumption to the freely diffusing enzyme allows Equation 6.10 to be developed, combining Langmuir adsorption kinetics with classical enzyme kinetic principals into a single rate expression. Fitting Equation 6.10 to the enzyme reaction rates with tethered NAD experimentally determined at different enzyme concentrations gave estimates for the various kinetic rate constants. The values of the calculated rate constants were then verified using kinetic simulation of the reaction model. Enhancement in the rate of enzyme catalysis on the surface tethered NAD was observed compared to equivalent amounts of aqueous NAD in both the EcG3PD and ADH reaction systems. Surface adsorbed EcG3PD was found to rapidly complex with tethered NAD, with a 1.9 fold enhancement in complexation rate (k_1/k_{-1}) with NAD tethered to thiol terminated SiNPs and a 2.4 fold enhancement with the vinyl terminated SiNP platform. Catalysis rates (k_{cat}) were similarly enhanced with a 14 fold enhancement observed when EcG3PD reacted with NAD tethered to thiol terminated SiNPs and a 25 fold enhancement with NAD tethered to vinyl terminated SiNPs. ADH, however, showed a 26 fold decrease in the rate of complexation with NAD tethered to the surface of thiol terminated SiNPs compared to an equivalent amount of freely diffusing NAD, but did show a 7 fold enhancement in catalytic rate. These changes in the kinetic processes are tabulated in Table 6.2 below.

Table 6.2: Changes in the rate of complexation and catalysis of EcG3PD with NAD tethered to the surface of SiNPs compared to that of freely diffusing NAD.

		Enhancement/Reduction (fold)	
Enzyme	NAD source	Complexation (k_1/k_{-1})	Catalysis (k_{cat})
EcG3PD	Thiol SiNP tethered NAD	1.9	14
	Vinyl SiNP tethered NAD	2.4	25
ADH	Thiol SiNP tethered NAD	-26	7

Catalytic rate enhancement with enzymes acting on surface tethered reactants, compared to the aqueous reactants, have been recently observed [4, 33, 110, 126,

140]. Although the exact enhancement mechanisms within these studies remain to be fully characterised, they can be attributed to several critical factors. Co-localisation of the enzyme with high concentrations of reactant at the nanoparticle interface, thus saturating the enzyme with localised reactant, is thought to be the general underlying mechanism of enhancement. Interfacial characteristics such as charge, configuration of surface reactant and attractive forces between the enzyme and surface are responsible for fine tuning of the surface enzyme activity [4, 33, 110, 126, 140]. In order to help explain the differences in catalytic rate enhancement of EcG3PD and ADH with NAD tethered to thiol and vinyl terminated SiNP surfaces, physiochemical properties such as the structure and surface chemistry of both enzymes and the SiNP surface must therefore be considered. These factors were investigated using a combination of molecular dynamic (MD) simulations and experimental data.

6.4.1 Proposal of enhancement mechanism

Due to the positively charged surface region surrounding the active sites it is likely that EcG3PD will orientate with this positive face adjacent to the negatively charged SiNP surface with strong electrostatic interactions as shown schematically in Figure 6.9. This is a favourable adsorption orientation as the NAD binding sites should face the NAD tethered to the SiNP surface. However, the strength of the electrostatic attraction between the positively charged NAD binding face of the enzyme and negatively charged SiNP surface may hinder the reaction for two reasons.

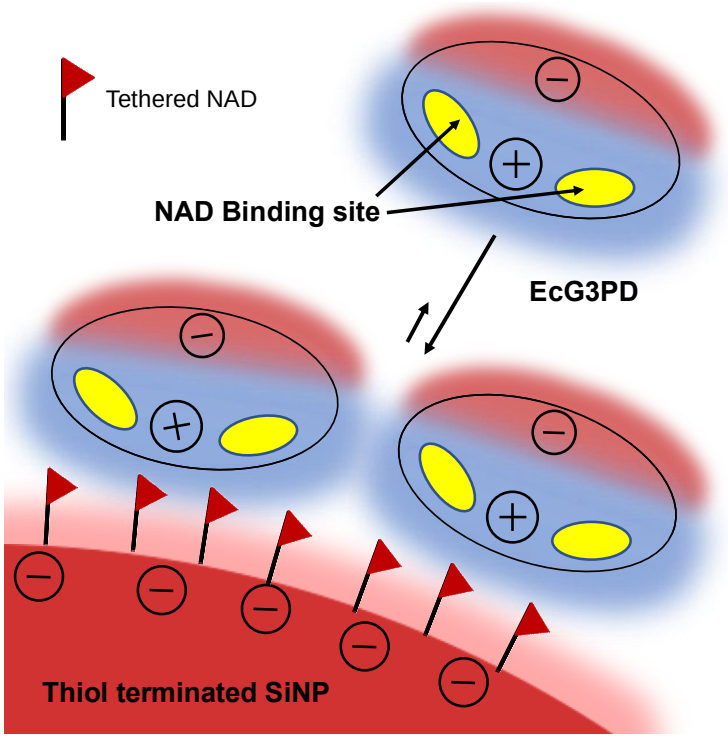

Figure 6.9: Proposed adsorption orientation of EcG3PD onto the thiol terminated SiNP surface with tethered NAD

Firstly, the opposing charges of each face of EcG3PD may facilitate strong protein-protein electrostatic interactions, resulting in stacking of the enzyme on the particle surface, as shown in Figure 6.10. This can block or hinder the diffusion of other reactants such as G3P, DHAP, resazurin, PMS^+ and resorufin to and from the reaction vicinity. Stacking and multilayer formation of EcG3PD due to these protein-protein electrostatic interactions is a probable cause of the high adsorption capacity observed with EcG3PD in the Langmuir adsorption analysis. Hindered diffusion of reactants to and from the surface due to multi-layer formation of EcG3PD may also explain the lower reaction rate of EcG3PD with NAD tethered to thiol terminated SiNPs at high EcG3PD concentrations, as shown in Figure 6.2(d), compared to vinyl SiNP tethered NAD and free NAD.

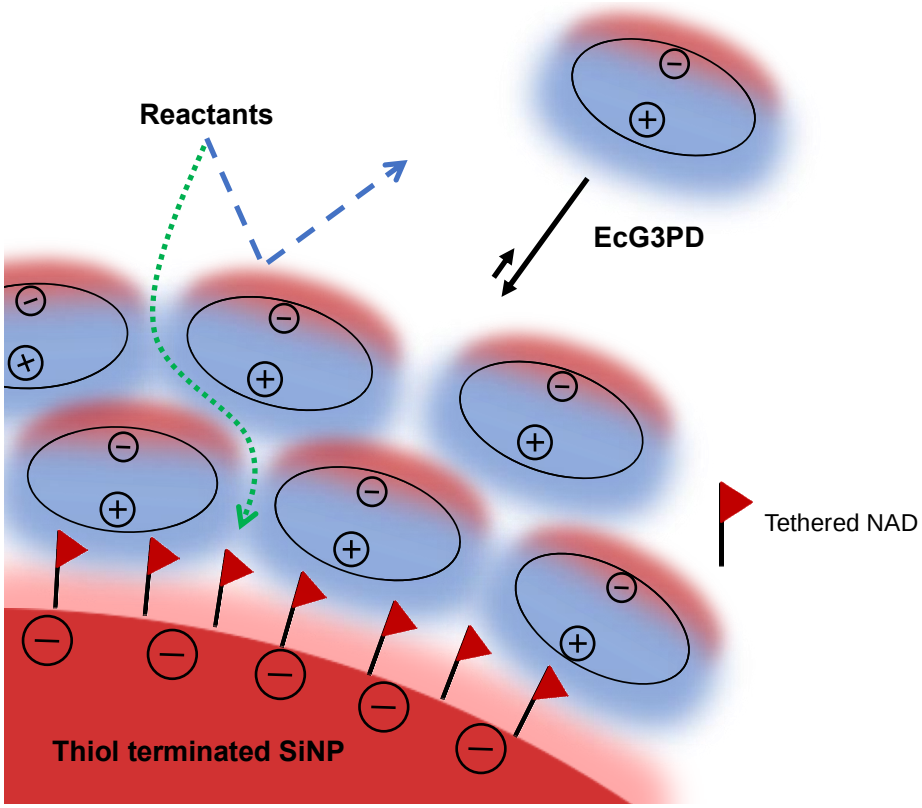

Figure 6.10: Schematic of proposed model of EcG3PD stacking due to strong protein-protein electrostatic interactions resulting in the blocking (blue dashed arrow) or hindered diffusion (green dotted arrow) of reactants such as G3P, resazurin and PMS^+ to and from the active particle surface.

Secondly, strong electrostatic attraction between EcG3PD and the thiol terminated SiNP surface with tethered NAD may hinder the lateral movement of the enzyme across the nanoparticle surface as shown in Figure 6.11. This may explain the reduced rate of surface NAD complexation (k_1) and catalysis (k_{cat}) of EcG3PD with NAD tethered to thiol terminated SiNP than with NAD tethered to vinyl terminated SiNPs, as shown in Table 6.1. Less electrostatic attraction between EcG3PD and the vinyl terminated SiNP surface may facilitate more rapid lateral movement of the enzyme across the particle surface (Figure 6.12) such as in the enzyme 'hopping' model previously proposed for enzymes acting on surface reactants [33, 110, 126, 133]. This may explain the increased rate of surface NAD complexation and catalysis of EcG3PD with NAD tethered to vinyl terminated SiNP. In the ADH system, weak electrostatic interactions also existed between the enzyme and particle surface, resulting in slow adsorption but extremely rapid complexation, catalysis and re-complexation as indicated by the rate constants determined for these processes in Table 6.1 and

simulated in Figure 6.8. This is shown schematically in Figure 6.11. A similar phenomena was observed by Wu *et al.* [110]. In their work, described in detail in Chapter 1, the least amount of surface proteolytic enzyme activity was observed with the protease, thrombin, which was shown to strongly adsorb to QD surfaces capped with negatively charged ligands through two anion binding exo-sites [110]. The surface proteolytic activity of thrombin was found to increase when the QD surface was capped with zwitterions, which showed less adsorption due to the restriction of non-specific protein adsorption [110]. The greatest amount of surface proteolytic activity was observed with the enzyme trypsin which had a net negative surface charge and displayed weak adsorption interactions with the terminal negative charge of the zwitterionic QD surfaces. Like thrombin, trypsin showed the greatest activity with the zwitterionic surfaces, with kinetic enhancement in the specificity constant (k_{cat}/K_M) reaching up to 80 fold over that of the free reactant system [110]. Comparatively, in this work, the specificity constant of the EcG3PD reaction with NAD tethered to vinyl terminated SiNPs is enhanced by 40 fold compared to free NAD.

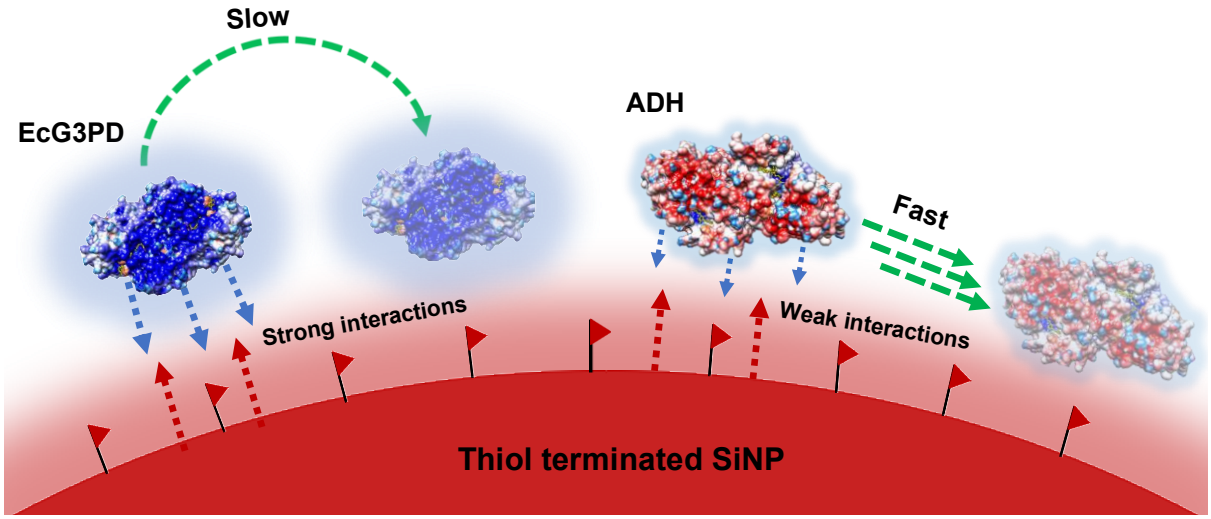

Figure 6.11: Schematic of the slow lateral movement of EcG3PD across the thiol terminated SiNP surface with tethered NAD due to strong electrostatic interactions (a) and fast lateral movement of ADH due to much weaker electrostatic interactions (b).

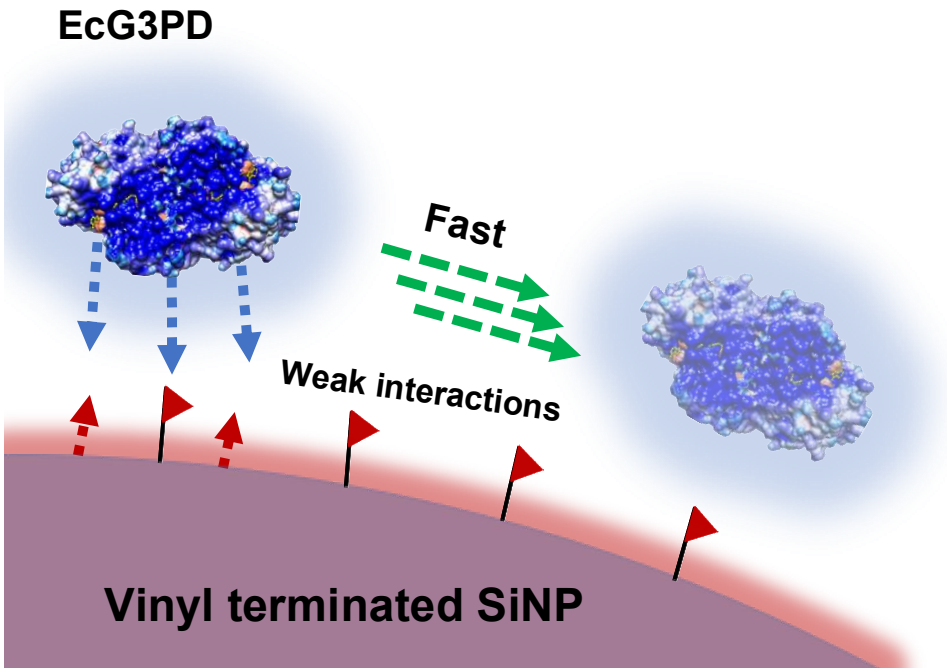

Figure 6.12: Schematic of the rapid lateral movement of EcG3PD across the vinyl terminated SiNP surface with tethered NAD due to weak electrostatic interactions.

The kinetic enhancement of catalytic enzyme activity observed with SiNP tethered NAD compared to freely diffusing NAD is likely due to adsorption of the enzyme to a high density of NAD localised to the SiNP surface. The enzyme can then rapidly complex, perform its catalytic function and re-complex with the high concentration of NAD localised to the SiNP surface, eliminating diffusion limitations experienced by an equivalent concentration of NAD and enzyme freely diffusing in solution. The rate and strength of the reversible surface adsorption and complexation of the enzyme to the tethered NAD surface has been shown to be strongly dependent on the correlation between the surface properties of the platform material and enzyme.

6.5 Conclusion

NAD tethered to the surface of thiol and vinyl terminated SiNPs has been applied to the catalytic reactions of the oxidoreductase enzymes, EcG3PD and ADH, and kinetic profiles obtained by varying the concentration of the enzymes. A kinetic model combinig Langmuir adsorption of the enzymes onto the SiNP surfaces, discussed in Chapter 5, and classical Michaelis-Menten Briggs-Haldane kinetic concepts was derived. Fitting experimental data to the derived rate expression allowed determination

of the critical kinetic constants describing complexation of the enzyme with surface tethered NAD (k_1), decomplexation (k_{-1}) and surface catalysis (k_{cat}). Kinetic simulations confirmed the validity of the derived kinetic constants, which indicated an enhancement in the rate of surface catalysis of EcG3PD and ADH compared to equivalent concentrations of freely diffusing NAD. Catalytic rates were found to be enhanced with SiNP tethered NAD up to ~2.4 fold for complexation and ~25 fold for catalysis. Kinetic analysis, along with molecular dynamic simulation of the interfacial interactions between the NAD/SiNP surface and enzymes revealed a combination of tuneable factors giving rise to the observed kinetic enhancement. These factors included the strength of the electrostatic attraction or repulsion between the enzymes and SiNP surface functionality, the enzyme size, adsorption orientation and protein-protein interactions.

CHAPTER 7 : SURFACE CATALYSIS KINETICS OF TETHERED NAD: AN EXCESS REACTANT APPROACH

7.1 Overview

This chapter explores the surface enzyme kinetics of the EcG3PD reaction with surface tethered NAD via an excess NAD approach, as opposed to the excess enzyme approach in Chapter 6. Increasing NAD (and hence SiNP) concentration resulted in inhibition of the enzyme reaction. In order to account for this, a competitive mechanism of enzyme inhibition is proposed, resulting from adsorption of the enzyme in non-productive conformations, restricting access of reactants and tethered NAD to the active site, attenuating the surface complexation kinetics. A kinetic rate expression is derived relating the rate of surface enzyme catalysis with surface tethered NAD to the total concentration of available surface adsorption sites and an equilibrium constant for the non-productive adsorption of enzyme onto the particle surface (inhibition). In order to gain an estimate for this inhibition constant, the inhibition of EcG3PD by plain thiol and vinyl terminated SiNPs with freely diffusing NAD is used as model system. Applying the derived 'free NAD' rate constants to kinetic analysis of EcG3PD measured under NAD excess conditions with NAD tethered to the surface of thiol and vinyl terminated SiNP produced kinetic rate constants that were similar to those derived using the enzyme excess approach to interfacial enzyme kinetics analysis. In order to reduce the inhibitory effects caused by the strong electrostatic interactions between EcG3PD and the thiol terminated SiNP surface with tethered NAD, the residual surface thiol groups on the particle surface were chemically 'capped' with several different common alkylating agents. Covalent capping of thiols was found to significantly reduce inhibition of the EcG3PD catalysed reaction with surface tethered NAD due to the reduction in non-productive adsorption of EcG3PD due to a reduction in the electrostatic interactions between the enzyme and particle surface.

7.2 Introduction

In Chapters 5 and 6 it was assumed that all adsorption of enzyme to the SiNP surface, as determined by Langmuir adsorption analysis, resulted in the enzyme adsorbing in a productive orientation. However, non-specific binding of proteins to the surface of nanoparticles can lead to deactivation or inhibition of the enzyme due to adsorption orientations that block reactant from accessing the active site, or orientations that lead to conformational changes of the enzyme modifying this function [110, 111, 118, 139]. This is essentially a form of competitive enzyme inhibition. High concentrations of nanoparticle support materials in solution have been shown to act as competitive inhibitors. [110, 111]. This is especially common in the breakdown of insoluble cellulose by cellulase, where surface adsorption of cellulase often results in non-productive binding, leading to enzyme inhibition [118, 139]. For this reason, in Chapter 6, the interfacial enzyme kinetics of the catalysis of surface tethered NAD was measured at very low NAD (and hence particle) concentration, and the enzyme concentration varied to an excess amount.

In this chapter we investigate the kinetics of the interfacial catalysis of EcG3PD with NAD tethered to the surface of SiNPs as a function of tethered NAD concentration. As the concentration of tethered NAD is increased, so too is the SiNP support concentration. High concentrations of SiNPs in the system lead to an unexpected rapid plateau in EcG3PD activity, especially in the case of thiol SiNPs. This observed inhibition is assumed to be due to adsorption of EcG3PD in non-productive conformations leading to enzyme deactivation. A method is then proposed in order to account for this inhibitory effect, where enzyme inhibition by thiol and vinyl SiNPs is investigated and an equilibrium inhibition constant (K_i) derived for each particle species. The interfacial rate equation derived in Chapter 6 is expanded to include this inhibition constant, accounting for the enzyme inhibition by the SiNPs. This expression describing the enzyme reaction rate with enzyme inhibition by non-productive adsorption is then fitted to kinetic data for EcG3PD when the SiNP tethered NAD concentration is varied in order to extract rate constants. These rate constants are then compared to those determined in Chapter 6. Lastly, chemical modification of the residual surface thiol groups with small alkylating agents is shown to reduce inhibitory

effects on the EcG3PD surface catalysed reaction with high tethered NAD concentrations.

7.3 Kinetic model of enzyme inhibition by non-productive binding

Figure 7.1 shows a schematic of the adsorption of enzyme onto the particle surface resulting in a productive and non-productive (inhibited) orientation. Although there are other mechanisms of enzyme inhibition by the addition of nanoparticles such as an increase in mass transfer resistance as a result of the increasing solid to liquid mass ratio, this model assumes that all inhibition observed in the kinetic analysis is due to non-productive binding of the enzyme to the particle surface [48].

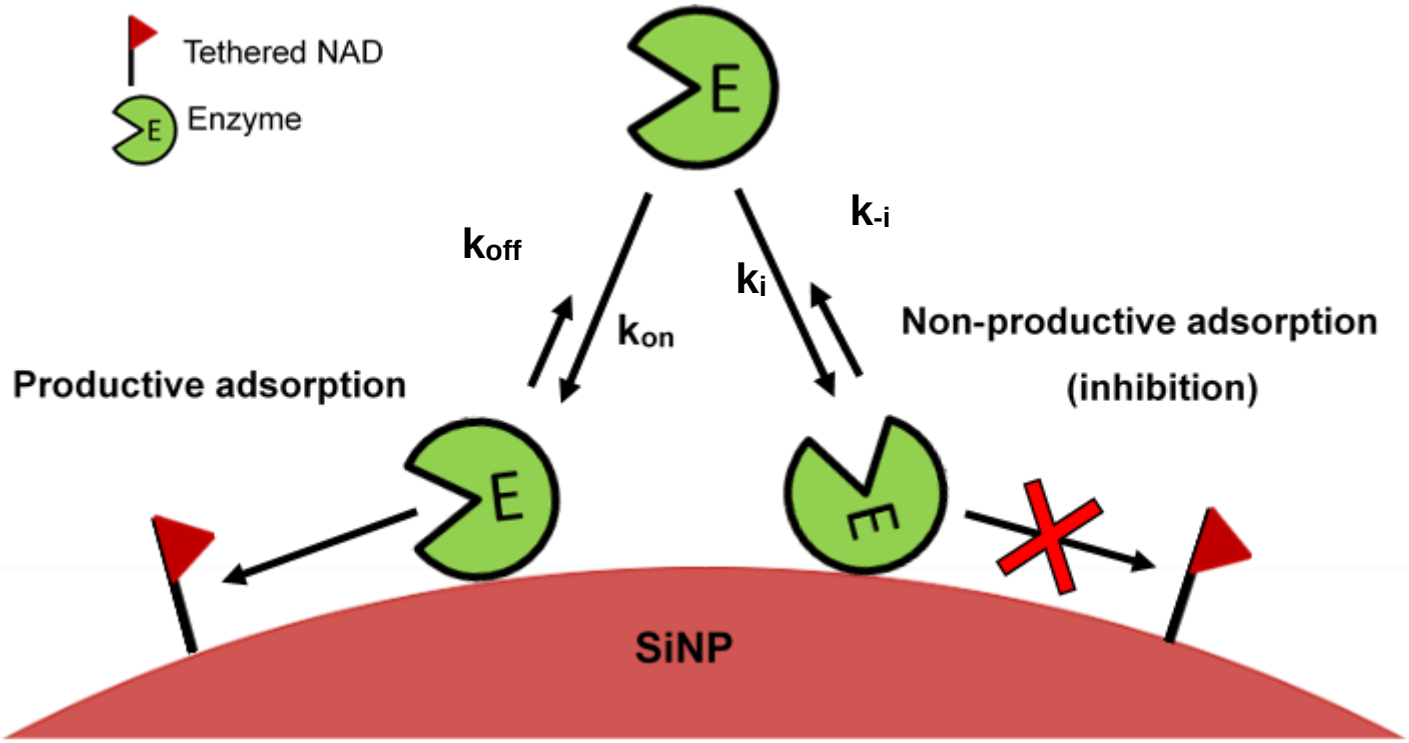

Figure 7.1: Schematic of enzyme adsorption leading to productive and non-productive (inhibited) orientations.

7.3.1 Development of the mathematical model

In Chapter 6 the following interfacial enzyme reaction model was proposed:

$$E_{free} + * \underset{k_{off}}{\overset{k_{on}}{\rightleftharpoons}} E^* + NAD \underset{k_{-1}}{\overset{k_1}{\rightleftharpoons}} ENAD^* \xrightarrow{k_{cat}} P + E^* + NADH \quad (7.1)$$

Addition of competitive inhibition of enzyme by SiNP surface adsorption as depicted in Figure 7.1 is as follows:

$$E_{free} + * \underset{k_{-i}}{\overset{k_i}{\rightleftharpoons}} EI^* \quad (7.2)$$

Where $*$ is a free surface adsorption site and *EI** is the inhibited adsorbed enzyme. The total concentration of available surface sites $[*]_{max}$ can therefore be expressed by:

$$[*]_{max} = [*] + [E^*] + [EI^*] + [ENAD^*] \quad (7.3)$$

The productive and inhibitory adsorption of enzyme onto the nanoparticle surface, complexation with surface bound NAD and catalytic formation of product and decomplexation of the surface bound enzyme/NAD complex can be described with the following differential equations:

$$\frac{d[E^*]}{dt} = k_{on}\left[E_{free}\right]\left([*]_{max} - ([E^*] + [EI^*] + [ENAD^*])\right) - k_{off}[E^*] - k_1[E^*][NAD] + k_{-1}[ENAD^*] \quad (7.4)$$

$$\frac{d[ENAD^*]}{dt} = k_1[E^*][NAD] - k_{-1}[ENAD^*] \quad (7.5)$$

$$\frac{d[EI^*]}{dt} = k_i\left[E_{free}\right][*] - k_{-i}[EI^*] \tag{7.6}$$

$$\frac{d[P]}{dt} = k_{cat}[ENAD^*] \tag{7.7}$$

Assuming the system reaches a QSS, the concentration of each enzyme species will not change, as discussed in the previous Chapter. Therefore:

$$\frac{d\left[E_{free}\right]}{dt} = \frac{d[E^*]}{dt} = \frac{d[EI^*]}{dt} = \frac{d[ENAD^*]}{dt} = 0 \tag{7.8}$$

Combining Equations 7.4-7.8 results in the following rate expression relating the rate of product formation to the aqueous enzyme concentration, surface concentration of tethered NAD and available surface sites for adsorption $[*]_{max}$:

$$\frac{d[P]}{dt} = v_0 = \frac{k_{cat}k_1[NAD][*]_{max}K_L\left[E_{free}\right]}{k_{-1} + \left(1 + \frac{[*]_{max}}{K_i}\right) + K_L\left[E_{free}\right](k_{-1} + k_1[NAD])} \tag{7.9}$$

Where:

$$K_i = \frac{k_{-i}}{k_i} \tag{7.10}$$

Equation 7.9 accounts for the decrease in the rate of complexation of adsorbed enzyme with surface tethered NAD due to the decrease in productively adsorbed enzyme as a result of competing adsorption of non-productively adsorbed enzyme. Therefore, knowing the inhibition constant (K_i) for the non-productive adsorption of enzyme onto the particle surface, it is possible to use Equation 7.9 to accurately quantify the rate constants of complexation (k_1 and k_{-1}) and catalysis (k_{cat}) when the

reaction kinetics are instead determined as a function of NAD concentration rather than enzyme concentration as in Chapter 6.

7.3.2 Inhibition of EcG3PD by thiol terminated SiNPs

In order to estimate the inhibition constant (K_i) for the non-productive adsorption of EcG3PD to the SiNP surface, the inhibitory effect of thiol and vinyl terminated SiNPs on the EcG3PD catalysed reaction with free NAD was determined. This was achieved by measuring the EcG3PD catalysed reaction kinetics with free NAD, containing different quantities of thiol and vinyl terminated SiNPs dispersed within the system. It is proposed that adsorption of the EcG3PD onto the particle surface will result in deactivation due to non-productive adsorption conformations, resulting in inhibition of the enzyme, as shown in Figure 7.1. This quantity of inhibited EcG3PD will increase as the concentration of particles, and therefore adsorption sites, is increased. Figure 7.2(a-f) show the increase in NADH produced over time in the EcG3PD catalysed reaction, as measured by the resazurin/PMS^+ coupled assay. EcG3PD activity is measured as a function of NAD concentration, with increasing quantities of dispersed SiNPs, expressed as the concentration of available surface adsorption sites ($*$). The EcG3PD reaction rate is plotted as a function of free NAD concentration at the different concentrations of total available adsorption sites on the thiol and vinyl terminated SiNP surfaces as shown in Figure 7.2(g). It can be seen that as the quantity of thiol terminated SiNPs is increased, the EcG3PD reaction rate significantly decreases. A similar quantity of vinyl terminated SiNPs (14 μM) is shown to have a far smaller inhibitory effect on the EcG3PD reaction, indicating that the observed inhibition is related to the interactions between the enzyme and particle surface as discussed in Chapter 6.

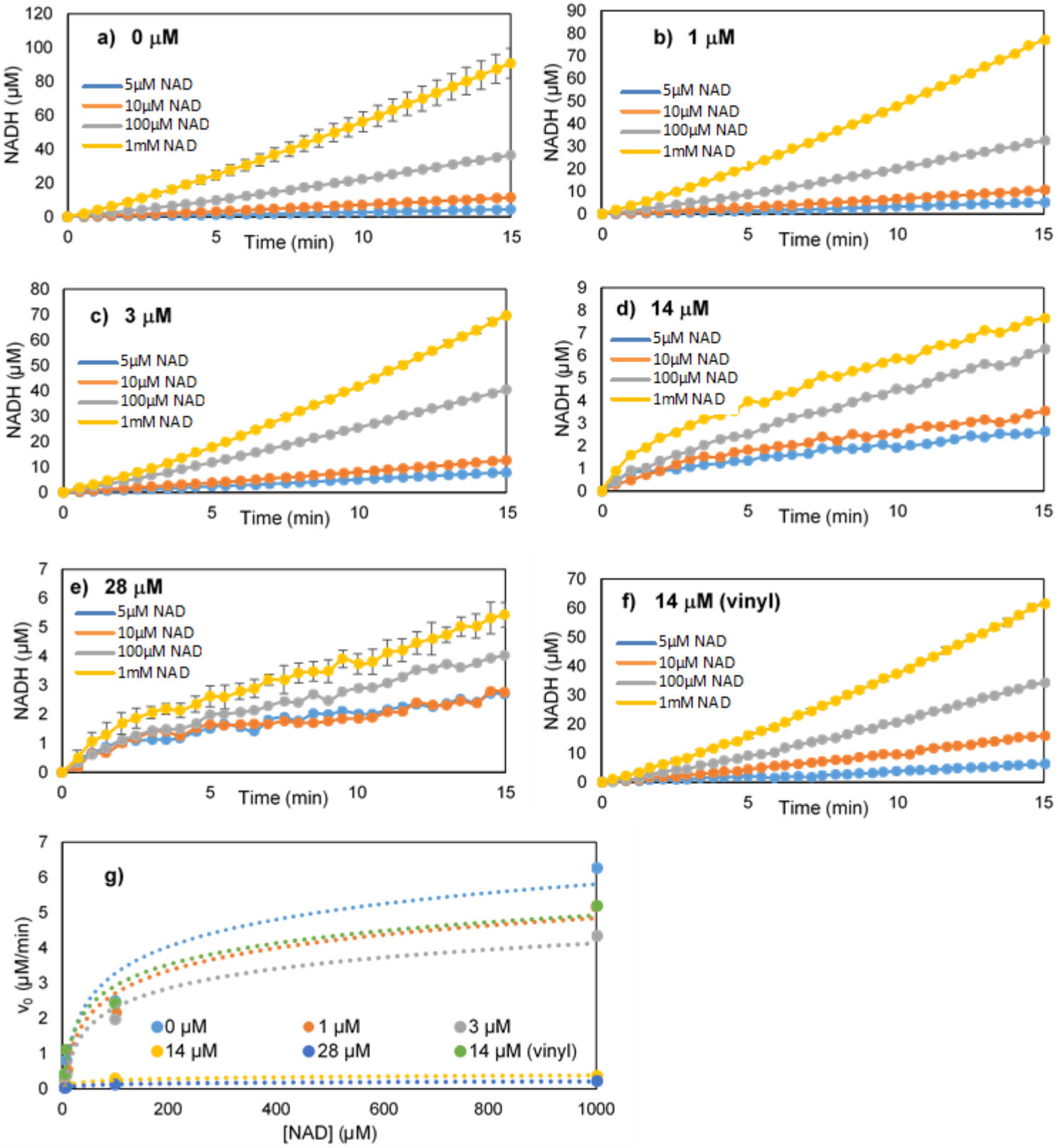

Figure 7.2: Increase in NADH production over time, as measured by the resazurin/PMS^{+} coupled assay, by EcG3PD at different NAD concentrations containing (a) 0 µM, (b) 1 µM, (c) 3 µM, (d) 14 µM, (e) 28 µM available adsorption sites

on thiol terminated SiNPs and (f) 14 μM vinyl available adsorption sites on vinyl terminated SiNPs The rate of EcG3PD reaction is then plotted as a function of NAD concentration for each particle concentration (g).

Fitting the kinetic data in Figure 7.2(g) to the rate equation for competitive inhibition (Equation 7.11), discussed in Chapter 1, allows the inhibition constant for the thiol ($Ki_{thiolSiNP}$) and vinyl ($Ki_{vinylSiNP}$) terminated SiNPs with EcG3PD to be determined. These values are specified in Table 7.1.

$$v_0 = \frac{k_{cat}[E_{free}][NAD]}{\frac{k_{-1} + k_{cat}}{k_1}\left(1 + \frac{[*]_{max}}{K_i}\right) + [NAD]} \tag{7.11}$$

Table 7.1: : Inhibition dissociation constants of thiol ($Ki_{thiolSiNP}$) and vinyl ($Ki_{vinylSiNP}$) terminated SiNPs with EcG3PD.

$Ki_{thiolSiNP}$ (μmol)	$Ki_{vinylSiNP}$ (μmol)
15000	220000

K_i is an equilibrium constant describing the dissociation of the inhibited enzyme (EI) back to the native state (E_{free}). Therefore, the lower $Ki_{thiolSiNP}$ value indicates strong binding interactions between EcG3PD and the thiol terminated SiNP surface resulting in enzyme inhibition by non-productive adsorption. This correlates well with the Langmuir adsorption analysis performed in Chapter 6, where EcG3PD was found to have strong interactions with the thiol terminated SiNP surface with tethered NAD. Conversely, the larger $Ki_{vinylSiNP}$ value indicates much weaker binding interactions between EcG3PD and the vinyl terminated SiNP surface, leading to less enzyme inhibition by non-productive adsorption. This also correlates well with the findings in the Langmuir adsorption analysis, where EcG3PD showed much weaker adsorption interactions with vinyl terminated SiNPs with tethered NAD.

The derived inhibition constants can then be applied to Equation 7.9 as an estimate value for the inhibition of the EcG3PD catalysed reaction with tethered NAD by non-productive adsorption of EcG3PD onto the particle surface, as depicted in Figure 7.1.

7.4 Excess reactant approach to determination of EcG3PD surface kinetics

The rate of the EcG3PD catalysed reaction was measured as a function of tethered NAD concentration using the fluorometric resazurin/PMS^+ coupled assay. Figure 7.3 shows the increase in NADH production with time by EcG3PD at different concentrations of NAD tethered to thiol (Figure 7.3(a)) and vinyl (Figure 7.3(b)) terminated SiNPS. The EcG3PD reaction rate is then plotted as a function of NAD concentration (Figure 7.3(c)). It can be seen that the increase in concentration of NAD tethered to the surface of vinyl terminated SiNPs leads to a linear increase in the rate of EcG3PD catalysis, even up to 50 μM NAD. However, the increase in concentration of NAD tethered to thiol terminated SiNPs results in a linear increase in EcG3PD reaction rate up to only 1 μM, before the reaction rate plateaus. According to the proposed model of inhibition, this suggests that at low NAD concentrations, a higher degree of EcG3PD is adsorbed onto the particle surface in productive conformations than non-productive conformations. However, as the NAD concentration, and therefore SiNP concentration, is increased, non-productive conformations of EcG3PD adsorption dominates, resulting in a plateau in EcG3PD activity.

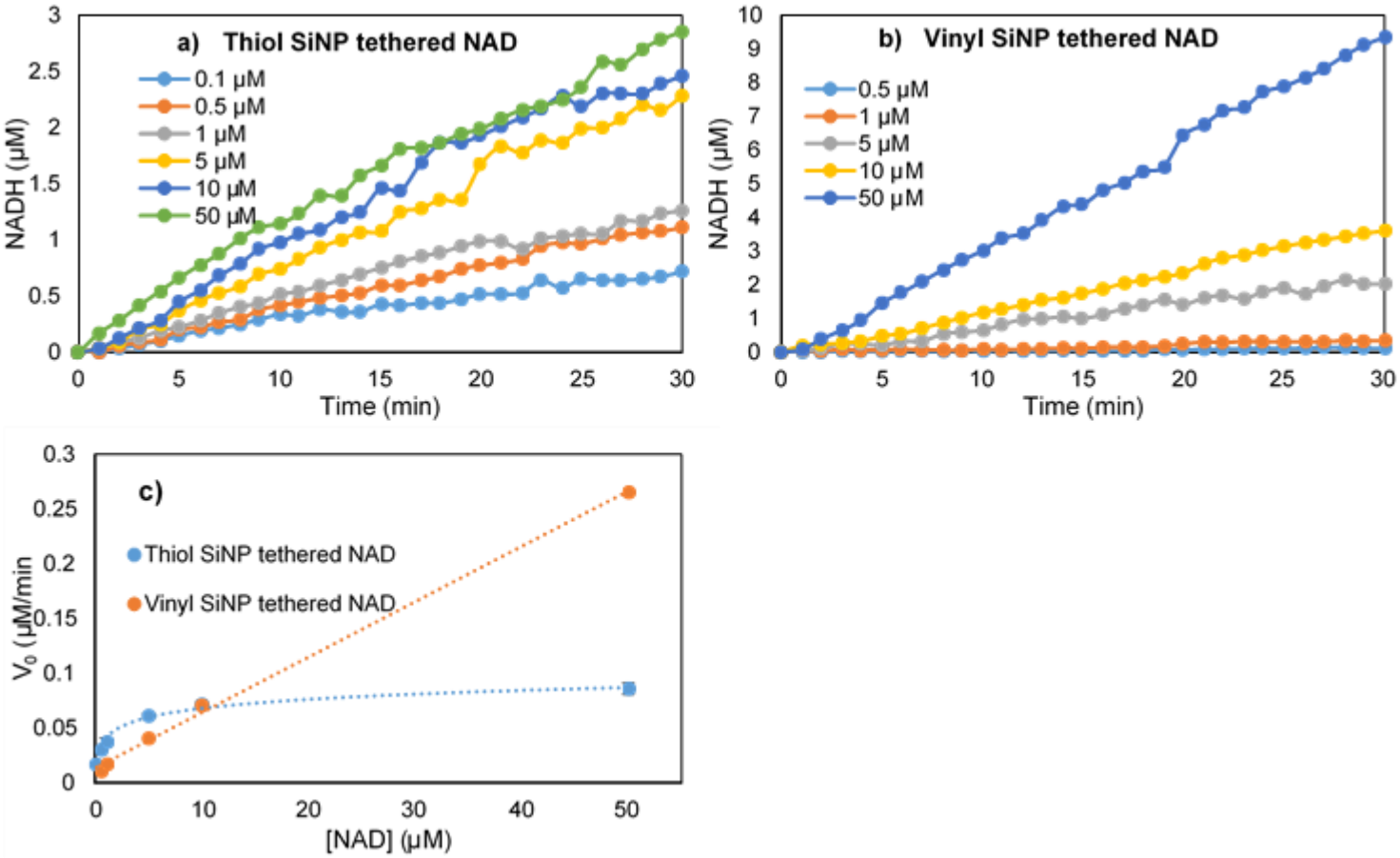

Figure 7.3: Amount of resorufin (NADH) produced over time by EcG3PD as measured by the resazurin/PMS^+ coupled assay with different concentrations of (a) nonane-2AE-NAD tethered to the surface of thiol terminated SiNPs and (b) PEG_4-2AE-NAD tethered to the surface of vinyl terminated SiNPs. EcG3PD reaction rates are plotted as a function of tethered NAD concentration (c).

Inhibition by non-productive adsorption attenuates the observed rate of surface complexation and catalysis of EcG3PD with surface tethered NAD. In order to account for this, Equation 7.9 relates the enzyme reaction rate when the total amount of enzyme adsorption sites in the system and an equilibrium constant describing the dissociation of enzyme from the inhibited to native state. To gain an estimate for this inhibition constant, the inhibition of the EcG3PD reaction with free NAD by thiol and vinyl terminated SiNPs ($K_{ithiolSiNP}$ and $K_{ivinylSiNP}$) was used. Fitting Equation 7.9 to the kinetic data in Figure 7.3(c), using $K_{ithiolSiNP}$ and $K_{ivinylSiNP}$ as the inhibition constants gave the kinetic rate constants shown in Table 7.2 (Excess reactant rows). Table 7.2 also shows that the kinetic rate constants for the EcG3PD catalysis of surface tethered

NAD determined using Equation 7.9 under excess reactant conditions are similar to those determined under excess enzyme conditions in Chapter 6.

Table 7.2: Comparison of kinetic rate constants of complexation, decomplexation and catalysis of EcG3PD with NAD tethered to the surface of thiol and vinyl terminated SiNPs determined by the excess enzyme (Chapter 6) and excess reactant approach.

NAD source	Kinetic approach	k_1 (μmol^{-1} min^{-1})	k_{-1} (min^{-1})	k_{cat} (min^{-1})
Free NAD	Excess enzyme	631	0.0047	0.54
Thiol SiNP tethered NAD	Excess enzyme	19361	0.076	8
	Excess reactant	22300	0.085	7.8
Vinyl SiNP tethered NAD	Excess enzyme	26187	0.043	13.6
	Excess reactant	33100	0.066	15

The rate of complexation (k_1) of EcG3PD with NAD tethered to the surface of thiol terminated SiNPs determined by the excess reactant approach was found to be 13% higher than that determined by the enzyme excess approach. Similarly, the rate of decomplexation (k_{-1}) was found to be 10% higher than the enzyme excess approach while the catalysis rate (k_{cat}) is almost identical. A 20% higher value for the rate of complexation and a 35% higher value for the rate of decomplexation EcG3PD with NAD tethered to the surface of vinyl terminated SiNPs was obtained from the excess reactant approach compared to the enzyme excess approach. Like thiol SiNP tethered NAD, the value for the rate of catalysis was relatively similar to that obtained from the enzyme excess approach. The differences in the complexation and decomplexation rates is due to errors associated with using the inhibition constant for the free enzyme system as an estimate for the observed inhibition in the tethered NAD system. However, the small amount of difference between the values of the kinetic constants derived from the enzyme excess approach and the reactant excess approach with estimated inhibition shows there is validity in the method.

7.5 Strategy to reduce inhibition by thiol terminated SiNPs

In order to reduce the inhibition of EcG3P with NAD tethered to the surface of thiol terminated SiNPs, residual thiol groups on the particle surface have been partially 'capped' with a series of common alkylating agents. Figure 7.4(a-b) shows the resazurin/PMS^+ coupled assay of EcG3PD with NAD tethered to the surface of SiNPs with the residual thiols capped with different alkylating agents.

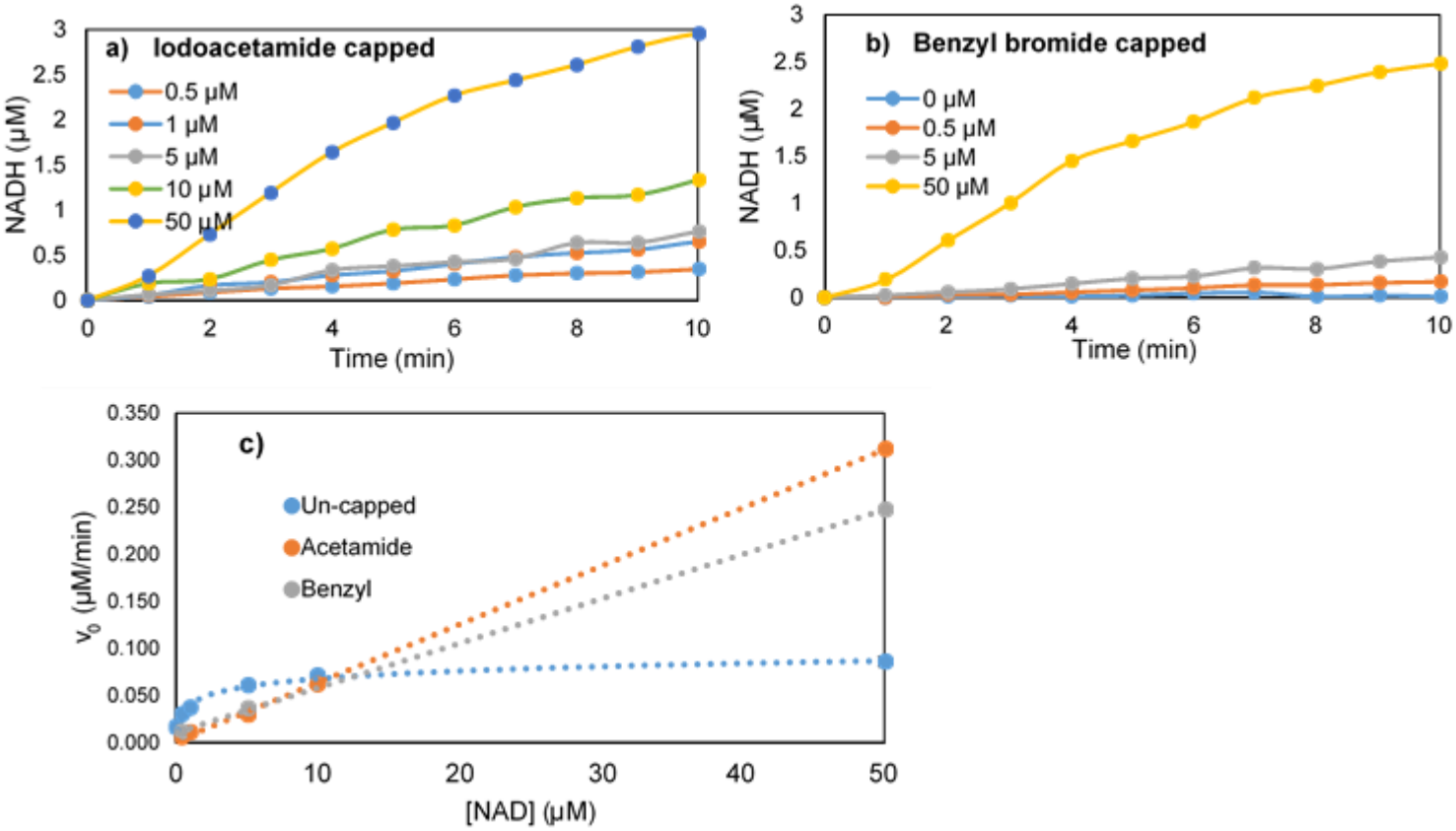

Figure 7.4: Activity of EcG3PD at different concentrations of NAD tethered to SiNPs with residual thiol groups capped with iodoacetamide (a) and benzyl bromide (b). Initial reaction rates ae plotted as a function of tethered NAD concentration with the different surface chemistries (c).

The rate of EcG3PD catalysis with NAD tethered to the surface of thiol terminated SiNPs plateaus after 1 µM NAD. However, when the residual surface thiols are capped by small alkylating agents, the rate of EcG3PD reaction increases linearly with NAD concentration. This is similar to EcG3PD catalysis with NAD tethered to the surface of vinyl terminated SiNPs. This suggests that capping of the residual thiol groups reduces

the inhibition of EcG3PD catalysis by reducing the amount of non-productive EcG3PD binding. This is due to a reduction in the surface charge by alkylating the residual hydrolysable thiol groups with small unhydrolysable groups. Assuming that the complexation and catalysis kinetic rate constants (k_1, k_{-1} and k_{cat}) are unchanged for the catalysis of surface tethered NAD on the particle surface, the Langmuir adsorption constants (K_L) and the inhibition constants (K_i) of these NAD surface structures can be calculated by fitting Equation 7.2 to the experimental data in Figure 7.4. These are shown in Table 7.3.

Table 7.3: Estimated Langmuir and inhibition constants of EcG3PD with NAD tethered to the surface of SiNPs with residual thiol groups capped with different alkylating agents.

Alkylating agent	K_L (μmol^{-1})	K_i (μmol)
Uncapped thiol	44000	15000
Vinyl	6800	220000
Iodoacetamide	9400	750000
Benzyl Bromide	7450	360000

Table 7.3 shows a significant reduction in the calculated Langmuir adsorption constants and significant increase in the inhibition constants for the iodoacetamide and benzyl bromide capped SiNPs. This suggests that capping the residual surface thiols with these molecules significantly reduced the magnitude of the EcG3PD/SiNP surface interactions. It can be seen that the calculated Langmuir adsorption constants the iodoacetamide and benzyl bromide capped SiNPs were similar to that of vinyl terminated SiNPs with tethered NAD. The calculated inhibition constants were significantly increased compared to vinyl terminated SiNPs with tethered NAD, suggesting a large reduction in the proposed enzyme inhibition by non-productive binding of EcG3PD. The mechanism of this observed decrease in interactions between EcG3PD and NAD tethered to capped thiol surfaces is likely due to that discussed in Chapters 5 and 6. Capping of the residual surface thiols with the

alkylating agents results in a decrease in the negative surface electrostatic charge of the thiol terminated SiNPs with tethered NAD, therefore decreasing the strong electrostatic interactions with EcG3PD. This results in weaker interactions between EcG3PD and the particle surface, leading to decreased surface adsorption and inhibition. Previous reports investigating the dependence of the base nanoparticle surface functionality on the surface enzyme catalysis with surface bound reactants have shown similar outcomes [33, 110]. As discussed in Chapter 1, Wu *et al.* were able to increases the enzyme efficiency when the surface ligand chemistry of the zinc sulphide (ZnS) QD was varied with several different small anionic thiol compounds [110]. Strong interactions between the positively charged region of the thrombin with the negatively charged surface was found to enhance enzyme efficiency less compared to the weaker, non-specific interactions of zwitterionic ligands. This was further explored by Diaz *et al.* where factors such as the charge and length of the surface capping ligand was explored. Similarly, the greatest enhancement was observed with the shortest zwitterionic ligand, which through MD simulations, was shown to allow the surface bound reactant to be prominently presented for enzymatic catalysis, while facilitating non-specific interactions and suitable attractive forces with the enzyme. Here, the acetamide capped surface resulting from alkylation by iodoacetamide was found to result in the greatest decrease in EcG3PD inhibition, followed by the benzyl capped surface. Resonance stabilisation of acetamide by sp^2 hybridisation of the nitrogen atom results in acetamide switching between a zwitterionic resonance structure as shown in Figure 7.5 [177]. It is proposed that this zwitterionic state decreases the non-specific adsorption of EcG3PD as observed by Wu *et al.* and Algar *et al.*, decreasing inhibition while retaining the ability of the enzyme to move laterally across the particle surface resulting in highly efficient complexation and catalysis with surface tethered NAD [33, 110]. The short length of acetamide also suggests prominent display of surface tethered NAD to the enzyme.

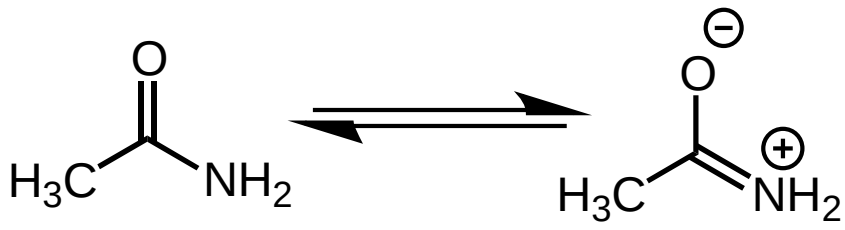

Figure 7.5: Resonance structures of acetamide

The observed kinetic enhancement was the second greatest when surface thiols were capped with benzyl bromide, resulting in benzyl surface functionality. Like vinyl groups, phenyl groups are uncharged and hydrophobic, decreasing the electrostatic interactions between EcG3PD and the thiol surface. However, the tendency of enzymes to undergo aromatic π stacking between interfacial aromatic amino acids and the surface phenyl groups may have introduced attractive forces between the enzyme and NAD tethered surface leading to a lower degree of enhancement compared to the acetamide capped surface [178].

7.6 Conclusion

The reactant excess approach to enzyme kinetics has been utilised to determine the kinetics of EcG3PD catalysis with NAD tethered to surface of thiol and vinyl terminated SiNPs. In order to account for inhibition due to adsorption of EcG3PD in non-productive conformations as the particle concentration in the system is increased, Equation 6.10 from Chapter 6 was modified to include a term for inhibition. In order to estimate the inhibition constant for the non-productive binding of EcG3PD to the surface of SiNPs with tethered, the inhibition constant of EcG3PD with free NAD with thiol and vinyl terminated SiNPs was determined. This inhibition constant was applied to the inhibition rate expression which was fitted to experimental rate data of EcG3PD measured at different tethered NAD concentrations. The rate constants determined correlated well with those determined by the enzyme excess approach in Chapter 6, showing the validity of the approach. Lastly, in order to reduce the inhibitory effects of the residual thiol groups of NAD tethered to the surface of thiol terminated SiNPs in the EcG3PD catalysed reaction, thiol groups were ‘capped’ with common alkylating agents. Kinetic analysis revealed that capping of the residual surface thiols with iodoacetamide resulted in the greatest decrease in EcG3PD inhibition, due to a decrease in the electrostatic interactions and non-specific binding resulting from the zwitterionic character of the acetamide resonance structure.

CHAPTER 8 : KINETICS OF COFACTOR REGENERATION

8. 1 Overview

This chapter describes the regeneration of surface tethered NAD within a multi-enzyme coupled reaction. The reaction kinetics are determined through analysis of product formation over time by HPLC and modelling the reaction with numerical Euler integration of the ordered differential equations of the proposed model of multi-enzyme biocatalysis. The kinetic constants for ADH catalysis of surface tethered NAD derived in Chapter 6 are used along with the adsorption kinetics of GluDH, the cofactor regenerating enzyme. This allowed the derivation of estimated kinetic rate constants of complexation, decomplexation and catalysis of surface tethered NADH by GluDH which could be compared to those of the free NAD system. Strategies to maximise the efficiency of the system are subsequently discussed.

8.2 Introduction

Due to the high costs and stoichiometric consumption, it is essential for cofactors to be regenerated *in situ* for industrial viability [18, 23, 44]. As discussed in Chapter 1, the most common approach to cofactor regeneration in biocatalytic processes is by coupling a second cofactor dependent enzyme to perform the cofactor regenerating reaction. This approach has the added potential of affording the production of multiple valuable chemicals within the same system [43]. Several previous studies have regenerated tethered NAD within a multi-enzyme system [18, 48, 52-54]. However, these studies have neglected to analyse the kinetics of the multi-enzyme cofactor regeneration system. In this chapter, NAD is enzymatically regenerated in the ADH/GluDH coupled reaction (Figure 8.2). Acetaldehyde produced in the reaction is reacted with 2,4-dinitrophenylhydrazine (2,4-DNP) to form acetaldehyde-2,4-dinitrophenylhydrazine (ADNP), which is quantitatively analysed by HPLC in order to determine the reaction rate of the system. Knowing the Langmuir adsorption kinetics of ADH and GluDH from Chapter 5 along with the kinetics of the reduction of surface tethered NAD by ADH from kinetic analysis in Chapter 6, reaction modelling is used to estimate the kinetics of complexation and catalysis of the oxidation of surface tethered NADH back to NAD by GluDH. Similar to experimental observations in Chapters 6 and 7, a kinetic enhancement in the rate constants for complexation and catalysis of GluDH and surface tethered NADH was revealed. This further shows the potential for tethered NAD to improve the efficiency of NAD dependent biosynthetic applications.

8.3 Kinetic model of multi-enzyme regeneration of surface tethered NAD

Figure 8.1 shows a schematic of the kinetic steps of the multi-enzyme regeneration of NAD tethered to the SiNP surface. In the first step, the enzyme that catalyses the oxidation of NAD ($E1_{free}$) reversibly adsorbs to the surface of the SiNP, occupying an available surface adsorption site ($*$) (Figure 8.1(i)). The surface adsorbed enzyme ($E1^{*}$) reversibly binds to surface tethered NAD to form the surface-bound-enzyme/NAD-complex ($ENAD^{*}$) (Figure 8.1(ii)). Catalysis results in the oxidation of surface tethered NAD to NADH, with simultaneous transformation of the enzyme's

reactant (Reactant 1) to product (Product 1) and regeneration of the surface adsorbed enzyme ($E1^{*}$) (Figure 8.1(iii)). In order to enzymatically regenerate the surface tethered NADH back to NAD, a second enzyme ($E2_{free}$) reversibly (and competitively) adsorbs to the surface of the SiNP, occupying an available surface adsorption site (∗) (Figure 8.1(iv)). The adsorbed enzyme ($E2^{*}$) reversibly complexes with surface tethered NADH to surface-bound-enzyme/NADH-complex ($ENADH^{*}$) (Figure 8.1(v)). Catalysis regenerates surface tethered NAD from NADH with simultaneous conversion of the second enzyme's reactant (Reactant 2) to product (Product 2) and release of the surface bound enzyme ($E2^{*}$).

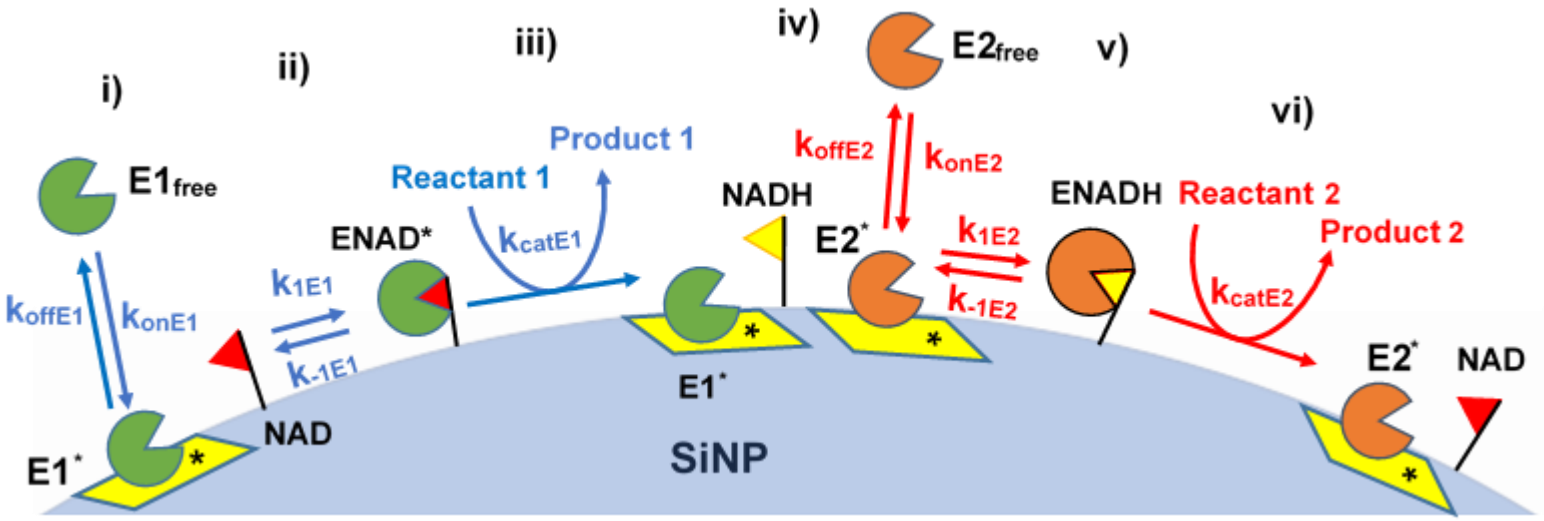

Figure 8.1: Schematic of multi-enzyme regeneration of surface tethered NAD showing adsorption of Enzyme 1 (i), complexation of Enzyme 1 with surface tethered NAD (ii), catalysis of the surface-bound-Enzyme/NAD-complex with transformation of reactant 1 to product 1 and reduction of surface tethered NAD to NADH (iii). Surface tethered NAD is then regenerated by adsorption of Enzyme 2 (iv), complexation of Enzyme 2 with surface tethered NADH (v) and then catalysis of the surface-bound-Enzyme/NADH-complex with transformation of Reactant 2 to Product 2 and oxidation of surface tethered NADH back to NAD (vi).

8.4 ADH/GluDH coupled reaction

The complex multi-enzyme regeneration reaction of surface tethered NAD in Figure 8.1 involves the continuous competitive adsorption, complexation, catalysis and re-complexation of two different enzymes, simultaneously on the particle surface. Due to the limited available surface area onto which the enzymes can adsorb and perform their catalysis reaction, high surface mobility of the enzymes is a critical factor in achieving efficient cofactor regeneration, and thus, product conversion. In Chapter 6, ADH showed high surface mobility and surface catalysis with NAD tethered to the surface of thiol terminated SiNPs. This was correlated to the weak electrostatic interactions between the negatively charged particle surface and the weakly positively charged surface of ADH. Figure 8.2 shows a schematic of the ADH/GluDH coupled reaction with regeneration of tethered NAD. In the ADH catalysed reaction, ethanol is oxidised to acetaldehyde with simultaneous reduction of surface tethered NAD to NADH. GluDH catalyses the reductive amination of α-ketoglutarate to glutamate with simultaneous oxidation of surface tethered NADH back to NAD. In order to characterise this reaction, the production of acetaldehyde was monitored over time by HPLC analysis. This was achieved by derivatising acetaldehyde with 2,4-DNP in order to make the highly coloured acetaldehyde-DNP (ADNP) as shown in Figure 8.3. This allows the reaction to be accurately monitored with high sensitivity.

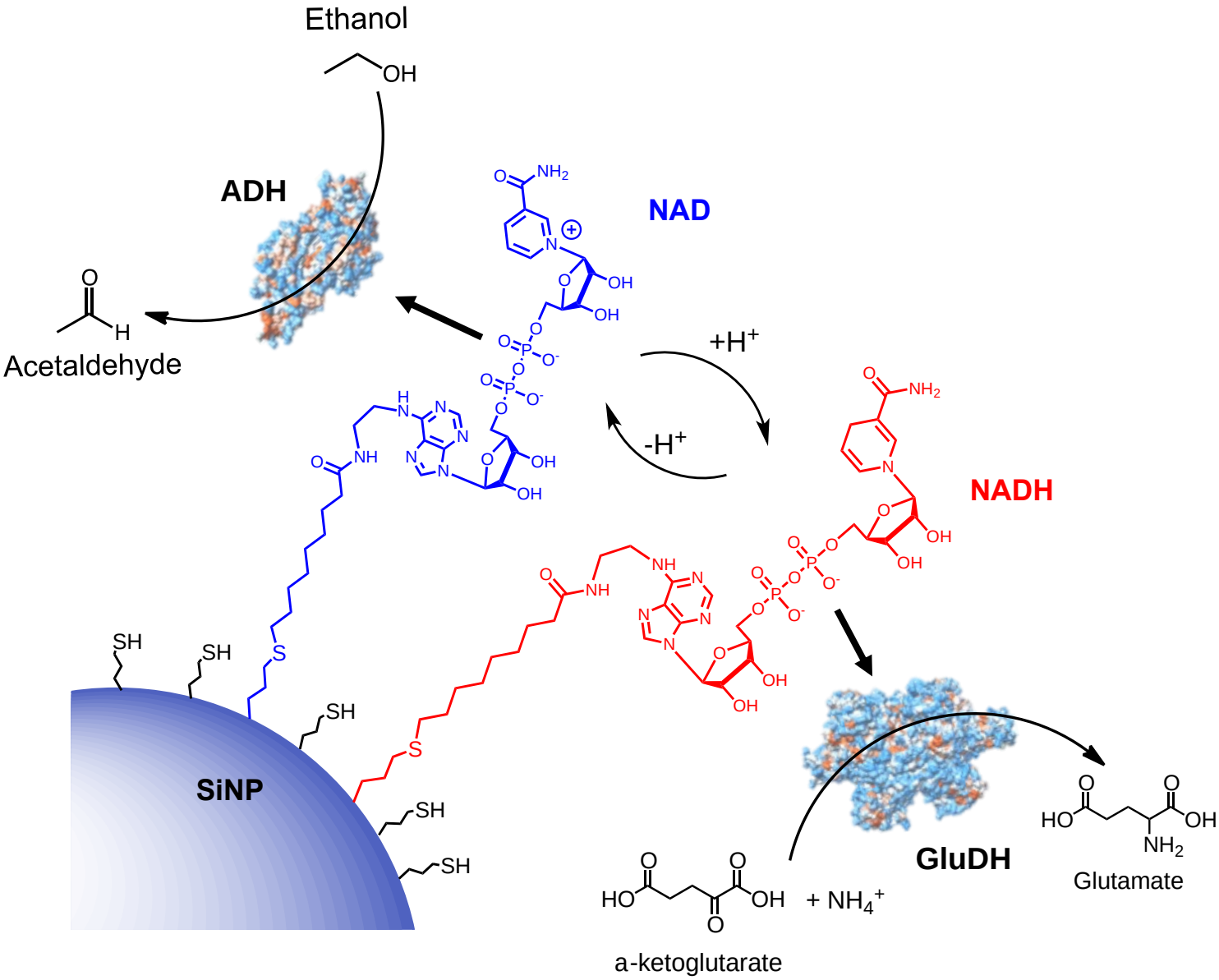

Figure 8.2: Reaction scheme of the enzymatic regeneration of surface tethered NAD by the ADH/GluDH coupled reaction.

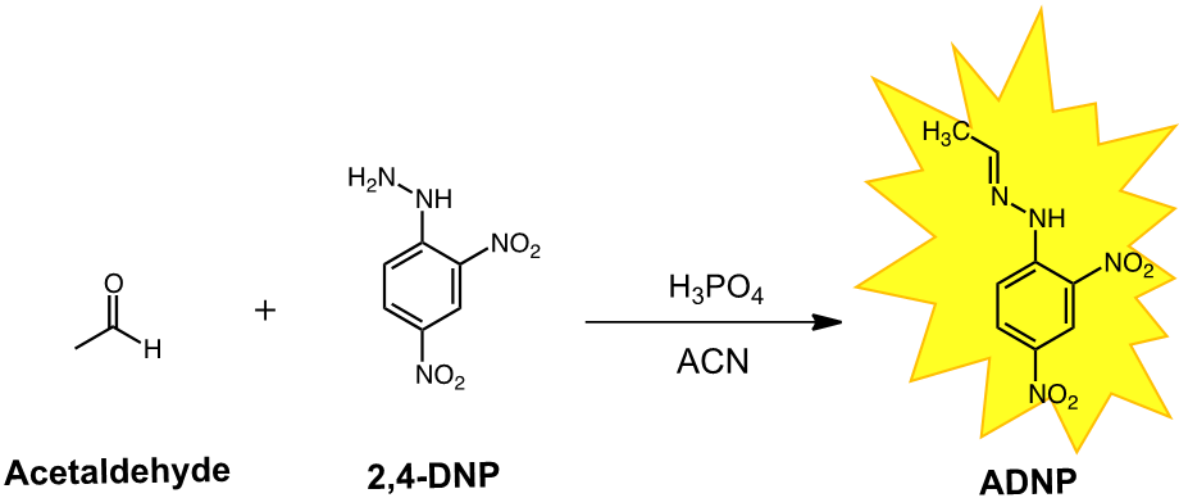

Figure 8.3: Conversion of colourless acetaldehyde to highly coloured acetaldehyde-2,4-DNP by conjugation with 2,4-DNP.

8.4.1 Analysis of the ADH/GluDH coupled reaction

In order to accurately quantify the amount of acetaldehyde produced in the ADH/GluDH coupled reaction, an ADNP calibration curve was constructed. [162]. ADNP standards of different concentrations were dissolved in acetonitrile and analysed via HPLC with UV/Vis detection. Figure 8.4 shows the increase in peak height with increasing ADNP concentration. Increasing ADNP concentration resulted in a highly linear increase in peak area as shown in the calibration cure in Figure 8.5.

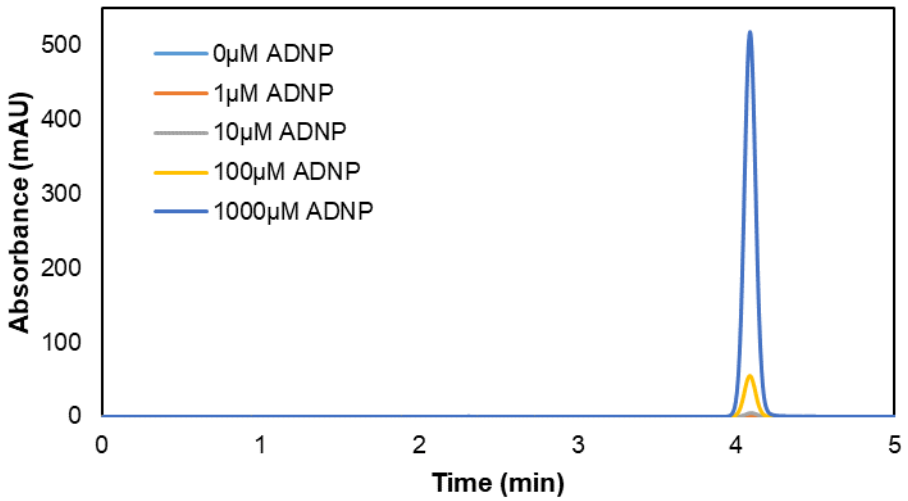

Figure 8.4: Overlaid HPLC chromatogram of ADNP standards eluting at 4.1 minutes, measured at 365 nm.

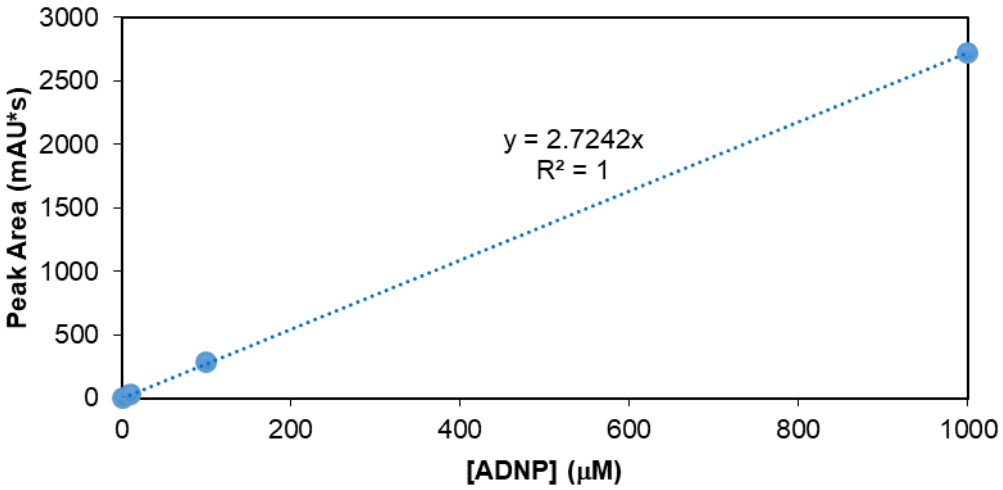

Figure 8.5: ADNP HPLC standard curve

8.4.2 NAD dependent kinetics of ADH/GluDH coupled reaction

ADH and GluDH were mixed with different concentrations of NAD tethered to the surface of thiol terminated SiNPs and mixed at 37°C. Aliquots were taken at different time points to which an acidified solution of 2,4-DNP in acetonitrile added to convert the acetaldehyde formed in the coupled reaction into ADNP for HPLC detection. This also has the added bonus of quenching the reaction, stopping further formation of acetaldehyde, giving accurate time-based results. Figure 8.6(a-d) shows the overlaid HPLC chromatograms of acetaldehyde-2,4-DNP produced at different time points with 0.5 μM and 5 μM free NAD and NAD tethered to the surface of thiol terminated SiNPs. The amount of acetaldehyde-2,4-DNP (and therefore acetaldehyde) produced is plotted as a function of time in Figure 8.7 for free NAD and tethered NAD, revealing a linear increase in acetaldehyde production over the first 2-5 hours. The rate of acetaldehyde production was calculated from the slope of the time points collected over the initial two hours of the reaction where acetaldehyde production was linear with time. The rates for 0.1μM and 1 μM NAD for free NAD and NAD tethered to the surface of thiol terminated SiNPs were calculated from a single time point recorded after two hours of reaction, shown in Figure 8.8. The initial rate of acetaldehyde production (v_0) is then plotted as a function of NAD concentration (Figure 8.8(c)).

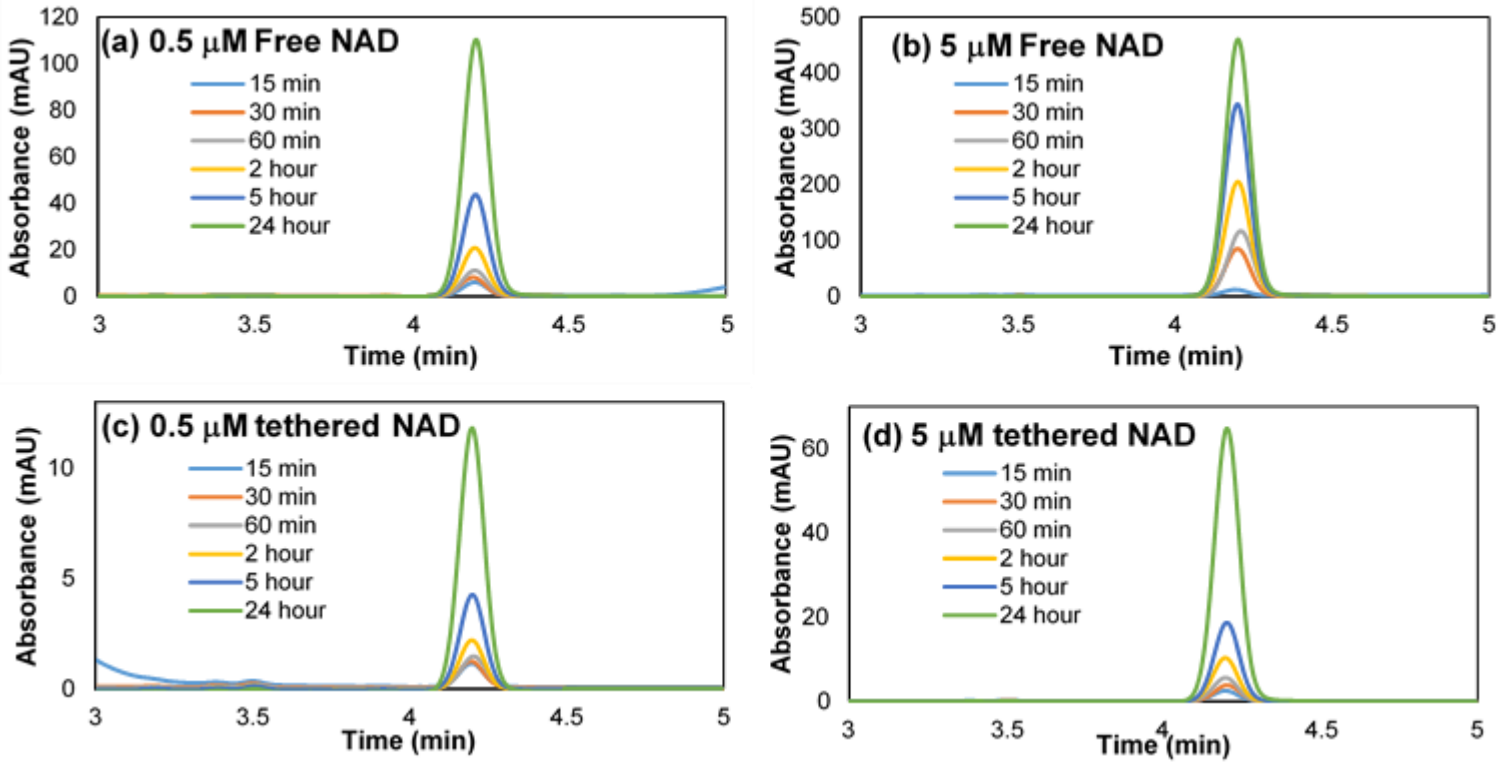

Figure 8.6: HPLC traces showing the ADNP produced overtime in the GluDH/ADH coupled assay with (a) 0.5 μM free NAD (b) 5 μM free NAD (c) 0.5 μM thiol SiNP tethered NAD and (d) 5 μM thiol SiNP tethered NAD.

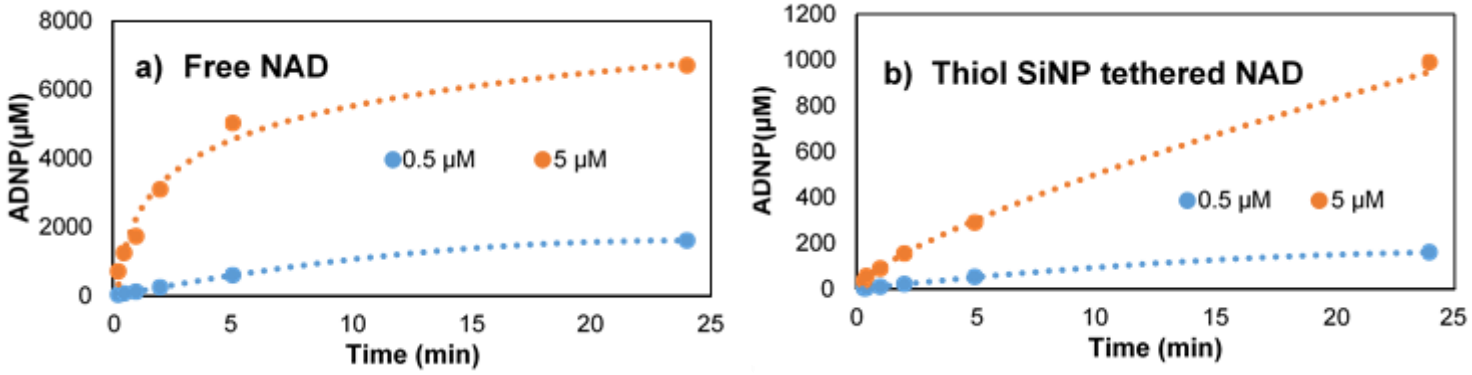

Figure 8.7: Acetaldehyde, as indicated by HPLC analysis of ADNP concentration, produced over time by the ADH/GluDH coupled reaction with free NAD (a) and NAD tethered to the surface of thiol terminated SiNPs (b)

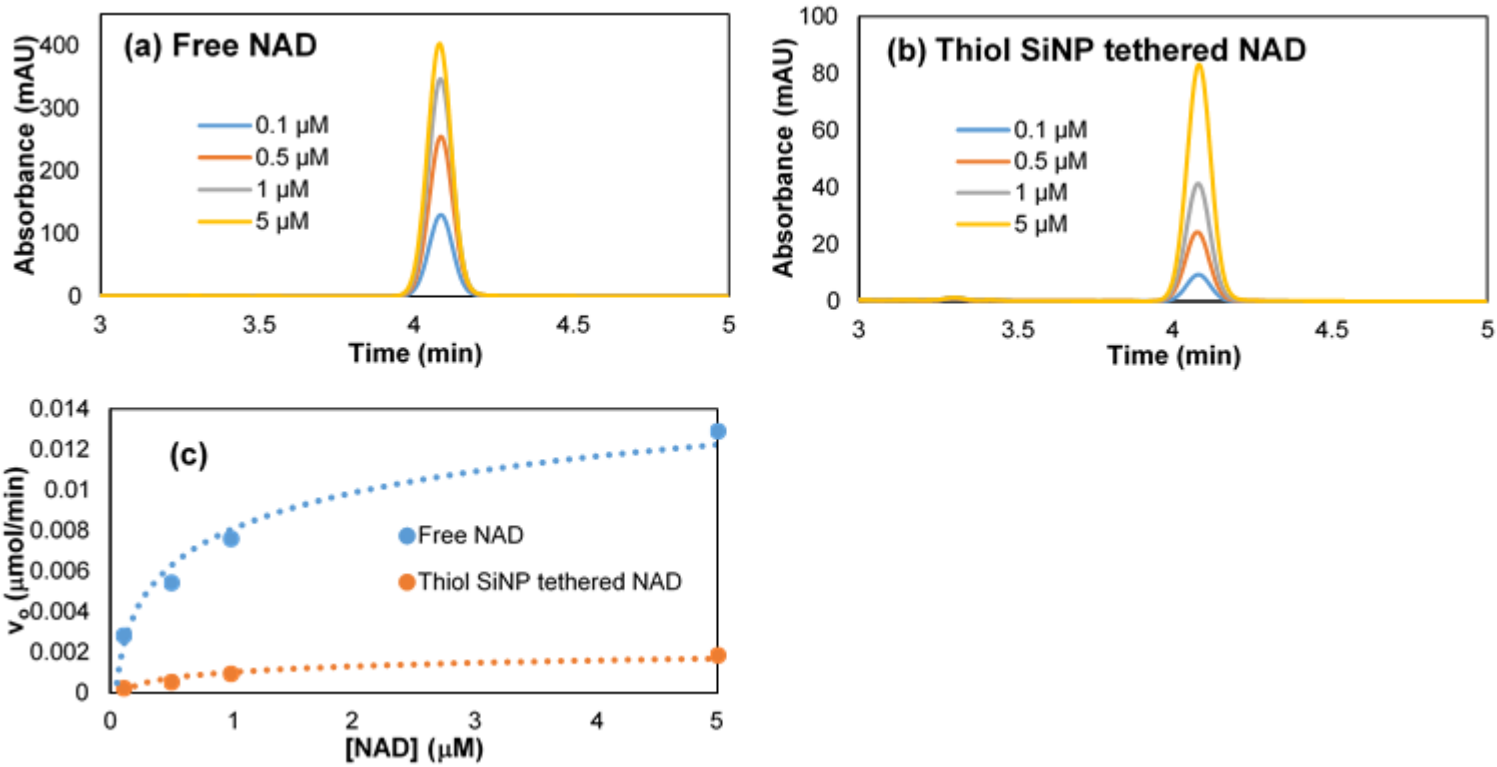

Figure 8.8: HPLC traces showing the ADNP produced after two hours in the GluDH/ADH coupled assay by different concentrations of (a) free NAD and (b) NAD tethered to the surface of thiol terminated SiNPs. The Initial reaction rates of the ADH/GluDH coupled reaction is plotted as a function of free and SiNP tethered NAD concentration (c).

Similar to results in Chapter 6 and 7, reaction rates were significantly higher when NAD was free in solution. This is due to all free NAD molecules being available for complexation and catalysis at any point in time whereas tethered NAD is restricted by the amount of surface adsorption sites for the enzymes. This problem is compounded when a second enzyme is required to catalyse the NAD regeneration at the surface resulting in competitive adsorption.

Since the kinetics of adsorption, complexation and catalysis of ADH with surface tethered NAD are known from the kinetic analysis performed in Chapter 6-7, and the adsorption kinetics of GluDH known from Langmuir adsorption analysis in Chapter 5, kinetic simulation can be used to estimate the kinetic rate constants of complexation and catalysis of GluDH with tethered NAD. Gaining a kinetic understanding of the multi-enzyme reaction allows reaction parameters such as the concentration of each enzyme to be fine-tuned in order to optimise the system for maximum efficiency.

8.5 Derivation of GluDH kinetic constants by kinetic simulation

Kinetic modelling was performed using numerical integration as in Chapter 6. Eulers method was used to integrate the mass balance equations associated with the kinetic steps in Figure 8.1. Applying the known rate constants for ADH, i.e. k_{onE1}, k_{offE1}, k_{1E1}, k_{-1E1}, and k_{catE1}, the simulated production of acetaldehyde over time was fitted to experimental values determined by HPLC analysis in order to determine the analogous GluDH rate constants. Figure 8.9-8.10 shows example kinetic simulations of these systems for both free and SiNP tethered NAD. The kinetic rate constants derived for GluDH are shown below in Table 8.1.

Table 8.1: Kinetic rate constants for GluDH with free and SiNP tethered NAD as determined by kinetic modelling of the ADH/GluDH multi-enzyme coupled reaction.

NAD source	k_{on} ($\propto$mol^{-1} min^{-1})	k_{off} (min^{-1})	K_L ($\propto$mol^{-1})	k_1 ($\propto$mol^{-1} min^{-1})	k_{-1} (min^{-1})	k_{cat} (min^{-1})
Free NAD	N/A	N/A	N/A	52500	0.011	27
Thiol SiNP tethered NAD	700	0.05	14000	64000	0.044	138

8.5.1 Kinetic simulation of ADH/GluDH coupled reaction with free NAD

Figure 8.9(a-e) shows the kinetic simulation of the ADH/GluDH coupled reaction at 5μM free NAD. Figure 8.9(a) shows the rapid complexation of ADH with almost all of the freely diffusing NAD within the first few seconds of, resulting in a rapid decrease in NAD concentration (Figure 8.9(c)) and a rapid increase in the ADH/NAD complex (ADHNAD) (Figure 8.9(d)). Catalysis results in the production of acetaldehyde (P) (Figure 8.9(e)) and NADH, with which, GluDH can complex, resulting in the rapid decrease in GluDH concentration (Figure 8.9(b)) and the appearance of the GluDH/NADH complex (GluDHNADH) reaction (k_1 = 52500 μmol^{-1}min^{-1}, k_{-1} = 0.011 min^{-1}). Catalysis of GluDHNADH results in the regeneration of NAD, along with the equimolar conversion of α-ketoglutarate and ammonia to glutamate (k_{cat} = 27 min^{-1}). A steady state between all the reactive species is established after ~15 seconds of reaction resulting in the linear formation of acetaldehyde over time which correlated

with the average experimentally measured acetaldehyde production over time (Experimental).

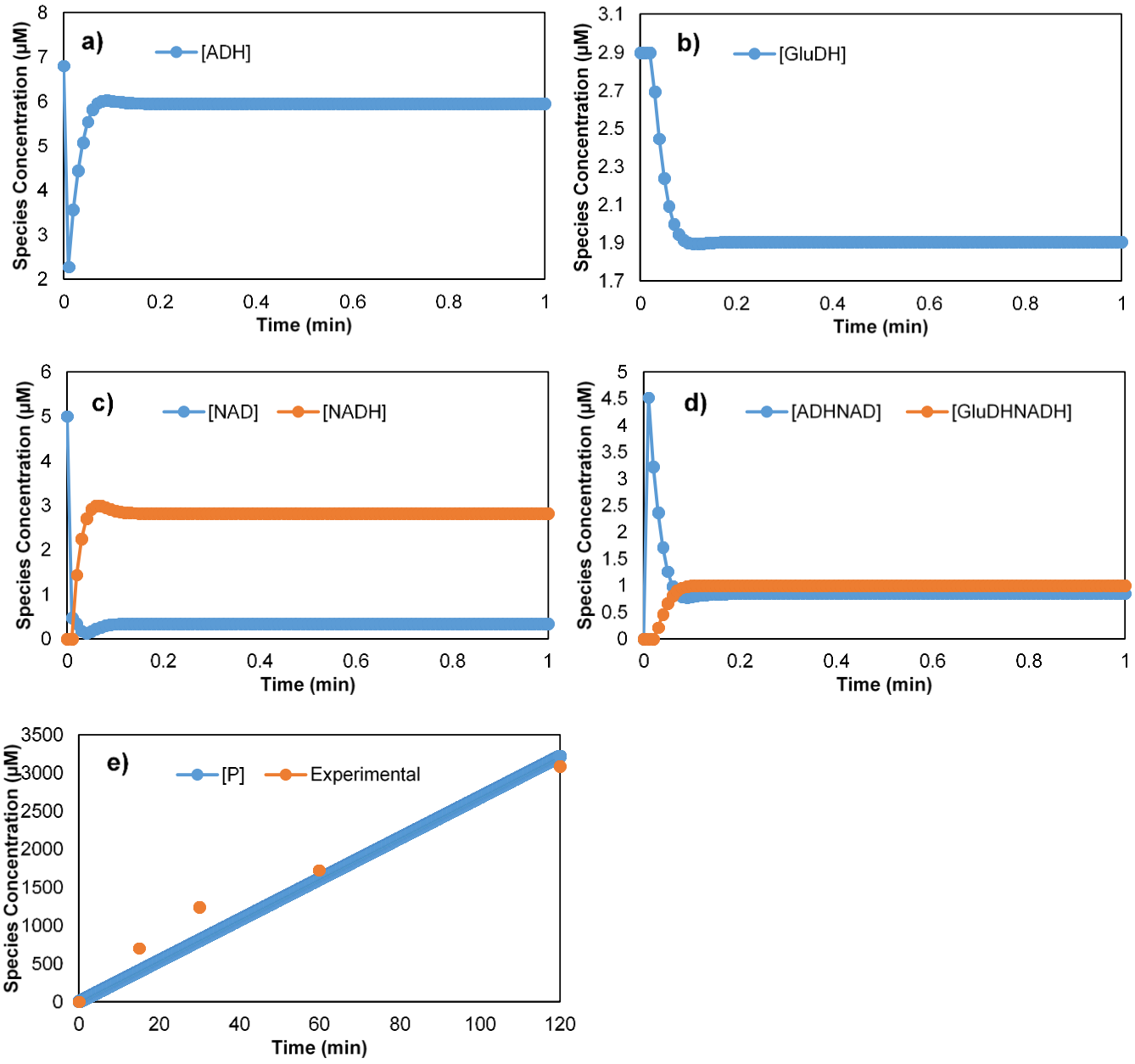

Figure 8.9: Reaction simulation of the ADH/GluDH coupled reaction showing the concentration of each reaction species with time. Reactions contain 6.8 µM ADH, 2.9 µM GluDH and 5 µM free NAD. Note that a-d are on 1 minute time scale while e is on 120 minute scale.

8.5.2 Kinetic simulation of ADH/GluDH coupled reaction with thiol SiNP tethered NAD

Figure 8.10(a-g) shows the kinetic simulation of the ADH/GluDH coupled reaction with NAD tethered to the surface of thiol terminated SiNPs at a total concentration of 5 μM. Figure 8.10(a-b) show the first steps of the surface catalysed multi-enzyme reaction, the competitive adsorption of ADH and GluDH, which is dictated by the previously determined Langmuir surface adsorption kinetics. The second order rate constant of adsorption of GluDH k_{on} was found to be 700 $\mu mol^{-1}\,min^{-1}$ and the first order desorption rate constant k_{off} was found to be 0.05 min^{-1}). Competitive adsorption results in the rapid decrease in available surface adsorption sites (*) over the first 15 minutes of reaction 8.10(c) and the formation of surface adsorbed ADH and GluDH (ADH* and GluDH*) 8.10(d). The chosen enzyme concentrations (6.8 μM ADH and 2.9 μM GluDH) resulted in a relatively even adsorption concentration of the two competitively adsorbing enzymes, with a slightly higher surface coverage of GluDH*. Adsorbed ADH then reversibly complexes with surface tethered NAD, resulting the formation of the surface-tethered-NAD/ADH complex (ADHNAD*) (Figure 8.10(e)) and the decrease in surface tethered NAD concentration (Figure 8.10(f)). Catalysis of ADHNAD* results in the formation of acetaldehyde (P) Figure 8.10(g), surface tethered NADH and ADH* which can desorb or re-complex with surface tethered NAD. NADH formed is then reversibly complexed with GluDH* to from the surface-tethered-NADH/GluDH complex (GluDHNADH*) (k_1 = 64000 $\mu mol^{-1}min^{-1}$, k_{-1} = 0.044 min^{-1}). Catalysis of GluDHNADH* regenerates surface tethered NAD and forms GluDH* which can desorb or re-complex with surface tethered NADH. The rate constant of NADH catalysis by GluDH k_{cat} was determined to be 138 min^{-1}. After ~10 minutes, a steady state is established and the concentration all the reactive species remain constant. The rate of acetaldehyde production is linear with time and correlates well with the experimentally determined values.

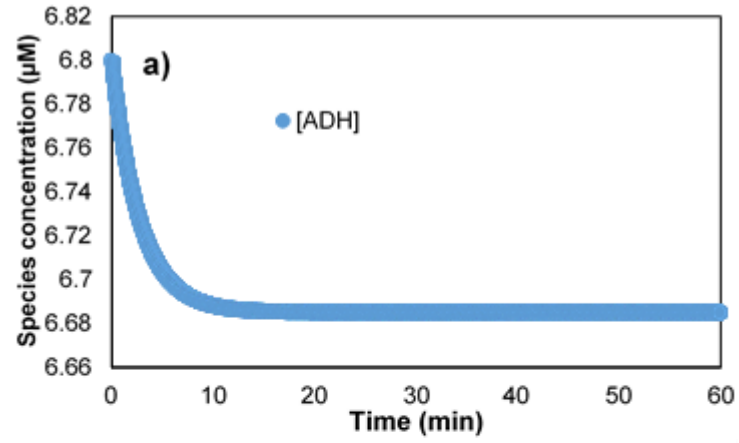
a)
[ADH]
Species concentration (μM)
Time (min)

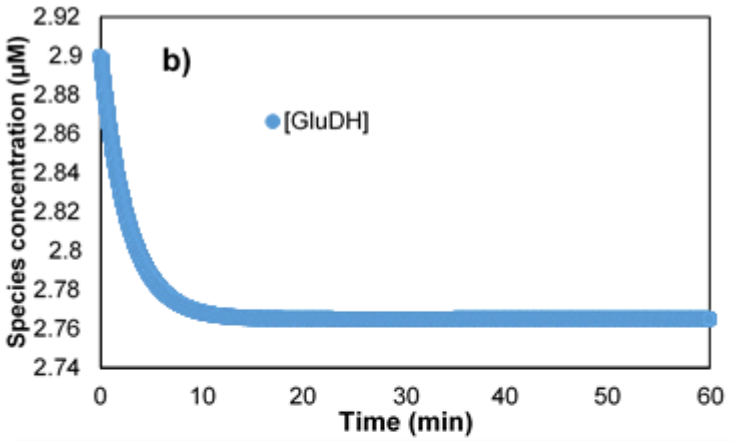
b)
[GluDH]
Species concentration (μM)
Time (min)

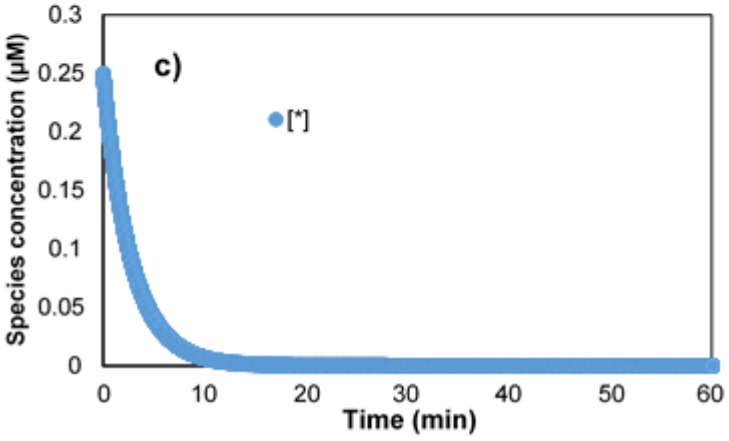
c)
[*]
Species concentration (μM)
Time (min)

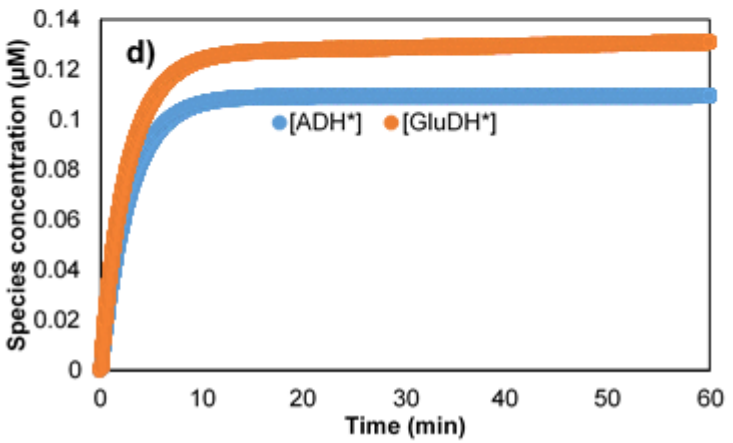
d)
[ADH*]
[GluDH*]
Species concentration (μM)
Time (min)

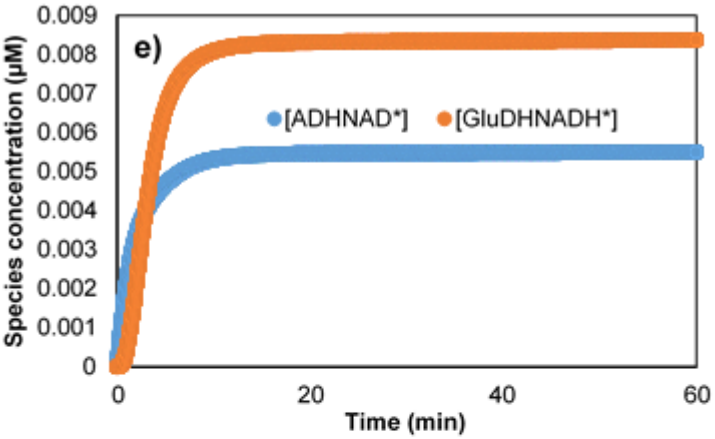
e)
[ADHNAD*]
[GluDHNADH*]
Species concentration (μM)
Time (min)

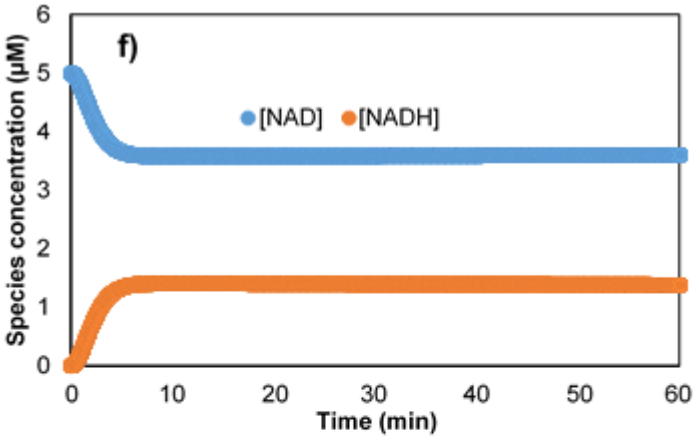
f)
[NAD]
[NADH]
Species concentration (μM)
Time (min)

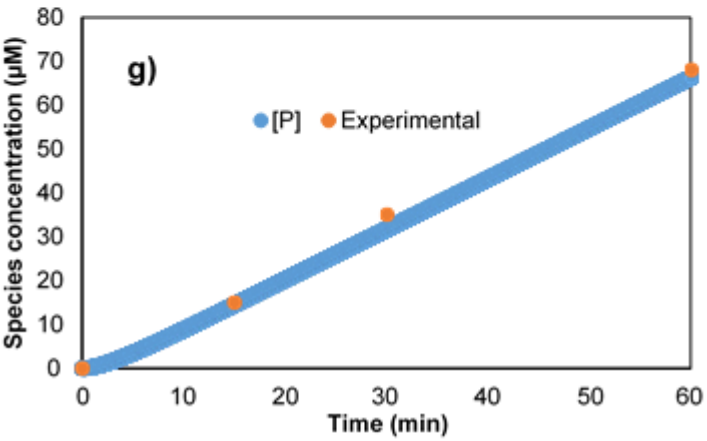
g)
[P]
Experimental
Species concentration (μM)
Time (min)

Figure 8.10: Reaction simulation of the ADH/GluDH coupled reaction showing the concentration of each reaction species with time. Reactions contain 6.8 μM ADH, 2.9 μM GluDH and 5 μM thiol SiNP tethered NAD.

Applying the kinetic rate constants for the surface adsoprtion and catalysis of ADH with NAD tethered to the surface of thiol terminated SiNPs, along with Langmuir adsorption kinetics of GluDH has allowed the surface complexation and catalysis kinetics of GluDH with tethered NAD to be determined by numerical integration modelling. Similar to the mono-enzyme kinetic analysis performed in Chapters 6 and 7, a kinetic enhancement in the kinetics of multi-enzyme cofactor regenerating catalysis of NAD tethered to the surface of thiol terminated SiNPs has been revealed. The rate constant for the oxidation of surface tethered NADH by GluDH k_{cat} was found to be enhanced by ~5 fold compared to free NAD with a ~20% enhancement in the forward complexation rate constant k_1.

8.6 Conclusion

NAD tethered to the surface of thiol terminated SiNPs has been applied to a multi-enzyme cofactor regenerating coupled reaction of ADH and GluDH. The colourless acetaldehyde produced in the reaction was reacted with 2,4-dinitrophenylhydrazine (DNP), converting it into the highly coloured yellow acetaldehyde-2,4-dinitrophenylhydrazine (ADNP) which was simply, sensitively and efficiently separated and quantified by HPLC analysis. This method was used to detect the formation of acetaldehyde over time at different free NAD and thiol SiNP tethered NAD concentrations. A mechanism involving the competitive adsorption of ADH and GluDH to the particle surface, complexation and catalysis of surface tethered NAD by ADH, complexation and catalysis of adsorbed GluDH with surface tethered NADH, regenerating NAD, was proposed. Numerical integration by Euler's method was then used, along with rate constants for adsorption, complexation and catalysis of ADH with surface tethered NAD determined in Chapter 6 and the Langmuir adsorption kinetics for GluDH determined in Chapter 5, in order to model the highly complex reaction. This allowing the determination of the complexation and catalysis rate constants of GluDH with surface tethered NADH, revealing a 20% enhancement in k_1 and a 5 fold enhancement in k_{cat} compared to the equivalent free NAD reaction.

CHAPTER 9 : STABILITY OF SINP TETHERED NAD

9.1 Overview

In this chapter, the stability of NAD tethered to the surface of thiol terminated SiNPs is investigated and compared to that of free NAD. SiNP tethered NAD and free NAD are heated at between 37°C and 100°C with aliquots taken at different time points and applied to the EcG3PD catalysed reaction performed at 37°C. The change in EcG3PD activity is is determined to be a first order process with a 16-fold longer half-life for the tethered NAD compared to free NAD.

In a second part of this chapter, the thermal stability of EcG3PD in dynamic adsorption equilibrium with the surface of thiol terminated SiNPs with tethered NAD is also investigated, revealing an 11-fold enhancement in thermal stability compared to freely diffusing EcG3PD.

9.2 Introduction

The instability of enzymes to heat, long term use, pH and harsh solvents is one of the biggest challenges in the field of biocatalysis [179]. Several different methods have been used to stabilise biocatalysts including the use of thermophilic enzymes, genetic engineering and immobilisation [179, 180].

Immobilisation of enzymes onto the surface of nanoparticles has been shown to enhance their stability while facilitating simplistic product separations [27, 121, 179-181]. Multimeric oxidoreductases, such as EcG3PD and ADH, are highly sensitive to extreme temperature, pH and co-solvents, which cause dissociation of the enzyme subunits and their subsequent deactivation. [182, 183] The stability of oxidoreductase enzymes is therefore a fundamental limitation of their use in industrial biocatalytic processes. Strategies to improve the stability of oxidoreductase enzymes include protein engineering, chemical crosslinking and immobilisation by covalent bonding, entrapment or adsorption [182, 183]. However, immobilisation of oxidoreductases rarely results in both enhanced stability and maintained enzyme activity. Enzymes isolated from thermophilic bacteria, as well as enzymes genetically modified to be heat resistant offer enhanced rates at high temperatures [179]. However, the degradation products of the hydrolytic cleavage of NAD have been shown to inhibit the catalysis of these enzymes [184].

Several reports have investigated the thermal degradation of NAD [168, 184-186] and it has been shown to proceed by the hydrolytic cleavage of the nicotinamide-ribose linkage, generating nicotinamide and adenosine diphosphate ribose (ADP-ribose) as shown in Figure 9.1 [168, 184]. The disappearance of NAD due to thermal degradation has been quantified by several methods. These include a UV/Vis cyanide assay [168, 186], HPLC analysis [184, 185] and using ADH to track the decrease in enzymatic reaction rate due to NAD degradation as illustrated in Figure 8.2 [168]. The high cost and instability of NAD necessitates its stabilisation for the development of industrially viable biosynthetic processes [185]. Therefore, the enhancement of the thermal stability of NAD has the potential to significantly improve the efficiency of these systems.

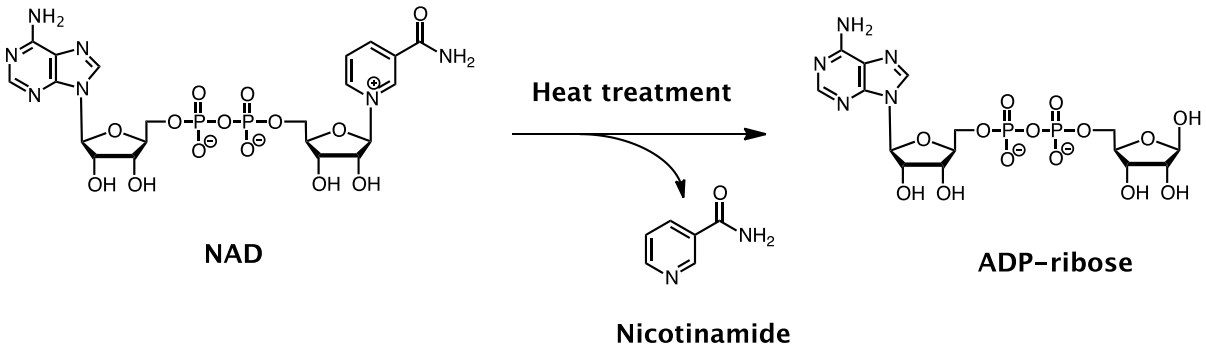

Figure 9.1: Thermal degradation of NAD to nicotinamide and ADP-ribose. Adapted from [184].

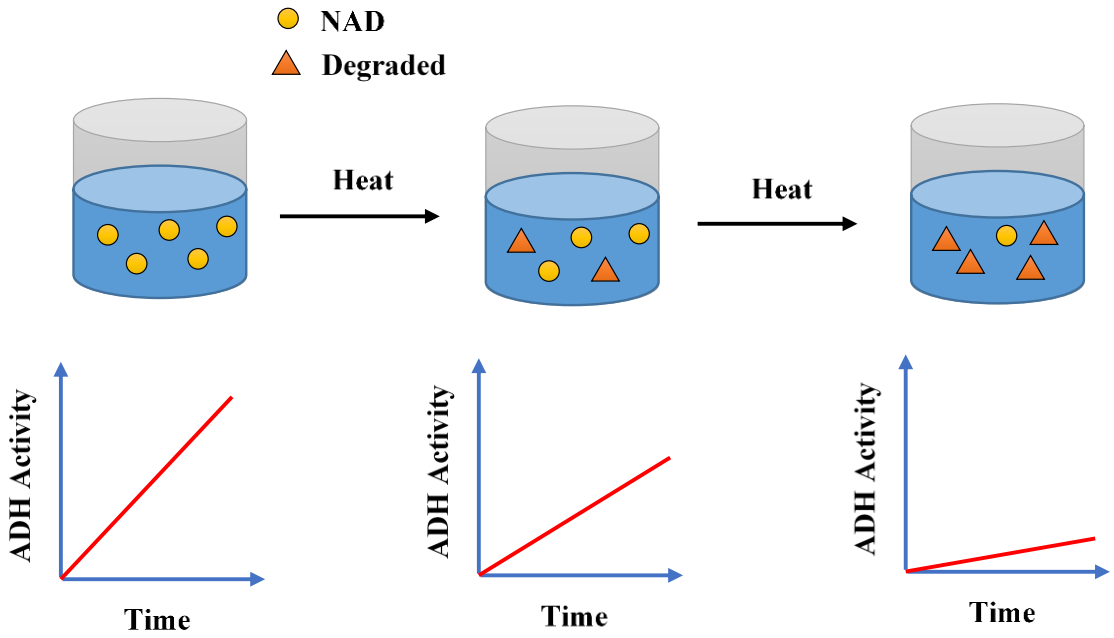

Figure 9.2: Method for tracking the decrease in NAD concentration due to thermal degradation by tracking the decrease in ADH activity with NAD [168].

In this chapter, the thermal stability of NAD tethered to the surface of thiol terminated SiNPs compared to free NAD is investigated. This is achieved by determining the change in reaction rate of EcG3PD due to the thermal degradation of free and SiNP tethered NAD at 37°C and 100°C. Degradation of NAD is shown to follow first order kinetics, allowing the extraction of the degradation rate constant (k) and half-life ($t_{1/2}$). The thermal stability of EcG3PD in adsorption equilibrium with the surface of thiol terminated SiNPs with tethered NAD is then determined at 60°C by a similar method and compared to free EcG3PD.

9.3 Analysis of the thermal stability of tethered NAD

The stability of tethered NAD and free NAD was investigated by heating the particles and solution respectively at two different temperatures, 37 °C and 100 °C. Small aliquots were taken during the heating process and refrigerated until all samples had been collected. The heat treated tethered NAD was subsequently used in a EcG3PD catalysed reaction and the activity was determined using the resazurin/PMS^+ coupled assay.

Figure 9.2(a-b) shows the decrease in EcG3PD activity with increasing heating time of the NAD. This decrease in activity is attributed to the thermal degradation of free and SiNP tethered NAD and can thus be used to indicate the change in concentration of NAD over time as shown in Figure 9.2(c) [168]. The linear relationship between ln[NAD] and heating time as shown in Figure 9.2(d) indicates that the thermal degradation of both free NAD and tethered NAD are first order reactions with a first order rate constant of 0.0198 $hour^{-1}$ and 0.0012 $hour^{-1}$, respectively. This allows the stability of free and SiNP tethered NAD to be expressed as the half-life ($t_{1/2}$), the time taken for half of NAD to be thermally degraded under given conditions as calculated by:

$$t_{\frac{1}{2}} = \frac{ln2}{k} \tag{9.1}$$

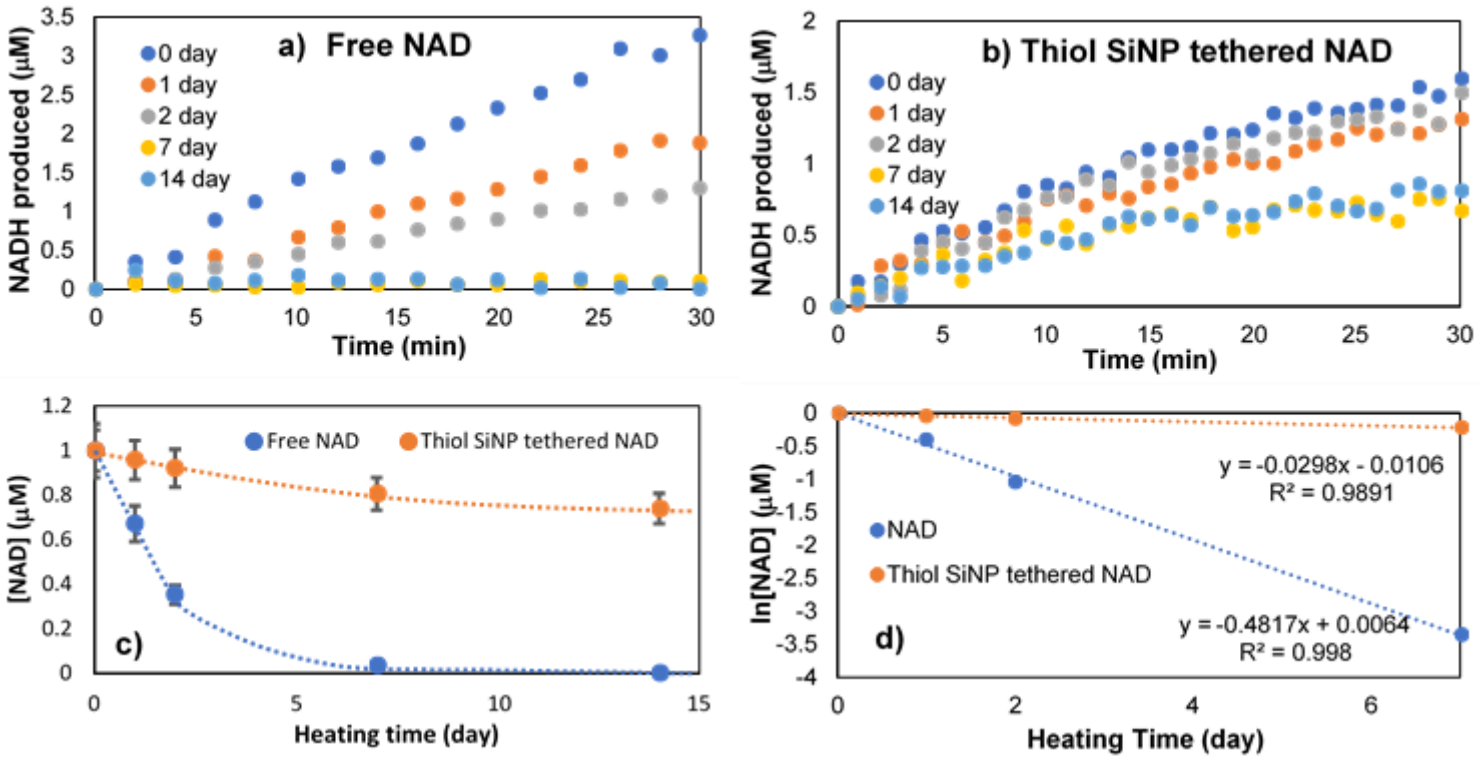

Figure 9.2: Increase in total NADH production over time as indicated by the resazurin/PMS^+ fluorometric assay of EcG3PD with (a) free NAD (b) thiol SiNP tethered NAD heated at 37°C for up to 14 days. The change in activity is then plotted as a function of heating time (c) and a first order kinetics plot between ln[NAD] and heating time (d).

Figure 9.2(c) shows a steep decline in free NAD concentration (blue line) over the first 7 days of heating. No EcG3PD activity was detected with NAD heated at 37°C after 7 days. NAD tethered to the surface of thiol terminated SiNPs appeared to degrade at a much slower rate, with ~25% degradation after 14 days of heating at 37°C, as indicated by the decrease in EcG3PD activity in Figure 9.2(b).

In order to test the applicability of SiNP tethered NAD to high temperature systems, NAD tethered to the surface of thiol terminated SiNPs was heated at 100 °C for 12 hours and evaluated using a similar procedure to that above. The resazurin/PMS^+ coupled assay of the heat-treated NAD activity is shown in Figure 9.3(a-b) and the change in NAD concentration as indicated by the change in EcG3PD reaction rate is plotted as a function of heating time as shown in Figure 9.3(c).

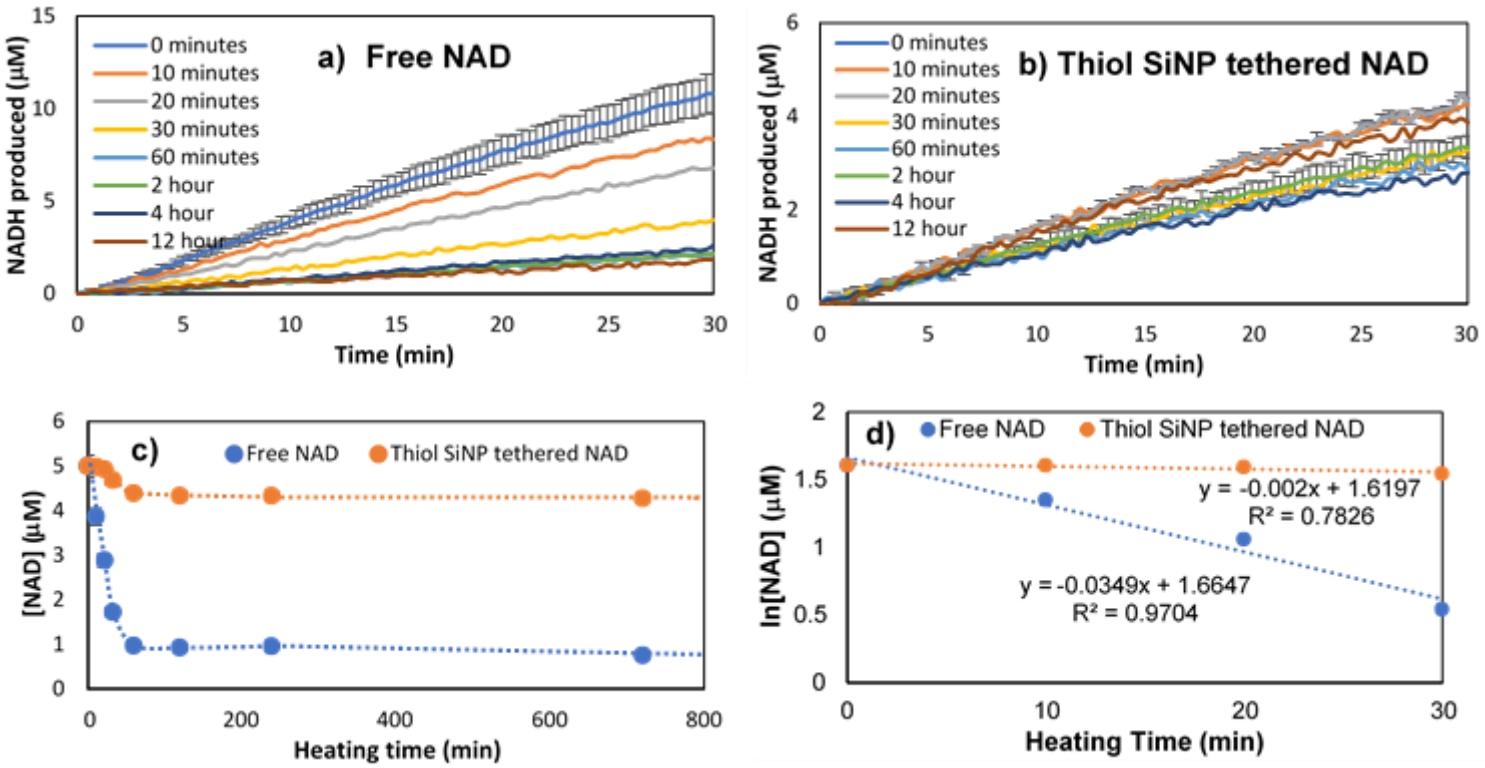

Figure 9.3: Increase in total NADH production over time as indicated by the resazurin/PMS^+ fluorometric assay of EcG3PD with (a) free NAD (b) thiol SiNP tethered NAD heated at 100 °C for up to 12 hours. The change in activity is assumed to be due to thermal degradation of NAD, which is then plotted as a function of heating time (c) and a first order kinetics plot between ln[NAD] and heating time (d).

Figure 9.3(c) shows a rapid decrease in the concentration of free NAD within the first 60 minutes of heating at 100 °C, as indicated by the decrease in EcG3PD reaction rate with heat treated free NAD (Figure 9.3(a)). The first order kinetics plot in Figure 9.3(d) allowed the extraction of the first order rate degradation constants of free and tethered NAD, which were determined to be 2.09 $hour^{-1}$ and 0.138 $hour^{-1}$, respectively.

Table 8.1 shows the first order rate constant of degradation and half-life of free and SiNP tethered NAD determined at 37 °C and 100 °C. At 37 °C, free NAD degraded with a first order rate constant of 0.0198 $hour^{-1}$ and with a 34.5-hour half-life. The first order rate constant of tethered NAD degradation was found to be 0.0012 $hour^{-1}$ and

exhibited a 558-hour half-life. This equates to a remarkable ~15-fold enhancement in the half-life of NAD tethered to the surface of thiol terminated SiNPs compared to free NAD. This large enhancement in long-term thermal stability of NAD under operational temperature has the potential to allow NAD dependent biosynthetic processes to be performed over much longer time periods without replacement of NAD, significantly increasing the efficiency of these processes.

At 100 °C, the first order rate constant of degradation of free NAD was found to be 2.09 $hour^{-1}$ with a 20-minute half-life. As above, NAD tethered to the surface of thiol terminated SiNPs degrades at a much slower rate, degrading just 15% after 12 hours of heating at 100 °C with a first order rate constant of 0.138 $hour^{-1}$ and a half-life of 5 hours. Similarly to the degradation analysis at 37 °C, the half-life of SiNP tethered NAD at 100°C is enhanced by ~15 fold compared to free NAD. NAD is known to thermally degrade by the hydrolytic cleavage of the nicotinamide-ribose linkage as shown in Figure 9.1 [168, 184]. Therefore, the observed increase in thermal stability of SiNP tethered NAD suggests a mechanism that reduces the rate of this hydrolytic process. Similarly, the observed enhancement of the thermal stability of NAD tethered to the surface of thiol terminated SiNPs implicates extended use in biosynthetic applications at physiological and high operational temperatures. This has the potential to increase the efficiency of these processes by reducing costs associated with constant replacement of costly cofactors.

Table 9.1: First order rate constants of degradation (k) and half-lives ($t_{1/2}$) of free and SiNP tethered NAD at 37 °C and 100 °C.

	37 °C		100 °C	
	k ($hour^{-1}$)	$t_{1/2}$ (hour)	k ($hour^{-1}$)	$t_{1/2}$ (hour)
Free NAD	0.0198	34.5	2.09	0.33
Thiol SiNP tethered NAD	0.0012	558	0.138	5
Enhancement (fold)	16		15	

Table 9.2 shows the values of the first order rate constant of the degradation of free NAD and the corresponding half-lives measured under similar conditions found in the literature [168, 184]. The experimentally determined values agree well with these literature values and also fit to make a linear Arrhenius plot in Figure 9.4.

Table 9.2: Literature values of the rate of thermal degradation and half-life of free NAD.

Ref	Temperature	Method	k ($hour^{-1}$)	$t_{1/2}$ (hour)
[184]	85 °C	HPLC	1.73	0.4
[168]	100 °C	ADH assay	3	0.17

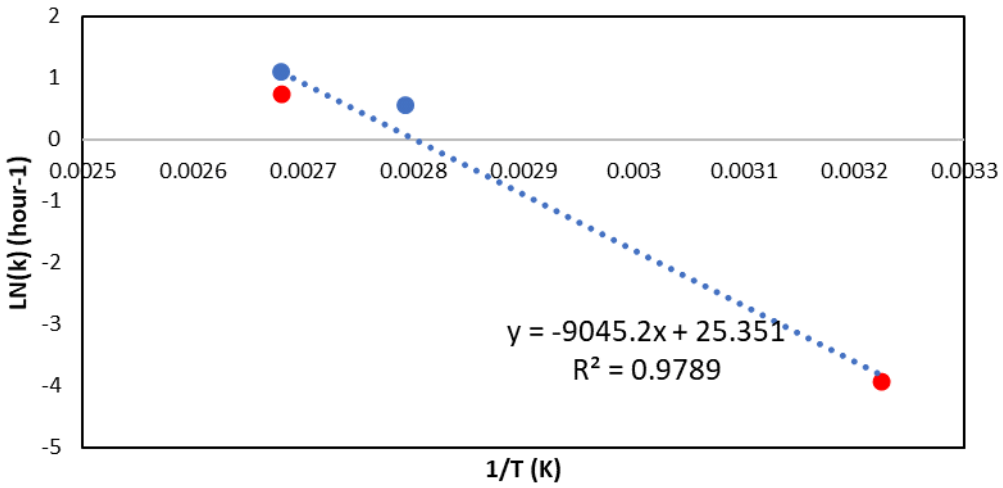

Figure 9.4: Arrhenius plot including literature rate constants (blue) and our experimental rate constants (red) [168, 184].

9.4 Stability of EcG3PD

The thermal stability of EcG3PD while in a dynamic adsorption equilibrium with the surface of thiol terminated SiNPs compared to EcG3PD free in solution was investigated.

EcG3PD adsorbed onto the surface of thiol terminated SiNPs by mixing for one hour and separated by centrifugation. The quantity of EcG3PD adsorbed onto the particle surface was determined by UV/Vis analysis at 280 nm. The SiNPs were then resuspended and heated at 60 °C for 5 hours with aliquots taken at different time points before the activity of the EcG3PD was assayed at 37 °C. This was compared to an equivalent amount of free NAD and free EcG3PD. The decrease in activity with increasing heating time was assumed to be due to only the degradation of EcG3PD, as the NAD was fresh

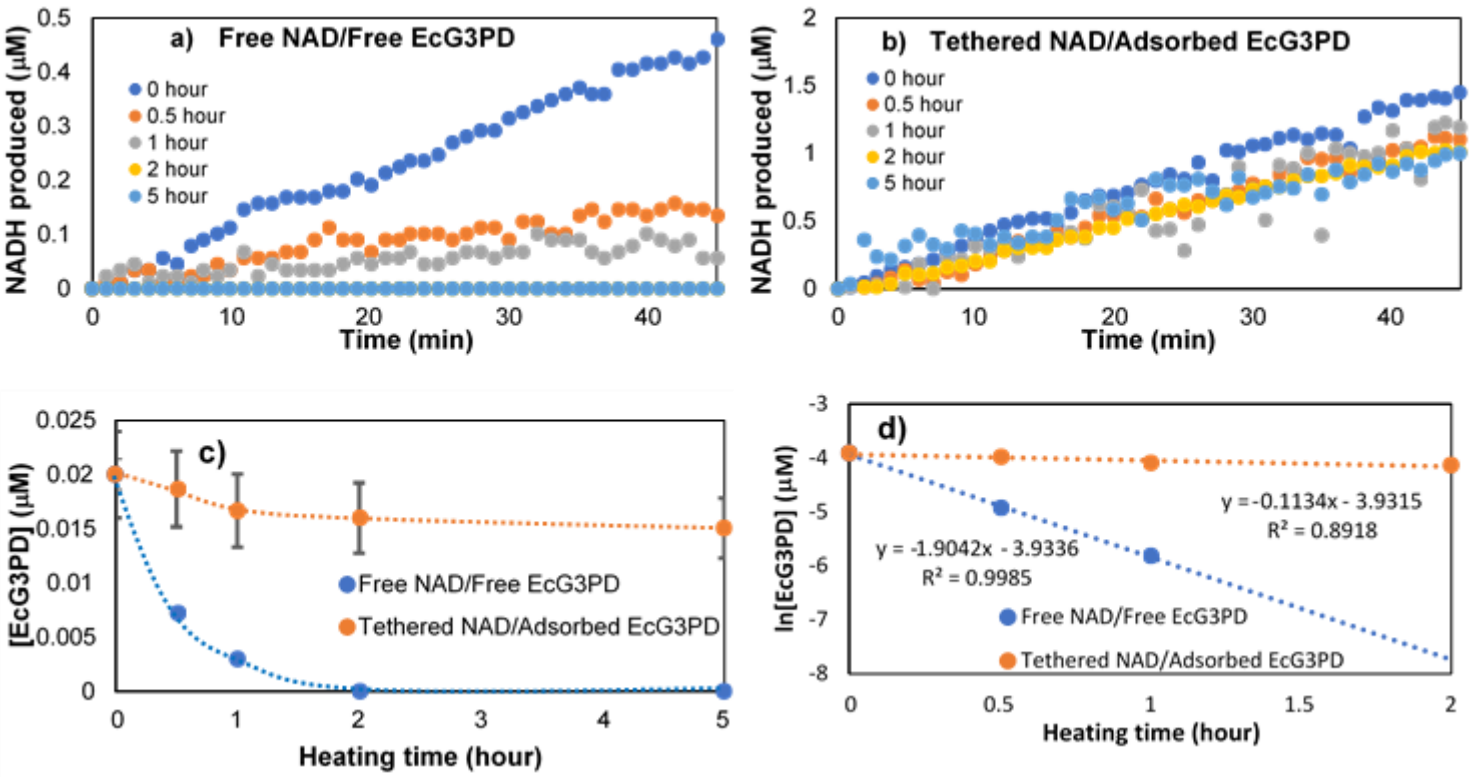

Figure 9.5: Increase in total NADH production over time in the resazurin/PMS^+ fluorometric assay of (a) heat treated free EcG3PD reacted with free NAD and (b) heat treated EcG3PD that has been in adsorption equilibrium with the surface of thiol terminated SiNPs with tethered NAD. The change in activity is assumed to be due to thermal degradation of EcG3PD, which is then plotted as a function of heating time (c) and a first order kinetics plot between ln[EcG3PD] and heating time (d).

Table 9.3: First order rate constants of degradation and half-lives of free and SiNP adsorbed EcG3PD at 60 °C.

	k ($hour^{-1}$)	$t_{1/2}$ (hour)
Free NAD/Free EcG3PD	1.9	0.36
Tethered NAD/Adsorbed EcG3PD	0.18	3.85
Enhancement (Fold)		11

Figure 9.5(c) shows a steep decline in free EcG3PD concentration (blue line) over the first 2 hours of heating. EcG3PD that was heated while in an adsorption equilibrium with the surface of thiol terminated SiNPs with tethered NAD degraded at a much

slower rate. Table 9.3 shows the first order rate constant of degradation and half-life of free and adsorbed EcG3PD determined from Figure 9.5(d). Free EcG3PD degraded with a first order rate constant of 1.9 $hour^{-1}$ and with a 22-minute half-life. The first order rate constant of adsorbed EcG3PD degradation was found to be 0.18 $hour^{-1}$ and exhibited a 3.9-hour half-life, 11-fold longer than that of free EcG3PD. Like tethered NAD, adsorption of EcG3PD to the particle surface has shown to significantly increase the thermal stability of the enzyme. Covalent immobilisation of biomolecules such as DNA [187, 188], enzymes [182, 189, 190] and pharmaceuticals [191], to the surface of nanostructures has previously been reported to enhance their thermal stability. enzymes thermally denature and deactivate in solution due to loss of tertiary structure by disruption of hydrogen bonds and hydrolysis [182]. On the nanoparticle surface, electrostatic interactions between the enzyme and surface increase structural rigidity of the quaternary structure, preventing dissociation of subunits and thus improving thermal stability [190]. The strong electrostatic interactions between EcG3PD and the thiol terminated SiNP surface investigated in Chapter 5 may therefore hold the key to the observed 11-fold enhancement in EcG3PD thermal stability at 60 °C, when in dynamic adsorption equilibrium with the SiNP surface.

9.5 Conclusion

The thermal stability of NAD tethered to the surface of thiol terminated SiNPs was investigated at 37°C and 100°C and compared to that of free NAD at an equivalent concentration. This was achieved by heating the NAD at the appropriate temperature and taking aliquots at different time points, before applying them to the EcG3PD catalysed reaction with resazurin/PMS^+ coupled fluorescence detection. The observed reduction in EcG3PD activity was assumed to be due to thermal degradation of the NAD, allowing determination of first order rate constant of degradation (k), as well as the half-life of NAD. A 16-fold enhancement in the half-life of NAD tethered to the surface of thiol terminated SiNPs was observed at 37°C, and a 15-fold enhancement at 100°C, compared to free NAD. A similar method was used to investigate the thermal stability of EcG3PD in dynamic adsorption equilibrium with the surface of thiol terminated SiNPs with tethered NAD is also investigated, revealing a 11-fold enhancement in thermal stability compared to freely diffusing EcG3PD. This shows great potential for the long term use of tethered NAD and enzymes at high operational

conditions, reducing costs associated with constant replacement of costly enzymes and cofactors.

CHAPTER 10 : CONCLUSIONS

Prior to this work, the covalent attachment of NAD to the surface of nanoparticles had only been achieved through non-specific routes without the integration of spacer arms, resulting in relatively low biocatalytic efficiencies of the tethered NAD. Most previous studies have also neglected to explore the interfacial enzyme kinetics of these systems, and a detailed knowledge of the dynamic chemistry goes unknown. Chapter 1 introduces the concept of modifying NAD at the N^6-position with intelligently designed flexible linker arms with specific terminal functionality, supplying a chemical handle for highly specific and directed chemical immobilisation while allowing the modified NAD to retain maximum native efficiency once tethered. Chapter 2 describes the detailed experimental protocol regarding the synthesis and characterisation of the chosen solid support materials, silica nanoparticles, along with the subsequent tethering and surface attachment density quantification.

The synthesis and characterisation of thiol and vinyl terminated silica nanoparticles is explored in Chapter 3, with the development of a new method for the preparation of a range of SiNPs with different terminal hydrophobic functionalities from their singular hydrophobic organosilane. The size of the SiNPs prepared using this method was demonstrated to be controlled between ~100-1000 nm by altering the organosilane precursor concentration.

Careful selection of a suitable aqueous radical initiator in Chapter 4 allowed thiol-ene 'click' chemistry to be applied to tether of N^6-linked-2AE-NAD to the surface of thiol and vinyl terminated SiNPs. Quantitative ATR-FTIR analysis revealed NAD attachment densities up to 0.5 attachments/nm^2 on the thiol and vinyl terminated SiNPs, a physically obtainable density as revealed by MD simulations.

In Chapter 5, the Langmuir adsorption isotherm is applied to determine the adsorption kinetics of the enzymes EcG3PD, ADH and GluDH onto the surface of thiol and vinyl terminated SiNPs with tethered NAD. MD simulations of the interfacial enzyme properties was used to describe the adsorption characteristics of the different enzymes

on the different surfaces, where the electrostatic interactions were found to play a significant role.

In Chapter 6, Langmuir surface adsorption kinetics were combined with classical Michaelis-Menten enzyme kinetics concepts, allowing the mathematical development of a kinetic model describing the observed rate of enzyme catalysis of surface tethered NAD as a function of enzyme concentration. Fitting experimental data to the derived kinetic model revealed enhancement in the surface complexation and surface catalysis of both EcG3PD and ADH with surface tethered NAD on thiol and vinyl terminated SiNPs compared to free NAD. These kinetic results were supported by kinetic modelling of the reaction systems using numerical integration by Eulers' method. The mechanism of the observed kinetic enhancement was proposed to be due to the high localised concentration within the SiNP surface microenvironment, where the lateral mobility of the surface adsorbed enzyme is dictated by the strength of the electrostatic interactions between enzyme and surface.

In Chapter 7, inhibition of EcG3PD by thiol terminated SiNPs was proposed to be due to non-productive adsorption of EcG3PD onto the particle surface leading to enzyme deactivation. This allowed the development of a mathematical model describing the observed rate of enzyme catalysis of surface tethered NAD as a function of NAD concentration, while accounting for inhibitory effects of non-productive EcG3PD adsorption. Fitting of experimental data to this model, resulted in the determination of kinetic rate constants for the EcG3PD comparable to those derived in Chapter 6, demonstrating the validity of the method. The observed inhibitory effects were then successfully reduced by alkylating residual surface thiols with several small alkylating agents, introducing different base surface functionality. Alkylation by iodoacetamide was shown to provide the greatest enhancement in EcG3PD activity due to the its ability to undergo resonance stabilisation to a zwitterionic conformation.

In Chapter 8, NAD tethered to the surface of thiol terminated SiNPs was regenerated an ADH/GluDH coupled reaction, where acetaldehyde produced was conjugated with 2,4-dinitrophenolhydrazine facilitating sensitive detection and quantification by HPLC analysis. The experimentally determined production of acetaldehyde with time at

different NAD concentrations was mathematically modelled using numerical integration of the proposed reaction mechanism by Euler's method allowing the complexation and catalysis kinetics of GluDH to be determined, revealing a kinetic enhancement similar to that observed in Chapters 6 and 7.

Lastly, in Chapter 9, the thermal stability of tethered NAD was investigated, along with the thermal stability of EcG3PD when it is in dynamic adsorption equilibrium with the surface of thiol terminated SiNPs with tethered NAD. Heating tethered and free NAD at physiological and an extreme temperature for resulted in a decrease in the observed EcG3PD activity with heating time. Assuming this decrease in activity to be due to thermal degradation of NAD, first order kinetics were used to determine the thermal degradation rate constants and half-lives of free and tethered NAD. Tethered NAD was found to have a ~15 fold enhancement in half-life compared to free NAD, while EcG3PD was found to have an 11~fold enhancement in thermal stability when in adsorption equilibrium.

The findings from this thesis can be summarised as:

- NAD can be covalently attached to a surface through a flexible tether arm in a highly specific way via a mild thiol-ene 'click' reaction, thereby ensuring that all attached species are available for reaction.
- The concentration of NAD on the surface of both thiol and vinyl terminated silica nanoparticles can be controlled and quantified using a simple ATR-FTIR approach, with up to 0.5 NAD molecules per square nanometre of particle surface achieved.
- The mechanism of enzymatic catalysis of surface tethered NAD involves reversible adsorption of the enzyme to the active SiNP surface, binding of the enzyme with tethered NAD and subsequent catalysis. Adsorption was found to be a highly important factor, dictated by the electrostatic interactions between the enzyme and SiNP surface, with generally stronger interactions and greater adsorption between the thiol/NAD surface and enzymes compared to the vinyl/NAD surface. EcG3PD was found to adsorb stronger than GluDH and ADH and could form multiple adsorption layers on both thiol and vinyl SiNPs.

- When the volumetric concentration of NAD is low, but the concentration of freely diffusing enzyme (EcG3PD or ADH) is sufficiently high to saturate the active surface by reversible adsorption, the rate of catalysis of SiNP tethered NAD is decreased compared to an equivalent concentration of freely diffusing NAD. This was speculated to be due to several reasons:
    - blocking of reactive NAD sites on the surface by the enzyme
    - enzyme crowding at the active surface reducing enzyme mobility
    - blocking the diffusion of other reactants to the active surface
- When both the volumetric concentrations of NAD and freely diffusing enzyme are low, less enzyme is adsorbed to the surface resulting in higher reaction rates with SiNP tethered NAD compared to freely diffusing NAD at equivalent volumetric concentrations. This was thought to be due to several reasons:
    - Less enzyme crowding at the surface allows much greater enzyme mobility and more exposed NAD reactive surface sites
    - The enzyme is effectively saturated by the high localised concentration of tethered NAD on the particle surface
- Less electrostatic attraction between the vinyl SiNP surface and EcG3PD facilitate a higher degree of surface mobility of the enzyme resulting in a greater enhancement in complexation and catalysis rate constants of NAD compared to that of the thiol SiNP surface. A similar effect was observed with ADH with thiol SiNP tethered NAD where there was little electrostatic attraction.
- When the concentration of EcG3PD is low and the volumetric concentration of NAD varied, a sharp decrease in activity was observed at a low concentration of thiol SiNP tethered NAD compared to vinyl SiNP tethered NAD. This was proposed to be due to inhibition of EcG3PD by non-productive enzyme adsorption as a result of the strong electrostatic interactions between the two. The effect of this inhibition could be accurately accounted for by using an inhibition constant derived from an inhibition plot generated using freely diffusing NAD and EcG3PD and various concentrations of unmodified thiol terminated SiNPs.
- Kinetic analysis performed using the enzyme excess and reactant excess approach gave very similar rate constants.

- Capping of residual unreacted thiols on the SiNP surface with small alkylating agents greatly reduced the surface adsorption and inhibition of EcG3PD resulting in higher reaction rates at high NAD concentrations.
- SiNP tethered NAD could be enzymatically regenerated in a coupled enzyme reaction with ADH and GluDH. Knowing the forward reaction rate constants of ADH and assuming a mechanism of competitive adsorption, followed by complexation and catalysis, allowed the rate constants of the reverse NAD regenerating GluDH reaction to be determined.
- The lifetime of NAD tethered to the surface of thiol SiNPs is significantly longer than that of freely diffusing NAD.
- The lifetime of EcG3PD is significantly increased when in adsorption equilibrium with the surface of thiol terminated SiNPs with tethered NAD.

Modification of NAD at the N^6 position of with a flexible tether arm has allowed NAD to be tethered in a highly specific orientation, facilitating the accessible binding and catalysis of all attached species with freely diffusing enzymes. Detailed and in-depth kinetic analysis of NAD with different spacer arms tethered to two different species of SiNPs with two different enzymes has revealed a great deal of information on factors that dictate the interactions, binding and catalysis of enzymes with tethered NAD. A kinetic enhancement mechanism of enzyme catalysis has been revealed at low NAD and enzyme concentrations compared to the free NAD and enzyme reaction system. This enhancement was also observed when two enzyme reactions were coupled together to regenerate the surface tethered NAD. The lifetime of NAD tethered to the surface of SiNPs and EcG3PD in adsorption equilibrium were also found to be greatly enhanced compared to their freely diffusing counterparts. Together, these factors demonstrate that SiNP tethered NAD is an ideal candidate for the integration into industrial biosynthetic processes, as well as having great potential in bio-sensing and medical applications.

CHAPTER 11 REFERENCES

1. Reetz, M.T., *Biocatalysis in organic chemistry and biotechnology: past, present, and future.* J Am Chem Soc, 2013. **135**(34): p. 12480-96.
2. Gomaa, A.M., *Application of Enzymes in Brewing.* Journal of Nutrition and Food Science Forecast, 2018. **1**(1): p. 1002.
3. Illanes, A., et al., *Heterogeneous Enzyme Kinetics*, in *Enzyme Biocatalysis*. 2008. p. 155-203.
4. Vranish, J.N., et al., *Pursuing the Promise of Enzymatic Enhancement with Nanoparticle Assemblies.* Langmuir, 2018. **34**(9): p. 2901-2925.
5. Truppo, M.D., *Biocatalysis in the Pharmaceutical Industry: The Need for Speed.* ACS Med Chem Lett, 2017. **8**(5): p. 476-480.
6. Choi, J.-M., S.-S. Han, and H.-S. Kim, *Industrial applications of enzyme biocatalysis: Current status and future aspects.* Biotechnology Advances, 2015. **33**(7): p. 1443-1454.
7. Zhao, H. and W.A. van der Donk, *Regeneration of cofactors for use in biocatalysis.* Current Opinion in Biotechnology, 2003. **14**(6): p. 583-589.
8. Illanes, A., et al., *Recent trends in biocatalysis engineering.* Bioresour Technol, 2012. **115**: p. 48-57.
9. Wong, K.M.K.C.-H., *Enzymes for chemical synthesis.* Nature, 2001. **409**: p. 232-240.
10. Sheldon, R.A., *Enzyme Immobilization: The Quest for Optimum Performance.* Advanced Synthesis & Catalysis, 2007. **349**(8-9): p. 1289-1307.
11. Burton, S.G., *Development of bioreactors for application of biocatalysts in biotransformations and bioremediation.* Pure Appl. Chem., 2001. **73**(1): p. 77-83.
12. Li, J., L. Zhang, and W. Liu, *Cell-free synthetic biology for in vitro biosynthesis of pharmaceutical natural products.* Synth Syst Biotechnol, 2018. **3**(2): p. 83-89.
13. Korman, T.P., P.H. Opgenorth, and J.U. Bowie, *A synthetic biochemistry platform for cell free production of monoterpenes from glucose.* Nat Commun, 2017. **8**: p. 15526.
14. Hartley, C.J., et al., *Sugar analog synthesis by in vitro biocatalytic cascade: A comparison of alternative enzyme complements for dihydroxyacetone phosphate production as a precursor to rare chiral sugar synthesis.* PLoS One, 2017. **12**(11): p. e0184183.
15. Toru Nagasawa, M.W., Tetsuji Nakamura, Hitomi Iwahara, Toyokazu Yoshida and Kunihiko Gekko, *Nitrilase of Rhodococcus rhodochrous J1 Conversion into the active form by subunit association.* Eur J Biochem, 2000. **267**: p. 138-144.
16. Desai, A.A., *Sitagliptin manufacture: a compelling tale of green chemistry, process intensification, and industrial asymmetric catalysis.* Angew Chem Int Ed Engl, 2011. **50**(9): p. 1974-6.
17. Christopher K. Savile, J.M.J., Emily C. Mundorff, Jeffrey C. Moore, Sarena Tam, William R. Jarvis, Jeffrey C. Colbeck, Anke Krebber, Fred J. Fleitz, Jos Brands, and G.W.H. Paul N. Devine, Gregory J. Hughes, *Biocatalytic Asymmetric Synthesis of Chiral Amines from Ketones Applied to Sitagliptin Manufacture.* Science, 2010. **329**: p. 305-309.
18. El-Zahab, B., D. Donnelly, and P. Wang, *Particle-tethered NADH for production of methanol from CO(2) catalyzed by coimmobilized enzymes.* Biotechnol Bioeng, 2008. **99**(3): p. 508-14.
19. Vranish, J.N., et al., *Enhancing Coupled Enzymatic Activity by Colocalization on Nanoparticle Surfaces: Kinetic Evidence for Directed Channeling of Intermediates.* ACS Nano, 2018. **12**(8): p. 7911-7926.
20. Vranish, J.N., et al., *Enhancing coupled enzymatic activity by conjugating one enzyme to a nanoparticle.* Nanoscale, 2017. **9**(16): p. 5172-5187.
21. Smith, M.T., et al., *The emerging age of cell-free synthetic biology.* FEBS Lett, 2014. **588**(17): p. 2755-61.
22. Jia, H., G. Zhu, and P. Wang, *Catalytic behaviors of enzymes attached to nanoparticles: the effect of particle mobility.* Biotechnol Bioeng, 2003. **84**(4): p. 406-14.

23. Velasco-Lozano, S., A.I. Benitez-Mateos, and F. Lopez-Gallego, *Co-immobilized Phosphorylated Cofactors and Enzymes as Self-Sufficient Heterogeneous Biocatalysts for Chemical Processes.* Angew Chem Int Ed Engl, 2017. **56**(3): p. 771-775.
24. Malanoski, A.P., et al., *Kinetic enhancement in high-activity enzyme complexes attached to nanoparticles.* Nanoscale Horizons, 2017. **2**(5): p. 241-252.
25. Keon Hee Kim, O.K.L.a.E.Y.L., *Nano-Immobilized Biocatalysts for Biodiesel Production from Renewable and Sustainable Resources.* Catalysts, 2018. **8**(2).
26. Kim, J., J.W. Grate, and P. Wang, *Nanobiocatalysis and its potential applications.* Trends Biotechnol, 2008. **26**(11): p. 639-46.
27. Verma, M.L., C.J. Barrow, and M. Puri, *Nanobiotechnology as a novel paradigm for enzyme immobilisation and stabilisation with potential applications in biodiesel production.* Appl Microbiol Biotechnol, 2013. **97**(1): p. 23-39.
28. Olga V. Shulga, K.J., Abdul R. Khan, Valerian T. D'Souza, Jingyue Liu, Alexei V. Demchenko, and Keith J. Stine, *Preparation and Characterization of Porous Gold and Its Application as a Platform for Immobilization of Acetylcholine Esterase.* Chem. Mater., 2007. **19**: p. 3902-3911.
29. Dai, T., et al., *Electrospinning of Poly[acrylonitrile-co-(glycidyl methacrylate)] Nanofibrous Mats for the Immobilization of Candida Antarctica Lipase B.* Macromolecular Chemistry and Physics, 2010: p. n/a-n/a.
30. Forest, V., et al., *Adsorption of lactate dehydrogenase enzyme on carbon nanotubes: how to get accurate results for the cytotoxicity of these nanomaterials.* Langmuir, 2015. **31**(12): p. 3635-43.
31. Fu, J., et al., *Assembly of multienzyme complexes on DNA nanostructures.* Nature Protocols, 2016. **11**(11): p. 2243-2273.
32. Xu, S., et al., *Real-time reliable determination of binding kinetics of DNA hybridization using a multi-channel graphene biosensor.* Nat Commun, 2017. **8**: p. 14902.
33. Diaz, S.A., et al., *Elucidating Surface Ligand-Dependent Kinetic Enhancement of Proteolytic Activity at Surface-Modified Quantum Dots.* ACS Nano, 2017. **11**(6): p. 5884-5896.
34. McKay, C.S. and M.G. Finn, *Polyvalent Catalysts Operating on Polyvalent Substrates: A Model for Surface-Controlled Reactivity.* Angew Chem Int Ed Engl, 2016. **55**(41): p. 12643-9.
35. Li, B., et al., *An Enzyme Net Coating the Surface of Nanoparticles: A Simple and Efficient Method for the Immobilization of Phospholipase D.* Industrial & Engineering Chemistry Research, 2016. **55**(40): p. 10555-10565.
36. Zheng, M., et al., *Effect of molecular mobility on coupled enzymatic reactions involving cofactor regeneration using nanoparticle-attached enzymes.* J Biotechnol, 2011. **154**(4): p. 274-80.
37. Karimi, M., *Immobilization of lipase onto mesoporous magnetic nanoparticles for enzymatic synthesis of biodiesel.* Biocatalysis and Agricultural Biotechnology, 2016. **8**: p. 182-188.
38. Richter, M., *Functional diversity of organic molecule enzyme cofactors.* Nat Prod Rep, 2013. **30**(10): p. 1324-45.
39. A. Schmid, J.S.D., B. Hauer, A. Kiener, M. Wubbolts|| & B. Witholt, *Industrial biocatalysis today and tomorrow.* Nature, 2001. **409**: p. 258-268.
40. Nelson, D.L., et al., *Lehninger principles of biochemistry*. 2008, New York: W.H. Freeman.
41. Petkova, G.A., K. Zaruba, and V. Kral, *Synthesis of silica particles and their application as supports for alcohol dehydrogenases and cofactor immobilizations: conformational changes that lead to switch in enzyme stereoselectivity.* Biochim Biophys Acta, 2012. **1824**(6): p. 792-801.
42. Kawasaki, S., et al., *Purification and characterization of an H2O-forming NADH oxidase from Clostridium aminovalericum: existence of an oxygen-detoxifying enzyme in an obligate anaerobic bacteria.* Arch Microbiol, 2004. **181**(4): p. 324-30.

43. Liu, W. and P. Wang, *Cofactor regeneration for sustainable enzymatic biosynthesis.* Biotechnol Adv, 2007. **25**(4): p. 369-84.
44. Demir, A.S., et al., *Selective oxidation and reduction reactions with cofactor regeneration mediated by galactitol-, lactate-, and formate dehydrogenases immobilized on magnetic nanoparticles.* J Biotechnol, 2011. **152**(4): p. 176-83.
45. Luis P. Candeias, D.P.S.M., Sean L. W. McWhinnie, Nicola L. Maidwell, and P.G.S.a.R.W. Carl A. Roeschlaub, *The catalysed NADH reduction of resazurin to resorufin.* J. Chem. Soc., 1998. **2**: p. 2333-2334.
46. Yano, O.M.a.T., *Electrochemical bioreactor with regeneration of NAD+ by rotating graphite disk electrode with PMS adsorbed.* Enzyme and Microbial Technology, 1992. **14**: p. 474-478.
47. Gomez-Moreno, J.J.P.a.C., *Photochemical regeneration of NADPH using the enzyme ferredoxin-NADP+ reductase.* Enzyme and Microbial Technology, 1992. **14**(8-12).
48. Liu, W., S. Zhang, and P. Wang, *Nanoparticle-supported multi-enzyme biocatalysis with in situ cofactor regeneration.* J Biotechnol, 2009. **139**(1): p. 102-7.
49. Xiaoyuan Ji, Z.S., Ping Wang, Guanghui Ma, and Songping Zhang, *Tethering of Nicotinamide Adenine Dinucleotide Inside Hollow Nanofibers for High-Yield Synthesis of Methanol from Carbon Dioxide Catalyzed by Coencapsulated Multienzymes.* ACS Nano, 2015. **9**(4): p. 4600-4610.
50. Chen, G., Z. Wu, and Y. Ma, *A novel method for preparation of MNP@CS-tethered coenzyme for coupled oxidoreductase system.* J Biotechnol, 2015. **196-197**: p. 52-7.
51. Narvaez Villarrubia, C.W., et al., *NAD+/NADH Tethering on MWNTs-Bucky Papers for Glucose Dehydrogenase-Based Anodes.* Journal of the Electrochemical Society, 2014. **161**(13): p. H3020-H3028.
52. Fu, J., et al., *Multi-enzyme complexes on DNA scaffolds capable of substrate channelling with an artificial swinging arm.* Nat Nanotechnol, 2014. **9**(7): p. 531-6.
53. Zheng, M., et al., *Magnetic field intensified bi-enzyme system with in situ cofactor regeneration supported by magnetic nanoparticles.* J Biotechnol, 2013. **168**(2): p. 212-7.
54. Li, Y., et al., *Nanoparticle-tethered NAD(+) with in situ cofactor regeneration.* Biotechnol Lett, 2013. **35**(6): p. 915-9.
55. Zhang, Y., et al., *Simultaneous production of 1,3-dihydroxyacetone and xylitol from glycerol and xylose using a nanoparticle-supported multi-enzyme system with in situ cofactor regeneration.* Bioresour Technol, 2011. **102**(2): p. 1837-43.
56. Wilner, O.I., et al., *Enzyme cascades activated on topologically programmed DNA scaffolds.* Nat Nanotechnol, 2009. **4**(4): p. 249-54.
57. Wang, P., et al., *Enabling multienzyme bioactive systems using a multiscale approach.* China Particuology, 2005. **3**(6): p. 304-309.
58. Riva, S., et al., *Effect of coupling site and nature of the polymer on the coenzymatic properties of water-soluble macromolecular NAD derivatives with selected dehydrogenase enzymes.* Enzyme and Microbial Technology, 1986. **8**(9): p. 556-560.
59. Chang, J.C.a.T.M.S., *The Recycling of NAD+ (Free and Immobilized) Within Semipermeable Aqueous Microcapsules Containing a Multi-Enzyme System.* Biochemical and Biophysical Research communications, 1976. **69**(2).
60. Lyagin, E., et al., *Continuous membrane-based screening system for biocatalysis.* Membranes (Basel), 2011. **1**(1): p. 70-9.
61. Johannes, T.W., R.D. Woodyer, and H. Zhao, *Efficient regeneration of NADPH using an engineered phosphite dehydrogenase.* Biotechnology and Bioengineering, 2007. **96**(1): p. 18-26.
62. Lütz, S., N.N. Rao, and C. Wandrey, *Membranes in Biotechnology.* Chemical Engineering & Technology, 2006. **29**(12): p. 1404-1415.
63. J.R. WYKES, P.D., M.D. LILIY, *THE PREPARATION OF SOLUBLE HIGH MOLECULAR WEIGHT NAD DERIVATIVE ACTIVE AS A COFACTOR.* Biochim Biophys Acta, 1972. **286**: p. 260-268.

64. Raweewan Klaewkla, M.A.a.W.F.H., *A Review of Mass Transfer Controlling the Reaction Rate in Heterogeneous Catalytic Systems.* Mass Transfer - Advanced Aspects, 2011: p. 667-684.
65. Vartzouma, C., et al., *Synthesis and characterization of NAD+-modified silica: a convenient immobilization of biomolecule via its phosphate group.* Materials Science and Engineering: C, 2004. **24**(4): p. 473-477.
66. Zappelli, P., A. Rossodivita, and L. Re, *Synthesis of Coenzymically Active Soluble and Insoluble Macromolecularized NAD+ Derivatives.* European Journal of Biochemistry, 1975. **54**(2): p. 475-482.
67. Wykes, J.R., P. Dunnill, and M.D. Lilly, *Cofactor recycling in an enzyme reactor. A comparison Using free and immobilized dehydrogenases with free and immobilized NAD.* Biotechnology and Bioengineering, 1975. **17**(1): p. 51-68.
68. Ukeda, H., et al., *Co-immobilization of Alcohol Dehydrogenase, Diaphorase and NAD and Its Application to Flow Injection Analytical System for Ethanol.* Agricultural and Biological Chemistry, 1989. **53**(11): p. 2909-2915.
69. Forde, J., et al., *Fundamental differences in bioaffinity of amino acid dehydrogenases for N6- and S6-linked immobilized cofactors using kinetic-based enzyme-capture strategies.* Anal Biochem, 2005. **338**(1): p. 102-12.
70. Bückmann AF, K.M., Wichmann R, Wandrey C, *An efficient synthesis of high-molecular-weight NAD(H) derivatives suitable for continuous operation with cofactor-dependent enzyme systems.* J Appl Biochem, 1981. **3**(1): p. 301-315.
71. Mangos, D.N., T. Nakanishi, and D.A. Lewis, *A simple method for the quantification of molecular decorations on silica particles.* Science and Technology of Advanced Materials, 2014. **15**(1): p. 015002.
72. Liu, M., et al., *A DNA tweezer-actuated enzyme nanoreactor.* Nat Commun, 2013. **4**: p. 2127.
73. Carcouet, C.C., et al., *Nucleation and growth of monodisperse silica nanoparticles.* Nano Lett, 2014. **14**(3): p. 1433-8.
74. Davies, G.-L., A. Barry, and Y.K. Gun'ko, *Preparation and size optimisation of silica nanoparticles using statistical analyses.* Chemical Physics Letters, 2009. **468**(4-6): p. 239-244.
75. Takeda, Y., Y. Komori, and H. Yoshitake, *Direct stöber synthesis of monodisperse silica particles functionalized with mercapto-, vinyl- and aminopropylsilanes in alcohol–water mixed solvents.* Colloids and Surfaces A: Physicochemical and Engineering Aspects, 2013. **422**: p. 68-74.
76. Effati, E. and B. Pourabbas, *One-pot synthesis of sub-50nm vinyl- and acrylate-modified silica nanoparticles.* Powder Technology, 2012. **219**: p. 276-283.
77. Ishimura, M.N.a.K., *One-Pot Synthesis and Characterization of Three Kinds of Thiol-Organosilica Nanoparticles.* Langmuir, 2008. **24**: p. 5099-5108.
78. Qhobosheane, M., et al., *Biochemically functionalized silica nanoparticles.* The Analyst, 2001. **126**(8): p. 1274-1278.
79. WERNER STOBER, A.F., *Controlled Growth of Monodisperse Silica Spheres in the Micron Size Range.* Journal of Colloid and Interface Science, 1968. **26**: p. 62-69.
80. Lim, J.-H., S.-W. Ha, and J.-K. Lee, *Precise Size-control of Silica Nanoparticles via Alkoxy Exchange Equilibrium of Tetraethyl Orthosilicate (TEOS) in the Mixed Alcohol Solution.* Bulletin of the Korean Chemical Society, 2012. **33**(3): p. 1067-1070.
81. Tavassoli, M., et al., *Copper Dithiol Complex Supported on Silica Nanoparticles: A Sustainable, Efficient, and Eco-friendly Catalyst for Multicomponent Click Reaction.* ACS Sustainable Chemistry & Engineering, 2016. **4**(3): p. 1454-1462.
82. Han, S.W., et al., *Polydimethylsiloxane thin-film coating on silica nanoparticles and its influence on the properties of SiO 2 –polyethylene composite materials.* Polymer, 2018. **138**: p. 24-32.
83. Véliz, B., et al., *Impedance modeling of silica nanoparticle metal insulator metal capacitors.* Electrochimica Acta, 2018. **280**: p. 62-70.

84. Ding, M., et al., *The excellent anti-wear and friction reduction properties of silica nanoparticles as ceramic water lubrication additives.* Ceramics International, 2018. **44**(12): p. 14901-14906.
85. Dhapte, V., et al., *Versatile SiO2 Nanoparticles@Polymer Composites with Pragmatic Properties.* ISRN Inorganic Chemistry, 2014. **2014**: p. 1-8.
86. Aydogan, C. and Z. El Rassi, *Monolithic stationary phases with incorporated fumed silica nanoparticles. Part I. Polymethacrylate-based monolithic column with incorporated bare fumed silica nanoparticles for hydrophilic interaction liquid chromatography.* J Chromatogr A, 2016. **1445**: p. 55-61.
87. Ruizendaal, L., et al., *Biofunctional silicon nanoparticles by means of thiol-ene click chemistry.* Chem Asian J, 2011. **6**(10): p. 2776-86.
88. Han, Y., et al., *Unraveling the Growth Mechanism of Silica Particles in the Stober Method: In Situ Seeded Growth Model.* Langmuir, 2017. **33**(23): p. 5879-5890.
89. Liberman, A., et al., *Synthesis and surface functionalization of silica nanoparticles for nanomedicine.* Surf Sci Rep, 2014. **69**(2-3): p. 132-158.
90. Schladt, T.D., et al., *Synthesis and bio-functionalization of magnetic nanoparticles for medical diagnosis and treatment.* Dalton Trans, 2011. **40**(24): p. 6315-43.
91. C. C. Ballard, E.C.B., R. K. Iler, D. S. St. John and J. R. McWhorter, *ESTERIFICATION OF THE SURFACE OF AMORPHOUS SILICA.* The Journal of Physical Chemistry, 1961. **65**(1): p. 20-25.
92. Azioune, A.S., Amel Ben ; Hamou, Lobnat Ait ; Pleuvy, Anne ; Chehimi, Mohamed M ; Perruchot, Christian ; Armes, Steven P, *Synthesis and Characterization of Active Ester-Functionalized Polypyrrole−Silica Nanoparticles: Application to the Covalent Attachment of Proteins.* Langmuir, 2004. **20**(8): p. 3350-3356.
93. Mangos, D.N., *Silica nanoparticles grown from organofunctionalised trialkoxysilanes: Synthesis, High Density Modification Strategies and Application.* PhD Thesis, 2016.
94. Toster, J. and D. Lewis, *Investigation of Roughness Periodicity on the Hydrophobic Properties of Surfaces*.* Australian Journal of Chemistry, 2015.
95. Zhenda Lu, L.S., Kevin Nguyen, Chuanbo Gao, and Yadong Yin, *Formation Mechanism and Size Control in One-Pot Synthesis of Mercapto-Silica Colloidal Spheres.* Langmuir, 2011. **27**: p. 3372–3380.
96. Ishimura, M.N.a.K., *Synthesis and Characterization of Organosilica Nanoparticles Prepared from 3-Mercaptopropyltrimethoxysilane as the Single Silica Source.* J. Phys. Chem. C, 2007. **111**: p. 18892-18898.
97. Innocenzi, P., *From the Precursor to a Sol*, in *The Sol to Gel Transition*. 2016. p. 7-25.
98. Uygun, M.T., Mehmet Atilla and Y. Yagci, *Influence of Type of Initiation on Thiol-Ene "Click" Chemistry.* Macromolecular Chemistry and Physics, 2010. **211**(1): p. 103-110.
99. Tucker-Schwartz, A.K., R.A. Farrell, and R.L. Garrell, *Thiol-ene click reaction as a general route to functional trialkoxysilanes for surface coating applications.* J Am Chem Soc, 2011. **133**(29): p. 11026-9.
100. Tyson, E.L., M.S. Ament, and T.P. Yoon, *Transition metal photoredox catalysis of radical thiol-ene reactions.* J Org Chem, 2013. **78**(5): p. 2046-50.
101. Lowe, A.B., *Thiol-ene "click" reactions and recent applications in polymer and materials synthesis.* Polymer Chemistry, 2010. **1**(1): p. 17.
102. Hartmuth C. Kolb, M.G.F., and K. Barry Sharpless, *Click Chemistry: Diverse Chemical Function from a Few Good Reactions.* Angew Chem Int Ed, 2001. **40**: p. 2004-2021.
103. Mai, T.B., et al., *Covalent functionalization of silica nanoparticles with poly(N-isopropylacrylamide) employing thiol-ene chemistry and activator regenerated by electron transfer ATRP protocol.* Journal of Materials Science, 2013. **49**(4): p. 1519-1526.
104. Kotsuchibashi, Y., et al., *Fabrication of doubly responsive polymer functionalized silica nanoparticles via a simple thiol-ene click chemistry.* Polymer Chemistry, 2012. **3**(9): p. 2545-2550.

105. Cheng, X., et al., *One-pot synthesis of colloidal silicon quantum dots and surface functionalization via thiol-ene click chemistry.* Chem Commun (Camb), 2012. **48**(97): p. 11874-6.
106. Chen, Y., et al., *Vinyl functionalized silica hybrid monolith-based trypsin microreactor for on line digestion and separation via thiol-ene "click" strategy.* J Chromatogr A, 2011. **1218**(44): p. 7982-8.
107. Michaelis, L., and Menten, M, *Die kinetik der invertinwirkung.* Biochemistry Zeitung, 1913. **49**: p. 333-369.
108. Briggs, G.E., and Haldane, J. B., *A Note on the Kinetics of Enzyme Action.* Biochem J, 1925. **19**: p. 338-339.
109. Chang, R., *Enzyme kinetics*, in *Physical Chemistry for the Biosciences*. 2005, University Science Books.
110. Wu, M. and W.R. Algar, *Acceleration of proteolytic activity associated with selection of thiol ligand coatings on quantum dots.* ACS Appl Mater Interfaces, 2015. **7**(4): p. 2535-45.
111. Wang, J., et al., *Soft interactions at nanoparticles alter protein function and conformation in a size dependent manner.* Nano Lett, 2011. **11**(11): p. 4985-91.
112. Anne, A. and C. Demaille, *Kinetics of enzyme action on surface-attached substrates: a practical guide to progress curve analysis in any kinetic situation.* Langmuir, 2012. **28**(41): p. 14665-71.
113. Satish Nayak, W.-S.Y., and Milan Mrksich, *Determination of Kinetic Parameters for Interfacial Enzymatic Reactions on Self-Assembled Monolayers.* Langmuir, 2007. **23**(10): p. 5578-5583.
114. Hye Jin Lee, A.W.W., and Robert M. Corn, *Creating Advanced Multifunctional Biosensors with Surface Enzymatic Transformations.* Langmuir, 2006. **22**(12): p. 5241-5250.
115. Hye Jin Lee, A.W.W., Terry T. Goodrich, Shiping Fang, and and R.M. Cor, *Surface Enzyme Kinetics for Biopolymer Microarrays: a Combination of Langmuir and Michaelis-Menten Concepts.* Langmuir, 2005. **21**(9): p. 4050-4057.
116. Shiping Fang, H.J.L., Alastair W. Wark, Hyun Min Kim, and Robert M. Corn, *Determination of Ribonuclease H Surface Enzyme Kinetics by Surface Plasmon Resonance Imaging and Surface Plasmon Fluorescence Spectroscopy.* Anal. Chem, 2005. **77**(20): p. 6528-6534.
117. Kari, J., et al., *An Inverse Michaelis–Menten Approach for Interfacial Enzyme Kinetics.* ACS Catalysis, 2017: p. 4904-4914.
118. Jeoh, T., et al., *Mechanistic kinetic models of enzymatic cellulose hydrolysis-A review.* Biotechnol Bioeng, 2017. **114**(7): p. 1369-1385.
119. Dennis, A.M., J.B. Delehanty, and I.L. Medintz, *Emerging Physicochemical Phenomena along with New Opportunities at the Biomolecular-Nanoparticle Interface.* J Phys Chem Lett, 2016. **7**(11): p. 2139-50.
120. Joyce C. Breger, M.G.A., Scott A. Walper, Eunkeu Oh, Kimihiro Susumu, and J.R.D. Michael H. Stewart, and Igor L. Medintz, *Understanding How Nanoparticle Attachment Enhances Phosphotriesterase Kinetic Efficiency.* ACS Nano, 2015. **9**(8): p. 8491-8503.
121. Ding, S., et al., *Increasing the activity of immobilized enzymes with nanoparticle conjugation.* Curr Opin Biotechnol, 2015. **34**: p. 242-50.
122. Brown Iii, C.W., et al., *Kinetic enhancement of the diffusion-limited enzyme beta-galactosidase when displayed with quantum dots.* RSC Advances, 2015. **5**(113): p. 93089-93094.
123. Johnson, B.J., et al., *Understanding enzymatic acceleration at nanoparticle interfaces: Approaches and challenges.* Nano Today, 2014. **9**(1): p. 102-131.
124. Ghosh, S., et al., *Modulation of glyceraldehyde-3-phosphate dehydrogenase activity by surface functionalized quantum dots.* Phys Chem Chem Phys, 2014. **16**(11): p. 5276-83.
125. Kartal, O. and O. Ebenhoh, *A generic rate law for surface-active enzymes.* FEBS Lett, 2013. **587**(17): p. 2882-90.

126. Algar, W.R., et al., *Proteolytic activity at quantum dot-conjugates: kinetic analysis reveals enhanced enzyme activity and localized interfacial "hopping".* Nano Lett, 2012. **12**(7): p. 3793-802.
127. Jing Li, S.N., and Milan Mrksich, *Rate Enhancement of an Interfacial Biochemical Reaction through Localization of Substrate and Enzyme by an Adaptor Domain.* J. Phys. Chem. B, 2010. **114**(46): p. 15113-15118.
128. Xu, W., J.S. Kong, and P. Chen, *Single-Molecule Kinetic Theory of Heterogeneous and Enzyme Catalysis.* The Journal of Physical Chemistry C, 2009. **113**(6): p. 2393-2404.
129. Joseph Deere, R.F.D.O., Bartłomiej Tomaszewski, Sarah Millar, Antonia Lalaouni, Laura F. Solares, Sabine L. Flitsch, and Peter J. Halling, *Kinetics of Enzyme Attack on Substrates Covalently Attached to Solid Surfaces: Influence of Spacer Chain Length, Immobilized Substrate Surface Concentration and Surface Charge.* Langmuir, 2008. **24**(20): p. 11762-11769.
130. Xu, F. and H. Ding, *A new kinetic model for heterogeneous (or spatially confined) enzymatic catalysis: Contributions from the fractal and jamming (overcrowding) effects.* Applied Catalysis A: General, 2007. **317**(1): p. 70-81.
131. Medintz, I.L., et al., *Proteolytic activity monitored by fluorescence resonance energy transfer through quantum-dot-peptide conjugates.* Nat Mater, 2006. **5**(7): p. 581-9.
132. C. Wua, b., T.F. Jima, Z. Gana,c, Y. Zhaob, S. Wang, *A heterogeneous catalytic kinetics for enzymatic biodegradation of poly(e-caprolactone) nanoparticles in aqueous solution.* Polymer, 2000. **41**: p. 3593-3597.
133. Otto G. Berg, B.-Z.Y., Joe Rogers and Mahendra Kumar Jain, *Interfacial Catalysis by Phospholipase A2: Determination of the Interfacial Kinetic rate Constants.* Biochemistry, 1991. **30**(29): p. 7283-7297.
134. Robert Verger, M.C.E.M.a.H.D.H., *Action of Phopholipase A at Interfaces*.* Journal of Biological Chemistry, 1973. **248**(11): p. 4023-4034.
135. Ladan L. Foose, H.W.B., and C. J. Radke, *Kinetics of Adsorption and Proteolytic Cleavage of a Multilayer Ovalbumin Film by Subtilisin Carlsberg.* Langmuir, 2008. **24**(14): p. 7388-7393.
136. Tzafriri, A., *Michaelis–Menten kinetics at high enzyme concentrations.* Bulletin of Mathematical Biology, 2003. **65**(6): p. 1111-1129.
137. Pamela B. Gaspers, C.R.R., and Alice P. Gast, *Enzymes on Immobilized Substrate Surfaces: Diffusion.* Langmuir, 1994. **10**(8): p. 2699-2704.
138. Joon-H. Kim, S.R., James T. Kellis Jr., A. J. Poulose, Alice P. Gast and Channing R. Robertson, *Protease Adsorption and Reaction on an Immobilized Substrate Surface.* Langmuir, 2002. **18**(16): p. 6312-6318.
139. Bansal, P., et al., *Modeling cellulase kinetics on lignocellulosic substrates.* Biotechnol Adv, 2009. **27**(6): p. 833-48.
140. Prigodich, A.E., A.H. Alhasan, and C.A. Mirkin, *Selective enhancement of nucleases by polyvalent DNA-functionalized gold nanoparticles.* J Am Chem Soc, 2011. **133**(7): p. 2120-3.
141. Stephen Suresh, S.T., Fred R Opperdoes, Paul AM Michels and Wim GJ Hol, *A potential target enzyme for trypanocidal drugs revealed by the crystal structure of NAD-dependent glycerol-3-phosphate dehydrogenase from Leishmania mexicana.* Structure, 2000. **8**: p. 541.
142. Pizer, M.K.a.L.I., *Purification and Regulatory Properties of the Biosynthetic l-Glycerol 3-Phosphate Dehydrogenase from Escherichia coli.* J. Biol. Chem, 1969. **244**: p. 3316-3323.
143. The UniProt, C., *UniProt: the universal protein knowledgebase.* Nucleic Acids Res, 2017. **45**(D1): p. D158-D169.
144. Pettersen, E.F., et al., *UCSF Chimera--a visualization system for exploratory research and analysis.* J Comput Chem, 2004. **25**(13): p. 1605-12.
145. Raj, S.B., S. Ramaswamy, and B.V. Plapp, *Yeast alcohol dehydrogenase structure and catalysis.* Biochemistry, 2014. **53**(36): p. 5791-803.

146. Thomas J. Smith, P.E.P., Timothy Schmidt, Jie Fang, Charles A. Stanley, *Structures of bovine glutamate dehydrogenase complexes elucidate the mechanism of purine regulation.* Journal of Molecular Biology, 2001. **307**(2): p. 707-720.
147. Smith, P.E.P.a.T.J., *The structure of bovine glutamate dehydrogenase provides insights into the mechanism of allostery.* Structure, 1999. **7**(7): p. 769-782.
148. Jenie, S.N., B. Prieto-Simon, and N.H. Voelcker, *Development of L-lactate dehydrogenase biosensor based on porous silicon resonant microcavities as fluorescence enhancers.* Biosens Bioelectron, 2015. **74**: p. 637-43.
149. Larsen, T., *Determination of lactate dehydrogenase (LDH) activity in milk by a fluorometric assay.* Journal of Dairy Research, 2005. **72**(2): p. 209-216.
150. Rampersad, S.N., *Multiple applications of Alamar Blue as an indicator of metabolic function and cellular health in cell viability bioassays.* Sensors (Basel), 2012. **12**(9): p. 12347-60.
151. Ödman, P., W.B. Wellborn, and A.S. Bommarius, *An enzymatic process to α-ketoglutarate from l-glutamate: the coupled system l-glutamate dehydrogenase/NADH oxidase.* Tetrahedron: Asymmetry, 2004. **15**(18): p. 2933-2937.
152. P. Pietta, P.M., M. Pace *HPLC Assay Of Enzymatic Activities.* Chromatographia, 1987. **24**: p. 439-441.
153. Carlos A. R. Costa, C.A.P.L., and Fernando Galembeck, *Size Dependence of Stober Silica Nanoparticle Microchemistry.* J. Phys. Chem. B, 2003. **107**: p. 4747-4755.
154. Vernon-Parry, K.D., *Scanning electron microscopy: an introduction.* III-Vs Review, 2000. **13**(4): p. 40-44.
155. Rosen, J.E. and F.X. Gu, *Surface functionalization of silica nanoparticles with cysteine: a low-fouling zwitterionic surface.* Langmuir, 2011. **27**(17): p. 10507-13.
156. Kato, H., et al., *Accurate Size and Size-Distribution Determination of Polystyrene Latex Nanoparticles in Aqueous Medium Using Dynamic Light Scattering and Asymmetrical Flow Field Flow Fractionation with Multi-Angle Light Scattering.* Nanomaterials, 2012. **2**(4): p. 15-30.
157. Lim, J., et al., *Characterization of magnetic nanoparticle by dynamic light scattering.* Nanoscale Research Letters, 2013. **8**(1): p. 381.
158. Tadros, T., *Encyclopedia of Colloid and Interface Science*. 2013.
159. Shields, S.L.a.J.E., *Powder Surface Area and Porosity.* 1991: p. 14-27.
160. Elmer, P., *FT-IR Spectroscopy: Attenuated Total Reflectance (ATR).* Technical Note, 2005: p. 1-5.
161. Bellamy, M.K., *Using FTIR-ATR Spectroscopy To Teach the Internal Standard Method.* Journal of Chemical Education, 2010. **87**(12): p. 1300-1401.
162. Saczk, A.A., et al., *Rapid and sensitive method for the determination of acetaldehyde in fuel ethanol by high-performance liquid chromatography with UV-Vis detection.* Anal Bioanal Chem, 2005. **381**(8): p. 1619-24.
163. Schneider, C.A.R., W. S. & Eliceiri, K. W, *NIH Image to ImageJ: 25 years of image analysis.* Nature methods, 2012. **9**(7): p. 671-675.
164. Yoshino, J. and S. Imai, *Accurate measurement of nicotinamide adenine dinucleotide (NAD(+)) with high-performance liquid chromatography.* Methods Mol Biol, 2013. **1077**: p. 203-15.
165. Hung-Chang Chou, S.-J.C., Ying-Ling Liu, and Teh-Min Hu, *Direct Formation of S-Nitroso Silica Nanoparticles from a Single Silica Source.* Langmuir, 2014. **30**: p. 812-882.
166. Li, B., et al., *Biofunctionalization of silica microspheres for protein separation.* Mater Sci Eng C Mater Biol Appl, 2013. **33**(5): p. 2595-600.
167. Jia, S., et al., *Facile and scalable preparation of highly wear-resistance superhydrophobic surface on wood substrates using silica nanoparticles modified by VTES.* Applied Surface Science, 2016. **386**: p. 115-124.
168. Anderson, B.M.A.a.C.D., *The Effect of Buffers on Nicotinamide Adenine Dinucleotide Hydrolysis.* Journal of Biological Chemistry, 1963. **238**: p. 1475-1478.
169. Sarac, A.S., *Redox Polymerisation.* Prog. Polym. Sci., 1999. **24**: p. 1149-1204.

170. Fales, E.S.B.a.H.M., *Overalkylation of a Protein Digest with Iodoacetamide.* Anal. Chem, 2001. **73**: p. 3576-3582.
171. Chait, S.S.a.B.T., *Modification of Cysteine Residues by Alkylation. A Tool in Peptide Mapping and Protein Identification.* Anal. Chem, 1998. **70**: p. 5150-5158.
172. Maurer, S.A., C.N. Bedbrook, and C.J. Radke, *Cellulase Adsorption and Reactivity on a Cellulose Surface from Flow Ellipsometry.* Industrial & Engineering Chemistry Research, 2012. **51**(35): p. 11389-11400.
173. Vilanova, O., et al., *Understanding the Kinetics of Protein-Nanoparticle Corona Formation.* ACS Nano, 2016. **10**(12): p. 10842-10850.
174. Bekdemir, A. and F. Stellacci, *A centrifugation-based physicochemical characterization method for the interaction between proteins and nanoparticles.* Nat Commun, 2016. **7**: p. 13121.
175. Liu, L., et al., *Determining the Secondary Structure of Membrane Proteins and Peptides Via Electron Spin Echo Envelope Modulation (ESEEM) Spectroscopy.* Methods Enzymol, 2015. **564**: p. 289-313.
176. Folin G. Halaka, G.T.B.a.J.L.D., *Properties of 5-Methylphenazinium Methyl Sulfate: REACTION OF THE OXIDIZED FORM WITH NADH AND OF THE REDUCED FORM WITH OXYGEN.* Journal of Biological Chemistry, 1982. **257**(3): p. 1458-1461.
177. Loewen, C.R.K.a.M.J., *Amide Resonance" Correlates with a Breadth of C-N Rotation Barriers.* J Am Chem Soc, 2007. **129**: p. 2521-2528.
178. Rahman, M., et al., *The Aromatic Stacking Interactions Between Proteins and their Macromolecular Ligands.* Current Protein & Peptide Science, 2015. **16**(6): p. 502-512.
179. Wilding, K.M., et al., *The emerging impact of cell-free chemical biosynthesis.* Curr Opin Biotechnol, 2018. **53**: p. 115-121.
180. Cipolatti, E.P., et al., *Current status and trends in enzymatic nanoimmobilization.* Journal of Molecular Catalysis B: Enzymatic, 2014. **99**: p. 56-67.
181. Datta, S., L.R. Christena, and Y.R.S. Rajaram, *Enzyme immobilization: an overview on techniques and support materials.* 3 Biotech, 2012. **3**(1): p. 1-9.
182. Zhang, Y., et al., *Bioinspired Immobilization of Glycerol Dehydrogenase by Metal Ion-Chelated Polyethyleneimines as Artificial Polypeptides.* Sci Rep, 2016. **6**: p. 24163.
183. Guzik, U., K. Hupert-Kocurek, and D. Wojcieszynska, *Immobilization as a strategy for improving enzyme properties-application to oxidoreductases.* Molecules, 2014. **19**(7): p. 8995-9018.
184. Hachisuka, S.I., T. Sato, and H. Atomi, *Metabolism Dealing with Thermal Degradation of NAD(+) in the Hyperthermophilic Archaeon Thermococcus kodakarensis.* J Bacteriol, 2017. **199**(19).
185. Hofmann, D., et al., *Structure elucidation of the thermal degradation products of the nucleotide cofactors NADH and NADPH by nano-ESI-FTICR-MS and HPLC-MS.* Anal Bioanal Chem, 2010. **398**(7-8): p. 2803-11.
186. NATHAN 0. KAPLAN, S.P.C., AND CATHERINE CARR BARNES, *EFFECT OF ALKALI ON DIPHOSPHOPYRIDINE NUCLEOTIDE*.* THe Journal of Biological Chemistry, 1951. **191**: p. 461-472.
187. Li, F., et al., *Thermal stability of DNA functionalized gold nanoparticles.* Bioconjug Chem, 2013. **24**(11): p. 1790-7.
188. Kensuke Akamatsu, M.K., Yoko Shibata, Shu-ichi Nakano, Daisuke Miyoshi, Hidemi Nawafune, and Naoki Sugimoto, *A DNA Duplex with Extremely Enhanced Thermal Stability Based on Controlled Immobilization on Gold Nanoparticles.* Nano Lett, 2006. **6**(3): p. 491–495.
189. Nicole Herra, Juliane Ratzkaa,, Lars Lauterbachb, Oliver Lenzc, Marion B. Ansorge-Schumache, *Stability enhancement of an O2-tolerant NAD+-reducing [NiFe]-hydrogenase by a combination of immobilisation and chemical modification.* Journal of Molecular Catalysis B: Enzymatic, 2013. **97**: p. 169-174.
190. Clemons, T.D., et al., *Multifunctional nanoadditives for the thermodynamic and kinetic stabilization of enzymes.* Nanoscale, 2011. **3**(10): p. 4085-7.

191. Rizvi, S.A.A. and A.M. Saleh, *Applications of nanoparticle systems in drug delivery technology.* Saudi Pharm J, 2018. **26**(1): p. 64-70.

APPENDIX

A.1: BET isotherms of thiol SiNPs

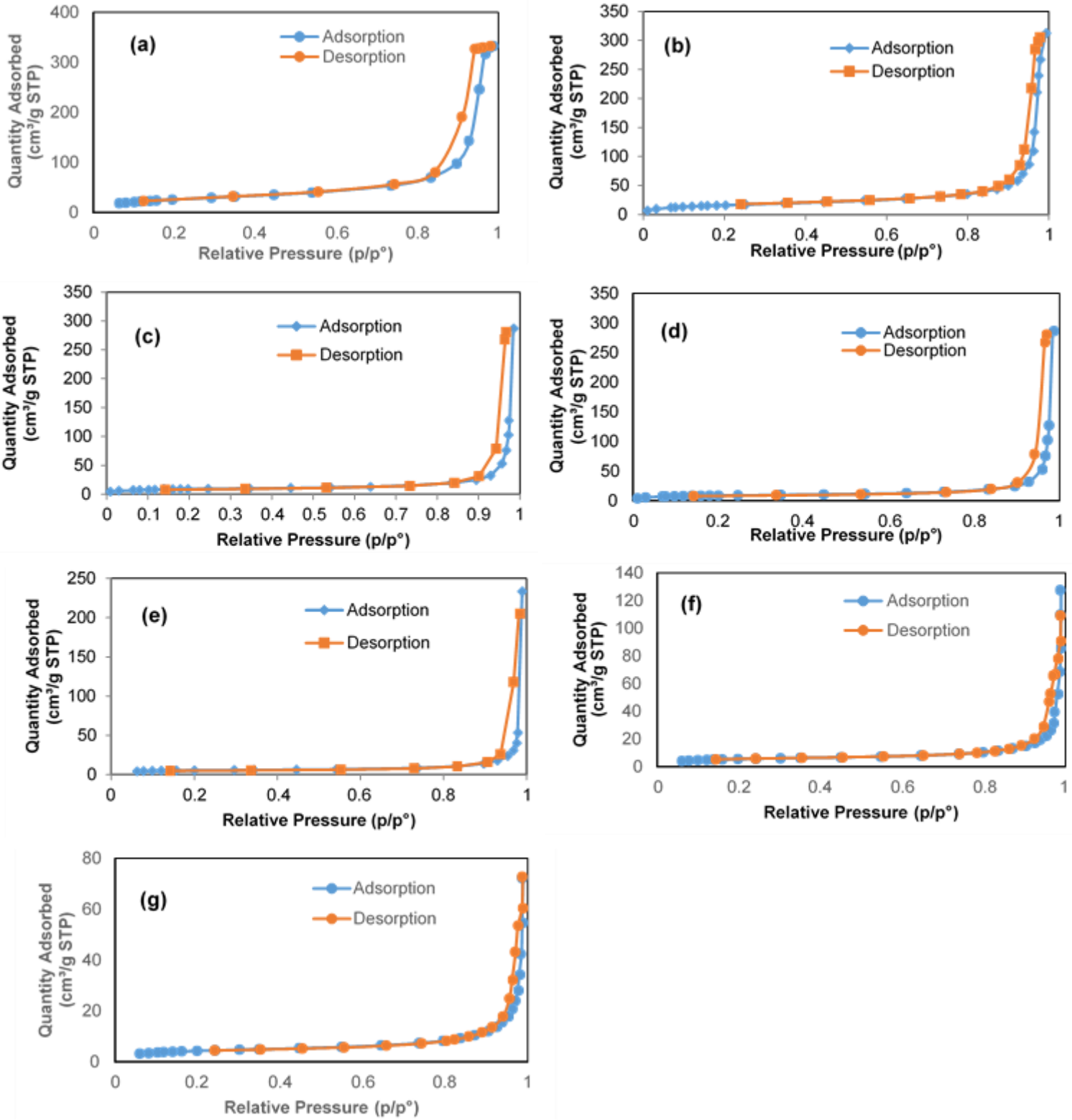

Figure A1: BET Isotherm of thiol terminated SiNPs with average diameter of a) 50 ± 4 nm, b) 98 ± 8 nm, c) 149 ± 12 nm, d) 167 ± 10 nm, e) 204 ± 17 nm, f) 247 ± 9 nm, g) 296 ± 7 nm.

A.2: BET isotherms of vinyl SiNPs

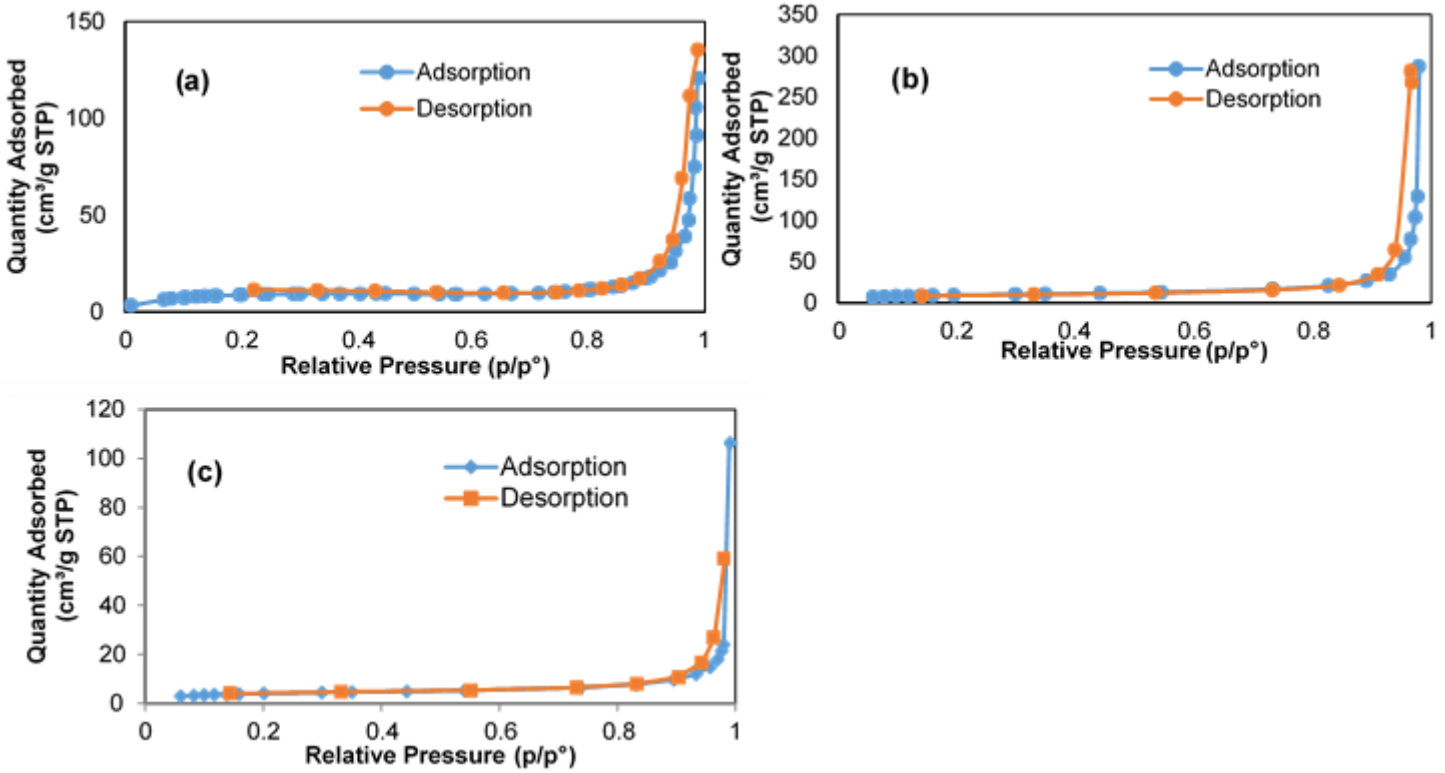

Figure A2: BET Isotherm of vinyl terminated SiNPs with average diameter of a) 104 nm, b) 175 nm and c) 204 nm.

A.3: SEM images of thiol SiNPs

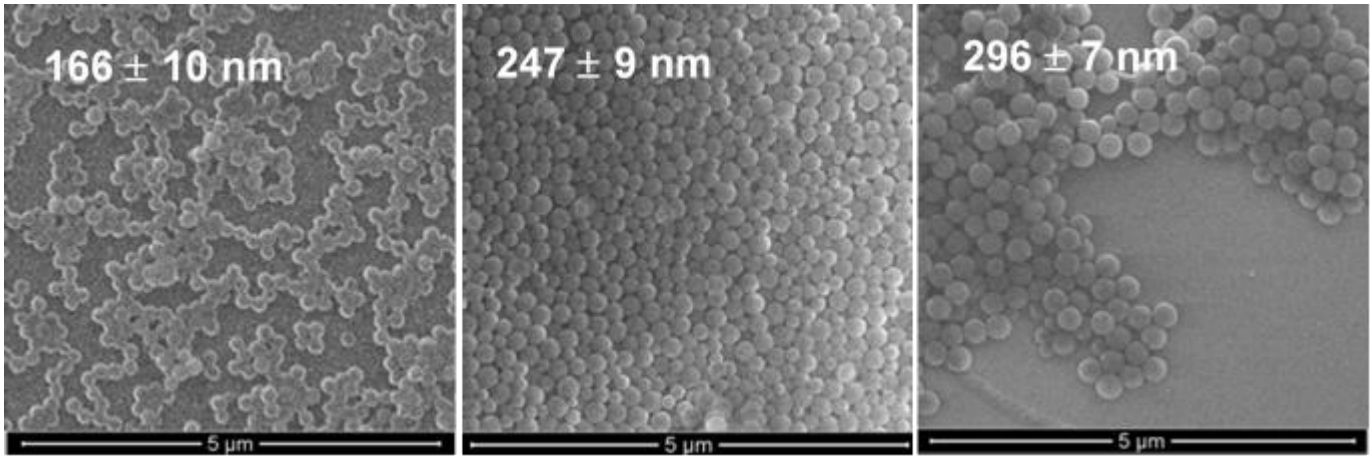

Figure A3: SEM images of thiol terminated SiNPs with an average diamter of 167 ± 10 nm, 247 ± 9 nm, and 296 ± 7 nm.

A.4 Correction for the NAD/SiNP FTIR spectral overlap

Figure A4 shows an ATR-FTIR spectrum of NAD overlaid on a thiol SiNP spectrum. It can be seen that the NAD spectra overlaps every peak of the SiNP spectra, and thus no peaks will be unaffected by the addition of NAD.

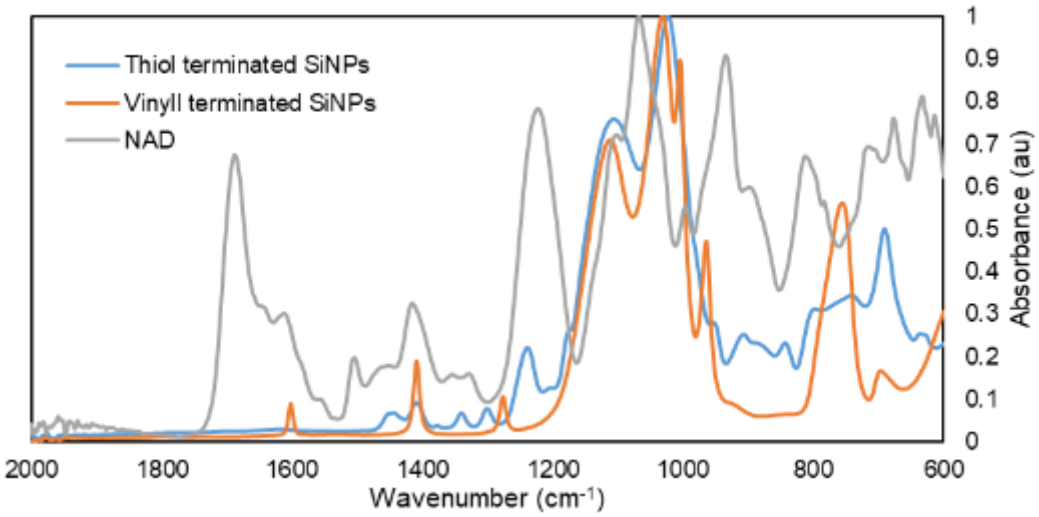

Figure A4**:** Overlay of normalized NAD FTIR spectrum over normalized thiol terminated SiNP FTIR spectrum.

In order to use the Si-O-Si band at ~1020cm^{-1} of the SiNPs as an internal reference as previous, the peak has to be corrected for the addition of NAD. This was achieved by determining the peak height ratio of the amide C=O stretch at 1700cm^{-1} due to NAD in the SiNP mixture to that of a normalized NAD spectrum. This ratio was then multiplied by every data point of the NAD spectrum The scaled NAD spectra is then subtracted from the FTIR spectra of the SiNP/NAD mixture in the overlap region from 600 to 1200 cm^{-1}. Figure A5 confirms that this method accurately corrects the NAD spectrum to the absorbance contribution of NAD in the NAD/SiNP spectrum.

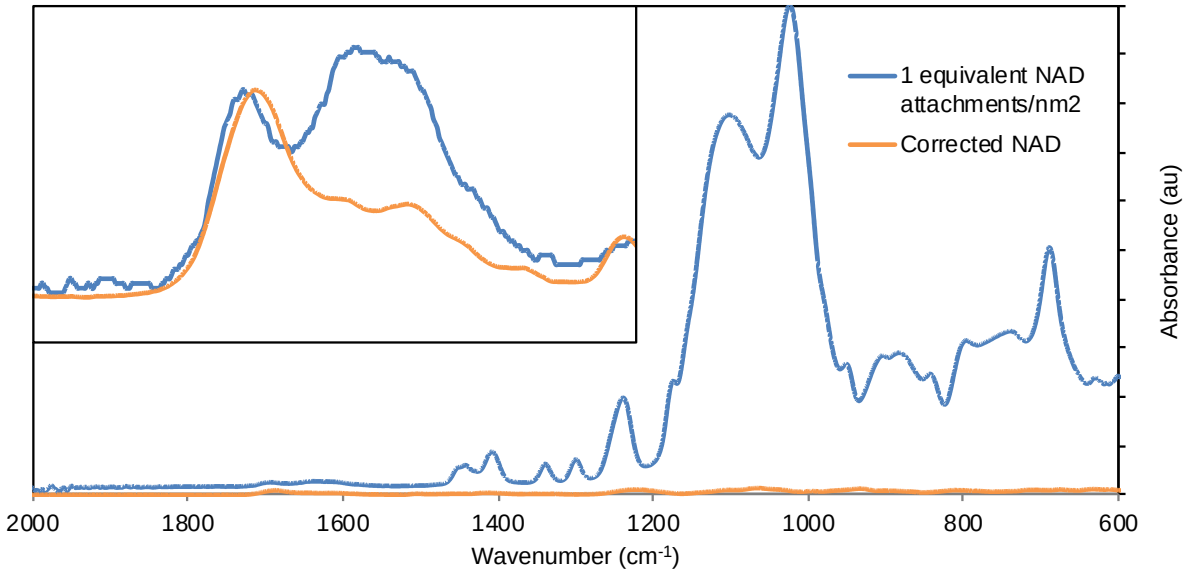

Figure A5: ATR-FTIR spectra of thiol terminated SiNPs mixed with the equivalent of 1 NAD attachment/nm^2 and overlay of NAD FTIR spectra scaled to match contribution in the SiNP/NAD mixture.

A.5: Analysis of NAD attachment washings by HPLC

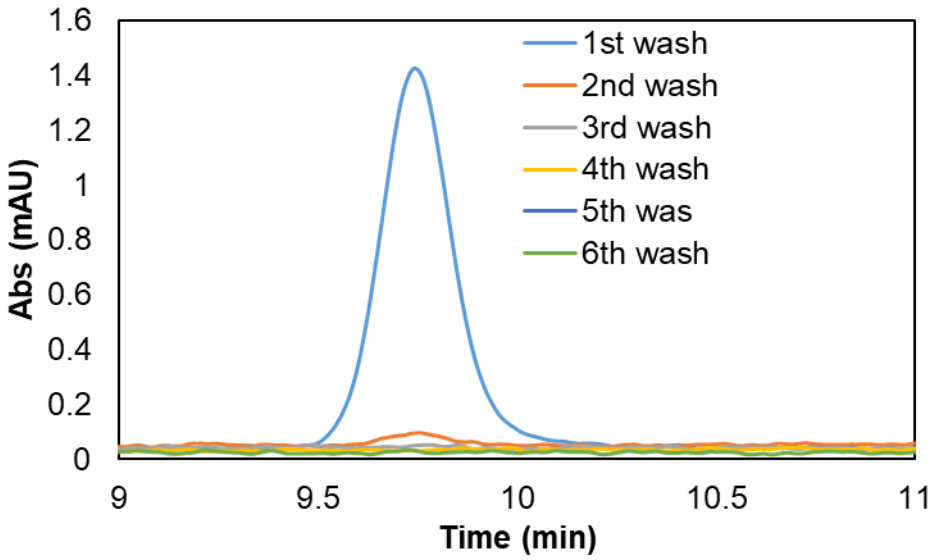

Figure A6: HPLC chromatogram of washing after attachment of nonene-2AE-NAD to the surface of thiol terminated SiNPs. No nonene-2AE-NAD is detected after 3 washes,

A.6 ATR-FTIR spectra of alkylating agents

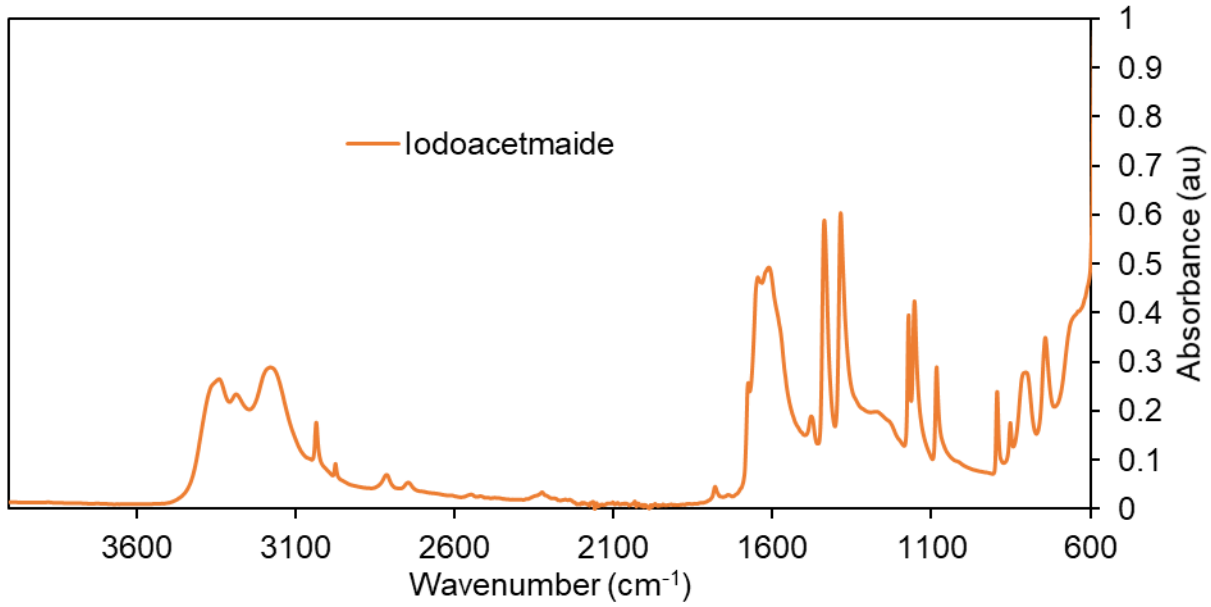

Figure A7: ATR-FTIR spectra of iodoacetamide.

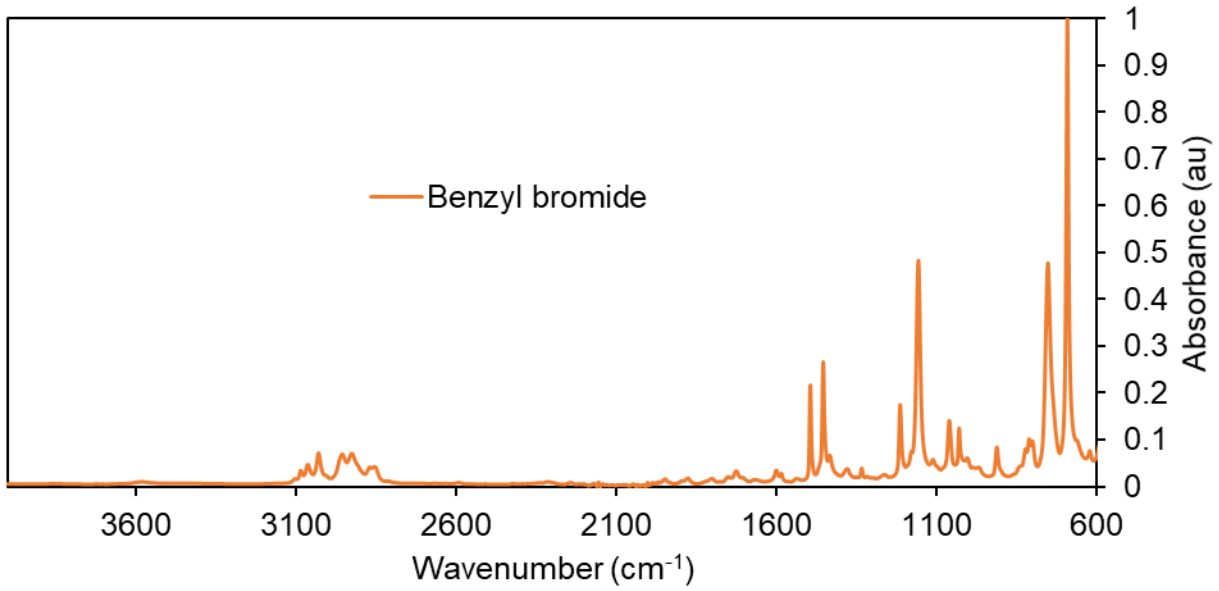

Figure A8: ATR-FTIR spectra of benzyl bromide

A.7: Quantification of NADH/resorufin concentration

In the resazurin/PMS^+ coupled assay, the NADH formed by the catalytic cycle of EcG3PD or ADH reduces resazurin to the highly fluorescent resorufin in the presence of PMS^+ in a 1:1 molar ratio, as per Scheme 6.1(iv) [45]. In order to quantify the concentration of resorufin, and thus NADH, produced in the coupled assay reaction, controlled amounts of free NADH were applied to the resazurin/PMS^+ coupled assay containing no enzyme or NAD. The reaction was allowed to go to completion and the resulting fluorescence intensity of these standards was then measured and plotted as a function of NADH concentration in order to prepare the calibration curve shown in Figure A9. Using linear regression, the calibration curve in Figure A9 is applied to the increase in fluorescence intensity measured by the resazurin/PMS^+ coupled enzyme reactions in order to determine the rate of NADH formation. This allows the fluorometrically measured reaction rates of enzymes to be expressed in standard molar units, *i.e.* μmol/min.

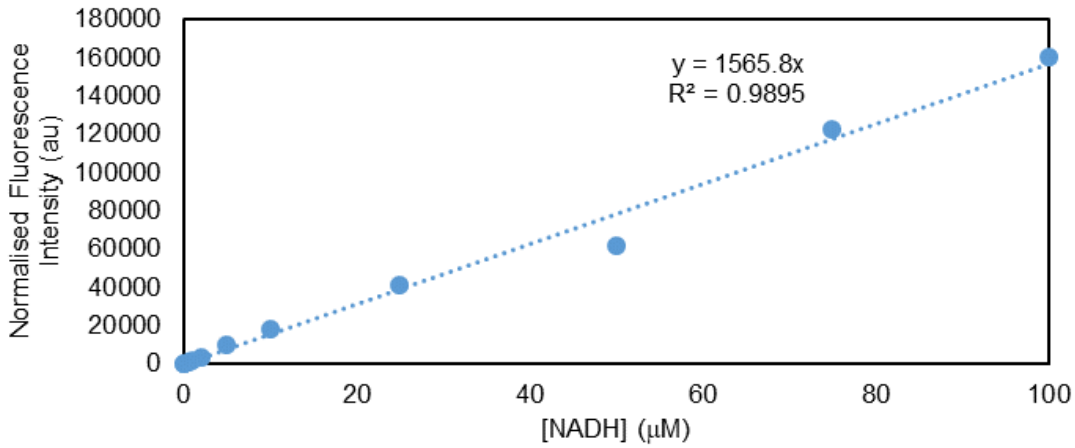

Figure A9: Fluorescence intensity of resorufin produced after applying different concentrations of NADH to the resazurin/PMS^+ coupled assay without enzyme or NAD.